Additive Manufacturing on Chip

Von der Fakultät 1 - MINT - Mathematik, Informatik, Physik,
Elektro- und Informationstechnik
der Brandenburgischen Technischen Universität Cottbus–Senftenberg
genehmigte Dissertation
zur Erlangung des akademischen Grades eines

Doktor der Ingenieurwissenschaften

vorgelegt von

Severin Franziskus Georg Schweiger
geboren am 27.9.1988 in Göggingen

Vorsitzender: Prof. Dr. rer. nat. habil. Götz Seibold

Gutachter: Prof. Dr.-Ing. Dr. rer. nat. habil. Harald Schenk

Gutachter: Prof. Dr. mont. Mario Kupnik

Tag der mündlichen Prüfung: 5.7.2023

DOI: https://doi.org/10.26127/BTUOpen-6455

Preface

This dissertation was written during my work as a scientific researcher at the Fraunhofer Institute for Photonic Microsystems. At this point I would like to acknowledge all those who contributed to the success of this work.

In particular, I would like to thank Prof. Dr.-Ing. Dr. rer. nat. habil. Harald Schenk and Prof. Dr. mont. Mario Kupnik for enabling this work and for their consultations. Furthermore, I appreciate the diligent supervision and the precise advice I received from Dr. Sebastian Meyer and Dr. Sandro G. Koch, especially regarding my thesis but for my professional career as well. I would like to thank my colleagues Dr. Tim Schulze, Sören Köble, Dr. Anton Melnikov, Marco Kircher, Dr. Marcel Krenkel, Shashank and Dr. Nicolas Lange for their enormous wealth of experience and their kind helpfulness. I want to thank the students I supervised and gladly cooperated with: Maria C. Mesa Ortega, Karuna S. Nagaral, Sushma S. Sennakesavaperumal and Ajeesh Ajay.

The friendly, open-minded and extremely supportive atmosphere within Fraunhofer has greatly facilitated the preparation of this work. Sincerely, I would like to thank all those not mentioned by name for their support.

I want to communicate my immense gratitude towards my family and especially my parents. I dedicate this work to Renate M. Schweiger and Johann Schweiger for their life-long support for, and steadfast trust in all their children.

Finally, I would like to thank Lucille M. S. Friebel for her skillful support and devoted patience. I hope to be able to repay her in kind.

Content

Abstract

Recent advances in additive manufacturing offer promising opportunities for the fabrication of structures on existing micro-(opto-acoustic-)electro-mechanical systems, i.e., chips. This is of particular significance in research and development due to the adaptability and adaptation speed of additive manufacturing. These advantages provide the ability to individualize the fabrication of structures and to enable the rapid prototyping approach. The combination of additive manufacturing on chip already enables current research, especially in photonic and microfluidic fields. Despite this, additive manufacturing on chip has never been applied to acoustic sensors or micro-positioning chips. Such devices could benefit from the mentioned advantages, especially for the fabrication of beam shaping waveguides, packaging, grating and end effector structures. Additive manufacturing by two-photon polymerization lithography gathers interest in industry and research due to its capabilities for the fabrication of structures with minimum feature sizes beyond the diffraction limit. The objective of this work is the investigation of additive manufacturing on chip by two-photon polymerization lithography at the example of an acoustic sensor and a micro-positioning chip. One of the greatest challenges is posed by the optical, thermodynamic, adhesion and alignment effects, which are introduced to the fabrication process by these complex substrates. Optical and thermodynamic models were established, and simulations were performed, culminating in a compensation method to address these effects, which was verified by parameter studies. The substrate alignment was investigated via optical technique, resulting in the development, manufacturing and verification of a novel alignment upgrade to the fabrication system employed in this work. The influence of process materials posed another challenge, as they led to chip performance alterations and restrictions. Chips treated with these materials were characterized, e.g., using high frequency optical microphones. Owing to the high precision of the alignment upgrade and the compensation method developed in this work, additive manufacturing on chip using two-photon polymerization lithography on the investigated devices was reported for the first time and presented for expedient examples, e.g., waveguides, end effectors and gratings. The residue contamination was determined as the main origin of the exhibited performance issues. Development strategies were recommended for further research, to enable additive manufacturing on chip insensitive to residual materials. In this work, the requirements for additive manufacturing on chip were illustrated and the fundamental arrangement to enable the rapid prototyping approach as well as design individualization were demonstrated. The compensation methods developed in this work facilitate upcoming research on desirable chip types that form the basis for optical and microfluidic applications.

Zusammenfassung

Jüngste Fortschritte in der additiven Fertigung bieten vielversprechende Möglichkeiten zur Herstellung von Strukturen auf mikro-(opto-akustischen) elektromechanischen Systemen, d.h. Chips. Dies ist aufgrund der Anpassungsfähigkeit und -geschwindigkeit der additiven Fertigung von besonderer Bedeutung für die Forschung und Entwicklung. Diese Vorteile bieten die Möglichkeit, die Herstellung von Strukturen zu individualisieren und die Rapid-Prototyping-Methode einzusetzen. Der Kombinationsansatz der additiven Fertigung auf Chipoberflächen ermöglicht bereits Forschung, insbesondere in der Photonik und Mikrofluidik. Es wurde auf akustischen Sensoren oder Mikro-Positionierungschips bisher nie angewendet. Solche Komponenten könnten von den genannten Vorteilen profitieren, insbesondere bei der Herstellung von strahlformenden Wellenleitern sowie von Gitter- und Endeffektorstrukturen. Additive Fertigung mittels Zwei-Photonen-Polymerisationslithographie stößt auf großes Interesse, da der Prozess die Fertigung von Strukturen mit minimalen Dimensionen jenseits der Beugungsgrenze ermöglicht. Ziel dieser Arbeit ist die Untersuchung von dieses Fertigungsansatzes am Beispiel eines akustischen Sensors und eines Mikro-Positionierungschips. Eine der größten Herausforderungen stellen die optischen, thermodynamischen, Adhäsions- und Ausrichtungseffekte dar, die durch diese komplexen Substrate eingebracht werden. Auf der Grundlage von optischen und thermodynamischen Modellen wurden Simulationen durchgeführt, die in einer Kompensationsmethode zur Bewältigung der Effekte kulminierten, welche durch Parameterstudien verifiziert wurde. Die Substratausrichtung wurde untersucht, was zur Entwicklung und Herstellung eines Ausrichtungs-Upgrades für das hier verwendete Fertigungssystem führte. Der Einfluss der Prozessmaterialien stellte eine weitere Herausforderung dar, da sie zu Veränderungen der Leistungsfähigkeit der Chips führten. Mit Entwicklungsmitteln und Fotolacken behandelte Chips wurden unter anderem mit optischen Hochfrequenzmikrofonen charakterisiert. Aufgrund der hohen Präzision der Kompensationsmethode und des Ausrichtungs-Upgrades, wurde erstmals die additive Fertigung mittels Zwei-Photonen-Polymerisationslithographie auf den untersuchten Bauelementen berichtet und an Wellenleitern, Endeffektoren und Gittern demonstriert. Die Kontamination durch Rückstände wurde als Hauptursache für die aufgezeigten Leistungsprobleme ermittelt. Es wurden Entwicklungsstrategien für die weitere Forschung empfohlen, um den Fertigungsansatz unempfindlich gegenüber Reststoffen zu machen. In dieser Arbeit wurden die Anforderungen an den Fertigungsansatz veranschaulicht und die grundlegende Anordnung zur Ermöglichung des Rapid-Prototyping-Ansatzes sowie der Design-Individualisierung demonstriert. Die in dieser Arbeit entwickelten Kompensationsmethoden ermöglichen die künftige Forschung an weiteren Chiptypen, die z. B. die Grundlage für optische oder mikrofluidische Anwendungen bilden.

Nomenclature

Abbreviations

Al	Aluminum
Al_2O_3	Aluminum oxide
AM	Additive manufacturing
AMOC	Additive manufacturing on chip
AOM	Acousto-optic modulator
CAD	Computer aided design
CMOS	Complementary metal-oxide semiconductor
CMUT	Capacitive micromachined ultrasonic transducer
DOF	Degree of freedom
DPN	Dip pen nanolithography
DRIE	Deep reactive ion etching
FEM	Finite element modeling
FFF	Fused filament fabrication
FOV	Field of view
FWHP	Full width at half prominence
GmbH	Gesellschaft mit beschränkter Haftung
IC	Integrated circuit
Inc.	Increment
IPA	2-propanol
IPMS	Institute for Photonic Microsystems
LOC	Lab-on-a-chip
MB-TPP	Multi-beam two-photon polymerization lithography (TPP)
MEMS	Micro-(opto-acoustic-)electro-mechanical system
µCT	Micro-computed tomography
µSLA	Micro-stereolithography
MPA	Multi-photon absorption
NED	Nanoscopic electrostatic drive
NED-µPS	NED-based micro-positioning platform
NIL	Nano-imprint lithography
NOVEC	NOVEC 7100

OK	Viable exposure
OPA	One-photon absorption
OX	Overexposure
PDMS	Polydimethylsiloxane
PGEMA	1-methoxy-2-propanol acetate
Resist	Photoresist
RLM	Reflective light microscope
RMS	Root mean squared
RoHS	Restriction of certain hazardous substances
SEM	Scanning electron microscope
SF	Semiconductor fabrication
Si	Silicon
SiO_2	Silicon dioxide
SLM	Selective laser melting
STED-TPP	Stimulated emission depletion TPP
TEM	Transverse electromagnetic
TiAl	Titanium aluminide
TPA	Two-photon absorption
TPP	Two-photon polymerization lithography
UV	Ultraviolet
UX	Underexposure
XO	Xolography

Latin Symbols

A	Cross-sectional area
a	Plate radius
a, b, c, f_P	Fit parameters
b	Bow reference plane distance
B	Substrate bow
c_0	Velocity of light in vacuum
c_H	Heat compensation factor
c_R	Reflection compensation factor
C_n	CMUT capacity of plates
c_P	Heat capacity
D	Exposure dose
D_0	Set exposure dose
D_c	Compensated exposure dose
D_H	Heat dose

d_h	Hatch distance
d_A	Side length of the square aperture of piezo stage 2
d_C	Microchannel width
d_{CD}	Distance between chip and detector in the acoustic measurement setup
d_{Glob}	Glob top epoxy height
d_W	Microchannel wall thickness
d_{WD}	Objective working distance
d_l	Line thickness
d_o	Line overlap
d_{path}	Beam path
d_s	Slice distance
d_G	Grating bar width
$\vec{E}$	Electrical field of the fundamental transverse electromagnetic mode
$\vec{E}_0$	Constant complex amplitude of $\vec{E}$
F_L	Lateral strain
h	Substrate thickness
h_P	Plate thickness
h_{gap}	Gap height
h_G	Grating height
$\hbar$	Planck constant
I	Spatial intensity distribution
I_0	Set intensity
I_a	Absorbed intensity
I_F	Intensity at the focal point
I_S	Intensity at the substrate interface
I_c	Compensated intensity
I_i	Incident intensity
I_r	Reflected intensity
I_t	Transmitted intensity
I_{th}	Threshold intensity
J_P	Pulse energy
K	Flexural stiffness
K_c	Thermal diffusivity
k	Wavenumber
k_0	Fundamental mode's spring constant
k_c	Thermal conductivity
k_m	Gradient coefficient
k_r	Rayleigh coefficient
L_P	Penetration length
m	Gradient, correlation of thermal behavior including geometric constraints
m_{FEM}	Gradient originated FEM

NA	Numerical aperture
N	Nonlinearity of the absorption process
n	Number of plates on a CMUT
n_i	Real part of the refractive index
n_p	Repeated scans per line
$\hat{n}_i$	Complex refractive index
p	Pressure
P_L	Set laser power
P_c	Compensated laser power
P_{lim}	Laser power limit
P_a	Absorbed power
Q_c	Heat at which vaporization events occur
Q_a	Heat absorbed by the substrate
Q_{ac}	Accumulated heat
$\dot{Q}_a$	Absorbed heat flow
$\dot{Q}_c$	Maximum heat flow before vaporization events occur
r	Radial distance from the center axis of the beam
R	Repetition rate
$R(z)$	Curvature of the wave fronts
R_a	Mean roughness
R_{max}	Maximum to minimum height deviation
$R_{q,RMS}$	Quadratic average roughness
$\mathcal{R}_{TE}$	Reflectance, transverse electric mode
$\mathcal{R}_{TM}$	Reflectance, transverse magnetic mode
r_H	Waveguide radius
r_c	Contour radius
r_{cap}	Average radius of the capillary
S	Cross section of the exponential waveguide
S_0	Initial cross section of the exponential waveguide
t_{dev}	Development time
ΔT	Temperature difference
$\mathcal{T}$	Transmittance
T_C	Chamber temperature
T_F	Resist boiling point temperature
T_a	Substrate temperature after beam absorption
T_0	Boundary temperature
T_r	Tension due to residual stress
T_S	Substrate center temperature
t_{dif}	Time frame of thermal diffusion
t_G	Grating bar thickness
u	Modifier of the waveguide’s exponential slope

U	Driving potential
U_{PI}	Pull-in voltage
U_{ac}	Alternating driving potential
U_{dc}	Bias potential
V	Structure volume
v	Scan speed
$w(z)$	Beam radius
w_0	Beam waist
w_D	Displacement
x_s	Lateral size after shrinkage
Y	Young's modulus
z	Axial distance from the focal point
Δz	Residual height difference over the chip size due to tilt after compensation
$z_{r,G}$	Rayleigh length originated from Gaussian calculations
z_r	Rayleigh length

Greek Symbols

α	Attenuation coefficient
α, β	Tilt angles for the x- and y-axes, respectively
γ	Surface tension
γ, δ	Bow contributions to the tilt angles, respectively
δ_2	Two-photon absorption cross section
ε	Electric permittivity
ε_0	Permittivity of free space, dielectric constant
ε_{rel}	Relative electric permittivity
ϵ	Recalculated boundary temperature error
η_a	Absorbed fraction
θ	Positioning angle of the acoustic measurement setup
θ_B	Beam divergence
θ_{cap}	Contact angle between liquid and solid
κ	Extinction coefficient
λ	Wavelength
λ_0^2	Eigenvalue of the first mode
μ	Magnetic permeability
μ_0	Magnetic permeability of free space
μ_d	Dynamic viscosity
μ_{rel}	Relative magnetic permeability
ν	Poisson ratio

ξ	Gouy phase shift
ρ	Density of radicals
ρ_0	Density of radicals in non-polymerized resist
ρ_P	Plate density
τ	Fabrication time
$\acute{\tau}$	Beam operation time
τ_Q	Heat flow period
τ_{dif}	Thermal diffusion period
ϕ	Tilt angle for the z-axis
χ	Volume magnetic susceptibility
Ψ	Beam divergence
ω	Angular frequency
ω_0	Angular frequency of the first mode

List of Figures

List of Tables

1 Introduction

What do a beating human heart organoid [1], an experiment on an acoustic sensor [2] and a vision for habitats on mars [3] have in common? They were fabricated by additive manufacturing (AM).

AM is a comprehensive term for fabrication processes, in which material is applied volume element by volume element to create three-dimensional objects. Analogously to “pixel”, this volume element is called “voxel”, a combination of the words “volume” and “element”. In these processes, the successive joining of one or more materials follows specified dimensions and shapes supplied by computer aided design (CAD) models. This approach results in a product that does not require previously fabricated masks or molds that store its geometry, although the underlying physical and/or chemical processes generally include phase transitions or solidification via polymerization. The solidified voxels are assembled to add up to the product. The assembly concept entails the adaptability and the pace with which products that are different from their predecessors can be created. Furthermore, the assembly facilitates the fabrication of objects that would be unfeasible if traditional production processes were employed.

The adaptability of AM – placing material where it needs to be – enables the user to fit their design according to structural [4, 5], acoustical [6, 7], fluidic [8–10], optical [11, 12], or other requirements. The product can be personalized, adjusted to the user or the environment and advanced by locally tailorable properties [13, 14]. As cost usually does not increase with complexity, the fabrication can follow topology optimized designs down to the resolution limit [15].

Due to the pace of its adaptability, AM was also called “rapid prototyping” during its onset. The idea remains, the fabrication of iterative prototypes using AM is popular in industry, medicine and research, where – with maturing processes – it also gets implemented to produce tools and end products. The average global market growth from 2009 to 2019 was 27.4 %, while in 2020, the COVID-19 pandemic reduced growth to 7.5 %, resulting in a market size of $12.8 billion [16]. However, it recovered in 2021 to 19.5 % [17].

One of the most competitive areas for AM process developers is the attainable minimum feature size, as it predicts the resolution with which objects like biomedical and electronic devices and sensors can be created [18, 19].

Before the emergence of AM, the processes of semiconductor fabrication (SF) were the most expedient way to reliably create structures in the micro- to nanoscale. SF processes like bulk and surface micromachining can be used to create moveable three-dimensional structures by sequential deposition, photolithography, etching and cleaning as well as polishing and implanting. The latter could be counted towards AM, as it assembles a product layer by layer.

An advantage of SF and its primary function of generating small scale electronic devices, is still a goal for many AM processes [19]. Other advantages of SF over AM processes are the extensive standardization and the scalability of production via parallelization. The mass fabrication generally takes place on silicon (Si) substrates called wafers. The individual integrated circuit (IC) or micro-(opto-acoustic-)electro-mechanical system (MEMS) is usually obtained by sawing the finished wafer into rectangular pieces. This process is called dicing, from which the name “die” originates for these products. Another common name for die is “chip”, as it usually represents a piece of Si.

1.1 Relevance

At a first glance, AM on chip (AMOC) seems counter-intuitive. The pattern reproduction processes of SF suit mass production, while AM currently performs at smaller scale quantities. However, the initial cost of fabrication is generally higher for SF, due to its complexity, dependence on specialized equipment and maintenance costs of clean-room environments [20]. Furthermore, the sequential processing is not exclusively advantageous, as it entails long lead times, making SF unsuitable for a rapid prototyping approach [20]. Another hindrance is the available material range [20], especially if complementary metal-oxide-semiconductor (CMOS) compatibility is required.

For research and development of MEMS, these problems may result in reduced efficacy and efficiency. As demonstrated by maker spaces [21] and on-demand services [22], AM can bring development costs down and thus enables the integration of individuals or groups without access to large funding backgrounds. The costs saved in fabrication can be spent on staff, which is where the essential ideation occurs.

Establishing a knowledge base regarding AMOC is pertinent for SF researchers, as fabrication systems available in the near future will overcome current limiting factors, e.g. automatic marker alignment, whole-wafer processing and low throughput [23, 24].

Fabrication of features individualized per chip could become a relevant application of AMOC, for example for chips that show a deviation during characterization and have the option of subsequent adjustment via AM. Individualization per customer can be beneficial to acquisition schemes and medical applications [25].

If the direct fabrication solely via SF or AM is not viable, the combination approach of AMOC may circumvent limitations. It could be employed in the final steps of SF, e.g. packaging [20] and integration of further functionalities, e.g. photonic bonding [26–29], THz-waveguides [30], microsensors [31], actuators stimulated by light [32] or optical tweezers [33].

Some of the references of the previous paragraph present structures that were fabricated using AMOC. Currently, the approach is employed in research, predominantly in photonics, e.g. optical lenses [34–36], encryption experiment [37], fluorescent light detection [38], optical gratings [39], optical waveguides [40].

Furthermore, AMOC is commonly employed in lab-on-a-chip (LOC) applications, due to the demands for compatibility to biological or chemical specimens, specific material characteristics, lower production costs and faster prototyping [18, 41, 42].

Chips based on non-photonic and non-microfluidic principles could benefit from AMOC as well. Publications are not available, indicating a gap in the research field.

1.2 Suitable Chips

The range of components and systems offered by the Fraunhofer Institute for Photonic Microsystems (IPMS) include – among others – sensors and actuators based on the nanoscopic electrostatic drive (NED) as well as the capacitive micromachined ultrasonic transducer (CMUT), the lateral CMUT and the piezoelectric micromachined ultrasonic transducer [43–46].

CMUT and NED devices were studied in this work, as they provide a suitable surface area which did not require alterations to the original design. A further reason was the availability of samples and inhouse characterization methods offered by the Fraunhofer IPMS.

The main advantages of CMUT and NED devices over traditional actuators, are the reliable mass production capability and compatibility to CMOS and restriction of certain hazardous substances (RoHS) requirements [47]. The MEMS environment also enables a high level of electronic integration, which makes these technologies suitable for high volume markets like automotive, medical, or smart mobile devices [47].

1.2.1 Capacitive Micromachined Ultrasonic Transducer (CMUT)

The first CMUT devices were presented in 1994 [48]. The sound generation principle relies on the electrostatic force between two electrodes, whereat one is movable. The CMUT dies employed in this work were fabricated at Fraunhofer IPMS via a sacrificial layer technique from Si, silicon dioxide (SiO_2), aluminum (Al) and titanium aluminide (TiAl).

Applications such as proximity sensors [49], otoscopes [50], gesture recognition [51, 52], or augmented reality via acoustic haptic feedback [53] make the CMUT a versatile component.

The task of the packaging phase in MEMS fabrication is to protect the chip from outside influence or damage, e.g., particle contamination or shorting via flooding, while still maintaining the functionality of the device.

A very common type of packaging is coating, which could be realized by AMOC. The chip can get covered in a material suitable for the subsequent application. Generally, polymers like silicones are used for CMUT devices [54–62], where the fluid precursor was solidified by various methods, e.g., spin coating, spray coating, manual or automated syringe application. Functionality integration like tactile sensing can be achieved by coating CMUT devices and is currently researched [63].

An increased protection of the CMUT could also be realized via gratings. Current research utilizes AM [64]. The fabrication of structures on the active acoustic element of CMUT devices enables the development of e.g. mechanically coupled actuators [65] or seismic masses [66].

Structures fabricated via AMOC can also be used to explore acoustic principles, e.g., via metagratings [15] or waveguides [67]. A type of acoustic waveguide, transmits wavefronts within a duct from the throat, where the inner diameter is generally smallest, to the mouth, where it maximizes [68, S. 227–234]. This can result in an improvement of the directivity of the sound wave, as side lobes are redistributed towards the main lobe, which can increase efficiency. It is further increased by acoustic impedance matching of the source to the load [68–70]. The fabrication of waveguides via AM for MEMS was studied in [71]. The implementation of such structures on CMUT chips via AMOC could benefit applications like the otoscope [50] even better by adjusting the waveguide design towards the individual patient's ear canal.

1.2.2 Nanoscopic Electrostatic Drive (NED)

The concept of the NED actuator class proposed in [72] operates based on the capacitive effect as well. An actuator cell translates capacitive forces into deflections based on a lever principle [72]. The electrode deflections can be stacked by a repetition of this cell, facilitating useful deflection at small electrode separation due to which the control voltage can be reduced, leading to a more efficient component with negligible hysteresis [72, 73]. The lateral motion NEDs employed in this work were fabricated at Fraunhofer IPMS from Si and Al_2O_3 mainly using deep reactive ion etching (DRIE) to form gaps and electrodes.

Applications of the NED comprise acoustic [74, 75] and ultrasonic transducers [76–78], inchworm drives [79], as well as drives for microscopic pumps and valves [80, 81]. Furthermore, multiple NED actuators can be arranged to form a micro-positioning platform (NED-µPS) [82]. The NED-µPS constitutes a NED-powered stage, which serves as a substrate for AMOC in this work.

The point of contact with the environment in robotics is commonly called end effector [83]. For the NED-µPS, many viable end effector types could be fabricated via AMOC, e.g. probe tips and micro needles [84, 85], micro-grippers [86], cell scaffolds [87]. Optical structures could be created on the chip directly, e.g. photonic crystals [88, 89], gratings [90], mirrors [91], lenses [92, 93]. Some AM processes facilitate the fabrication of movable parts [94]. Fabricated gears and levers driven by the NED-µPS could enable it to power new applications, e.g. variable control valves [95].

The NED-µPS could enable the alignment, vibration prevention, driving or positioning of secondary, pre-existing systems like specimen mounts, waveguides, or of pre-existing variants of the examples mentioned in the previous paragraph. Structures like these could be fitted and connected to the NED-µPS via adapter or mount structures that were fabricated via AMOC. For example, a store-bought lens could be attached to a NED-µPS by a mount that was fabricated via AMOC, resulting in a lens that could be aligned with respect to a beam.

Microfluidic systems can benefit from AM [96–101]. Reasonably, NED based microfluidic systems could benefit from AMOC. The conception according to fluid dynamic aspects could improve the efficiency of drug delivery [18], chip heat dissipation [102], lab on a chip [20] and capillary devices [103].

1.3 Research Questions & Solution Approach

The objective of this work is the investigation of AMOC at the example of the CMUT and the NED-µPS. Along the way, a suitable AMOC process needs to be found and fundamental experience gathered to prepare the adoption of future leaps in technology.

The initial chapter 2 describes suitable AM processes and defines the subsequently pursued two-photon polymerization lithography (TPP). Furthermore, the chapter elucidates TPP based fabrication and the system employed in this work. Chapter 3 covers the fundamentals of the CMUT and NED-µPS chips. With these foundations established, this work is focused on answering the following research questions:

1. Which additional process steps are necessary to realize fabrication via TPP on an assembled CMUT chip?
2. In what way do the fabrication materials and processes of TPP affect the behavior of an assembled CMUT chip?

Motivated by the relevance of AMOC and equipped with the systems and chips necessary to start the investigation, obstacles were encountered on the way to answer the first research question. The laser-based fabrication via TPP is affected by the employed substrate. The utilized beam can get partially reflected by and transmitted into the substrate.

The energy distribution model established in chapter 4 underpins the substrate reflection model designed for the compensation of these effects, which is described in chapter 5. The transmission was modeled on the same analytical basis, including an additional finite element modeling (FEM) of the thermodynamic behavior of the substrate. The completed compensation model is discussed and enhanced by a factorization method. The systematic verification of the model by experiments on substitute substrates is described and the established factors are gathered for the use in the subsequent verification on chip. Competing models use similar approaches [14, 104]. The features distinguishing this work are the reduction of the thermal behavior and structure composition to one factorizable parameter and the verification experiments including a parametrization of the voxel distance to the substrate. The former is relevant for the reduction of complexity of the model to enable edge-computation, the latter is relevant for the fabrication of three-dimensional structures.

The reflection and transmission compensated fabrication of structures on chip is only worthwhile, so long as the structures stay on the chip. The adhesion between the two, as well as possible improvements of it are discussed.

Not only the optical and thermal behavior of a chip as substrate for TPP fabrication required compensation, so did the alignment of the chip. The substrate tilt and its fundamentals are investigated, where a tilt compensation upgrade to the TPP fabrication system employed in this work was devised, manufactured and validated. The relevance of this aspect is illustrated by recent product developments [105].

With the fabrication process and substrate effects defined, as well as compensation and adaption methods established, AMOC is presented in chapter 6 for the CMUT chip. The fabrication of structures directly on the active element of the chip is attempted and the resulting, challenging parameter space is discussed. Then, examples for AMOC are given by the development of a base feature, on which further structures can be anchored, e.g., packaging via coatings and gratings. Another AMOC application anchors on this base feature: an acoustic waveguide.

With the first research question answered by the fabrication of viable structures on the CMUT chip, the second research question is prompted immediately. A study of the effect of individual TPP process steps on the electrical behavior of the chip is presented, as well as for the fabrication in the vicinity of the active elements. An investigation of structures fabricated by TPP on CMUT chips with contact to their active elements is presented. Lastly the waveguides fabricated on chip are acoustically characterized and their viability discussed.

To provide a second foothold for the illustration of the significance of AMOC, chapter 7 presents applications for NED-based systems. An end effector fabricated on the NED-µPS is presented and the implications are discussed. With AMOC presented for the NED-based system, the microfluidic capabilities of TPP are then illustrated to assess their feasibility. Microchannels underpin most microfluidic applications and are fabricated from silicone. As a non-cytotoxic material [106] the IP-PDMS (Nanoscribe GmbH) employed in this case enables access to the "foundational microfluidic material polydimethylsiloxane (PDMS)" [107] which might also be an attractive choice for medical applications [108]. The practicality of microchannels fabricated from TPP generally depends on the ability to fully remove material from within the channel. The new method was devised to determine the maximum attainable aspect ratio of a microchannel dependent on the development process.

Finally, chapter 8 completes this work by discussing the answers to the research questions and offers an outlook by presenting the potentials provided by this contribution.

2 Additive Manufacturing Methods

In this chapter, an overview of AM processes is given and their suitability regarding fabrication at MEMS scale discussed. Afterwards, the TPP process and system found suitable and employed in this work, as well as the utilized photoresists and chips are described.

2.1 Classification of Suitable Processes

The 6 categories of AM processes displayed in Fig. 2.1a give an overview of the available technologies. Due to their low cost of investment and operation, the extrusion category is well-known for fused filament fabrication (FFF) processes [109].

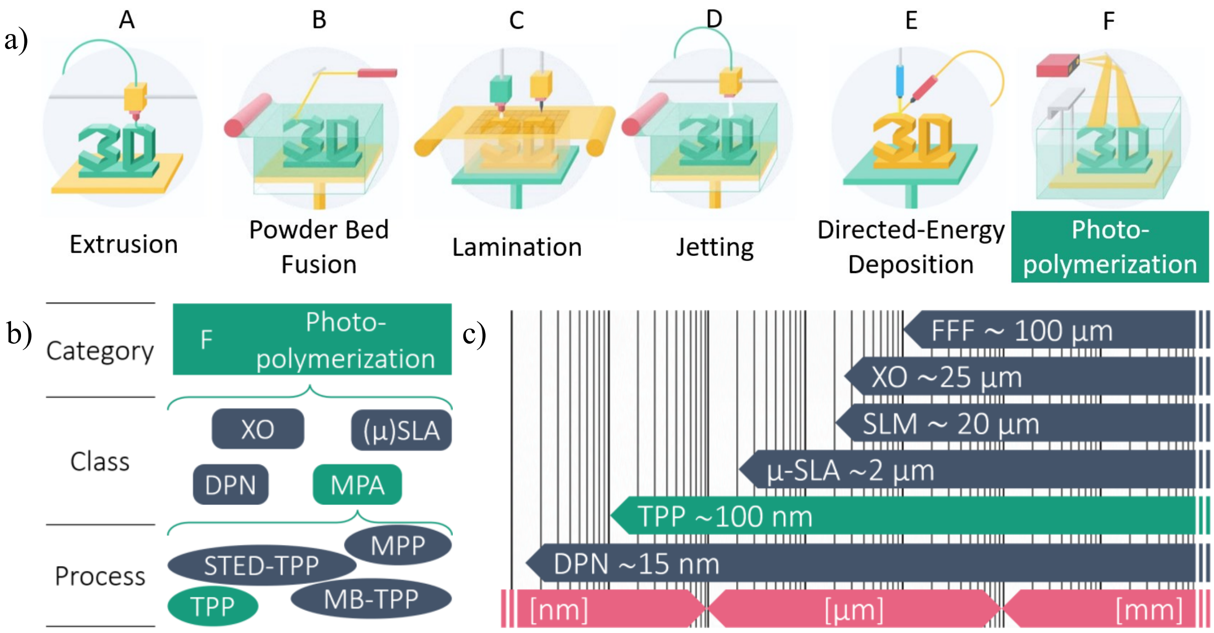

Fig. 2.1: a) Schematic of the AM process categories [110]. b) Chart of the category and class of the TPP process. c) Comparison of current commercially available minimum lateral feature size of various AM processes, e.g. fused filament fabrication (FFF) [109], xolography (XO) [111], selective laser melting (SLM) [112], micro-stereolithography (μSLA) [113], TPP [114, S. 197], dip pen nanolithography (DPN) [18].

The powder bed fusion category is popular due to processes established for metal materials like selective laser melting (SLM) [112]. The processes found in the lamination, jetting and directed-energy deposition classes have their own advantages and applications [115–117], however, they were not considered for this work, due to their minimum feature size. Here, the size required must be small enough to enable high resolution fabrication of structures with dimensions proportional to the employed chips. Furthermore, fabrication material performance, throughput limits and design freedom were considered. The photopolymerization category suits the identified requirements, especially with the multi-photon absorption (MPA) class. The micro-stereolithography (μSLA) [113], xolography (XO) [111] and dip pen nanolithography (DPN) classes were assigned to the same category, see Fig. 2.1b. They are based on photopolymerization of a liquid monomer in volumes smaller than the end product, which consolidate, resulting in the end product.

The comparison of minimum feature sizes depicted in Fig. 2.1c illustrates the main advantage of the MPA class. DPN enables high resolution fabrication via nanoscale tip [18], however, the material, fabrication speed and maximum structure size restrictions disqualified the method. TPP and multi-photon absorption polymerization lithography (MPP) induce polymerization based on simultaneous absorption of more than one photon, the latter being a theoretical process at the time of writing [118]. Multi-beam TPP (MB-TPP) [119] improves on the – when compared to μSLA – slower fabrication speed of TPP. Stimulated emission depletion-TPP (STED-TPP) [120] exhibits a reduced voxel size compared to TPP. However, only TPP and DPN were commercially available at the time of writing. TPP not only offers the resolution, but also a high range of addressable structure sizes and a flexibility of fabrication speed via exchangeable optics. In [121] and for many of the applications discussed in chapter 1, it was identified as the proper choice for fabrication of and on MEMS.

2.2 Two-Photon Polymerization Lithography

TPP was first presented in 1997 [122]. It is a photon induced polymerization process based on the two-photon absorption (TPA) phenomenon, which was theoretically established by Nobel Prize laureate Maria Göppert-Mayer in 1931 [123] and confirmed experimentally by Kaiser and Garret in 1961 [124]. TPA is an additional optical loss mechanism to the linear one photon absorption (OPA). The latter can facilitate a transition from the ground state of a system to an excited state by absorption of an incident photon with energy $2\hbar\omega$, see Fig. 2.2a.

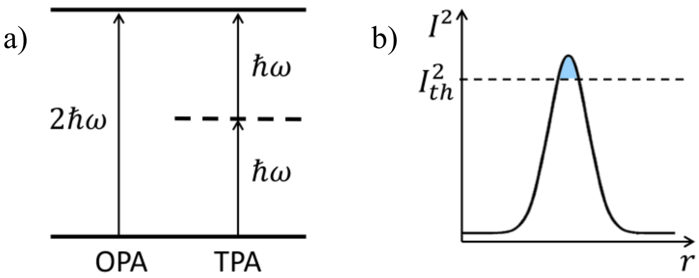

Fig. 2.2: a) Energy level schematic comparing excitation by one photon absorption (OPA) and two-photon absorption (TPA). b) Squared intensity I^2 vs. spatial coordinate r including graph of the threshold intensity I_{th} and the above threshold area indicated in blue.

To get to the same state using TPA, two photons of energy $\hbar\omega$ each must be absorbed simultaneously or sequentially. An intermediate state – which can be virtual [125] – halfway between ground and excited state can get excited by the first photon. The transition from intermediate to excited state only happens, if the second photon is absorbed before the virtual state collapses within a time frame of approximately one femtosecond [114, S. 60].

A photoresist (resist), in which this absorption process can happen, usually consists of organic monomers, solvents and photoinitiators. The latter can create radical species. Here, the photoreaction is usually initiated by the simultaneous absorption of two IR frequency photons resulting in a combined UV exposure. Monomers react with these radicals, forming chains and cross linking into networks. The longer the chains and the more intense the entanglement, the stronger the resulting polymer becomes [14, 126, 127]. The radical density and thus quantum yield can also be affected by, e.g., steric hindrance [14], quantum efficiency of the photoinitiator [114, S. 63], reaction paths and kinetics [104], radical trapping and quenching [114, 89-91, 188-189]. Due to the nonlinearity of the process, a quadratic dependency on intensity emerges. Only when the squared threshold intensity I_{th}^2 is exceeded, the number of absorptions and subsequent polymerization becomes prevalent and can form solids. The lateral voxel size is therefore indicated by the blue area in Fig. 2.2b. To improve the probability of TPA taking place during TPP, the photon density is increased, e.g., by focusing the beam spatially using an objective. The employment of femtosecond pulsed lasers as a light source further increases the temporal photon density [128]. By scanning the voxel through the resist according to positional data from digital three-dimensional models, the required structures can be created. As with other AM processes, complex structures are usually resolved into slices and hatch lines. One voxel scanned through a negative tone resist results in a hatch line. The subsequent lines written parallel to the first create a slice. Stacked slices resolve the total volume. After each cross section of the part is combined, the fabrication is terminated. Afterwards, excess resist can be removed using developing chemicals, leaving the cured structures.

2.3 Fabrication System and Methods

2.3.1 Fabrication Equipment

The TPP system employed in this work is the Photonics Professional GT2 (Nanoscribe GmbH & Co. KG, Germany). It is based on a 780 nm, mode-locked, Er-doped fiber laser with a power of >140 mW, operating at 80 MHz repetition rate and <100 fs pulse length 25 [129, S. 25]. The components of the fabrication setup, some essential preparation steps as well as a schematic of the setup are shown in Fig. 2.3 to give an overview. The nine-slot substrate holder Multi-DiLL (Nanoscribe GmbH & Co. KG, Germany) depicted in Fig. 2.3a, b and d was used for this work. Square 25.4 mm by 25.4 mm substrates – hereinafter referred to as standard substrates – can be fixed to it using sticky tape. The holder and substrate can then be inserted into piezo stage 2, which is located on piezo stage 1 indicated green and blue, respectively, see Fig. 2.3b. A transmittance of 65 % [14] was measured for the Plan-Apochromat 63× 1.4 Oil DIC M27 (Carl Zeiss AG), hereinafter referred to as the 63x objective.

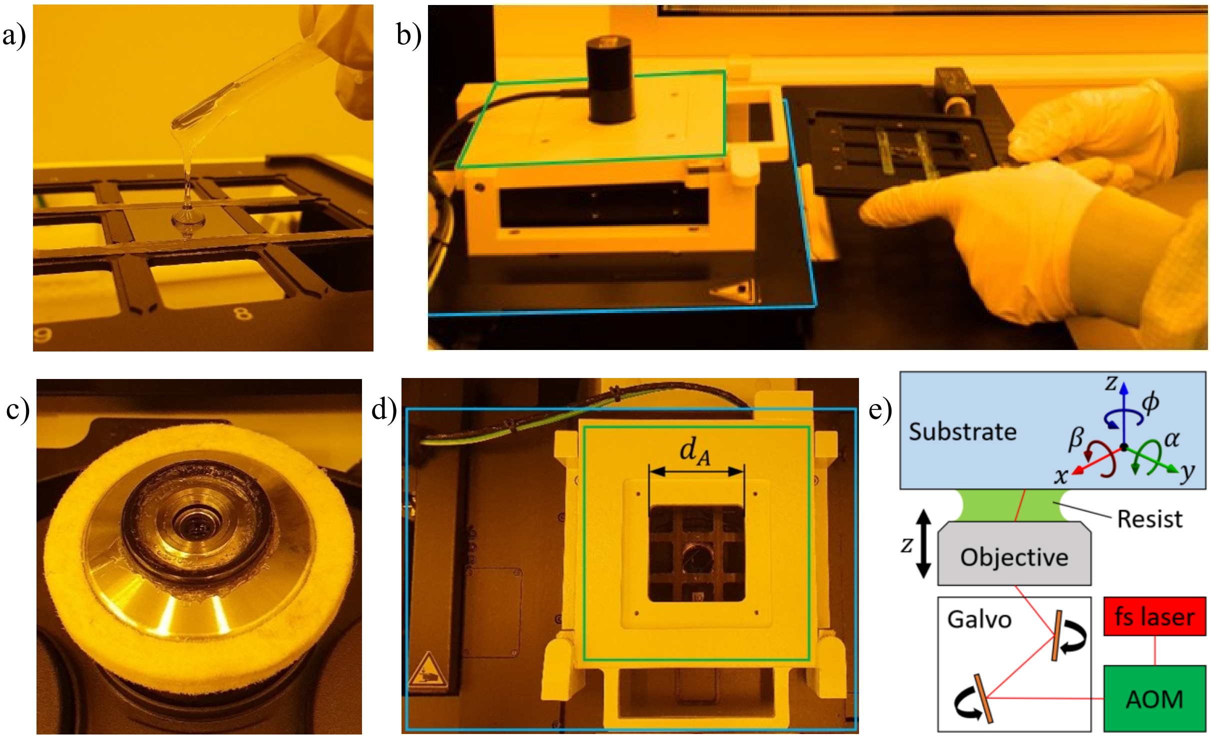

Fig. 2.3: a) Photograph of manual resist application on a standard substrate inserted in the nine-slot substrate holder and fixed to it using sticky tape. b) Photograph of the insertion of the nine-slot substrate holder into the TPP system including piezo stage 1 and 2 marked blue and green, respectively. c) Photograph of an objective including applied felt and O-rings as well as resist. d) Photograph of the fabrication chamber inside the TPP system from the top view including square stage aperture d_A, as well as piezo stage 1 and 2 marked blue and green, respectively. e) Schematic of the TPP setup including the laser, acousto-optic modulator (AOM), galvanometer scanner, objective, resist and the substrate as well as respective degrees of freedom x, y, z, α, β, ϕ.

The transmittance changes with the condition of the objective and would have to be measured before each fabrication session. To constitute uniformity, laser power values mentioned in this work are noted as laser power before entering the objective. The other objective used for this work shown in Fig. 2.3c is the Nanoscribe 3D Large Feature DiLL 2PP 10× 0.3 (Nanoscribe GmbH & Co. KG, Germany), hereinafter referred to as the 10x objective. It can be fitted with a felt ring to reduce dripping resist, as well as an elastomer O-ring to create a resist reservoir for the fabrication of large volume structures [130], see Fig. 2.3c.

The expected – hereinafter referred to as standard – voxel size in direction of the beam for these objectives is ~700 nm and ~12 µm, respectively [131]. The power at the objective aperture can be calibrated using an acousto-optic modulator (AOM) to reliably perform at 50 mW [131].

The schematic in Fig. 2.3e explains the basics of the fabrication system: (i) the fs laser emits a beam, (ii) it is optically adjusted, e.g. using the AOM, and (iii) the mirrors of the galvanometer scanner can move the beam within the field of view of the objective (FOV).

The optical path, which is partly depicted in Fig. 2.3e, can get misaligned, e.g. due to thermal fluctuations within its parts or vibrations from the environment like street traffic. Although the misalignment was not measured during this work, the realignment was part of periodical maintenance. Optical aberrations and a misaligned system can lead to exposure dose inconsistencies distributed across the FOV [132].

Positioning of the voxel in the respective degree of freedom (DOF) is realized by the system components described in table Tab. 2.1 and indicated by arrows in Fig. 2.3e. Piezo stage 1 and 2 allow an addressable fabrication area of 10 cm by 10 cm and 300 µm by 300 µm by movement in x and y direction, respectively. The objective turret and piezo stage 2 enable movement within a distance between the substrate and the objective of ~8 mm. A lateral repeatability of <1.5 µm was determined during the system acceptance. Three additional angular DOFs were made available by the tilt compensation upgrade to the TPP system devised in this work. It is described in section 5.6.4.

Tab. 2.1: Voxel DOFs adjustable by system components and the tilt compensation upgrade.

DOF	Parameter	Component
1	x-axis (r)	Galvanometer mirrors, piezo stage 1 and 2
2	y-axis (r)	Galvanometer mirrors, piezo stage 1 and 2
3	z-axis (z)	Objective Turret, piezo stage 2
4	α angle	Tilt compensation upgrade
5	β angle	Tilt compensation upgrade
6	ϕ angle	Tilt compensation upgrade (manual)

The fabrication system was installed in a grey room cabin to achieve the necessary temperature and humidity stability and to reduce contaminants. Furthermore, as shown in the photographs of Fig. 2.3, the lighting and windows are wavelength limited to <500 nm using filters to reduce unwanted polymerization of the resists. An optical table was used to reduce vibrations e.g., from outside traffic.

2.3.2 Preprocessing

Preprocessing surmises the various tasks that prepare the TPP system, substrate and resist before starting the fabrication process, e.g.

1. CAD or programmed model creation and transfer to machine readable code, including laser trajectories and system settings, using the software DeScribe (Nanoscribe GmbH & Co. KG, Germany). DeScribe allows programming of parameter sweep scripts, which result in repeated fabrication of a model, while iterating individual parameters.
2. Cleaning, e.g., via Acetone and 2-propanol (IPA) sluicing.
3. Ultraviolet (UV) flood light treatment using the 200 W metal-halide bulb of the BlueWave 200 (Dymax Europe GmbH) including a light guide.
4. Oxygen plasma treatment via the 100 W, 40 kHz Zepto A (Diener electronic GmbH & Co. KG, Germany).
5. Manual or automated resist application, see Fig. 2.3a and annex A. The latter was performed using the dispenser module of the manual die bonder FINEPLACER lambda2 (Finetech GmbH & Co. KG, Germany).
6. Temperature equilibrium adaption by allowing ~30 min before fabrication.
7. Interface detection, see section 2.3.3.
8. Tilt measurement and compensation, see section 5.6.
9. Positioning of the intended structure alongside preexisting features of the substrate, using the operating software of the TPP system used here, NanoWrite (Nanoscribe GmbH & Co. KG, Germany).

2.3.3 Interface Detection

As with many additive manufacturing processes, especially ones that employ liquid precursors, the intended structures must be connected to a substrate starting with the first layer. Otherwise, movement introduced by the stage, objective or internal to the liquid resist can move solidified material. It can drift away and subsequent layers cannot connect, impeding fabrication.

To establish a connection between structures and the substrate, the focal point of the objective must be positioned at the interface between the substrate and the liquid resist, see Fig. 2.4.

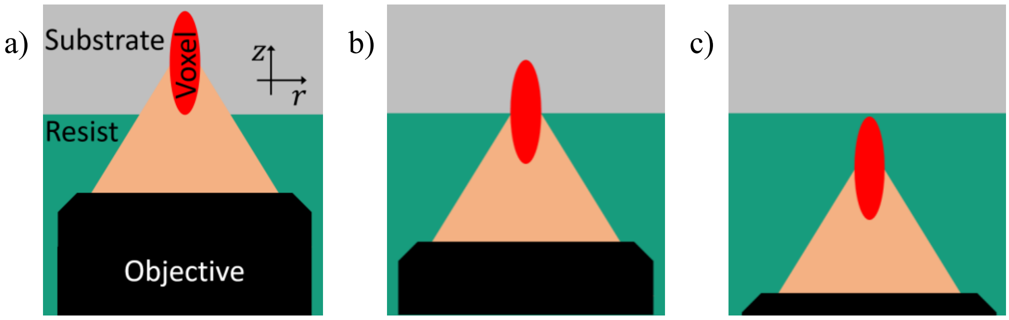

Fig. 2.4: a) Schematic of a section view through the substrate and objective with the voxel located inside the substrate. b) The same with the voxel at the interface. c) The same with the voxel inside the resist.

With the objective driven towards the substrate, see Fig. 2.4a, the voxel can be located inside the substrate, which might not lead to any polymerization of the resist. The voxel outside the substrate polymerizes the resist, see Fig. 2.4c, but starting the fabrication at a distance from the substrate is not recommended. Generally, the voxel is positioned inside the substrate to anchor the structure, e.g., 0.5 µm for the 63x objective. There are two ways to identify the interface position depicted in Fig. 2.4b with the TPP system used in this work.

The manual interface finding method requires the user to move the objective to a distance between substrate and objective less than the working distance d_{WD}, activate and set the fabrication laser to a polymerizing power value and then slowly increase the distance between the objective and the substrate until solidified material is created [131]. The distance at which polymerization occurs defines the interface position.

Manual interface detection is prone to errors and can be improved by driving the galvanometer mirrors to form a circle with the voxel [131]. This refines the detection because the larger solidified volume can be distinguished more easily.

The TPP system used in this work employs the interface detection hardware Definite Focus (Carl Zeiss AG) [133]. It allows the automatic detection of the location of the interface via projection of a grid pattern onto the substrate. The wavelength of the LED used for this projection is centered around 850 nm to prevent unintentional release of radicals in the resist through which it radiates. The grid is tilted towards the plane of the substrate. An interface signal gets established depending on the reflection from the substrate surpassing a determined threshold. The light reflected back to the detector based on a charge-coupled device must exceed a threshold value, which requires a significant refractive index mismatch between the substrate and the resist [131].

When automatic interface finding is initiated via button or script, the signal gets used to automatically position the objective so that the focal point sits on the surface of the substrate and the voxel is half buried in the substrate.

2.3.4 Postprocessing

After the fabrication of structures, the superfluous liquid resist is usually washed away in the developing step. The structures usually are developed using 60 ml each of the developing agents 1-methoxy-2-propanol acetate (PGMEA) and IPA were used for 20 min and 5 min, respectively. Furthermore, Novec 7100 Engineering Liquid (NOVEC, 3M Co.) was employed, which is based on methoxy-nonafluorobutane. Their electrical conductivities are 5.8 µS/m [134], 0.2 µS/m [135], NOVEC is non-conductive [136].

Development liquids were applied using the slowest injection speed of a Finnpipette Novus (Thermo Fisher Scientific Inc., USA). Drying was conducted in air at (21.5 ± 0.59) °C and (28.7 ± 5.9) % rH under a glass cover. Measurements of temperature and humidity were carried out using the Testo 174 H (Testo SE & Co. KGaA). The structures were analyzed using a Leica DM8000M (Leica Camera AG, Germany) reflective light microscope (RLM) and the FlexSEM 1000 II (Hitachi, Ltd.) scanning electron microscope (SEM). An additional flood curing can be performed using the UV point light [137], see section 2.3.2.

2.3.5 Photoresists & Solvents

The liquid resists IP-Dip, IP-Q, and IP-PDMS employed in this work were selected due to the comparably better availability of literature concerning TPP. They consist of organic monomers, solvents, and photoinitiators, making them negative tone. Positive tone resists were excluded, as they require a different fabrication setup [138]. The photoinitiator within resists decomposes, which can be reduced by low temperature storage [139]. This was provided by storing the resists in an explosion safe refrigerator at (8.0 ± 0.3) °C and by consuming them within their minimum storage life of ~2 months. The methacrylate-based IP-Q was designed with an additive that improves radical propagation, its characteristic parameters are listed in Tab. 2.2 [140].

Tab. 2.2: Parameters for the resist IP-Q.

IP-Q	Value	Unit	Additional Information	Reference
Young's modulus	0.5 … 1.3	GPa	Laser power: 15 … 50 mW Scan speed: 500 µm/s … 130 mm/s Slice & hatch distance: 5 µm, 1 µm	[127]
Poisson's ratio	0.3	-	-	[140]
Density	1200	kg/m³	Liquid	[140]
Shrinkage	5 … 15	%	-	[140]
Density	1260 … 1380	kg/m³	Solid, calculated from shrinkage	-
Refractive index	1.48	-	Liquid, wavelength 780 nm, real	[140]

The characteristic parameters of the acrylic-based IP-Dip are listed in Tab. 2.3.

Tab. 2.3: Parameters for the resist IP-Dip.

IP-Dip	Value	Unit	Additional Information	Reference
Poisson's ratio	0.3 … 0.35	-		[13, 141]
Young's modulus	0.6 … 3.6	GPa	Laser power 9 … 17 mW, scan speed 1000 µm/s, slice & hatch distance 0.05 µm and 0.1 µm	[14]
	0.75 … 3.6	GPa	Laser power 5 … 13 mW, scan speed 100 µm/s, slice & hatch distance unknown	[13]
	0.07 … 2.1	GPa	Laser power: 6 … 60 mW, S. speed: 0.1 …100 mm/s, slice & hatch distance 0.3 µm and 0.2 µm	[127]
Density	1170	kg/m³	Liquid	[142]
	1220 … 1250	kg/m³	Solid	[13, 14]
Relative Permittivity	3	-	SU-8: 4.5	[143]
Refractive index	1.53	-	Wavelength 780 nm, real	[144]
Extinction coefficient	1e-6	-	Wavelength 780 nm	[145]
Isotropic heat conductivity	0.21	W/m/K	-	[146, 147]
Specific heat capacity	1.466	J/g/K	-	[146, 147]
Boiling point	205	°C	-	[148, 149]
Shrinkage	5 … 17	%	-	[150]

The characteristic parameters of the methacrylate- and acrylate-functional siloxane IP-PDMS are listed in Tab. 2.4. Further resist information can be found in annex B.

Tab. 2.4: Parameters for the resist IP-PDMS.

IP-PDMS	Value	Unit	Additional Information	Reference
Density	1010	kg/m³	Liquid	[106]
Shrinkage	~10	%		[106]
Density	1111	kg/m³	Solid, calculated from shrinkage	-
Young's modulus	15.3	MPa	ISO 14577, ASTM E2546	[106]
Poisson's ratio	0.5	-		[151]

3 Fundamentals of the Selected Chips

An overview of the fabrication, common applications and possible AMOC implementations of the chips were given in section 1.2.1. In the present chapter, the essential knowledge of the chips that will serve as substrates for AMOC via TPP is illustrated.

3.1 Technological Basics of the Capacitive Micromachined Ultrasonic Transducer

3.1.1 System Architecture & Operating Principles

The CMUT constitutes at least one unit cell, which comprises the flexible plate electrode (labeled "Plate" in Fig. 3.1a) and the static electrode (labeled "Electrode"), separated by a cavity. A bias potential $U_{dc} \neq 0$ creates an electrostatic force between them, which deflects the plate towards the bottom electrode. U_{dc} is set, so that the plate lingers in the operating point. The alternating driving potential U_{ac} creates an oscillating displacement of the plate, which causes the emission of sonic waves into the load medium above the plate.

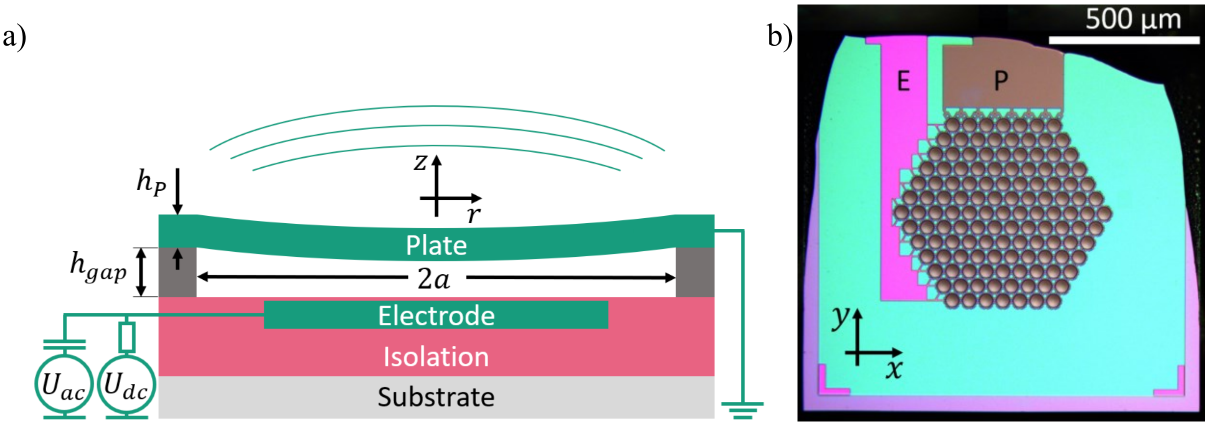

Fig. 3.1: a) Schematic of a CMUT unit cell cross section with plate radius and thickness a and h_P, as well as gap height h_{gap}. b) RLM image of a CMUT comprising multiple unit cells in a hexagonal arrangement of approximately 700 µm diameter. The contact pads for plate and electrode are marked "P" and "E".

In receive mode, an incoming soundwave deflects the plate from the operating point, resulting in a detectable current. Multiple unit cells are usually arranged to form an aperture on a chip as visualized in Fig. 3.1b, where they are commonly wired to work in parallel to increase output power. In Fig. 3.1b the contact pad marked “P” connects all plate electrodes, the one marked “E” connects all static electrodes, respectively. The difference in color originates from pad “E” being buried below an additional layer of SiO_2 due to the fabrication sequence. The top edge of the chip is encapsulated to protect the fragile bond wires, which appears black in Fig. 3.1b. The total lateral size of the chip is 1.6 by 1.3 mm^2 and the space between the two “L” shaped corner markers amounts to 1.2 mm.

The plate behavior depends on its dimensions, environmental characteristics and material parameters. Assuming uniform pressure, a thin and perfectly clamped plate, as well as isotropic and linear material properties, the dynamic behavior of the plate of a CMUT can be described by the equation of symmetric harmonic motion [152, S. 163]

$$K\nabla^4 w_D - T_r\nabla^2 w_D - \omega_0^2 h_P \rho_P w_D - p = 0 \tag{3.1}$$

with the following terms from left to right:

1. Restoring force due to out-of-plane deformation, including the flexural stiffness K and the displacement w_D,
2. residual stress T_r inherent to the plate due to fabrication processes (TiAl compressive film stress depends on plate thickness, 255 MPa at 500 nm [153]),
3. inertia due to distributed plate mass, including the eigenfrequency ω_0, the plate thickness h_P and its density ρ_P,
4. and instantaneous electrostatic pressure p.

Furthermore, the radiation resistance of the medium, cross coupling between plates in an array and excess pressure due to gas confined in the cavity and squeeze film damping were disregarded [154, 155]. CMUT plates can comprise a single phase [156], but can also consist of multiple layers of different materials. Equations for effective parameters of multilayered plates can be found in [157, 158] and have been calculated for CMUT devices in [159]. The following equation describes the flexural stiffness K of a plate [152, S. 158–161]

$$K = \frac{(Y + T_r)h_P^3}{12(1 - \nu^2)} \tag{3.2}$$

where Y and ν represent the Young’s modulus and the Poisson’s coefficient, respectively. The eigenfrequency [155] of the first mode can be calculated as

$$\omega_0 = \frac{\lambda_0^2}{a^2}\sqrt{\frac{K}{h_P \rho_P}} \tag{3.3}$$

with the eigenvalue of the first mode $\lambda_0^2 = 10.2$ [160] and the plate radius a. With that, the fundamental mode's spring constant of an isotropic plate becomes [155]

$$k_0 = 192.2\frac{\pi K}{a^2} \tag{3.4}$$

The capacity of a CMUT with n plates can be calculated as [155]

$$C_n(w) = n\frac{\varepsilon_0 a^2 \pi}{h_{gap} - w_D} \tag{3.5}$$

with the permittivity of free space ε_0 and the gap height h_{gap}. Assuming a small signal voltage compared to the bias voltage $U_{dc} \gg U_{ac} \approx 0$, the pull-in voltage becomes

$$U_{PI} = \sqrt{\frac{8}{27}\frac{k_0 h_{gap}^3}{\varepsilon_0 a^2 \pi}} \tag{3.6}$$

Exceeding this voltage results in the collapse of the plate, it snaps to the static electrode and usually self-destructs the chip by electrically shorting.

3.1.2 Requirements to the Die Assembly

The CMUT dies employed in this work were assembled on TO-18 mounts using adhesive EP 601-T (Polytec PT GmbH), see Fig. 3.2a. In that model, the die is represented by a cuboid and placed between the three contact pins that lead through the TO-18.

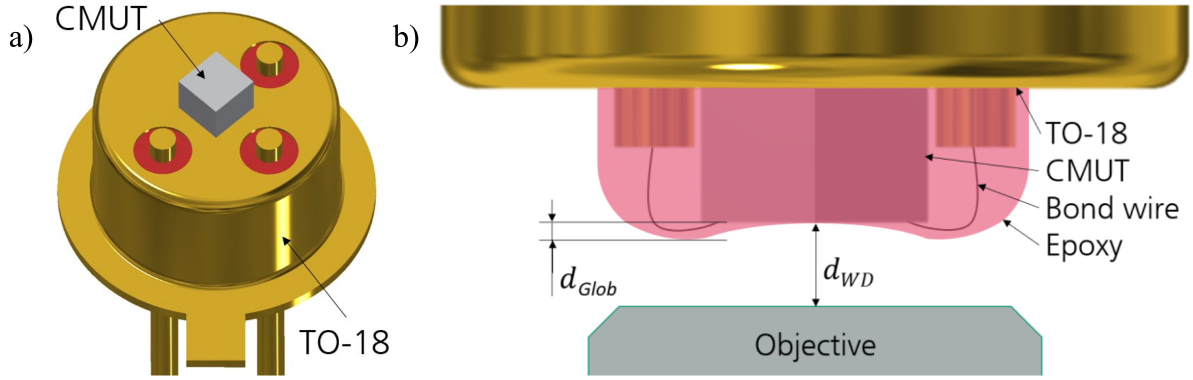

Fig. 3.2: a) 45° tilted view CAD model of a TO-18 with a mock CMUT mounted on it. b) Side view schematic of a TO-18 with a mock CMUT mounted, bonded and covered in glob top epoxy of height d_{Glob}. The objective is arranged close to it with the working distance d_{WD} in-between.

The wire bonds to connect the chip to the pins of the TO-18 were specialized to reduce their total height above the chip surface to <300 µm when encapsulated with glob top epoxy, illustrated in Fig. 3.2b. This mounting was required to provide space for the objectives to move close to the chip surface, with a d_{WD} of ~360 µm in case of the 63x objective.

The epoxies applied were proprietary blends, respective to the assembly companies named below. The standard bond method resulted in an encapsulated height d_{Glob} of (410 ± 1) µm (Holm Weber Microchip Montage, Germany). The same company improved d_{Glob} upon request to (131 ± 1) µm. Another company achieved (253 ± 1) µm (AIM Micro Systems GmbH, Germany). Both versions were successfully implemented for AMOC by TPP.

3.1.3 Electrical Measurement Setup

The resistance, reactance and capacitance of the CMUTs employed in this work were characterized using an experimental setup comprising the impedance analyzer Agilent E4990A (Keysight Inc., USA) and the source measurement unit Keithley 2450 (Tektronix Inc., USA), which were connected to the sample via a bias tee, see annex C. Due to the additional passive bias circuit, a calibration was conducted using open, short and 50 Ω samples [161].

The capacity was measured versus increasing bias voltages using a test frequency of 10 kHz and a signal voltage U_{ac} of root mean squared (RMS) 500 mV. At the same signal voltage, resistance and reactance were measured over the spectral ranges 50 to 500 kHz using 201 samples, 0.5 to 7 MHz using 801 samples and 7 to 20 MHz using 501 samples.

The resulting data was used to infer the performance of the characterized devices. Equivalent circuit models based on lumped elements are commonly applied to fit these results, however, they are limited and may not incorporate all aspects of these multi-physics systems [162].

Rather than using arbitrarily complex, approximation-based models, the Signal Processing Toolbox of MATLAB R2021b (The MathWorks, Inc.) was employed. The “findpeaks” function returns attributes for each peak found in a signal, e.g., height, location, prominence and full width at half prominence (FWHP) [163]. Via subsequent criterion selection, the characteristic resonance peak of the CMUT resistance was extracted and evaluated.

The typical voltage source noise for 10 Hz to 1 MHz of the Keithley 2450 is RMS 2 mV [164], which is equivalent to ±0.01 % of U_{dc} for the experiments of this work. The Agilent E4990A impedance accuracy is indicated ±0.08 % by the manufacturer [165, 166]. The error of the electrical characterization including the subsequent evaluation via the Signal Processing Toolbox was investigated at the example of an assembled CMUT chip, by repeating the measurement and evaluation ten times, including manual mounting, see Tab. 3.1.

Tab. 3.1: Results of the error investigation for a single CMUT chip over ten electrical characterizations and subsequent evaluation employing the Signal Processing Toolbox of Matlab R2021b.

	Peak Resistance [kΩ]	Peak Frequency [MHz]	FWHP [kHz]	Prominence [kΩ]	Capacity [pF]
Average	0.96	1.87	214	0.80	21.1
Standard deviation	0.06	0.01	1.58	0.05	0.11
Percentage error [%]	6.05	0.34	0.74	6.72	0.52

Assuming a combined error internal to the employed measurement systems of 0.1 %, the additional deviation of the resulting average of the peak resistance of 6.05 % most likely originated from the manual mounting and peak evaluation methods.

3.1.4 Acoustic Measurement Setup

To detect high frequency air-borne ultrasound, the optical microphone Eta450 Ultra (XARION Laser Acoustics GmbH, Austria) was employed. The assembled CMUT was mounted at a distance d_{CD} to the detector in a positioning system (Physical Instruments GmbH & Co. KG, Germany), see Fig. 3.3. It facilitated movement of the source relative to the microphone via three linear and one rotational DOFs, to perform radial and line scans.

The measurement technique is based on the detection of pressure and temperature dependent optical refractive index changes within a Fabry-Pérot etalon by passing a 1550 nm laser beam through it and measuring the intensity [167].

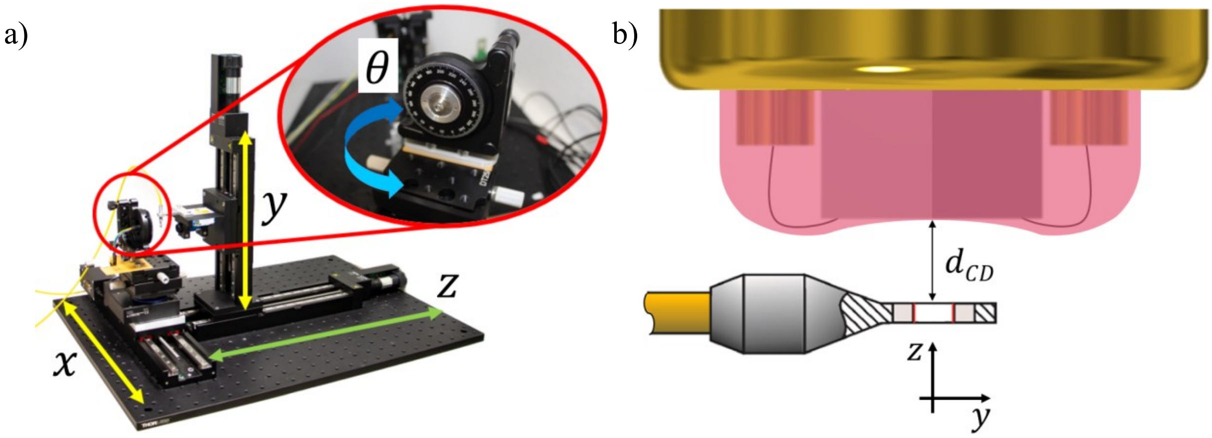

Fig. 3.3: a) Acoustic measurement setup comprising mount, positioning system and detector including inset close-up of the CMUT mount and indicated positioning directions x, y, z and angle θ [64]. b) Side view schematic of a mock assembled CMUT and the optical microphone arranged at a distance d_{CD}, including a section view of the Fabry-Pérot etalon [168].

The spectrum of the system, its sensitivity of 100 mV/Pa and its self-noise of 10 mPa was specified from 50 kHz to 2 MHz by the manufacturer [168]. A research group specified the same system model for 300 kHz to 3 MHz by detection of mechanical resonance of carbon fiber reinforced polymer plates [169].

As the CMUT devices fabricated at Fraunhofer IPMS exhibit frequencies that can exceed this interval, the measurements could be considered unreliable. Furthermore, the sensitivity of the microphone class might be strongly frequency dependent with ~7 dB deviations in the range of 10 to 100 kHz, a finding determined by researchers that prepared it for publication, but withdrew their submission [170]. For this work, the microphone has not been calibrated due to the lack of an appropriate reference sensor or reference ultrasonic source. However, error estimations were performed by time-of-flight measurement of standard deviations of an individual assembled CMUT as described in [171] to increase the significance of subsequent characterizations. Two measurement groups were established: (i) the CMUT was remounted between measurements to include user contributions to the deviation, and (ii) the CMUT was left in the setup to illustrate the setup's contributions.

The maximum sound pressure of the pulse received by the microphone averaged over ten measurements with and 18 without chip remounting resulted in (13.9 ± 0.72) and (14.0 ± 0.22) Pa, respectively. In this work, the sound pressure is recalculated to the sound pressure level, resulting in (56.9 ± 0.44) and (56.9 ± 0.14) dB for the deviation measurements, see annex D. The measurements were taken at an averaged distance between chip and detector d_{CD} of (7.54 ± 0.63) and (7.86 ± 0.12) mm, respectively.

During all acoustic characterizations, CMUTs were operated at maximally 85 % of their respective pull-in voltage U_{PI} to prevent pull-in [155]. With the bias voltage U_{dc} set to 42.5 %, stimulation was performed by a sinusoidal signal voltage $U_{ac} = U_{dc}$. Radial scans were measured for $-30° < \theta < +30°$ with 0° at the central z-axis at a resolution of 0.1°, see Fig. 3.3a. The central axis distance scans were performed at a distance d_{CD} between CMUT and detector, see Fig. 3.3b. In increments of 2 mm, 10 positions were passed through from a starting point of (1.44 ± 0.63) mm or (4.44 ± 0.63) mm.

3.2 System Architecture & Operating Principles of the Nanoscopic Electrostatic Drive

An introduction to the fabrication, common applications and possible AMOC implementations for the NED are given in section 1.2.2. The NED actuator cell shown in Fig. 3.4a comprises two electrodes in their resting shape. Together with the electrically insulating spacers, they resemble a one side clamped, asymmetric beam structure. The gap between the electrodes contains a dielectric, e.g., air. Any driving potential $U \neq 0$ leads to attractive electrostatic forces between the electrodes. Subsequently, the electrodes deflect towards each other resulting in lateral strain F_L, indicated by magenta arrows in Fig. 3.4a.

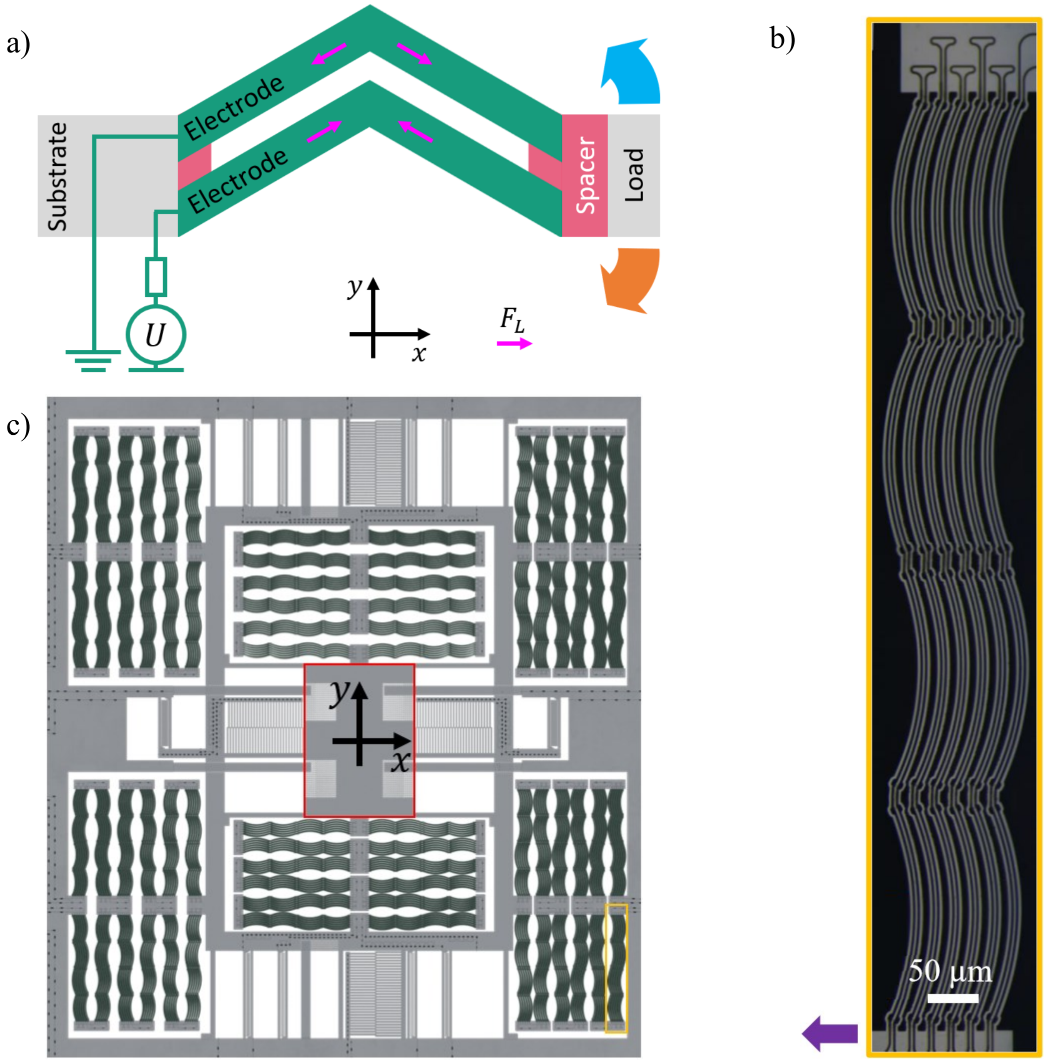

Fig. 3.4: a) Top view schematic of a NED actuator cell including driving potential U, lateral strain F_L and deflections indicated by arrows. b) Top view RLM image of a module comprising multiple cells, including movement direction indicated by a purple arrow [82, 172]. c) Top view schematic of a NED based micro-positioning platform including a module comparable to ‘b’ marked in yellow and the load area marked in red [82].

F_L induces a deflection of the load in the xy-plane, which is indicated by the orange arrow in Fig. 3.4a. The restoring mechanical spring force of the actuator cell results in the resetting deflection indicated by the blue arrow.

The NED-based chips employed in this work are composed of multiple cells. They are stacked in parallel and repeated in series to form bending modules, see Fig. 3.4b. The micrograph depicts a module comprising multiple cells to move the load, indicated by a purple arrow.

By arranging multiple actuator modules, a NED-μPS can be constructed, see Fig. 3.4c. The schematic includes a module comparable to what was displayed in Fig. 3.4b, indicated in yellow. The actuators above and below the central load area enable motion in y-direction. The load area is indicated in red in Fig. 3.4c. The actuators located to the left and right of the load area can drive it in the x-direction.

4 Energy Distribution Model

A model was designed to predict the behavior and the outcome of the physical system employed to fabricate structures on chip using TPP. To start with, the optical fundamentals are described. After that, the polymerization threshold model and findings on factors contributing to the fabrication performance are presented. The reliability of the theoretical model was determined by comparing the results to numerical simulations and the experiments they aim to predict in chapter 5, after further enhancements.

4.1 Optical Fundamentals of Two-Photon Polymerization Lithography

The setup found inside the TPP system is shown in Fig. 4.1 as a section view. To visualize the energy distribution, ray optics are overlaid on two schematics with different z-positions of the objective. The incident beam I_i used for TPP gets reflected from the substrate. The reflected beam I_r coincides with the incident beam. The resist material conforms in between objective and substrate and acts as an immersion fluid.

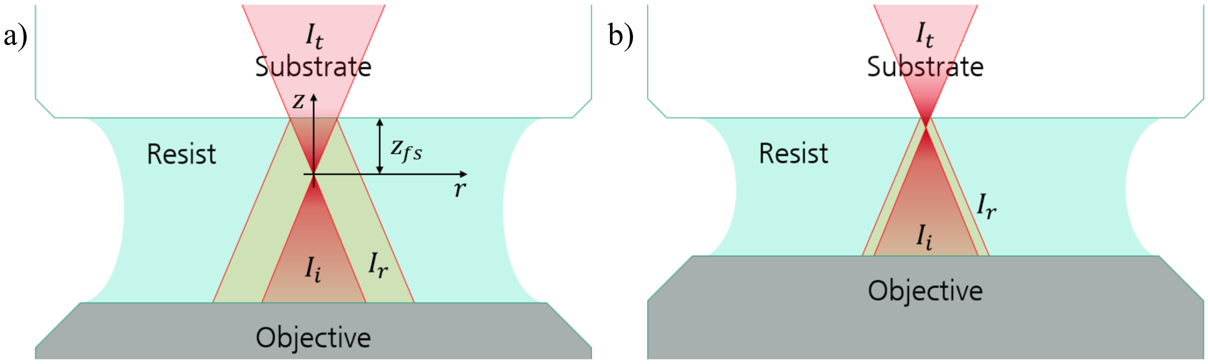

Fig. 4.1: a) Schematic of the TPP setup including ray optics of the incident, transmitted and reflected beam sections I_i, I_t and I_r including the distance between the focal point and substrate z_{fs}. b) The same schematic, but with the objective moved closer to the substrate.

The substrate is fixed while the objective is depicted at two positions in Fig. 4.1a and b, to illustrate how the reflected beam I_r changes. The superposition of I_i and I_r increases the intensity at the focal point. The closer the objective moves to the substrate, the more they overlap and the higher the overall intensity. A part of the incidence is transmitted as I_t into the substrate.

The model to describe the radiation exiting the objective of the TPP system is based on a paraxial Gaussian intensity distribution [173, S. 81–83]. The high numerical apertures of the utilized objectives do not justify this condition, but it is sufficient, as the highest intensity part of the light distribution at the focal point can be described by a Gaussian envelope, and the laser pulse width encompasses many optical cycles [14].

The electrical field of the 00 or fundamental transverse electromagnetic (TEM) mode of a Gaussian beam has an energy distribution of the following nature [173, pp. 81-83, p. 173]:

$$\vec{E}(r,z) = \vec{E}_0 \frac{w_0}{w(z)} e^{-\frac{r^2}{w(z)^2}} e^{-i(kz-\omega z)} e^{-i\frac{kr^2}{2R(z)}} e^{i\xi(z)} \tag{4.1}$$

with the constant complex amplitude $\vec{E}_0$, the radius of the beam waist w_0, the beam radius $w(z)$, the axial distance from the focal point z, the radial distance from the center axis of the beam r, the wavenumber k, the angular frequency ω, the radius of curvature of the wave fronts $R(z)$ and Gouy phase shift $\xi(z)$. The complex refractive index of the transmitting medium [173, S. 175–176]

$$\hat{n}_i = n_i + i\kappa_i \tag{4.2}$$

with n_i and κ_i representing the real part or refractive index and the imaginary part or extinction coefficient, respectively. The roof notation is used to distinguish between the complex total and the real part. The beam divergence in radian can be written as [173, S. 86]

$$\theta_B = \arcsin\left(\frac{NA}{n_i}\right) \tag{4.3}$$

with the numerical aperture of the focusing objective NA. For the paraxial case, the radius of the beam waist in the focal point can be approximated from the far field as [173, S. 86]

$$w_0 \cong \frac{\lambda}{\pi\theta_B} \tag{4.4}$$

An improvement of the beam waist for high NA objectives is given in [174] as

$$w_0 \cong \frac{\lambda}{\pi NA}\sqrt{n_i^2 - NA^2} \tag{4.5}$$

The distance from the beam waist to the point where the beam radius is increased from the waist by a factor of $\sqrt{2}$ is called Rayleigh length and can be calculated as [173, S. 83]

$$z_r = k_r z_{r,G} = k_r \frac{\pi {w_0}^2}{\lambda} \tag{4.6}$$

with the Rayleigh factor k_r used to adjust to the non-optimality of the simulation. The beam radius can be stated as [173, S. 85]

$$w(z) = w_0\sqrt{1 + \left(\frac{z}{z_r}\right)^2} \tag{4.7}$$

The radius of curvature of the wave fronts can be written as [173, S. 83]

$$R(z) = z + \frac{z_r^2}{z} \tag{4.8}$$

The Gouy phase shift of a fundamental Gaussian beam is stated in [175] as

$$\xi(z) = -\arctan\left(\frac{z}{z_r}\right) \tag{4.9}$$

The following equation can be used to calculate the intensity distribution of the Gaussian beam [104, 173, S. 81–83], including the Lambert-Beer attenuation experienced during the travel through the liquid resist

$$I(r,z) = I_0 \frac{{w_0}^2}{w(z)^2} e^{-\frac{2r^2}{w(z)^2}} e^{-\alpha d_{path}} \tag{4.10}$$

$$I_0 = \frac{\varepsilon_0 n_i c_0}{2\mu_{rel}} E_0^2 \tag{4.11}$$

with the maximum intensity I_0, the attenuation coefficient α, the path the beam travels along d_{path}, the dielectric field constant ε_0, the velocity of light in vacuum c_0 and the relative magnetic permeability μ_{rel}. The latter two are related by [173, S. 163]

$$\mu_{rel} = \mu/\mu_0 = \frac{n_i^2}{\varepsilon_{rel}} = \chi + 1 \tag{4.12}$$

with the magnetic permeability of free space μ_0 and the volume magnetic susceptibility χ. The relative electric permittivity is noted as $\varepsilon_{rel} = \varepsilon/\varepsilon_0$, where ε represents the permittivity of the material. The path d_{Path} includes the total distance travelled by the beam, e.g., for the reflected beam returning to the focal point, the distance from the objective to the focal point and twice the distance z_{fs} between focal point and the reflective interface with the substrate results in

$$d_{Path} = d_{WD} + 2z_{fs} \tag{4.13}$$

with the working distance d_{WD} and the attenuation coefficient, which can be calculated as [176]

$$\alpha = \frac{4\pi\kappa_i}{\lambda} \tag{4.14}$$

4.2 Exposure Dose

The exposure dose D describes the amount of energy incident on an object during the exposure period. According to [114, S. 177], the behavior of the absorbed exposure dose D at a voxel can be calculated by

$$D(N) \propto \acute{t} R J_P^N \tag{4.15}$$

where $\acute{t}$ represents the time period during which the beam is active and irradiates the voxel with the pulse energy J_P at a repetition rate R. The term N describes the nonlinearity of the absorption process. In the case of two-photon absorption, $N = 2$, so that similar to [114, S. 178] for this work, the exposure dose becomes

$$D(r, z) \propto \tau I(r, z)^2 \tag{4.16}$$

where τ represents the fabrication time and I the spatial intensity distribution. As $\tau \propto v^{-1}$, the other major influence besides beam intensity is its scan speed v.

Fig. 4.2a depicts the static dose distribution of an example Gaussian beam in the vicinity of the focal point and normalized to the maximum. It was calculated and plotted as a colormap via MATLAB R2021b, using the equations of the previous section.

The horizontal axis of Fig. 4.2a shows the radius r normalized to the beam waist w_0, see equ. 4.5. The vertical axis represents the axial distance from the focal point z normalized to the Rayleigh length z_r, see equ. 4.6. The shape of the focal area at a threshold dose I_{th}^2 can be approximated elliptic, compare Fig. 4.2 and Fig. 2.2b.

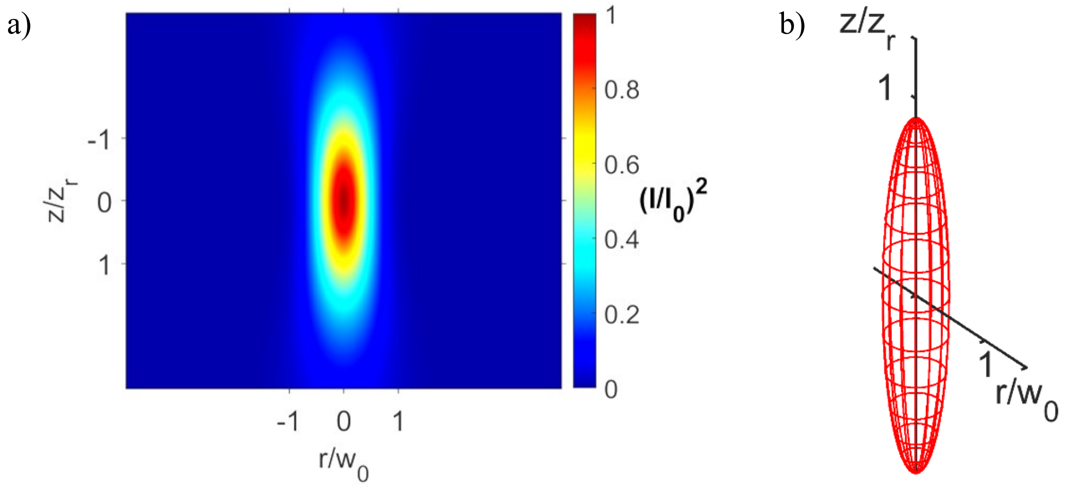

Fig. 4.2: a) Colormap of a Gaussian beam dose near the focal point normalized to the maximum. b) 3D contour approximation at equal dose in the vicinity of the focal point of an example Gaussian beam.

Rotating it along the z-axis gives the spheroid volume, recognizable as the voxel in structures fabricated by TPP, see Fig. 4.2b. Absorption and reflection are not considered here.

4.3 Polymerization Threshold Model

As described in [114, S. 177]: “The simple threshold model can be helpful for the analysis of experiments […] comparing similar structures.” Multiple thresholds can be established, as visualized in Fig. 4.3, where three examples of 20 x 20 x 20 µm³ cubes identical except for their exposure dose are displayed. They were fabricated by TPP using the 63x objective and IP-Dip. The main domains are under- and overexposure (UX, OX), where structures are not viable.

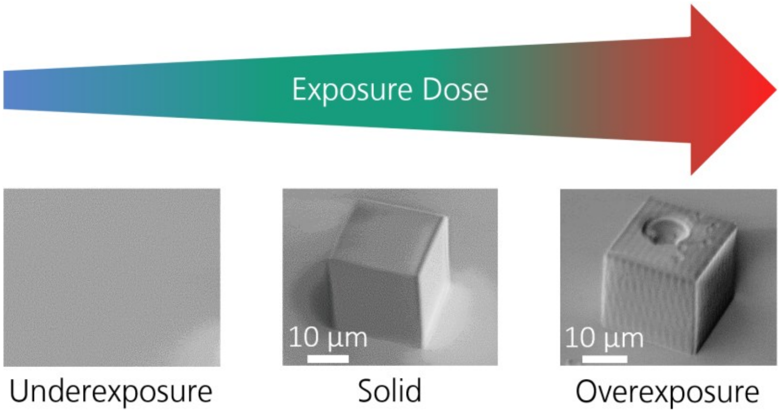

Fig. 4.3: Exposure dose thresholds for increasing exposure dose from left to right, including tilted view SEM micrographs of 20 x 20 x 20 µm³ cubes fabricated via TPP from IP-Dip. The image for underexposure depicts a cube that was washed away during development, the one for solid shows a valid example and the one for overexposure illustrates the damage that can be afflicted by incorrect selection of the exposure dose.

As stated in section 2.2, the chain length and entanglement scales with the radical generation and subsequent polymerization of a resist. This relation is described in [14] via the density of radicals

$$\rho = \rho_0\left(1 - e^{-D\delta_2}\right) \tag{4.17}$$

which depends on the photoinitiator concentration in non-polymerized resist ρ_0, the exposure dose D and the effective two-photon cross section δ_2, which describes the probability of the absorption process. Thus, the higher the dose, the stronger the material becomes [14, 126, 127]. As common in lithography, a threshold can be applied, where the structure fabricated via TPP survives the development, handling and characterization and any further postprocessing. Exposing less than that threshold leads to UX, even though gel-like structures can be achieved. Depending on the purpose of the fabrication, any structure that survives until characterization can be counted towards the solid domain, indicating viable exposure (OK).

Finally, the OX domain, where the energy absorbed by the resist or the substrate [177] can be transformed into heat, which can vaporize the components of the resist. As stated in [114, S. 186]: "[…] the dominant mechanism for radical formation is purely photochemical at all investigated repetition rates, while a (at least partly) photothermal process is connected to the sample damage in the overexposure domain."

This can be seen as bubble shapes or fractures in the structure, see Fig. 4.3. The so created bubbles can vary in size and the larger, the more problematic they become, as they move and/or destroy existing structures. They impede the polymerization of the volume they occupy, resulting in bubble shaped holes in the intended structures. These unpolymerized volumes reduce the density and the structural integrity of the intended structures. Bubbles can disconnect slices and reduce adhesion to the substrate.

A relevant heat source is the photon absorption itself, be it OPA or TPA. There are resists with an exothermal polymerization reaction [178], but these were not used in this work. Another heat source are previously fabricated structures, the substrate, or particles and other contaminants, where the incident beam can get absorbed.

Another possible heat source might be avalanche ionization [104, 125], where high intensity irradiation leads to chemical bond breaking and free radical generation via photo-cleavage. The multiplying nature of the behavior of bubbles would fit that hypothesis.

During this work, it was found, that the incident beam might diffuse on the interfaces between liquid and gaseous fluid, increasing the absorbed fraction. This could lead to the avalanche effect.

At the top end of the OX domain the pyrolysis of the resist starts, which can be useful in applications that require even further size reduction [179].

4.4 Findings on Hatched Structures

The cubes shown in Fig. 4.3 are examples of hatched structures. They were fabricated line by line to create slices and subsequently slice by slice to create volumes. In the OX sample, one can recognize the voxel shape and slice distance d_s. For a successful fabrication, the voxel needs to overlap, as displayed in Fig. 4.4a, where the hatch distance d_h, line thickness d_l and overlap d_o are displayed.

The line thickness d_l depends on the voxel size and can be modeled by radius of the beam waist w_0, see section 4.1. A sufficient overlap d_o can be configured via hatch distance d_h or via the exposure dose. The latter depends on the fabrication time τ, see equ. 4.16. For the hatched structures fabricated in this work it can be written as

$$\tau \propto \frac{V n_p}{d_h d_s v} \tag{4.18}$$

with the intended volume of the structure V, the number of repeated scans per line n_p and the scan speed v. The use of n_p builds upon the memory effect notable in the resist, which makes multiple exposure viable [14, 180].

Besides these factors, the laser power and the composition of the resist, the following factors can influence the total polymerized volume of a hatched structure:

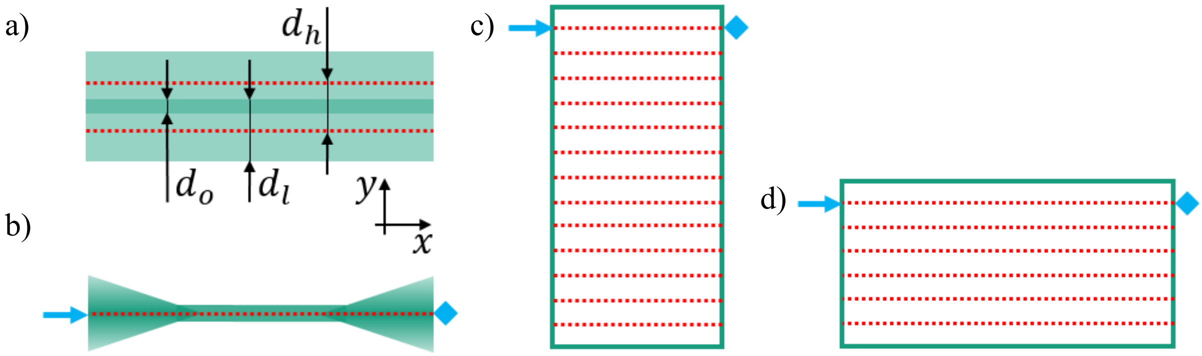

Fig. 4.4: a) Schematic of the top view of overlapping hatch lines including hatch distance d_h, line thickness d_l and overlap d_o. b) Schematic of the top view of a hatch line including acceleration and deceleration influence and start and stop point indicated via arrow and square, respectively. c) Schematic of the top view of a hatched slice including start and stop indicators. d) The same, using a different hatch strategy.

- The hatch strategy, which represents the order and arrangement of points, to which the fabrication laser moves in succession. The hatch strategy itself is dependent on the lateral size of a structure and thus can change in between layers for more complex parts. If one compares two rectangular cross sections that are identical except for the implemented hatch strategy, the one with longer lines will have more time between one line starting next to the previous, which may affect the dose, see Fig. 4.4c and d.
- The acceleration and deceleration, with which the voxel is driven, see Fig. 4.4b.
- The mutual influence of already polymerized volumes, see Fig. 4.4a [14, 149].
- Overlap/stitching blocks to form a structure larger than the FOV of the objective in use.
- Chemical restrictions, e.g. steric hindrance [14], oxygen or photoinitiator inhibition [114, 89-91, 188-189].

4.4.1 Hatch Strategy

To illustrate the influence of the chosen hatch strategy on fabricated structures, a toroid with a rectangular cross section – hereinafter referred to as contour – was analyzed. Common hatch strategy options, e.g., concentric circles, meander, or concentric lines in a sun beam form, are displayed in Fig. 4.5a, b and c, respectively.

The structures depicted in the RLM images were fabricated using the 10x objective and IP-Q, with an inner diameter of 1.04 mm and a set width of 50 µm. The z-height was set to 25 µm, the scan speed to 100 mm/s and the laser power to 20 mW. The slice distance was set to 1 µm and the hatch distance to 300 nm. The lines were illuminated once per line and slice.

To increase dose consistency, start and end points should be avoided. At these points, the galvanometer mirrors accelerate and decelerate, leading to variations in dose. Thus, the concentric circle strategy was the choice for the circular contour structure, see Fig. 4.5a.

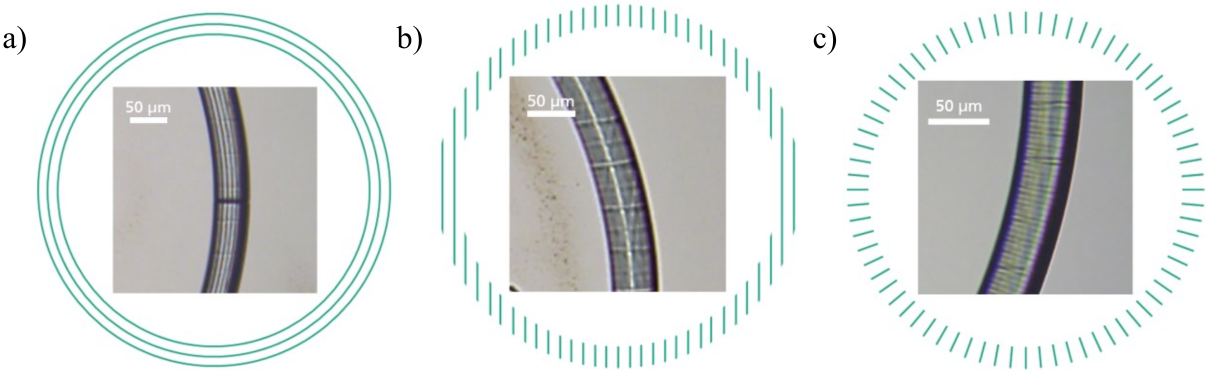

Fig. 4.5: Schematics of the top view of various hatch strategies for the circular contour structure, including top view RLM images of fabricated contours. a) Concentric lines. b) Meander. c) Sun beam.

The meander strategy would lead to the mentioned start and end points as well as inconsistencies in the hatch line length, see Fig. 4.5b. The sun beam strategy does not have the latter, but the former problem, see Fig. 4.5c.

Upon multiple exposure, which is sometimes necessary to increase dose without increasing laser power or reducing scan speed, the concentric circle strategy also makes the most sense. Here, the time before the same line gets hit with another dose is the longest, which allows a longer cool down period.

The programmed circular hatch lines were approximated by chord lines at an angle of $2\pi/x$, where x represents the number of separate lines per full circle. This way, one chord line after the next can be fabricated without interruption.

The only start and end points emerge at the start and end of each circular hatch line after completing 360°, see the inset in Fig. 4.5a. This leads to an increased dose in that area, especially if multiple hatch lines are created one after the other. To prevent this problem, the starting point of each subsequent hatch line was moved by an angle, which staggers the start and end points, eliminating the problem.

4.4.2 Acceleration

Common hatch strategies lead to a concentrated intensity distribution at start and end points of hatch lines, where the driving device directing the laser beam respective to the substrate has to accelerate and decelerate the beam, see Fig. 4.4b and Fig. 4.5a. For the structures fabricated in this work, galvanometer mirrors were employed.

The deflection angle, as well as the dynamic deformation [181] of the mirrors are dependent on the driving voltage. The acceleration can be adjusted before fabrication via the parameter GalvoAcceleration. Through the objective, the angle gets translated into a distance travelled by the beam.

A contour structure was used to investigate the impact of the acceleration setting. It was fabricated using the 10x objective and the resist IP-Q, see Fig. 4.6a. The set width was 50 µm and the inner and outer diameters were 1.04 and 1.14 mm, respectively. The height was set to 25 µm, the scan speed to 100 mm/s and the laser power to 20 mW. The slice distance was set to 1 µm and the hatch distance to 100 nm between the concentric circles. The lines were illuminated once per line. The acceleration setting was stepped from 1 to 20 $V/m/s^2$ in increments of 1 $V/m/s^2$, which is the range recommended by the manufacturer of the system. Increasing the acceleration further could lead to mirror deformation, which results in an increased fabrication error and decreased precision.

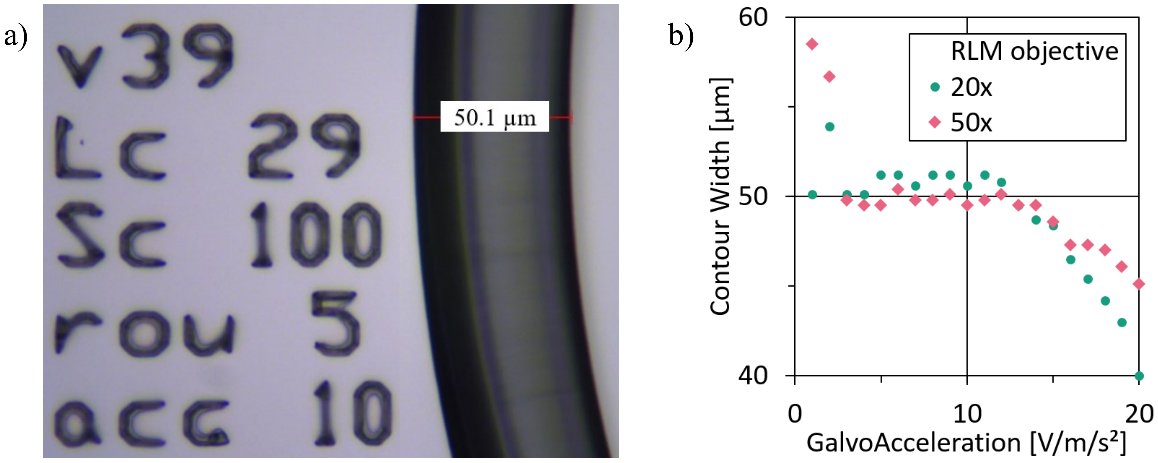

Fig. 4.6: a) Top view RLM image of a contour including measurement and structured parameter text. b) Contour width vs. galvanometer acceleration setting GalvoAcceleration, including objectives 20x and 50x.

The contour width of each contour was measured using the 20x and 50x objective of the RLM. The latter objective was employed to reduce measurement deviation. The Fig. 4.6b shows how the width and thus the dose of the contour structures was affected by the mirror acceleration. Based on this evaluation, the acceleration should be set between 3 and 12 V/m/s² for this specific structure if a consistent dose is required. Below that range, the width increases and above, it decreases. For the subsequent contour structures fabricated in this work, 10 V/m/s² was selected.

4.4.3 Fabrication Error & Shrinkage

Hatch strategies fill a structure so that the outer surfaces will be formed by the outermost voxels. After fabrication, the structure dimensions suffer from fabrication errors, e.g., due to

- dose inconsistencies, see section 4.4.1,
- shrinkage during TPP, development or drying [182, 183],
- positioning errors
  - of the piezo stages, see section 2.3.1,
  - from inertia based mirror deformation [181].

When complex structures are required, exact fabrication almost always can only be achieved by iteratively approaching from a best guess starting point, which can include for example a shrinkage factor calculated from dimensional measurements.

Ten identical specimens of the structure displayed in Fig. 4.7a were fabricated using the 10x objective and IP-Q. They were affected by the previously mentioned issues, which led to the deformation illustrated in Fig. 4.7d. Their set dose was identical for each specimen.

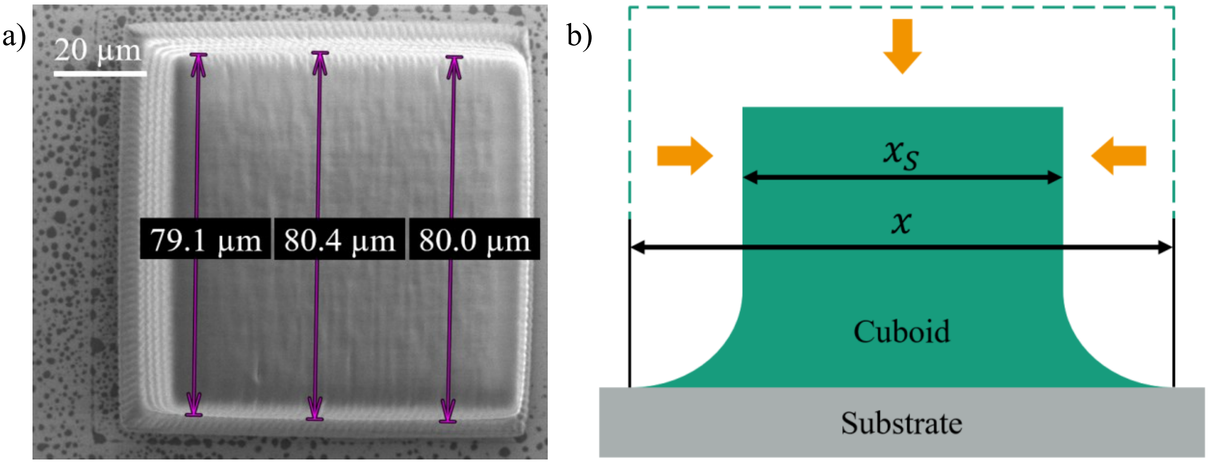

Fig. 4.7: a) Top view RLM image of a 100 x 100 x 100 µm³ cuboid fabricated from IP-Q using the 10x objective for error determination. b) Schematic of a deformed cuboid on a substrate, including lateral size before and after shrinkage x and x_S, respectively.

The ten-specimen set of 100 x 100 x 100 µm³ cuboids received three measurements each of the observed lateral cube size x_S, once using the RLM and once using the SEM. The evaluation of the lateral measurements is listed in Tab. 4.1, where the observed target deviation of the cuboids measured with the RLM and SEM illustrates that the transparency of the resist makes measurements via the RLM unreliable.

The target deviation observed by SEM shows a large deformation of almost 20 %, which is more than expected, see Tab. 2.2. This might be due to low adhesion because of the relatively small area connecting the structure to the substrate.

The measurement deviation represents the deviation between the three individual measurements per cuboid and can include shrinkage effects, for example corners receive more deformation due to shrinkage because of the lower ratio of volume.

The fabrication error noted in Tab. 4.1 represents the deviation between individual cuboids. This can include statistical errors during shrinkage processes, as well as the errors of the stages and mirrors.

Tab. 4.1: Size comparison of identical 100 x 100 x 100 µm³ cubes fabricated from IP-Q using the 10x objective for error determination from RLM and SEM measurements.

100 x 100 x 100 µm³ cubes	**Unit**	**RLM**	**SEM**
Average lateral cube size	**[µm]**	98.5	80.4
Observed target deviation	**[%]**	1.5	19.6
Measurement deviation	**[µm]**	0.13	0.32
Fabrication error	**[µm]**	0.32	0.32

5 Investigation & Compensation of Substrate Effects

After the incident beam passes through the voxel, it continues to transmit through the resist until it hits the substrate. Here, the material characteristics of the substrate affect the further path, as a part of the beam can get reflected and interfere with itself, and a part of it can get transmitted into and through the substrate.

Both can have an impact on the intended fabrication, not only the reflection off of the substrate interfering with the incidence matters, but also the thermodynamics of diffracting elements and structures with poor heat dissipation, like the thin plates on a CMUT die, for example. The contribution to the energy distribution model presented in the following, describes these effects with the intent to subsequently compensate any unwanted excess. To adapt the set dose D_0 in the vicinity of a problematic substrate, the compensated dose

$$D_c = D_0 c_R c_H \tag{5.1}$$

gets adjusted via the reflection and heat compensation factors c_R and c_H, respectively. Here, the modulation of the dose is provided by the laser power as

$$P_c = P_0 \sqrt{c_R c_H} \tag{5.2}$$

which can be interchanged with the intensities I_c and I_0. The factors c_R and c_H are described in more detail in sections 5.1 and 5.3, respectively.

The condition of the substrate can have further effects on fabrication. A structure's adhesion to the substrate can affect its intended functionality. However, utilizing the methods investigated in section 5.5, adhesion can be adjusted. Tilted substrates can lead to issues, e.g., disconnecting structures. In section 5.6, substrate tilt is investigated and subsequently compensated via the tilt compensation upgrade to the TPP system.

5.1 Substrate Reflection Model

An excess in intensity due to reflection of the fabrication laser by the substrate can be prevented by alteration of the parameters of the TPP process in the region where the effect is significant. For this purpose, the model described in chapter 4 including the following reflection effect model was simulated using MATLAB R2021b.

Assuming normal incidence and considering magnetic permeability μ, the reflectance follows from simplified Fresnel formulae are derived in annex E and can be written as

$$\mathcal{R}_{TE} = \left| \frac{\hat{n}_i \mu_t - \hat{n}_t \mu_i}{\hat{n}_i \mu_t + \hat{n}_t \mu_i} \right|^2 \tag{5.3}$$

$$\mathcal{R}_{TM} = \left| \frac{\hat{n}_t \mu_i - \hat{n}_i \mu_t}{\hat{n}_t \mu_i + \hat{n}_i \mu_t} \right|^2 \tag{5.4}$$

where $\mathcal{R}_{TE}$, $\mathcal{R}_{TM}$ and $\hat{n}$ are the reflectances of transverse electric and transverse magnetic modes and the complex refractive index, respectively. The indices i and t correspond to the material the incident and transverse wave travel within, respectively. The respective transmittances follow $\mathcal{T} = (1 - \mathcal{R})$.

As subsequent TPP fabrication on chip was mostly performed using the 10x objective and IP-Q resist, it is used in this chapter to provide an alternative parameter set. In cases where parameters were unknown for IP-Q, the ones for IP-Dip were used as recommended by the manufacturer. The input values for the calculation of the energy distribution model are noted in section 2.3.5 and Tab. 5.1. The magnetic susceptibility was calculated by equ. 4.12.

Tab. 5.1: Energy distribution model input values and computed results.

Parameter	**63x, IP-Dip**	**10x, IP-Q**
Numerical aperture NA	1.4	0.3
Working distance d_{WD} [µm]	360	700
Absorption lens to focus	0.9942	0.9888
Beam divergence [rad]	1.16	0.2
Beam waist w_0 [nm]	140	822
Extinction coefficient k_i [-]	$1.24 \cdot 10^{-6}$ [184]	$1.24 \cdot 10^{-6}$
Relative permittivity $\varepsilon_{r,i}$ [-]	1.43 [145]	1.43
Calculated volume magnetic susceptibility χ_i [-]	$6.4 \cdot 10^{-1}$	$5.3 \cdot 10^{-1}$
Laser power at the objective lens [mW]	50	
Scan speed [mm/s]	10	
Resist absorption coefficient [1/m]	19.98	

Tab. 5.2: Characteristics of various plate materials and calculated reflectances.

Material	TiAl	Si	SiO₂	Al
n_t Refractive index (real)	2.970 [153]	3.705 [185]	1.46 [186]	2.52 [187]
k_t Extinction coefficient	3.503 [153]	0.007 [185]	0.0013 [188]	5.2 [187]
χ_t Volume magn. susceptibility	$2.9 \cdot 10^{-6}$ [189]	$-3.74 \cdot 10^{-5}$ [190]	$-1.13 \cdot 10^{-5}$ [190]	$2.20 \cdot 10^{-5}$ [190]
$\mathcal{R}_{TE,a}$ Reflectance coefficient (air)	0.57 [153]	0.331 [191]	0.0366 [192]	0.89 [185]
$\mathcal{R}_{TE,a,c}$ Calc. refl. coefficient (air)	0.576	0.330	0.035	0.878
$\mathcal{R}_{TE,IP-D,c}$ Calc. refl. coefficient (IP-Dip)	0.596	0.357	0.048	0.885

The chip materials mentioned in sections 1.2.1 and 1.2.2 are already a subset of the commonly used materials in SF. For chapter 5, the selection was reduced to the CMUT with TiAl, Si, SiO_2 and Al. Their respective material characteristics and calculated reflectances can be found in Tab. 5.2. Measurements of amorphous TiAl films sputter deposited at Fraunhofer IPMS show a reflectance of 57 % at 780 nm [153], which is the center wavelength of the incident radiation of the TPP system used in this work. Using equation 5.3, this reflectance was recalculated, resulting in 57.6 %, see Tab. 5.2. This comparison to literature references shows an acceptable approximation. During testing, it was found that the contact pads and plates, which are commonly fabricated from TiAl, respond to TPP with the mentioned issues. In this section, the established model is exemplarily applied to TiAl as a substrate material.

The Gaussian beam simulation of the optical path was carried out for a plane r-z similar to Fig. 4.2a, including the linear Lambert-Beer OPA from the objective lens to the focal point. For the reflected and the transmitted beams, the OPA from the focal point to the substrate was included as well. For the reflected beam, the OPA from the substrate to the focal point was included. Thus, the intensities at the focal point I_F, the substrate interface I_S and the transmitted intensity I_t were calculated according to equ. 4.10.

Not included were constructive and destructive interference, as well as the time-dependence of individual laser pulses, as only the maximum dose necessitates compensation. These effects were studied intensely in [104, S. 98–101], where even with simulations enhanced by these considerations and exclusive averaging of experiments, differences between single voxel line experiments and simulations were non-negligible and subsequently corrected via factorization. This was realized by experimentally determined factors. Factorization was the approach utilized in the present work as well. Furthermore, non-orthogonal incidence was not included here, as compared to normal incidence it would only reduce the total intensity at the voxel. For the same reason Parasitic side reactions like non-radiative decay, spontaneous photoemission or (reverse) intersystem crossing [114, S. 178–181], were neglected as well as dose inconsistency due to aberrations [132]. OPA by already polymerized structures depends strongly on the given structure intended for fabrication [149]. This makes predictive modeling of the effect nearly impossible, which is why it was neglected.

A ray optical calculation of the contribution to the incident dose from backside reflections of a substrate as specified in Tab. 5.1 was performed, see annex F. With IP-Dip, the resulting effective backside reflected fraction of the dose of 0.00, 0.01, 0.00 and 0.00 % for TiAl, Si, SiO_2 and Al, respectively, was considered negligible due to its low impact.

The resulting dose distributions shown in Fig. 5.1a are based on the squared and normalized intensities at their respective location on the z-axis, for an example setup consisting of a Si wafer coated with 520 nm TiAl. The Rayleigh factor k_r was set to 7.25, so that combined with the Gaussian approximation of the Rayleigh length $z_{r,G}$ of 48 nm, the result represents the standard voxel size of 700 nm for the 63x objective and IP-Dip.

Depending on the distance of the focal point to the substrate z_{fs} normalized to the Rayleigh range z_r, the dose changes, compare Fig. 5.1a and Fig. 4.1a. A reference line was plotted for visualization of the excess. The blue line represents the dose at the focal point, which is more than doubled at the interface, only reduced by the transmission into the substrate and the attenuation by the resist.

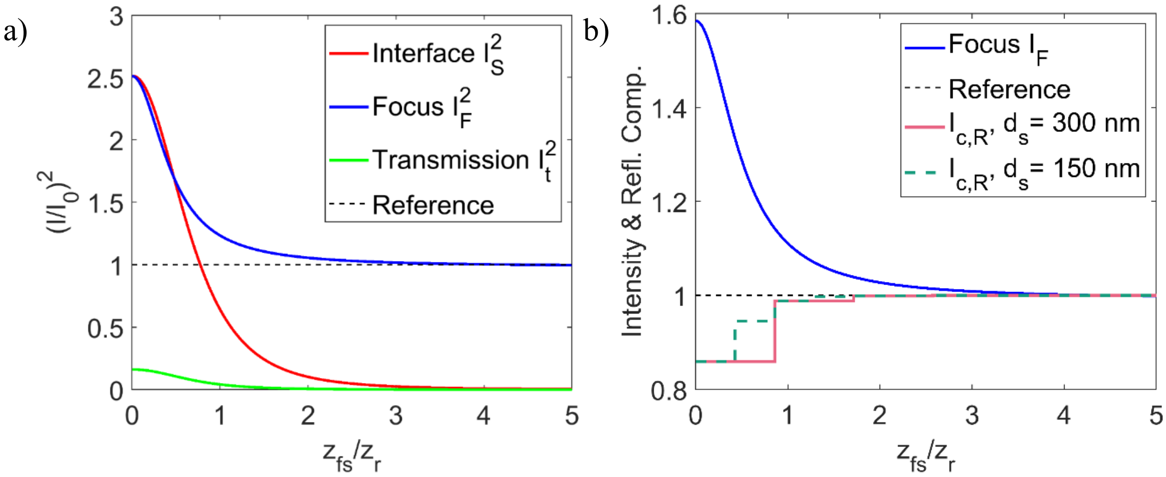

Fig. 5.1: a) Squared and normalized intensity increase at interface and focal point due to substrate reflection vs. focus to substrate distance, including transmission into the substrate, a Si wafer with 520 nm TiAl coating. IP-Dip and 63x objective. b) Same setup: Intensity excess at the focal point and laser power compensation per slice vs. focus to substrate distance z_{fs} for 300/150 nm slice distance d_s.

At about five times z_r from the interface, the focal dose reduces to the reference line. The red line represents the dose at the substrate/resist interface. As expected, when the focal point is very close to the interface, it matches the one at the focal point. Due to the divergence of the beam and the attenuation, the dose at the interface asymptotically approaches zero with increasing z_{fs}. The transmitted part of the beam represented by the green line, visualizes that a maximum of 16.1 % is transmitted and reduces in about one Rayleigh range.

The results of the optical simulation show the significantly enhanced dose in the vicinity of a reflective substrate, which was expected from experience gathered in experiments with CMUT chips as substrates. To compensate the excess, the reflection factor can be calculated as

$$c_R = \frac{D_i}{D_i + D_r} = \frac{I_i^2}{I_i^2 + I_r^2} \tag{5.5}$$

with the intensity at the focal point I_F based on the incident and reflected intensities I_i and I_r. Their respective equations can be found with the one for I_t in annex G. Fig. 5.1b depicts the intensity distribution and the necessary decrease in laser power per slice to compensate the excess for two variations of slice distance, calculated by multiplying the normalized focal intensity I_F/I_0 with $\sqrt{c_R}$. When using a per-layer-compensation, a lower slice distance is preferable due to the resulting increase in fitting accuracy.

5.2 Substrate Thermodynamic Model

Beside the optical effects, the thermodynamic influence of the substrate is another important impact factor on the manufacturing process. First, the environmental influences are established. Then, analytical and numerical approaches are followed to advance the model, resulting in a substrate effect compensation method.

Direct measurement of the temperature distributions during the TPP process at a comparable resolution was previously found to be complex [193]. For this work, a validation of the model was developed via dose and compensation experiments.

5.2.1 Thermal Environment

The TPP system used for this study was located inside a clean room cabin including air filter units in a temperature-controlled laboratory and itself has a thermally protective cover surrounding the work chamber. Thermal stability of the environment was not always given, see Fig. 5.2.

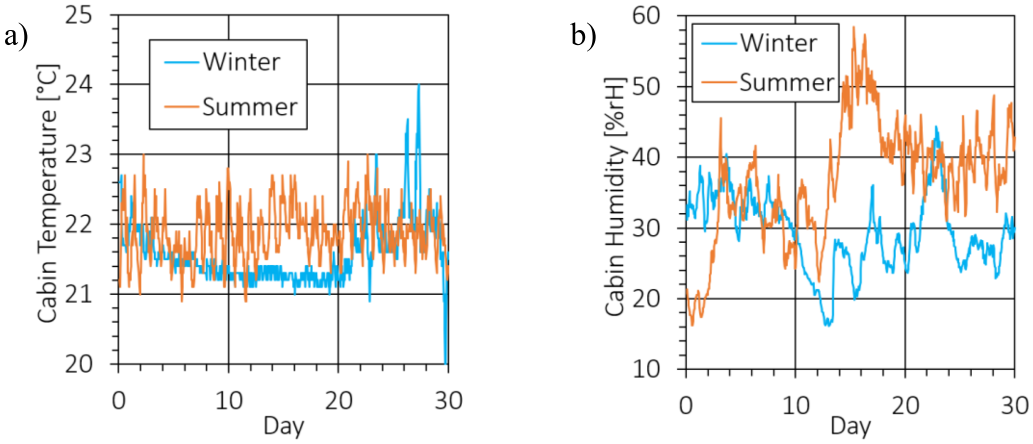

Fig. 5.2: a) Clean room cabin temperature of summer and winter month. b) Relative humidity.

Fluctuations can be influential, e.g., other laboratory equipment, temperature control failures and the body of the user.

The months selected for Fig. 5.2 are May and December of 2021, where the laboratory performed with increased activity. An all-time average temperature of the clean room cabin of (21.7 ± 0.44) °C was averaged from hourly measurements. During longer term experiments with personal presence, the temperature rose to (22.7 ± 0.76) °C. As depicted in Fig. 5.2a, the winter temperature is generally lower, but has less peaking. This could be due to the more active temperature control unit during warmer weather. The last ten days of December show increased peaking, due to the climate control shut off, leaving a rudimentary house control in charge.

The humidity values in Fig. 5.2b present slightly lower values for winter, as expected. The resist and TPP system manufacturer recommendations of <60 % relative humidity and (22 ± 1) °C were mostly achieved. The fabrication chamber air temperature of (33 ± 0.98) °C was measured before fabrication start using the AM-550-EUR (Beha-Amprobe GmbH).

5.2.2 Heat Compensation Factor

Using these environmental characteristics, the following analytical and subsequent numerical studies were conducted, to estimate the thermal behavior of the TPP process especially considering the substrate.

Part of the energy transmitted into the resist and subsequently into the substrate can convert to heat. As explained in section 4.3, excess heat can lead to problems like solvent vaporization. To elucidate the thermal behavior and allow for the compensation of these effects, a thermal dose and compensation factor c_H was established as

$$c_H = \frac{D_{H,c}}{D_{H,c} + D_{H,a}} \tag{5.6}$$

with the thermal dose of the resist threshold $D_{H,c}$ and the thermal dose absorbed by the substrate $D_{H,a}$. Using Fourier's law for thermal conduction, the heat flow absorbed in the substrate $\dot{Q}_a$ during fabrication and the maximum heat flow, before vaporization events occur, $\dot{Q}_c$ can be compared. The latter can be stated for a homogeneous one-dimensional material as

$$\dot{Q}_c = \frac{Q_c}{\Delta\tau} = -k_c A \frac{\Delta T_c}{\Delta x} \tag{5.7}$$

Here, k_c is the thermal conductivity and A is the cross-sectional area. The heat flowing during the period $\Delta\tau$ can then be written as

$$Q_c = -k_c A \frac{\Delta T_c}{\Delta x} \Delta\tau \tag{5.8}$$

with the temperature difference $\Delta T_c = (T_F - T_C)$ present when solvent vaporization starts to happen, where the chamber and resist boiling point temperatures are T_C and T_F, respectively. The heat absorbed by the substrate is then

$$Q_a = -k_c A \frac{\Delta T_a}{\Delta x} \Delta\tau \tag{5.9}$$

where the temperature difference

$$\Delta T_a = (T_a - T_C) \tag{5.10}$$

depends on the laser power absorbed by the substrate P_a by

$$T_a = T_C + mP_a = T_C + mI_a A \tag{5.11}$$

with the material and architecture dependent gradient

$$m = m_{FEM} k_m \tag{5.12}$$

where m_{FEM} can be found via FEM and the gradient factor k_m was used to adjust to the non-optimality of the simulations. The absorbed intensity depends on the absorbed fraction η_a, the transmittance $\mathcal{T}$ and the center intensity of the gaussian beam I_0. The latter depends on the set laser power P_L so that [173, S. 85]

$$I_a = \eta_a \mathcal{T} I_0 = 2\eta_a \mathcal{T} P_L / A \tag{5.13}$$

The absorbed fraction η_a can be written as

$$\eta_a = \frac{I_a}{I_t} = 1 - e^{-\alpha_S \cdot h} \tag{5.14}$$

with the absorption coefficient α_S, see equ. 4.14, and the substrate thickness h. The substrate temperature can then be written as

$$T_a = T_C + 2m\eta_a \mathcal{T} P_L \tag{5.15}$$

Thus, the thermal dose can be used to describe the absorption as

$$D_{H,a} \propto \acute{\tau} I_a^N = \acute{\tau} \frac{Q_a}{A} = -\acute{\tau} k_c \frac{\Delta T_a}{\Delta x} \Delta\tau \tag{5.16}$$

where $\acute{\tau}$ represents the period during which the beam is active and $N = 1$ the nonlinearity of the absorption process. With that, the heat compensation factor can be calculated as

$$c_H = \frac{D_{H,c}}{D_{H,c} + D_{H,a}} = \frac{\Delta T_c}{\Delta T_c + \Delta T_a} = \frac{T_F - T_C}{T_F - T_C + 2m\eta_a \mathcal{T} P_L} \tag{5.17}$$

5.2.3 Cooling between Laser Pulses and Exposure Repetitions

With the laser power at the objective lens in the milliwatt scale, additional cooling methods could be necessary. Increasing the time for heat conduction and thus cool down could help to alleviate this issue:

- Increase the scan speed of the fabrication laser.
- Increase the number of passes the voxel takes over the same volume via:
    - Reducing the slice distance,
    - reducing the hatch distance,
    - increasing the LineNumber, which is a setting that determines the amount of passes the beam automatically takes over each hatch line.

These measures must be counterbalanced by adjustment of other parameters, so that the resulting dose achieves suitable polymerization.

The thermal diffusion between laser pulses can affect the cooling process [193]. The time frame τ_{dif} of thermal diffusion on the length scale of the lateral voxel radius ($w_0 \approx 140\,nm$), was written in [193] as

$$\tau_{dif} = \frac{{w_0}^2}{4K_c} \tag{5.18}$$

with the thermal diffusivity K_c, which can be calculated by [194]

$$K_c = \frac{k_c}{\rho c_P} \tag{5.19}$$

where k_c, ρ and c_P are the thermal conductivity, density and specific heat capacity, respectively. In IP-Dip, τ_{dif} results to 40 ns, so thermal diffusion will not occur at the 80 MHz repetition rate of the TPP system used in this work. It leaves only 12.5 ns between two laser pulses, so heat gets accumulated. The pulse duration of <100 fs [129] does not impact this consideration. For TiAl the time frame is 2 ns, so heat can dissipate between pulses. The dependency of the cooling on the voxel movement was omitted here.

Another cooling effect is diffusion between repetitions of line exposures, or during hatched exposure. Given the circular contour design shown in Fig. 4.5 and Fig. 4.6, here with a radius r_c of 550 µm and multiple repetitions of each line exposure. Note that the LineNumber function of DeScribe was not used here, which would mean multiple exposure for each subsection of the circle line. The exposure here repeats, once a 360° line was exposed. The incident heat will accumulate if the speed of the voxel movement becomes fast enough. The accumulated heat is then

$$Q_{ac} = \frac{I}{v}\mathrm{n}_r \qquad \mathrm{n}_r \geq 1 \tag{5.20}$$

where n_r is the number of rounds as a ratio of the diffusion time t to the time it takes to complete one round. The accumulated heat is depicted in Fig. 5.3 for a variation of settings.

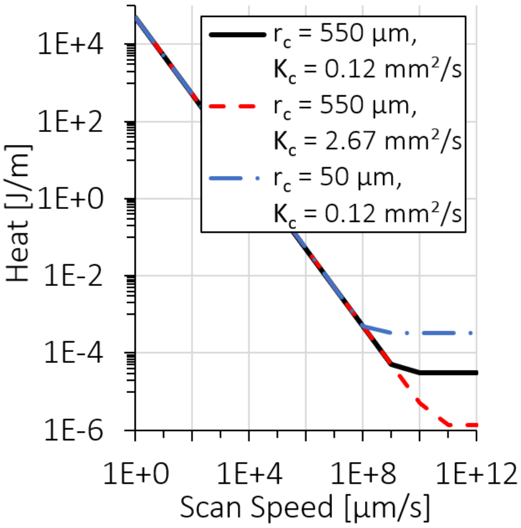

Fig. 5.3: Accumulated heat in a circular contour structure with radius r_c = 550 µm vs. scan speed for two different materials IP-Dip (K_c = 0.12 mm²/s) and TiAl (K_c = 2.67 mm²/s), as well as an IP-Dip version with radius r_c = 50 µm.

The selected laser power setting was 50 mW, the voxel radius w_0 was set to 0.5 µm. There are two diffusivities K_c depicted in Fig. 5.3, one for IP-Dip and one for TiAl with values of 0.12 and 2.67 mm²/s, respectively. The accumulated heat decreases with increasing scan speed, as long as the thermal diffusion time is less than the time required to complete one round of exposure. Due to the circular design, the heat levels out as soon as the scan speed is high enough to return around the circle before the heat can dissipate. Standard speed settings range up to 100 mm/s, above which accuracy decreases [131]. Both diffusivities show no accumulation below those settings. Decreasing the radius reduces the equilibrium point, but even at a radius r_c of 50 µm the standard settings were suitable.

5.2.4 Numerical Approach

The findings of the analytical considerations can help to understand the issue. But reducing the problem to two or one dimensions and only regarding individual parameters like diffusivity does not result in perfect parts fabricated via TPP.

To increase the understanding of the three-dimensional problem, FEM was performed using the static thermal analysis tool of ANSYS Workbench 19.2 (Ansys Inc.). In the following, the design of the study, the required analytical descriptions and material parameters are defined. Then, based on multiple substrate geometries, the temperature distributions along the significant positions, e.g., the interface between substrate and resist, are investigated.

The fluid motion of, e.g., air or resist, due to movements of the objective and due to thermal expansion, thus convection, was omitted to reduce computation time. Furthermore, thermal radiation was neglected, as the bodies investigated in the following are in direct contact. The thermal conductivity of the cured resist is expected to decrease with increasing temperature and increasing degree of conversion from monomer to polymer [195]. As these correlations have not been investigated for the resists employed in this work, the effects were neglected.

In this section, the chip materials mentioned in Tab. 5.2 were used as substrates for simulations based on the model established so far. The material characteristics listed in Tab. 2.3, Tab. 5.1, Tab. 5.2 and Tab. 5.3 were used in this simulation and to calculate the thermal diffusivity K_c, the transmitted fraction including backside reflections (annex F) and the absorbed power $P_a = AI_a$ calculated for IP-Dip and 50 mW laser power at the objective lens along equ. 5.19, 5.14 and 5.13, respectively. The beams active period $\tau_Q = 2w_0/v$ assumes a rectangular function where the laser switches on and then off, with a scan speed v of 10 mm/s. Compare the setup used during these simulations, which is shown in the schematic of Fig. 5.4, where the focal point is positioned on the interface between resist and substrate.

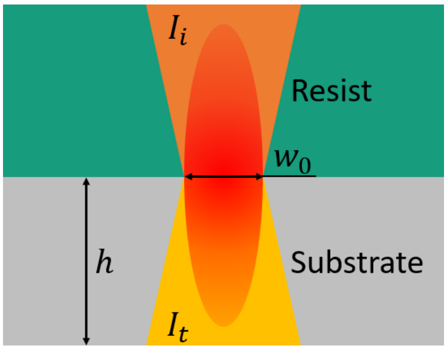

Fig. 5.4: Schematic of the substrate and resist interface including incident and transmitted beams I_i and I_t, respectively, as well as the substrate thickness h and the voxel radius w_0.

Further material characteristics and the calculated input values for FEM are listed in Tab. 5.3 and constitute the foundation for successive calculations, simulations and the compensation efforts.

Tab. 5.3: Material characteristics and heat simulation input values calculated for IP-Dip.

Material	**TiAl**	**Si**	**SiO₂**	**Al**
Density [g/cm³]	3.7 [196]	2.33 [197]	2.19 [186]	2.7 [196]
Isotropic heat conductivity [W/m/K]	5.44 [198]	156 [197]	1.4 [186]	237 [199]
Specific heat capacity [J/g/K]	0.55 [200]	0.7 [186]	1.4 [186]	0.89 [201]
Thermal diffusivity [mm²/s]	2.67	95.7	0.46	98.4
Transm. fraction incl. backs. refl. [%]	40.4	4.63	1.06	11.5
Absorbed Power P_a [W]	1.63	0.298	0.101	0.132

The first geometry considered in this study is visualized in Fig. 5.5a and consists of a substrate with a thickness of 520 nm and a radius of 50 µm. Above the substrate, a resist volume with a height of 25 µm was positioned.

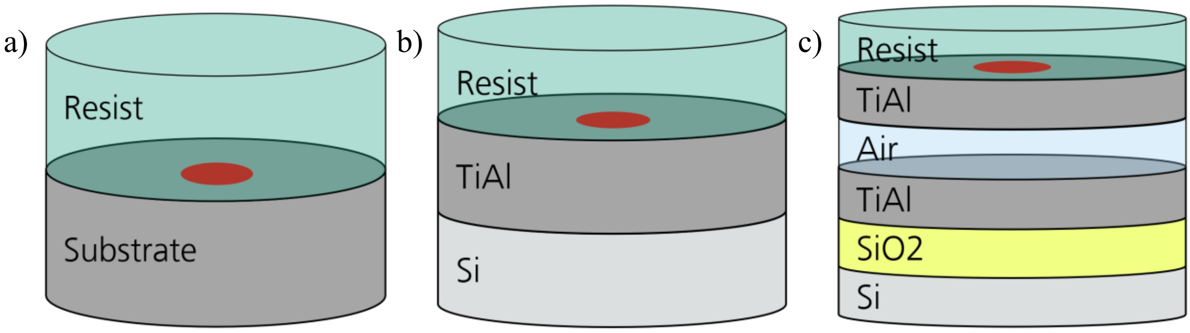

Fig. 5.5: a) Heat simulation substrate geometry schematic comprising any solid, liquid and gaseous components of a single material substrate covered in resist, including the absorbed heat indicated by a red area. b) The same for a substrate comprising Si coated with TiAl. c) The same for a mock CMUT plate comprising from top to bottom a flexible plate, a gap, an electrode and a substrate.

The boundaries on top of the resist volume and around its edge and the edge of the substrate were set to a static temperature of 306.15 K, the chamber temperature T_C. The bottom of the substrate was assumed isolated, analogous to the CMUT gap. The absorbed heat was assigned to an area as calculated before, located in the center on top of the substrate, highlighted red in the schematic.

Fig. 5.6a displays the element size convergence. It was performed for TiAl as substrate material in domain configuration a, with its corresponding heat for an incident 50 mW at the objective lens. The temperature was recorded at the substrate center, where the deviation was found to be the largest. A maximum element size below 0.5 µm allows a temperature result within 5 % of the normal at a reasonable calculation time and was applied to subsequent simulations.

As stated in [104], with increasing heat conduction, the transmitted energy gets dissipated quicker, which was shown for aluminum, steel and brass. As outlined in [104], the influence of heat conductivity on the resulting temperature increases exponentially, the lower it is.

Earlier measurements of the heat conductivity of TiAl at Fraunhofer IPMS yield 5.44 W/m/K for thin films of 200 and 500 nm [198]. This value is lower compared to other materials discussed here, see Tab. 5.3, or in [104]. With this finding and its lower reflectance compared to Al, TiAl takes in and holds on to heat, which is visualized in Fig. 5.6b. It depicts the normalized temperature in the center of the substrate for an incident laser power of 50 mW. The horizontal axis displays the radius from the center, where the incidence occurs, to the edge of the substrate, where the set boundary temperature of 306.15 K exists.

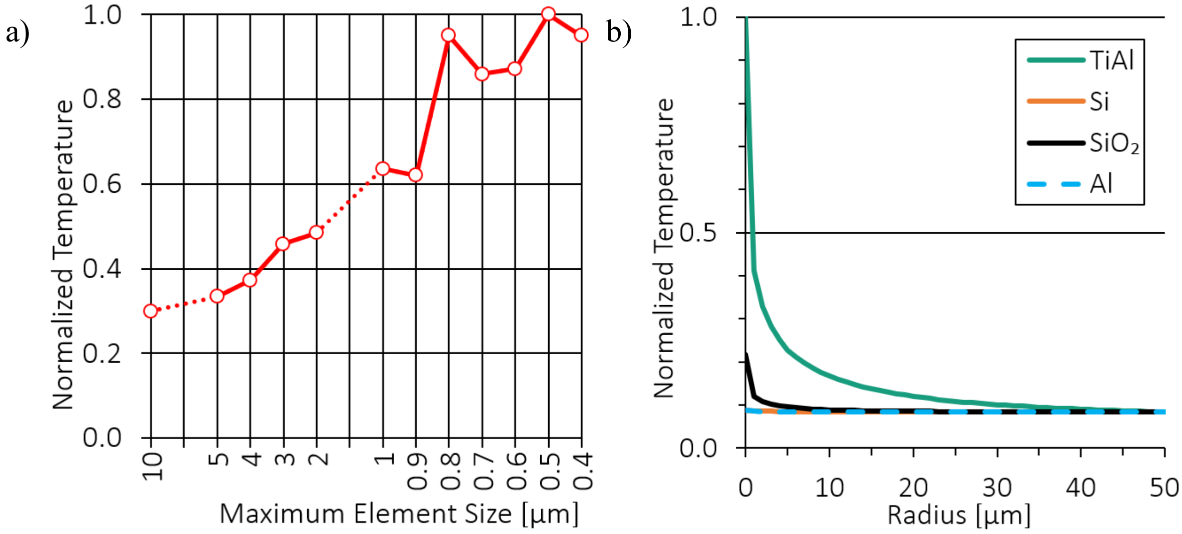

Fig. 5.6: a) Static thermal FEM element size convergence for substrate geometry a with TiAl. b) Temperature distribution over the substrate radius at the interface between resist and substrate for various materials normalized to the maximum vs. substrate radius at a static laser power of 50 mW for substrate geometry a.

The graph for TiAl expresses the problem. The incident beam does not reflect completely, ~40 % transmit and get almost completely absorbed in the TiAl substrate, see Tab. 5.3. The material transports the heat to the edge and to the resist, which itself has a low heat conductivity, see Tab. 2.3. The other materials of this comparison have larger heat conductivities, which increases the speed of heat dissipation. For Al, the large reflectance also means, that only a small part of the incident energy gets transferred to heat. When SiO_2 is used as the substrate material, most of the incident energy gets transmitted through the substrate, leaving only very little heat buildup in it.

Fig. 5.7a shows the temperature of the substrate for increasing laser power settings for a TiAl substrate using the geometry depicted in Fig. 5.6a. As expected, with increasing laser power, the temperature for each radial position increases. Fig. 5.7b shows the normalized temperature at the center of the substrate of geometry b vs. laser power for the materials of Tab. 5.3. The temperature rises with increasing power. The expected linear behavior is apparent, as well as the fact that an increasing laser power is more effective in materials with lower heat conductivity.

The gradient m_{FEM} noted in the legend of Fig. 5.7b represents a correlation of the thermal behavior of the material and the geometric constraints of the substrate. It can be calculated as

$$m = k_m m_{FEM} = k_m \frac{T_{max} - T_{min}}{P_{max} - P_{min}} \tag{5.21}$$

where $T_{max,min}$ is the maximum or minimum temperature correlating to the respective laser power values $P_{max,min}$, compare equ. 5.12.

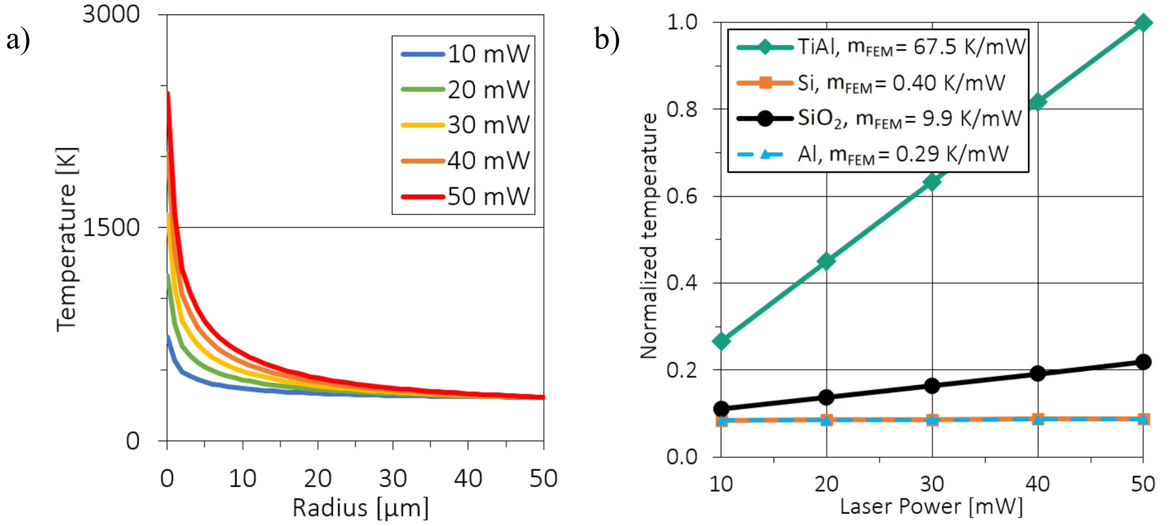

Fig. 5.7: a) Temperature of the substrate vs. radius for various laser power settings for substrate geometry a with TiAl. b) Normalized temperature at the center of the substrate vs. laser power for various materials and substrate geometry b.

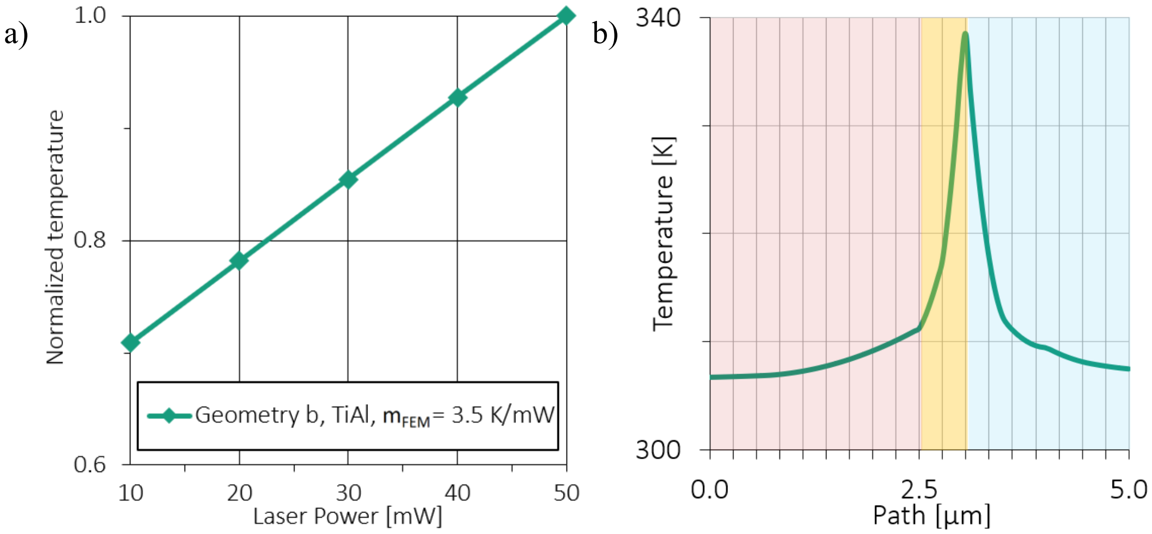

Fig. 5.8: a) Temperature in the center of a geometry b substrate comprising 725 µm Si coated with 520 nm of TiAl, normalized to the maximum vs. laser power, indicating a gradient m_{FEM} of 3.50 K/mW. b) On the same substrate geometry: center temperature distribution along a path starting 2.5 µm inside the Si (red), to 2 µm into the resist (blue) above the TiAl coating (yellow).

The inclination allows the comparison of the material properties, as well as the correlation of intensity distributions with temperature distributions.

The geometric differences between the investigated simulation domains can be compared using the gradient as well. The results depicted in Fig. 5.8 stem from the simulation setup shown in Fig. 5.5b, where the substrate geometry is not just a floating plate, but rests on a silicon wafer of 725 µm thickness. The resist dimensions and boundary conditions remain the same as in geometry a. Geometry b can be compared to the surrogate substrate used to verify the current study, see section 5.4.

The change in geometry affects the thermal behavior drastically. Comparing the inclination of TiAl as a substrate (see Fig. 5.7b) with m_{FEM} = 67.5 to the 3.50 K/mW for a coated wafer reveals, that fabrication issues due to heat should be more likely on the former. Fig. 5.8b displays the temperature distribution along a path from 2.5 µm below the TiAl coating, through the 520 nm coating, to 2 µm above the coating. The conduction of the substrate is just slightly better than that of the resist. The geometry b – in contrast to a – allows heat transfer to the Si wafer, which is the reason for the decreased gradient.

Due to the stated importance of the geometry, a more detailed representation of a CMUT geometry was created, see the schematic in Fig. 5.5c and the section view of the CAD file visualized in Fig. 5.9a. The latter includes the TiAl plate, resist and boundary conditions identical to the others, but also considers the static plate below the air gap and the Si wafer and its SiO_2 coating, as well as an Al clamp ring around the outside top of the top plate. The thermal distribution through these layers is of interest, see Fig. 5.9b.

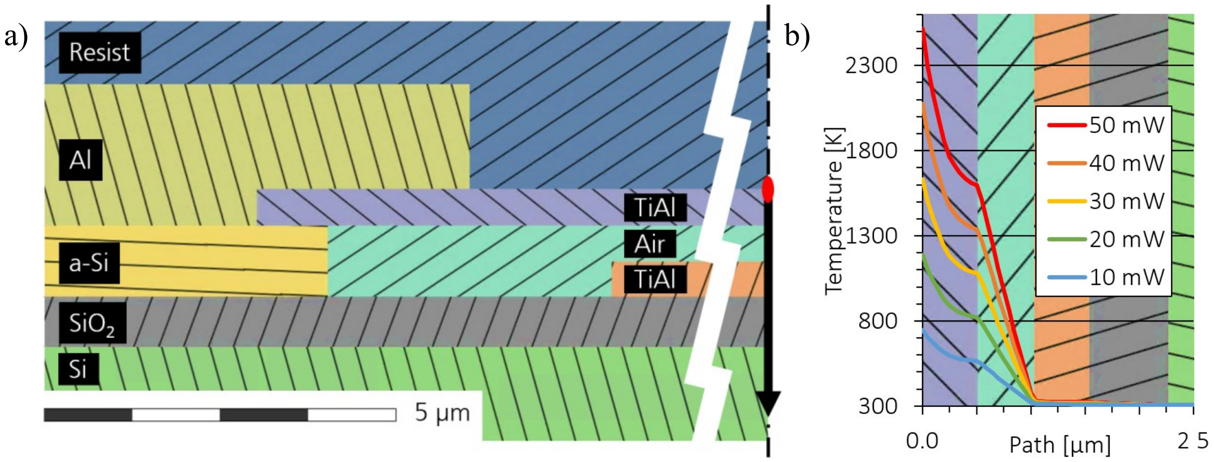

Fig. 5.9: a) Heat simulation model section view, compare Fig. 5.5c. b) Temperature distribution along a path in the center of a substrate of geometry c for a variation of laser power settings, including indicated layers, compare to Fig. 5.9a.

Here, the temperature distribution along a path in the center of the simulation domain is depicted. The incidence occurs at 0 µm, where the temperature is the largest for various laser power settings from 10 to 50 mW. Inside the top TiAl plate, the temperature slowly decays. The air-filled gap acts as an insulator, almost none of the heat passes through to the lower layers. Therefore, the increased detail in geometry leads to a drastic change in the thermal behavior and the gradient m_{FEM} rises sharply to 44.2 K/mW.

Compared to the free floating TiAl plate with 67.3 K/mW, this is only slightly decreased, which seems coherent, as instead of a hard boundary, there is contact to air on the underside and to the remaining structure via the Al clamp of the plate, see Fig. 5.9a.

Tab. 5.4 shows an error estimation for the current setup and the resulting gradients for the investigated heat simulation setups. The error was calculated by comparing a recalculated boundary temperature to the original assumption as

$$\epsilon = \frac{100(1 - T_C)}{T_S - m_{FEM} P_L} \tag{5.22}$$

with the substrate center temperature T_S. Only the error of TiAl is in the percentage range, and lower than expected from the element size convergence calculation in Fig. 5.6a.

Tab. 5.4: Resulting heat gradients and error estimation for various heat simulation setups.

Material	**TiAl**	**Si**	**SiO$_2$**	**Al**	**TiAl**	**TiAl**
Geometry, see Fig. 5.6	a	a	a	a	b	c
Gradient m_{FEM} [K/mW]	67.5	0.40	9.92	0.29	3.50	44.2
Recalculated boundary temperature [K]	304.1	306.2	306.2	306.2	306.1	304.8
Error ϵ [%]	-0.66	<0.00	<0.00	<0.00	-0.03	-0.43

The former could be due to the almost ten times larger temperatures for TiAl in the center of the substrate, where the high differential dominates. Tab. 5.4 reveals that TiAl is the material choice with the highest gradient of the given set. Furthermore, a more detailed geometry including air gaps can drastically change the behavior and raise the likelihood of the OX issues mentioned in section 4.3.

The gradient of a chip or MEMS like a CMUT would differ, depending on the considered location on its surface. The maximum will most likely be found in the center of the plates of the aperture, as the contribution to the conduction from the Al clamp is most likely stronger at the edge of the plate. As an approximation for the compensation of thermal issues during TPP on CMUTs, the maximum will be used. However, the changing gradient depending on, e.g., location or scan speed, should be investigated prospectively.

5.3 Substrate Effect Compensation Model

The previously presented results of the thermal analysis in section 5.2 – the temperature vs. intensity relation at the center of the substrate – was implemented into the simulation of the intensity distribution discussed in section 5.1 to find the temperature distribution depicted in Fig. 5.10. The temperatures in the center of the substrate of geometry b were calculated by equ. 5.11 for various materials. The values for m_{FEM} were determined in section 5.2.4 and presented in Tab. 5.4. For this simulation, P_L was set to 50 mW, and the boundary temperature T_0 was set to 33 °C. The factors k_r and k_m were set to 7.25 and 1 to achieve a 700 nm voxel size.

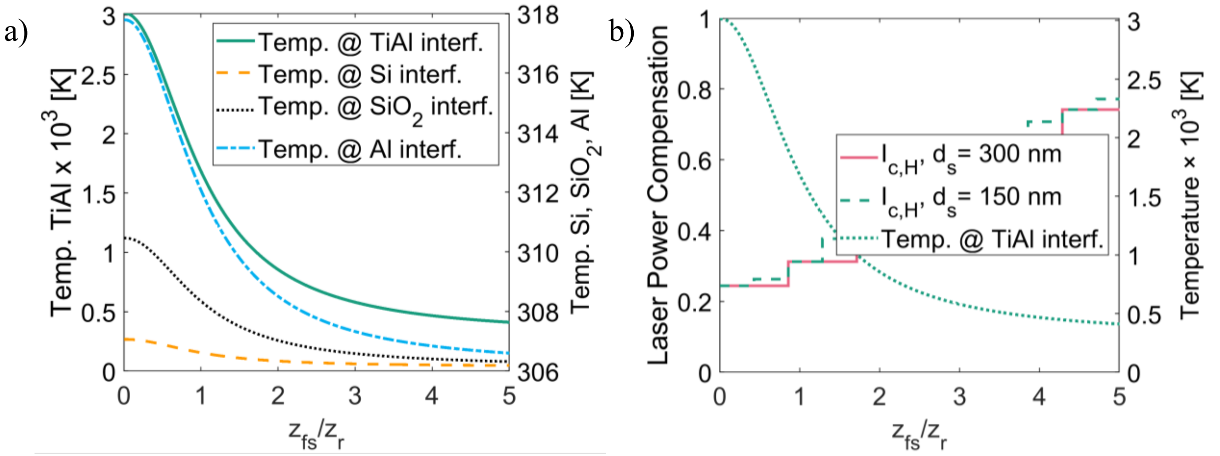

Fig. 5.10: a) Center substrate temperature at the interface vs. normalized focus distance from the substrate/resist interface z_{fs} at a laser power of 50 mW and a boundary temperature of 33 °C for various substrate materials in substrate geometry b. b) Temperature at the interface of a TiAl substrate of geometry b and layer-wise heat compensation vs. z_{fs}.

Fig. 5.10a also illustrates the center substrate temperature close to the interface for various materials. For a TiAl substrate, it rises above the resist boiling point. Although TiAl is reflective, the absorbed part is almost completely transferred to heat, the low heat conductivity inhibits dispersion. Si reflects the beam partially, the transmitted fraction almost completely passes through, due to its smaller extinction coefficient, resulting in low absorption. For SiO_2 most of the incident energy passes through. Al is strongly reflective. However, the transmitted fraction totally absorbs. Its high heat conductivity allows the heat to disperse, it still shows the second largest temperature at a z_{fs} of 0, with 45 °C.

The temperature at the interface between a TiAl plate and the resist material, calculated according to equ. 5.15 is shown in Fig. 5.10b. An intensity compensated by c_H is also displayed in Fig. 5.10b as a step function for slices with a slice distance d_S of 150 and 300 nm. In the example in Fig. 5.10b, the laser power would have to be reduced to ~30 %, when the focal point is located at the interface.

The Rayleigh and gradient factors k_r and k_m affect the laser power compensation factors c_R and c_H. Their influence is illustrated in Fig. 5.11, based on an example comprising a 63x objective, 50 mW laser power, 33 °C boundary temperature, 44.2 K/mW gradient, 300 nm distance between focus and substrate, IP-Dip and a Si wafer coated with 520 nm of TiAl.

The Rayleigh factor k_r increasing shrinks c_R down to minimally 50 %, although here it is limited to ~59 % by the reflectance of the substrate, see Fig. 5.11a. The heat compensation factor c_H can get reduced to 0 by k_r.

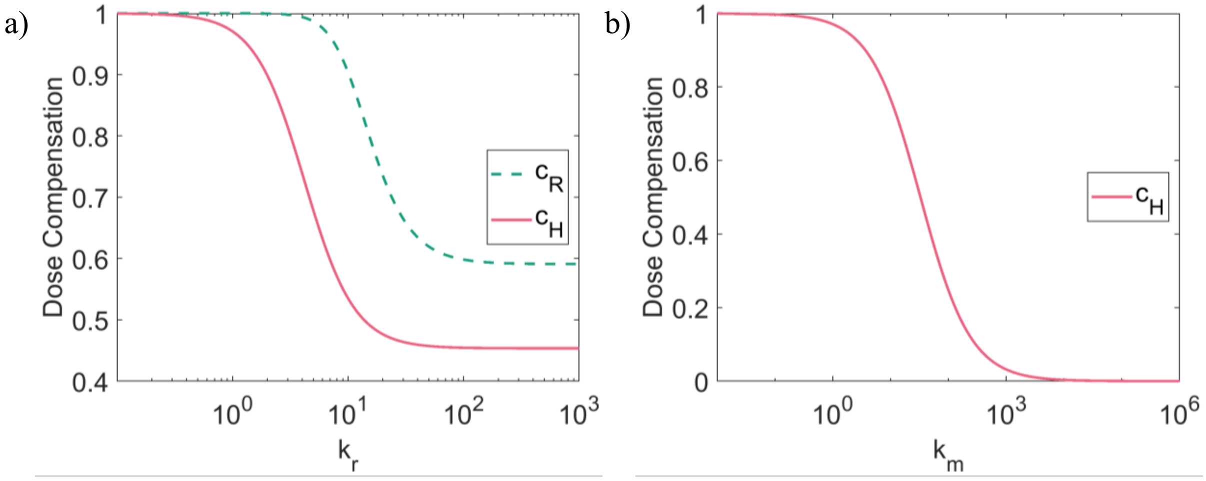

Fig. 5.11: a) Compensation factors c_R and c_m dependence on the Rayleigh factor k_r based on an example comprising a 63x objective, 50 mW laser power, 33 °C boundary temperature, 44.2 K/mW gradient, 300 nm distance between focus and substrate, IP-Dip and a Si wafer coated with 520 nm of TiAl. b) Compensation factor c_m dependence on gradient factor k_m based on the same example.

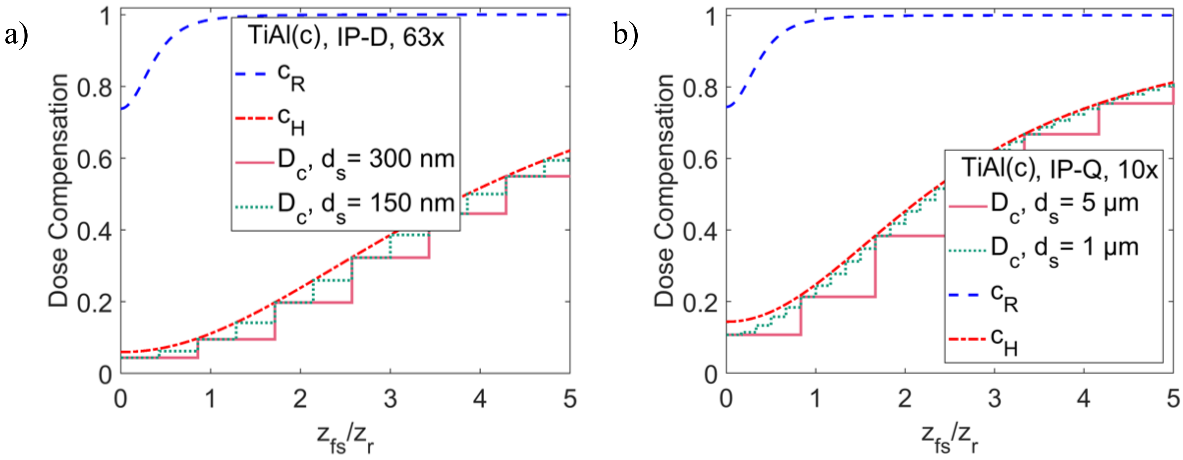

Fig. 5.12: a) Stepwise compensation of the excess reflection and heat of a substrate of geometry c with the 63x objective, IP-Dip, static laser power 50 mW, boundary temperature 33 °C, standard voxel size and 150 and 300 nm slice distance, including the respective constituents for illustration. b) The same for the 10x objective and resist IP-Q for 1 and 5 µm slice distance.

In Fig. 5.11a, however, it is limited to ~46 % by the reflectance and the FEM based gradient m_{FEM}. The factor c_H can also be affected by the gradient factor k_m, see Fig. 5.11b. As expected, with increasing k_m, the stronger the dose compensation becomes.

The compensation of the dose shown in Fig. 5.12 incorporates both the reflection and heat constituents, calculated from equ. 5.5 and 5.17, respectively. The 63x and 10x objectives were simulated including resists IP-Dip and IP-Q, respectively. The modeling was based on 50 mW laser power, 33 °C boundary temperature and a Si wafer coated with 520 nm TiAl.

Fig. 5.12a displays the constituents for the 63x objective in blue and red, respectively. Here, the thermal excess trumps the optical one. The combined compensated dose D_c in stepwise arrangement for 150 and 300 nm slices represents the proposed iterative reduction per layer to prevent OX. The values of the compensation factors c_R and c_H as well as the resulting dose at the interface between substrate and resist calculated for the illustration in Fig. 5.12 are listed in Tab. 5.5. Furthermore, the calculated Rayleigh length $z_{r,G}$ and the gradient m_{FEM}, as well as the fitting factors k_r and k_m selected for the illustration in Fig. 5.12 are listed Tab. 5.5 with the respective fitted Rayleigh length z_r and gradient m.

Tab. 5.5: Rayleigh length and gradient based on Gaussian calculations and FEM, factorized by Rayleigh and gradient factors as well as the respective results. Dose compensation factors and resulting compensated dose at the interface between substrate and resist. The values are listed for the 63x and 10x objectives.

Objective	$z_{r,G}$ **[µm]**	m_{FEM}	k_r	k_m	z_r **[µm]**	m	$z_{fs} = 0$		
							c_R	c_H	D_c **[%]**
63x	0.048	44.2	7.25	1	0.35	44.2	0.74	0.06	4.41
10x	5.79	25.1	1.036	1	6	25.1	0.74	0.14	10.7

In the case of the 63x objective, k_r was used to adjust z_r to approximate the standard voxel size of 700 µm, see section 2.3.1. For the 10x objective, the Rayleigh factor k_r was set to 1.036 to fit the 12 µm standard voxel size. The value of k_m was set to 1 to provide the originally deduced heat response.

For the 10x objective and IP-Q, a gradient m_{FEM} of 25.1 K/mW was determined numerically based on the high detail geometry depicted in Fig. 5.5c. The reduction compared to the 44.2 K/mW found for the 63x objective and IP-Dip originates not only from the material and setup changes, but also from the increased focal area, over which the incident heat is distributed, see equ. 4.5.

The comparison of the two objectives shown in Fig. 5.12a and b illustrates that, although the focal size changes, the optical principle stays the same.

5.4 Verification of the Excess Compensation

A systematic experimental study of the interplay between the TPP process and surrogate substrates used to substitute for chip constituents was performed. By fabrication of parameter sweeps (see section 2.3.2) with laser power, scan speed and z_{fs} variables, a viable fabrication space was determined. This parameter field was then utilized to compare substrate types and evaluate their optical and thermal behavior.

The compensation based on optical and thermal simulations was implemented and the experimental results were used to find suitable factors to correct for the real behavior of structures fabricated close to problematic substrates.

5.4.1 Exposure Dose & Compensation Test Structure Design

A test structure was employed to investigate the optical and thermal behavior of TPP based entities when in proximity to problematic substrates. The design requirements for this structure were found by a study of various significant manufacturing parameters, after initial trial-and-error experiments.

A line structure consisting of a single movement of the laser from one point to a second point was selected, because of its simplicity. There are two main customizable parameters affecting the dose of a line: scan speed and laser power. Other customizable parameters were kept static. Further parameters are dependent on substrate effects, resist composition and the immediate environment.

These characteristics make the line a preferable subject over a hatched structure, although an individual line exposure can receive a significantly higher dose before the OX threshold is reached [14]. Listed in the following are further design requirements, which were established during the development of the test structure:

1. The line must be connected to a mount, so that it can be fabricated at a vertical distance to the substrate without subsequently floating away.
2. The interference of the fabrication of the mount with the dose input to the line must be reduced as much as possible.
3. The minimum line length must allow for the set scan speed to be achieved by the galvanometer mirrors.
4. The maximum line length must allow for high scan speeds, which reduce the dose, leading to weaker lines. Weaker lines break more easily, leading to a smaller range of viable parameters.
5. The maximum line length overhanging between the mounts must allow low scan speeds, where the line could detach or break due to movement in the resist before it would be finished.
6. The maximum distance to the substrate must be larger than $\sim 10 \cdot z_r$ where the substrate effects reduce to normal, as established in section 5.3.
7. The line must be fabricated in the center of the FOV, to reduce dose inconsistencies from misalignment of the optical path of the TPP system, see section 2.3.1.
8. The mount must be connected to the substrate, in order to withstand development and characterization, see section 2.3.3.

The resulting design is visualized in Fig. 5.13a and poses a good compromise of the requirements. To fulfill requirement 1, it consists of two opposed triangle mounts. They support a single bridge line in-between, shown in Fig. 5.13a as a voxel line simulation created with the modeling software, see section 2.3.2. The colors represent the employed laser power setting. The voxel shape settings were fit to the 63x objective.

The triangle mounts depicted in Fig. 5.13a are not symmetrical, the missing left corner is intended as an indicator of the fabrication direction of the line (left to right) and of the fabrication sequence of a 4 x 4 set of these structures, see the bottom left inset in Fig. 5.13a. The mounts were imported from a CAD model created using Inventor (Autodesk, Inc.), which explains the change in voxel line direction right were the missing corner starts.

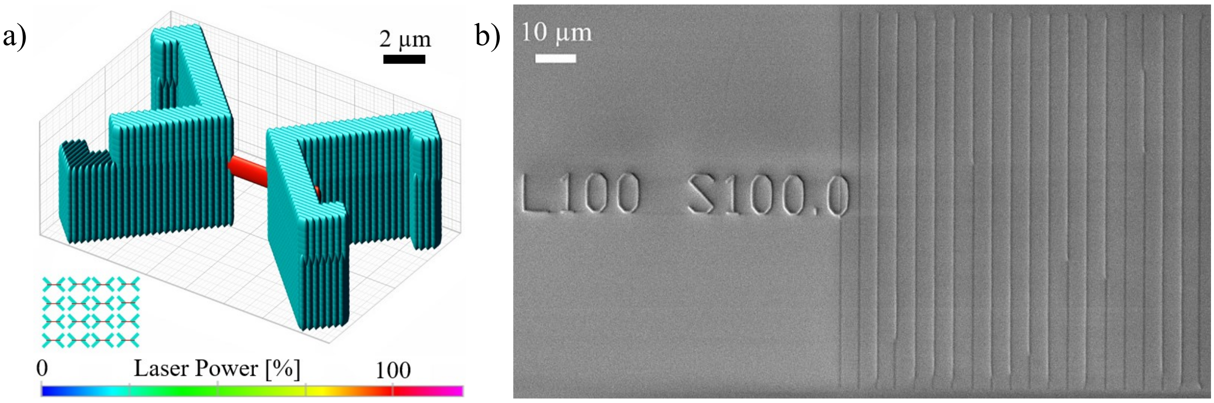

Fig. 5.13: a) Voxel line simulation of the exposure dose and compensation test structure comprising two mounts (turquoise) and a bridge line (red) including an insert of a top view schematic of a 4 x 4 field. b) Parameter sweep specimen of the line thickness experiment with 20 lines of 100 µm length, including 50 mW laser power and 100 mm/s scan speed as structured text fabricated in the vicinity.

The bent ends of the mount structure were designed for increased stiffness, which was recognized during the development phase. Requirements 4 and 5 call for short lines, number 3 suggests longer lines. The selected length between the mounts was 2 µm, which was chosen to establish structural rigidity due to the expected – dose dependent – voxel size of 700 nm in z direction.

A minimum length of 2 µm also helps with SEM characterization, where a low accelerating voltage – compared to system capabilities – was necessary. Voltages exceeding ~1 kV resulted in electrostatic charging of the dielectric TPP structures, which subsequently can cause artifacting, deformation of the structures and blinding of the electron detector. However, lower voltages lead to reduced resolution, which is why the minimum length was favorable. Sputtering conductive material onto the structures can increase the achievable voltage, but additional processing was omitted to prevent unwanted influences, e.g., thermal degradation.

Requirement 3 was researched via a parameter sweep study of the line thickness, see Fig. 5.13b. Sets of twenty lines of 100 µm length were fabricated at various laser power and scan speed values using the 63x objective and IP-Dip. The specimen at the maxima of 100 mm/s and 50 mW is displayed in Fig. 5.13b and was expected to show the most divergence between the line thickness at the start and center of the line. The line thickness was measured with a difference of 22 nm between the center and start. However, the measurement deviation using viable SEM settings was 20 nm, so the difference can be neglected. For the exposure and compensation experiments, the line starts and ends 3 µm before and after the main part to ensure requirement 3 is achieved. The line exceeding the mount can break off, leading to floating pieces within the resist or during development. This would disturb the measurements, so a shorter overhang was favorable.

The maximum distance of the line to the substrate was restricted by fabrication limits of the achievable aspect ratio of the mounts and by fabrication as well as characterization time limits. Requirement 6 was achieved by multiplying half of the standard voxel size in z-direction of the 63x objective by 10, making the distance 3.5 µm. Approximately 30 % were added to allow for simulation imperfections, making it 4.5 µm. The height of the mounts was set to 5 µm to compensate shrinkage, compare section 4.4.3.

The test structures were fabricated in sets of 4 x 4, which is visualized by the insertion in the bottom left of Fig. 5.13a. Each piece of the 4 x 4 set was fabricated in the center of the FOV, by moving to the respective position using piezo stage 1, thus fulfilling requirement 7. The line distance to the substrate z_{fs} changes from the bottom left at 0 to the top right at 4.5 µm in lexical order. The z_{fs} steps of 300 nm represent the standard slice distance setting for the 63x objective. Requirement 8 was achieved by starting the fabrication of the structure inside the substrate, which is the common approach to securely anchor a structure. Here, the focal point was set 0.5 µm above the interface, compare Fig. 2.4. This, and the error of the automatic interface detection can affect the result of the z_{fs} sweep. The latter was determined as explained in section 5.6.3 to be ±0.082 µm for the 63x objective, see below Tab. 5.11.

At a beam divergence of 66.2° calculated for the 63x objective using equ. 4.3 and a distance between the mounts of 2 µm, 100 % of the line space at any z_{fs} will already have radicals forming from the overlapping beam paths of the mount fabrication starting at 1.6 µm distance to the substrate. Below that, the radical generation is weaker, as only the part of the beam already past the focal point irradiates the space. This height limit would only be increased to reasonable values by increasing the distance between mounts drastically, violating other requirements. Thus, the mount design was adjusted to reduce its volume close to the line as much as possible. Furthermore, the line was fabricated after the mounts are finished, so that the radicals formed in the overlapping beam path have time to disperse. With these measures, requirement 2 is considered fulfilled. A waiting period between fabrication of mount and line could help to reduce the interference but was cut in favor of fabrication time.

The fabrication settings for the mounts were found via individual parameter sweeps per substrate type. They remain unchanged while the line parameters were altered during the experiments.

5.4.2 Exposure Dose Experiments

For investigations of the difference between an optically and thermally problematic and non-problematic substrate material, the test structures described in the previous section were fabricated on a 725 µm thickness Si wafer coated with 520 nm TiAl as well as on a SiO_2 substrate of (700 ± 25) µm thickness. The parameter sweep fabrication from IP-Dip was performed in the described 4 x 4 fields, which can be seen in Fig. 5.14. Each field shows 16 height variations for individual combinations of laser power and scan speed.

Both parameters were visualized as structured text in the vicinity of the fields. The units vary between substrates. The examples in Fig. 5.14 were taken from the sweeps, where the line laser power was increased by 1 mW per 4 x 4 field, starting at 0.5 mW. The scan speed was incremented from 1 to 5 for each order of magnitude from 10^{-2} to $5 \cdot 10^{6}$ µm/s.

The line condition was studied for each of the 25600 specimens. When lines were non-existent in the known low-dose domain, they were classified as UX. The OX classification was applied to lines with significant symptoms of vaporization, e.g., bubbles, jagged or fissured remnants. The OK classification was applied to viable lines that show none of the mentioned symptoms.

The micrograph in Fig. 5.14a presents an example field on the glass substrate, where every one of the 16 lines was created as intended (OK) using 3.5 mW laser power and 0.05 µm/s scan speed. The slanted edges of the mount structure might be a result of shrinkage. The bottom part of the structure is fixed to the substrate, leaving the top free to shrink. The top bridges most likely receive additional tension from the volume reduction due to shrinkage, while the bottom ones might not.

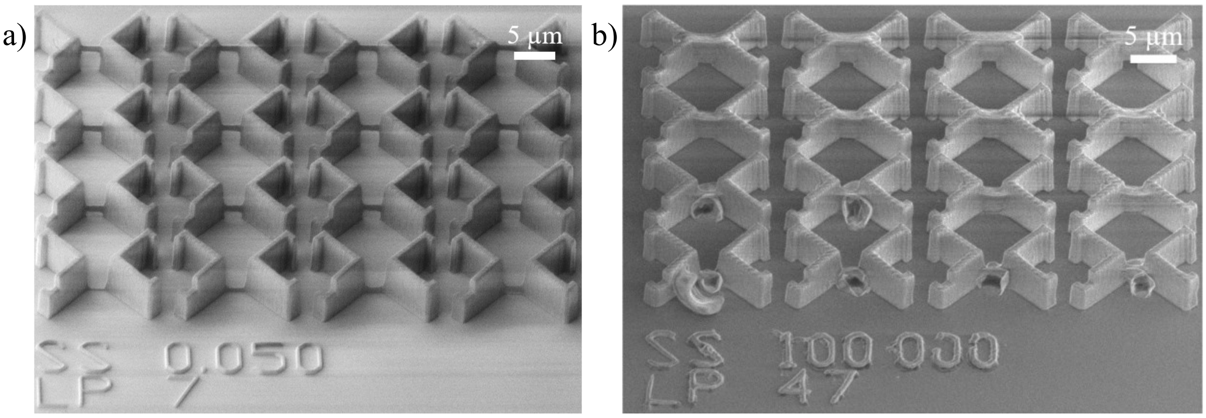

Fig. 5.14: a) 45° tilted SEM micrograph of an example 4 x 4 set of dose test structures fabricated from IP-Dip on a (700 ± 25) µm SiO_2 substrate. All 16 lines at 0 to 4.5 µm distance to the substrate were found viable at scan speed 0.05 µm/s and laser power 3.5 mW (represented by structured text). b) Micrograph of a similar example on a 725 µm thickness Si wafer coated with 520 nm TiAl. Enlarged line volume appears due to increased dose and OX on lines that are closer to the substrate for scan speed 100 mm/s and laser power 47 mW.

This should affect the lower dose domain more drastically, due to the dose-dependent reduction of voxel size as well as elastic capabilities of the polymer [14, 127]. This would result in fields, where the lines closer to the substrate would get fabricated, while the further away ones would break after shrinkage. However, this effect was not found in the experiments.

The field depicted in Fig. 5.14b was fabricated on the metal coated wafer using 47 mW laser power and 100 mm/s scan speed. The lines closer to the substrate at 0 to 1.5 µm distance show signs of OX. All others can be considered viable, although they are significantly enlarged, due to the increased dose compared to the sample in Fig. 5.14a. This enlargement occurs more below the set line distance than above, maybe due to a shadowing effect of the already polymerized structure.

The evaluation of the parameter sweeps resulted in the diagram depicted in Fig. 5.15a, where markers are used to reference the coordinates of OK fields that were the closest to OX or UX domains. The result delimits the viable parameter space per substrate.

A less compact presentation of the results is given in Fig. 5.15b. It shows a selection of the heat map of the evaluated field positions of the parameter sweeps for TiAl. The remaining part of the heat map and the version for SiO₂ can be found in annex H.

The red circle and purple asterisk markers in Fig. 5.15a present the last OK setting combination before OX for the SiO₂ and TiAl substrates, respectively. The blue circle and green asterisk markers represent the last viable setting combination before UX for the SiO₂ and TiAl substrates, respectively.

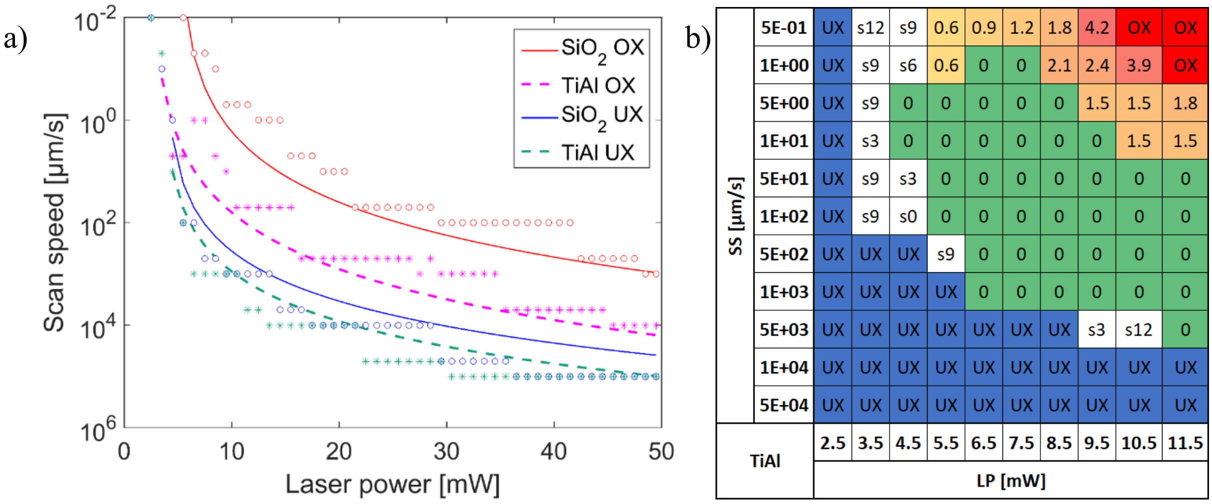

SS [µm/s]	5E-01	UX	s12	s9	0.6	0.9	1.2	1.8	4.2	OX	OX
	1E+00	UX	s9	s6	0.6	0	0	2.1	2.4	3.9	OX
	5E+00	UX	s9	0	0	0	0	0	1.5	1.5	1.8
	1E+01	UX	s3	0	0	0	0	0	0	1.5	1.5
	5E+01	UX	s9	s3	0	0	0	0	0	0	0
	1E+02	UX	s9	s0	0	0	0	0	0	0	0
	5E+02	UX	UX	UX	s9	0	0	0	0	0	0
	1E+03	UX	UX	UX	UX	0	0	0	0	0	0
	5E+03	UX	UX	UX	UX	UX	UX	UX	s3	s12	0
	1E+04	UX	UX	UX	UX	UX	UX	UX	UX	UX	UX
	5E+04	UX	UX	UX	UX	UX	UX	UX	UX	UX	UX
TiAl		2.5	3.5	4.5	5.5	6.5	7.5	8.5	9.5	10.5	11.5
		LP [mW]									

Fig. 5.15: a) Exposure dose viability for two substrates SiO₂ and Si coated with 520 nm TiAl. Solid lines and 'o' markers for SiO₂, dashed lines and '*' markers for TiAl. The OX and UX fits represent the respective thresholds. b) Heat map of a selection of the TiAl field positions showing the UX and OX as well as intermediate domains, where the number indicates the closest distance to the substrate in µm, where the bridge line was viable.

Tab. 5.6: Bělehrádek [202] fit parameters for OX and UX thresholds of the exposure dose experiments.

Fit parameters	**SiO_2**		**TiAl**	
	OX	**UX**	**OX**	**UX**
a [m/s/W^c]	0.0144	5.0	0.15	10
b [W]	4.9	3.8	3.6	3.5
c [-]	2.92	2.34	3.0	2.4

The lines are based on an adjusted Bělehrádek fit [202] which was used to create the limits of UX and OX with

$$v = a(P_L - b)^c \tag{5.23}$$

where v and P_0 are the scan speed and laser power of the bridge line, respectively. The parameters a, b and c determined in this study for each material can be found in Tab. 5.6.

The minimum exposure dose thresholds in Fig. 5.15a show a nonlinearity close to the expected value of ~2 in fit parameter c, see equation 4.16. Both maximum dose thresholds present a nonlinearity of ~3. Both nonlinearities are slightly lower for the glass substrate, which would indicate a correlation. However, the expected behavior should be exclusively resist-dependent. By decreasing the step size between laser power settings the accuracy of this experiment would be improved.

As proposed in [203], the strong electronic excitation near the focus leads to the creation of an epsilon-near-zero (ENZ) region. With $\varepsilon \rightarrow 0$ comes plasma formation at the focus and stronger absorption due to increased reflectance of the region $\mathcal{R} \rightarrow 1$ [203]. As proposed in [203] and [125] the absorbed energy density – or dose – of two-photon absorption including the contribution of an ENZ region relates to a nonlinearity of 3 as $D \propto P_L^3/v$.

On the Si wafer coated with TiAl, the thresholds are shifted towards lower exposure dose. While the lower minimum reduces the necessary energy input when compared to SiO_2, the reduced maximum dose narrows the viable parameter space significantly. When comparing the space between the threshold lines, one can find that for TiAl, the area is 44.9 % of the one for SiO_2. It has to be noted, that not all of the space per substrate is necessarily usable e.g., due to time restrictions when using low scan speed.

Two further classifications of the line condition were implemented, see Fig. 5.15b. In the transition from the OK to the UX domain, lines were found to have fallen towards the substrate after fabrication, where they adhere to it. This effect shows up at distances closer to the substrate. The remaining lines were usually created as intended starting at a certain distance, which was noted in μm after the indicator “s”, see Fig. 5.15b. The falling lines would profit from the increased dose in the vicinity of the substrate and from the reduced shrinkage in that range, still they are the ones to fall. No satisfactory explanation has been found for this effect so far. Prospective research should investigate the effect by decreasing the laser power increments for parameter sweeps of the UX to OX domain where the falling lines occur.

In the transition from the OK to the OX domain, the distance of the line closest to the substrate – showing no OX symptoms – was noted in μm, see Fig. 5.15b.

Both transitional domains are more exaggerated in the case of TiAl, when compared to SiO_2, where the switch from OK to OX or UX usually happens within one or two laser power steps. The same is valid for the minimum dose thresholds of both substrates, which exhibit almost no transition at the step size and line distance differential applied in this sweep study.

5.4.3 Exposure Dose Experiments with Alternative Photoresist and Objective

The findings of the previous section need to be recreated for the other expedient resist investigated in this work. Parameter sweeps were fabricated from IP-Q on a standard 725 μm thickness Si wafer. The line laser power was increased by 2 mW per 4 x 4 field and ranged from 31 to 50 mW, see Fig. 5.16. The scan speed was incremented from 1 to 5 for each order of magnitude from $5 \cdot 10^{-1}$ to $5 \cdot 10^{6}$ μm/s.

The larger voxel size of the 10x objective required changes to the test structure. The size was scaled by 15 times. The same for the line distance steps, resulting in 4.5 μm steps ranging from 0 to 67.5 μm, which resembles the standard layer height used for the objective.

The resulting heat map depicted in Fig. 5.16a displays UX for lines down to a scan speed of 1000 μm/s.

The main defect found with these sweeps was the detachment of the structures, indicated by “n” in Fig. 5.16a. This was found to happen increasingly with higher exposure dose. The increased dose should lead to less shrinkage, but the increased voxel volume of the 10x objective may have outside layers that receive a lesser number of radicals [14]. This could induce stress within the line, which subsequently detaches the line and its mounts from the substrate. This hypothesis could fit the finding that this effect reduces and even stops with lower scan speeds, where the voxel line volume and stiffness becomes large enough to provide resistance to the shrinkage-induced stress. Another defect found with higher dose lines was the destruction of the lines and even the mount at their top end, which can be seen in Fig. 5.16b and is indicated by “m” in Fig. 5.16a. The defect was noted to happen in concurrence with defect “n”, indicating a precursor or an evolution.

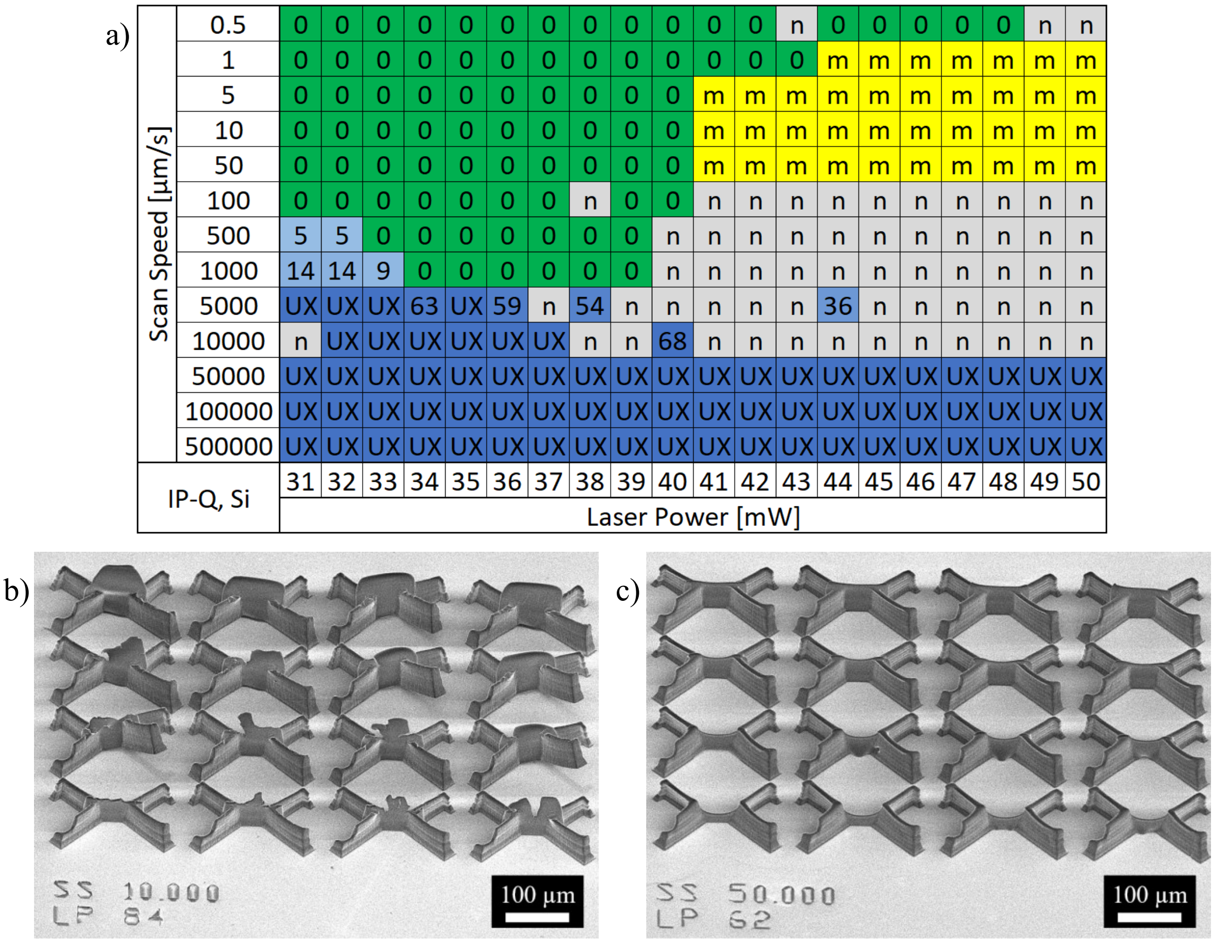

IP-Q, Si	Laser Power [mW]																			
Scan Speed [µm/s]	31	32	33	34	35	36	37	38	39	40	41	42	43	44	45	46	47	48	49	50
0.5	0	0	0	0	0	0	0	0	0	0	0	0	n	0	0	0	0	0	n	n
1	0	0	0	0	0	0	0	0	0	0	0	0	0	m	m	m	m	m	m	m
5	0	0	0	0	0	0	0	0	0	0	m	m	m	m	m	m	m	m	m	m
10	0	0	0	0	0	0	0	0	0	0	m	m	m	m	m	m	m	m	m	m
50	0	0	0	0	0	0	0	0	0	0	m	m	m	m	m	m	m	m	m	m
100	0	0	0	0	0	0	0	n	0	0	n	n	n	n	n	n	n	n	n	n
500	5	5	0	0	0	0	0	0	0	n	n	n	n	n	n	n	n	n	n	n
1000	14	14	9	0	0	0	0	0	0	n	n	n	n	n	n	n	n	n	n	n
5000	UX	UX	UX	63	UX	59	n	54	n	n	n	n	n	36	n	n	n	n	n	n
10000	n	UX	UX	UX	UX	UX	UX	n	n	68	n	n	n	n	n	n	n	n	n	n
50000	UX	UX	UX	UX	UX	UX	UX	UX	UX	UX	UX	UX	UX	UX	UX	UX	UX	UX	UX	UX
100000	UX	UX	UX	UX	UX	UX	UX	UX	UX	UX	UX	UX	UX	UX	UX	UX	UX	UX	UX	UX
500000	UX	UX	UX	UX	UX	UX	UX	UX	UX	UX	UX	UX	UX	UX	UX	UX	UX	UX	UX	UX

Fig. 5.16: a) Heat map of the parameter sweep field exhibiting UX, OK, as well as intermediate domains, indicated by “UX”, “0”, and numbers. The number indicates the distance to the substrate in µm, where the first bridge line was viable and not UX. Furthermore, the lines, where mount and line were detached, as well as where the top of the line was destroyed, are indicated by “n” and “m”, respectively. b) 45° tilted SEM micrograph of an example 4 x 4 set of dose test structures fabricated from IP-Q on a 725 µm Si substrate with line to substrate distance ranging from 0 to 68 µm, showing enlarged voxel size, fractured voxel tip and partly detached structures and including scan speed (10 mm/s) and laser power (42 mW) settings as structured text in the vicinity. c) The same of an example with different settings (50 mm/s, 31 mW), exhibiting concave and convex defect indicators.

At higher doses, the radical gradient within the voxel could lead to a more brittle exterior that breaks before it can deform and detach the structure. Defect “m” also ceases with very low scan speeds, which could indicate that, given enough time, the radical propagation reaches its maximum range, resulting in a more homogeneous radical distribution within the voxel volume. Another major difference to the previous experiments is, that OX indicators like bubbles and bubble shaped holes were not found, even for extremely slow speeds and maximum available laser power. The only defect found, which could indicate bubble formation was a slight concave or convex deformation of the line at the underside, see Fig. 5.16c. Assuming both indicate bubble formation within the line, there was no clear correlation of their appearance with line distance found, see annex I. Lines fabricated using scan speed settings of 5 µm/s and slower, as well as 5000 µm/s and faster did not show these indicators. The latter was expected, the former, however, does not fit a “more OX with higher dose” prediction.

A total of 4160 specimens were studied. A subsequent second and third batch were fabricated and developed using shorter development time and NOVEC instead of IPA, respectively. These measures were taken to improve the total available number of attached specimens, but both were disregarded due to similar results to the first batch.

Prospective works should investigate larger mount structures or mounts including base plates connecting the mount to the substrate. A sweep of base plate size at uniform line settings that would consistently result in detachment could be used to find a suitable value. In an exposure dose sweep comparable to the one depicted in Fig. 5.16a, square plates below the mounts would result in an estimated 20 % increase in fabrication time. At originally more than 100 h, this option was disregarded.

5.4.4 Compensation Experiments and Model Verification

The model established so far was designed to perform the compensation of excess via the reduction of laser power. To test this capability and to further verify the model, compensation experiments were performed based on the 4 x 4 fields of line specimen fabricated at a distance z_{fs} to the substrate surface stepping from 0 to 4.5 µm in 0.3 µm steps.

The 63x objective and IP-Dip were employed. Adapted laser power parameters were used on the line depending on z_{fs}, whereas the mount structure was fabricated without change. The line scan speed was kept constant at 500 µm/s, while P_{set} was compensated down from the set point of 50 mW. On a Si wafer coated with 520 nm TiAl, these settings would entail OX, if not compensated, see Fig. 5.15a.

The compensation experiment was subdivided into 13 individual parameter sweeps, whereat the increments were reduced step by step to find improved values. The successful compensation in sweep ten was published in [2]. With improvements to the quality of material parameters as well as other improvements, the results slightly changed with the ultimate, thirteenth sweep. Improved viable settings for k_m as well as k_r were found due to the latter sweep encompassing a larger parameter space.

The ultimate sweep with a total of 12800 specimens had $k_r \cdot z_{r,G}$ stepping from 900 nm to 1.8 µm in increments of 300 nm and $k_m \cdot m_{FEM}$ stepping from 68.5 to 82 in steps of 0.5. Each 4 x 4 field was repeated four times to increase significance. The successful compensation resulting in four viable fields was achieved for k_r and k_m at 31.09 and 1.067, respectively.

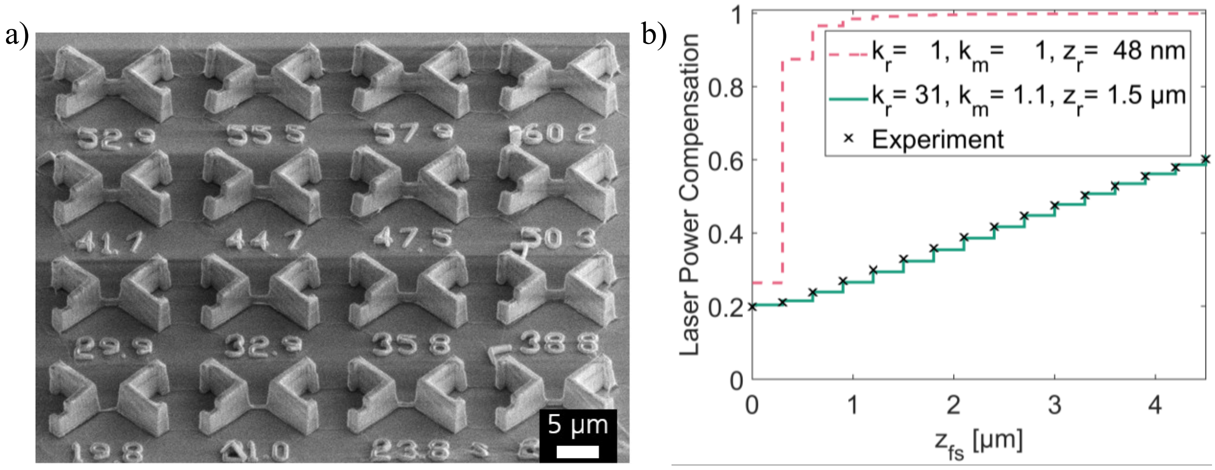

Fig. 5.17: a) 45° tilted view SEM micrograph of a successfully compensated 4 x 4 field of lines fabricated using the 63x objective from IP-Dip on a Si wafer coated with 520 nm TiAl, scan speed static at 500 µm/s, laser power compensated from 50 mW. All 16 lines at 0 (bottom left) to 4.5 µm (top right) distance to the substrate z_{fs} are viable. The percentual laser power was represented as structured text in the vicinity of each line. b) Comparison of the experiment (x) to the Gaussian/FEM simulation (pink) and the minimum (green) factors found to adjust laser power compensation for fabrication of a completely viable field based on substrate geometry a, including a step function approximation with 300 nm slice distance.

The micrograph depicted in Fig. 5.17a displays one of the four viable compensated 4 x 4 fields with the laser power value fabricated as structured text in the vicinity of each line. Each line of Fig. 5.17a was fabricated without any signs of OX or UX. The line size increases with each line distance step, indicating the increase in dose the further apart the line is from the substrate.

Fig. 5.17b shows the laser power compensation vs. z_{fs} for the minimum coefficients found to fabricate a completely viable field compared to the model-based prediction. The minimum found through these experiments is valid for the specified materials, environmental conditions and TPP system.

The successful compensation was found for a factorization of the Gaussian prediction of the Rayleigh length $z_{r,G}$ of 48.3 nm with a k_r of 31.09, resulting in a z_r of 1.5 µm. The increase was expected due to the dependence of the real-world polymerization thresholds on the utilized dose and process chemistry.

The gradient factor k_m of 1.067 found by this method indicates, that the predicted thermal behavior with a gradient m_{FEM} for substrate geometry a of 67.5 K/mW matched the experiment without much factorization. Assuming substrate geometry b, which more closely models the surrogate substrate used in this experiment, indicates a strong offset from the m_{FEM} of 3.5 K/mW. This could be due to the omitted effects mentioned in section 5.2.4, or the steady state type of the simulation compared to more extensive transient types. However, instead of using the resist boiling point T_F of 205 °C, one could instead implement an allowed window of

10 °C above T_C. With this, the behavior predicted by an m_{FEM} of 3.5 K/mW resembles the minimum viable set found in the presented experiment well with a k_m of 1.187.

A compensation experiment was also performed for the alternative resist and objective combination IP-Q and 10x, including the scaled-up test structure design, see section 5.4.3. Adapted laser power parameters were used on the line depending on z_{fs}, whereas the mount structure was fabricated without change. The line scan speed was kept constant at 10 µm/s, while P_{set} was compensated down from the set point of 50 mW. The successful compensation with viable settings for k_m as well as k_r was found after nine parameter sweeps with decreasing increments on Si wafers coated with 520 nm TiAl.

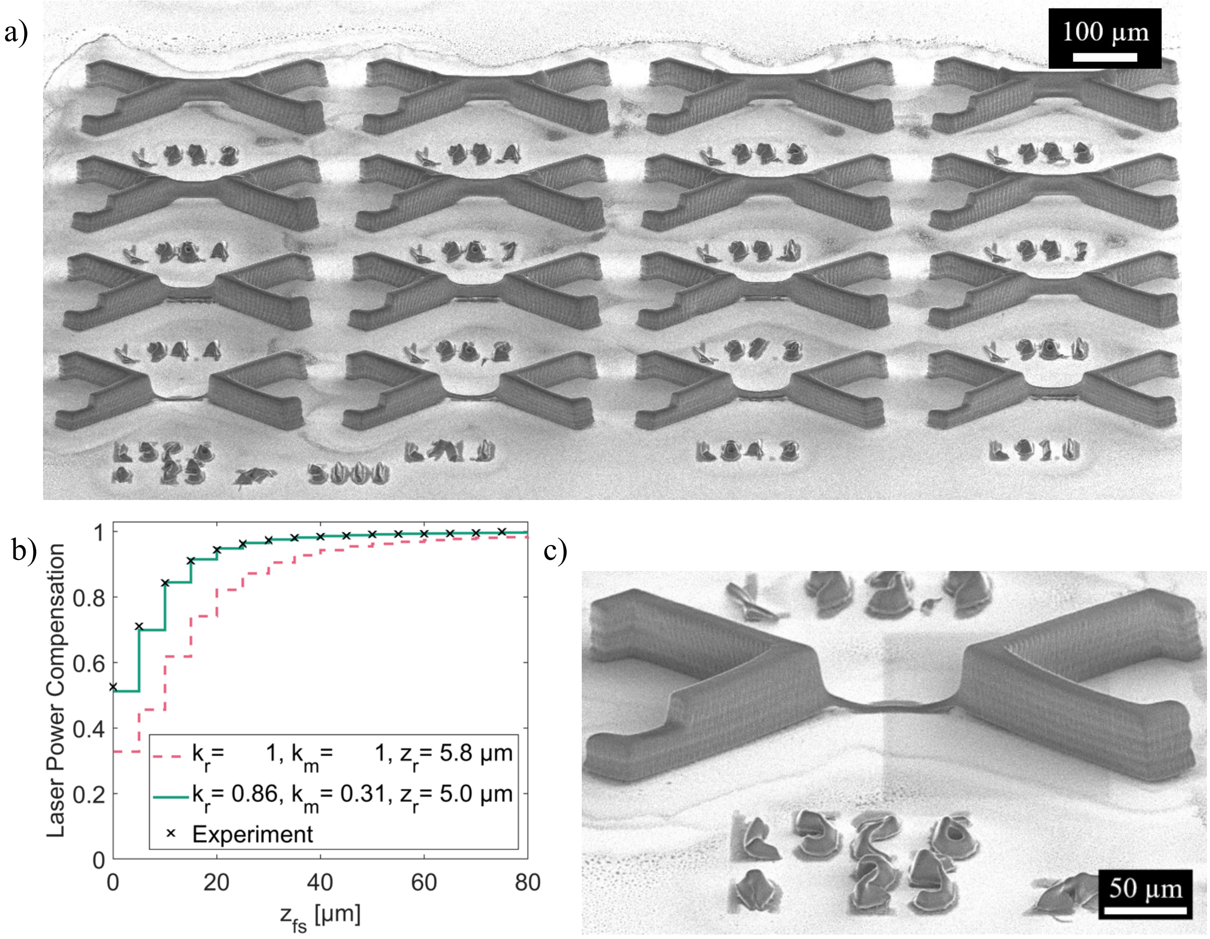

Fig. 5.18: a) 45° tilted view SEM micrograph of a successfully compensated 4 x 4 field of lines fabricated using the 10x objective from IP-Q on a Si wafer coated with 520 nm TiAl, scan speed static at 10 µm/s, laser power compensated with k_r and k_m at 0.86 and 0.31, respectively. All 16 lines at 0 (bottom left) to 67.5 µm (top right) distance to the substrate are viable. The percentual laser power was represented as structured text in the vicinity of each line. b) Comparison of the compensation experiment (x), the predicted (pink) and the minimum (green) factors found to adjust laser power compensation for fabrication of a completely viable field using a gradient m_{FEM} of 25.1 K/mW for simulation geometry c, including a step function approximation with 5 µm slice distance d_s. c) 45° tilted view SEM micrograph close-up of a line example with $z_{fs} = 0$.

The ultimate sweep with a total of 1792 specimens had $k_r \cdot z_{r,G}$ stepping from 2.5 µm to 6.25 µm in increments of 250 nm and $k_m \cdot m_{FEM}$ stepping from 22 to 28 in steps of 1. Each 4 x 4 field was repeated four times to increase significance.

The successful compensation resulting in four viable fields was achieved for k_r and k_m at 0.86 and 0.31, resulting in a z_r and m of 5.0 µm and 7.78 K/mW, respectively. The micrograph depicted in Fig. 5.18a displays one of the four successfully compensated 4 x 4 fields with the laser power value fabricated as structured text in the vicinity of each line. Fig. 5.18b shows the laser power compensation vs. z_{fs} for the minimum coefficients found to fabricate a completely viable field compared to the simulation-based prediction. The minimum found through experiments is valid for the specified materials, temperatures and TPP system.

The Rayleigh factor found in this experiment is similar to the one predicted by the Gaussian base model, which fits the real-world polymerization thresholds with the voxel size of ~10 µm. It was found at 86 % of the prediction, which might be due to the reduced viability of individual lines fabricated via the 10x objective that stems from their large aspect ratio, see section 2.3.1. The gradient factor of 0.31 found by this method indicates a strong difference to of the experiment to the thermal simulation. The distinction to the prediction could be due to the assumption of a substrate with geometry c instead of the more closely fitting geometry b. The thermal influence on the process was predicted lesser when using the 10x objective compared to the 63x objective, see Fig. 5.12.

A close-up of the viable line fabricated at the substrate level can be seen in Fig. 5.18c. The line gets warped away from the substrate at the connection points with the mount structures, from where the shrinkage dependent movement seems to originate.

As discussed in section 5.4.3, the OX threshold is more difficult to identify for the specimen fabricated with the 10x objective, compared to the 63x objective. However, the resulting compensation of substrate effects from reflection and transmission was successful in the experiments and led to expedient compensation factors. Their performance was further examined on substitute substrates and chips in chapter 6 for hatched structures.

5.4.5 Transitional Domain Investigation

The transitions between the OX and OK domains for two scan speeds selected from the exposure dose experiment in section 5.4.2 and annex H are shown in Fig. 5.19. The transitional domains of the other scan speeds of the exposure dose experiment can be found in annex J.

The 10 and 100 µm/s scan speed data points in Fig. 5.19 represent the z_{fs} value of the line closest to the substrate, below which most lines were found to exhibit OX.

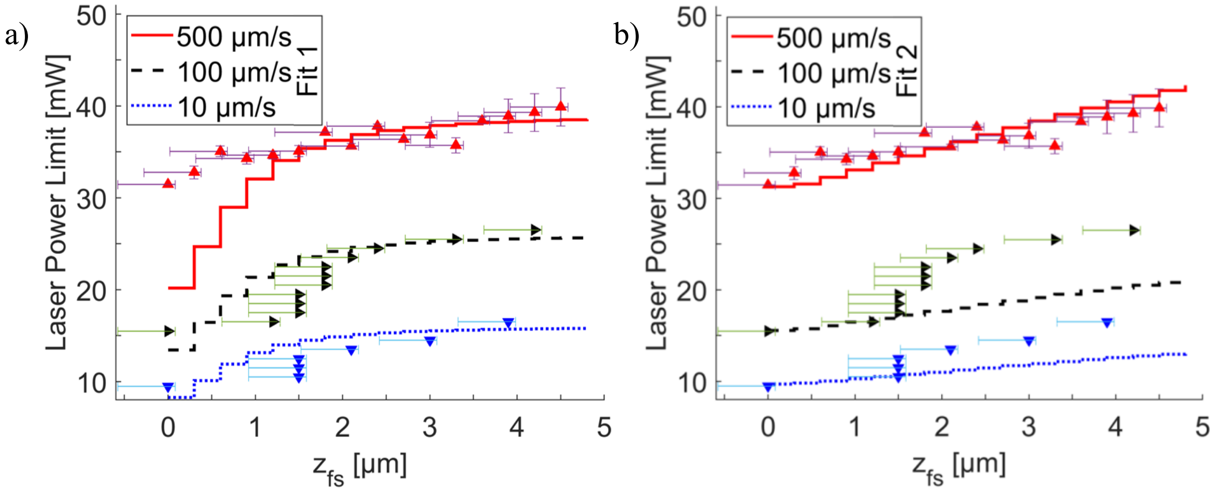

Fig. 5.19: a) Exposure dose experiments and transitional domain experiment on a 725 µm Si wafer coated with 520 nm TiAl fabricated from IP-Dip using the 63x objective for the investigation of selected scan speeds 10 and 100 µm/s, as well as 500 µm/s fitted using approach “Fit 1”. b) The same using approach “Fit 2”.

The laser power used to fabricate said line was correlated with this value and fitted applying two approaches, see Fig. 5.19. As there were only few laser power increments resolving the transitional domain of the exposure dose experiment, a transitional domain experiment exclusively for a scan speed of 500 µm/s was fabricated from IP-Dip on a Si wafer coated with 520 nm TiAl. The laser power was stepped through from 15 to 50 mW in increments of 0.25 mW.

As with the other two examples, the z_{fs} value of the line closest to the substrate, below which most lines were found to exhibit OX was correlated with its laser power. From the resulting distribution of laser power limit indications, an average P_{lim} including error margins was extracted. These margins are indicated as error bars in y-direction in Fig. 5.19. They were not available for the exposure dose experiment data points, as there were only individual lines fabricated for each.

The x-direction error bars of +0.082 and -0.582 µm originate from test structure design requirement 8, see section 5.4.1. As expected from the simulations performed in earlier sections, see Fig. 5.12a, the closer a line is fabricated to the substrate, the lower the laser power limit. Both fit approaches of Fig. 5.19 are based on the excess compensation model established in sections 5.1, 5.3 and 5.4. The Rayleigh length $z_{r,G}$ and the gradient m_{FEM} were factorized by k_r and k_m, resulting in a compensated power P_c, see equ. 5.2. The latter was then fitted to find the laser power limit P_{lim} using

$$P_{lim} = f_P P_c + f_P \tag{5.24}$$

Tab. 5.7: TiAl exposure dose experiment transitional domain fit parameters.

Fitting approach	**Fit 1**			**Fit 2**		
Scan speed [µm/s]	**10**	**100**	**500**	**10**	**100**	**500**
$\boldsymbol{k_r}$	1			31.09		
$\boldsymbol{k_m}$	400			1.067		
$\boldsymbol{f_P}$ **[mW]**	8	13	19.5	8	13	26.1

where the fit parameter f_P adjusts the model to the power used during the experiment. The fit parameters used in Fig. 5.19 are listed in Tab. 5.7. The two approaches differ in the employed coefficients. Fit 1 was adjusted to match the data points for the selected scan speeds 10 and 100 µm/s, with their characteristic step at a z_{fs} of ~1.5 µm. However, the more reliable data points of the transitional domain experiment at 500 µm/s were not met, see Fig. 5.19a.

A hypothesis to explain the deviation of Fit 1 from the 500 µm/s data points at z_{fs} <1.5 µm is, that at laser powers <25 mW, the contribution of the reflection towards the total dose becomes more determinative. This could originate from defects in the substrate's reflectivity, e.g., due to roughness. A less consistent contribution from reflection would lead to a less consistent polymerization. The lines closer to the substrate would therefore be more easily lost to UX, which is in line with the variation found between identical specimen of the compensation experiment.

The validation of that hypothesis is redundant however, as Fit 2, which is based on the results of the compensation experiment of section 5.4.4, matches the values of the transitional experiment more consistently, see Fig. 5.19b. Except for a few outliers, which also coincide with the z_{fs} locations, where less than three samples contribute to the average of the limit. Thus, the average at the locations 0.6, 0.9, 1.2, 1.8, 2.1, 2.4, 2.7 and 3.3 µm is less reliable. Fit 2 does not perfectly match the data points of the scan speeds selected from the exposure dose experiment. However, their limited reliability due to the individual instead of averaged data points reduces the impact of this fact.

A total of 12800 specimens were part of this investigation. An even further decrease of the laser power step size would increase the number examples found for the z_{fs} locations mentioned in the previous paragraph and improve the averaging. Prospective works should also investigate the transitional domains of other scan speed settings to enable a comparison and improve the fit parameter selection. These proposed experiments were postponed, as the factors k_r and k_m found for Fit 2 provided a successful compensation that was discussed in the previous section.

5.5 Structure to Substrate Adhesion

The adhesion of structures fabricated via TPP to substrates, e.g., MEMS and chips is relevant in applications that require the individual parts to stay in place or for the transmission of forces. It can be increased via surface treatments, e.g., oxygen plasma, silanization, UV illumination, as well as by structuring the substrate with interlocking or adhesive features.

Surface activation via oxygen plasma treatment aims to clean the substrate from contaminants and enriches covalent bonding by generating reactive chemical groups like silanol groups (-Si-OH) [204]. Covalent siloxane groups (Si-O-Si) can then be formed between the substrate and the applied resist material. Hydroxyl groups can also lead to strong intermolecular bonds [204]. Hydroxyl groups introduced via UV and plasma activation increase the bond strength of PDMS to Si [205], which can be improved by annealing [206]. Even deeper surface modification can be achieved [204].

Ozone generated via UV photons can eliminate hydrocarbon contamination from the substrate. Furthermore, the use of silanization, especially in combination with plasma activation, can improve substrate adhesion of structures fabricated via TPP [131].

Interlocking features require specialized chip design but likely improve adhesion the most. Form fitting techniques known from wood working could be implemented, e.g. dovetail joints [207]. Even adhesive microstructures fabricated via TPP could be employed [208].

To test the surface adhesion of structures fabricated via TPP in this work, two identical parameter sweeps of contour structures with 50 x 50 μm^2 profile were performed on standard Si substrates. The difference was their preprocessing: “Prep. 1” was only cleaned using Acetone and IPA, “Prep. 2” additionally received plasma activation and silanization after cleaning, see Fig. 5.20. The plasma was engaged after pressure equilibrium with an inflow of ~2.5 Nl/h O_2 was achieved at ~0.5 mbar. The treatment was performed for ~3 min at ~100 W. Then a silanization in a mixture of 150 µL 3-(trimethoxysilyl)propyl-methacrylate with 30 mL ethanol was performed for 1 hour.

As expected, a higher exposure dose leads to fewer detached structures (“d”) due to the reduced stress from shrinkage. However, lower scan speeds indicate an inversion of this principle, as they exhibit more detached structures. This could stem from other effects, e.g., bubble formation. At 1.4 µm slice distance, detached structures occur for both preprocessing methods, which could be due to the lower dose, see section 4.4. The improvement becomes obvious when one compares the two methods shown in Fig. 5.20.

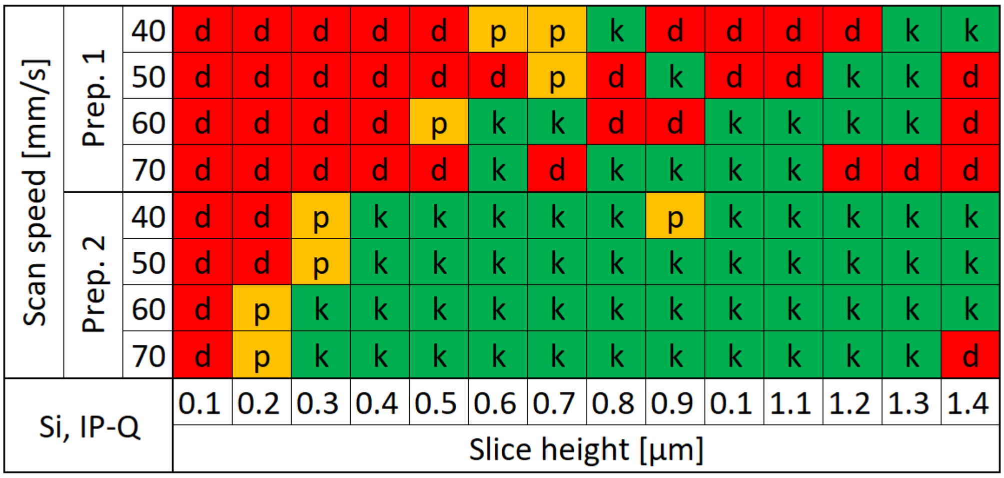

Scan speed [mm/s]																
	Prep. 1	40	d	d	d	d	d	p	p	k	d	d	d	d	k	k
		50	d	d	d	d	d	d	p	d	k	d	d	k	k	d
		60	d	d	d	d	p	k	k	d	d	k	k	k	k	d
		70	d	d	d	d	d	k	d	k	k	k	k	d	d	d
	Prep. 2	40	d	d	p	k	k	k	k	k	p	k	k	k	k	k
		50	d	d	p	k	k	k	k	k	k	k	k	k	k	k
		60	d	p	k	k	k	k	k	k	k	k	k	k	k	k
		70	d	p	k	k	k	k	k	k	k	k	k	k	k	d
Si, IP-Q			0.1	0.2	0.3	0.4	0.5	0.6	0.7	0.8	0.9	0.1	1.1	1.2	1.3	1.4
			Slice height [µm]													

Fig. 5.20: Comparison of the preprocessing methods standard and oxygen plasma/silanization treatment, indicated by "Prep. 1" and "Prep. 2", respectively. The contour structures were fabricated on a standard substrate Si wafer from resist IP-Q and showed detached, partially detached and viable results, indicated by "d", "p" and "k", respectively.

The treated substrates retain many more contour structures than the non-treated one. Activation process parameters like exposure time, pressure and silanization time most likely have significant effect on these reactions and need to be studied further. Structure adhesion requirements and recommendations for improvement methods are strongly application dependent. For this work, the unaltered adhesion between structure and chip was found sufficient.

5.6 Substrate Tilt

An important contribution of the substrate to the proper fabrication of structures using TPP comes from the tilt it exhibits, when compared to the optical beam. The following section explains the fundamentals of this phenomenon and describes measurements of various contributions to substrate tilt. Furthermore, the options of tilt compensation are investigated and a suitable system upgrade for the purpose is presented and verified.

5.6.1 Tilt Origin & Issues

Tilts describe the angles a plane is at in comparison to a primary plane. In the case of the TPP system used in this work, the primary plane is the x-y-plane which is orthogonal to the optical axis (z-axis). A tilt in x or y (x tilt angle α, y tilt angle β) describes the angle deviation component to the x- or y-axis, respectively (see Fig. 5.21a). Tilt between the substrate surface and the primary plane of the TPP system can have various and multiple origins. It is the sum total of all tilt factors combining, e.g.:

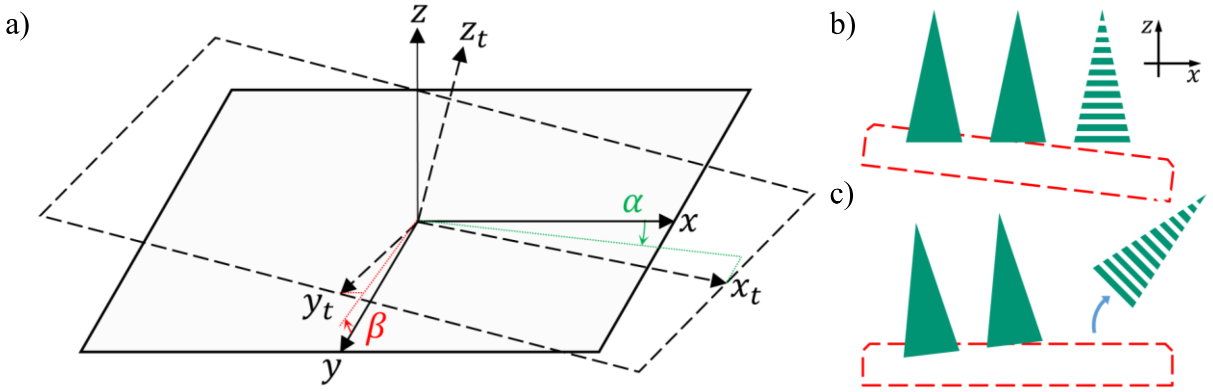

Fig. 5.21: a) Schematic of a primary plane (x, y, z) and a tilted secondary plane (x_t, y_t, z_t) including the x and y tilt angles α and β towards the projected auxiliary lines. b) Sketch of the issues structures (green) can suffer from when created on a tilted substrate (red). c) After development.

- Angle offsets internal to the TPP system originating from assembly deviations between the individual components, e.g.
    - the tilt of the slide-in substrate holder inserted into the slot attached to piezo stage 2, which can be increased by contamination,
    - the tilt standard substrates receive when attached to the substrate holder using duct tape, which can be increased by contamination,
- the tilt internal to the substrate due to
    - surface roughness (Fig. 5.22a) [209],
    - wafer bow (Fig. 5.22b) [210],
    - angle offsets originating from assembly deviations between individual components.

Contamination, in this case, refers to particles and residual resist, adhesives or solvents. Further factors can be found in additional features added to the fabrication system, e.g., the tilt compensation upgrade developed in this work, see section 5.6.4.

Surface roughness describes the unevenness of the surface height, see Fig. 5.22a. There are various calculation methods for its quantitative characterization, each of which takes into account different characteristics of the surface. It can be influenced by polishing, grinding, etching, vapor deposition, corrosion and many other methods or effects. Roughness can be measured by using for example white light interferometry or confocal microscopy.

Wafer bow, among other shape variations, describes the flatness of a wafer [210], but is a viable definition for the other substrates used in this work as well. Bow is a common occurrence in semiconductor fabrication, e.g. due to stresses introduced to the material by, often one-sided, processing [210, 211].

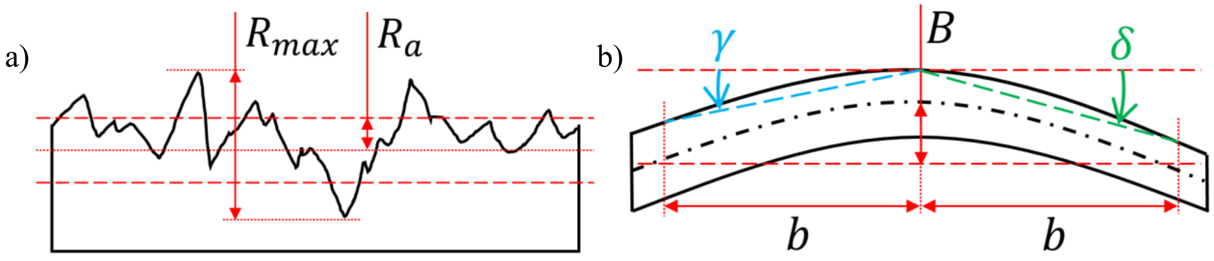

Fig. 5.22: a) Sketch of a surface with roughness including the arithmetic average of height deviations from the mean R_a and the maximum to minimum height R_{max}. b) Sketch of a substrate with bow B measured from the median surface to a reference plane fitted to the median at equidistance b. In this work, contributions γ and δ to the tilt angle are measured from the same distance towards the top central point.

Bow is the height deviation of a central point on the surface compared to a reference plane, e.g., the exterior of the surface or the backside, see Fig. 5.22b. In this work, both surface roughness and the shape variations are handled as contributions to tilt, although they are separate phenomena. If the surface plane of the substrate used during TPP is tilted in comparison to the primary plane, problems ensue. Fig. 5.21b and c show some of these issues, e.g.:

- Structures can get
    - fabricated at an angle,
    - partially detached from the substrate,
    - partially buried inside the substrate,
- the first layer may not connect to the substrate, so it as well as subsequent layers may drift away,
- the objective lens can get damaged by structures on, or by the substrate itself,
- or the fabrication laser can get reflected from the substrate at an angle.

The latter issue can lead to unintended interference patterns of the incident with the reflected beam, thereby changing the dose supplied to the voxel, which can result in weaker or even non-existent polymerization near the substrate.

To prevent these issues from affecting the fabrication, tilt has to be measured and its origins have to be determined to allow intervention by tilt reduction or compensation.

5.6.2 Tilt Measurements

A measurement of the substrate tilt can be accomplished, by employing the operating software of the TPP system used in this work. The system needs to be set up with objective, substrate and resist, and an automatic interface detection needs to be conducted, see section 2.3.3. After supplying initial parameters, an automatic tilt measurement can be initiated. First, multiple lateral positions are approached, where automatic interface detections are conducted. Then, the x- and y-tilt angles are calculated from the distances travelled along all degrees of freedom.

Automatic interface detection can become difficult, especially on MEMS, for example when there is no sufficiently large area that is consistent in reflectivity. Particles and other contaminants, any topology or arranged materials of dissimilar reflectivity can interrupt the flat, homogeneous surface necessary to execute a fruitful automatic interface detection. The default size of the required area is approximately one third of the field of view of the objective, which means it depends on the choice of objective. Alternatively, adjustments can be made to the selected area in size and position inside the field of view, at the cost of additional experimentation to find suitable settings for the other parameters of the interface detection software.

The semi-automatic tilt measurement method devised in this work combines the manual operation with features of the automatic interface detection, detailed in section 2.3.3. The manual submission of stage commands between measurements allows the permanent supervision of any issues arising during the measurement, e.g., positioning correction, contamination monitoring. When a suitable position is reached, the automatic interface detection can be initiated. After repetition at multiple locations, the tilt per axis can be calculated.

This method improves the safety when working with new or unknown substrates and increases the precision by excluding contaminated, or otherwise unsuitable areas. This way, it provides a measurement tailored to the substrate.

All substrates used in this work start off tilted, as indicated in Tab. 5.8, where measurements using the automatic and semi-automatic methods are presented. The employed resists and objectives vary between sets and samples. All substrate types, except the CMUT dies, were inserted into the standard substrate holder. The dies were inserted into the tilt compensation upgrade, which is described in section 5.6.4.

The maximum values indicate an angle that could be encountered, which is useful when considering the requirements for compensation approaches. In comparison to the CMUT samples, all other types are standard substrates and exhibit lesser maxima. The standard substrates also have lesser minima values. The values are absolutes of the measured tilt angles. Both x and y axes get measured, but only the larger value is subsequently compared to find the maximum of all maxima and the maximum of all minima. The latter is indicated by (*).

Tab. 5.8: Absolute maximum and minimum tilt values measured on various substrates. The (*) indicates the fact, that the minimum values noted here are the maximum of all minima measurements of a set of samples, respectively for each substrate type.

Substrate type	Method	Samples	Min.* [°]	Max. [°]
Fused Silica	Automatic	12	0.015	0.083
Si	Automatic	33	0.012	0.660
Soda-lime glass coated with (18 ± 5) nm indium tin oxide	Automatic	2	0.055	0.313
Si coated with 100 nm Al_2O_3	Automatic	6	0.020	0.078
Si coated with 520 nm TiAl	Automatic	4	0.003	0.036
CMUT die assembled on TO-18 (set 1)	Semi-auto.	53	0.026	2.102
CMUT die assembled on TO-18 (set 2)	Semi-auto.	29	0.138	3.104

This evaluation approach enables a clearer understanding of the substrates, as the minimum* is actually a value that can occur and subsequently has to be dealt with at least.

The average bow of 200 mm Si wafers at the start of clean room fabrication at Fraunhofer IPMS was estimated <±30 µm, measurements have been performed using a laser-based stress hysteresis measurement system 500TC (Frontier Semiconductor Inc.) [211]. The bow imparted on the Si standard substrates cut from wafers was calculated, to determine what part of the tilt angle recorded on standard substrates originates from it, see Tab. 5.8 and Fig. 5.22b.

After setting the substrate up with the 63x objective and IP-Q resist, the z-positions at five locations on a Si standard sample were measured using the automatic interface detection, see Tab. 5.9. The center position was determined by using the default x and y center of the TPP system. The quadrant positions were located at an x and y distance b of 10 mm from the center. The table shows the bow calculated from the perpendicular distance of the center point to a line connecting the measurement locations in quadrant two and four as well as three and one, named Bow II-IV and Bow III-I, respectively. Furthermore, the table shows the tilt contribution of the respective bow calculation.

In the examined sample, the center bows toward the objective. With approximately -1 µm of bow, the tilt contribution from bow of less than -0.01° is comparable to the minimum* tilt angle of Si noted in Tab. 5.8.

Previously conducted roughness measurements at Fraunhofer IPMS of an example 200 mm Si wafer exhibit a mean roughness R_a of 0.114 nm, a maximum R_{max} of 1.643 nm and a quadratic average $R_{q,RMS}$ of 0.149 nm [211].

Tab. 5.9: The tilt contribution from bow, calculated from measurements on a Si wafer using the 63x objective and IP-Q.

Quadrant	z-Position [µm]	Bow II-IV [nm]	Bow III-I [nm]	Tilt from bow II-IV [(×10^{-3})°]	Tilt from bow III-I [(×10^{-3})°]
Center	10531.558	-994 ± 78	-822 ± 74	-8.46 ± 0.66	-7.37 ± 0.66
I	10529.777				
II	10551.758				
III	10535.158				
IV	10513.445				

Subtracting R_a from R_{max} gives 1.529 nm, which can be assumed as a roughness contribution to the tilt angle resulting in 0.003° over the length of the Si substrate.

5.6.3 Interface Measurements

Interface measurements were conducted using both the automatic and manual interface detection methods (see section 2.3.3) to determine the standard deviation between individual measurements and to find the difference between the methods. The measurements of this section were conducted on standard, or tilt compensated substrates, where residual tilt was reduced to less than 0.04° per axis, see section 5.6.4.

Measurements were conducted using the 10x objective on standard Si substrates that were cleaned using Acetone and IPA. The resists and substrates were allowed >30 minutes to reach temperature equilibrium. Otherwise, a deviation of the measured z-position of (3.94 ± 1.01) µm emerges, due to thermal expansion of the objective and substrate and thermal alteration of the viscosity and subsequently the refractive index of the resist, which affect the optical interface detection procedure.

Twenty individual z-positions were recorded for each measurement named in Tab. 5.10. In between two measurements, the substrate was moved back and forth 1 mm using piezo stage 1 at a stage velocity of 2 mm/s. In the automatic detection case, the objective was retracted manually approximately 100 µm before each recording.

There are four groups in Tab. 5.10 for which the two detection methods were compared: (i) using the resist IP-Dip before a software based alignment of the optical path by a Nanoscribe engineer, (ii) the same after alignment and (iii) as well as (iv) using the resist IP-Q after the alignment.

The only resist available before the alignment was IP-Dip. The alignment reduces optical errors within the TPP system, see section 2.3.1.

Tab. 5.10: Manual to automatic interface detection method comparison, using the 10x objective, before and after an alignment of the optical path. The only resist available before the alignment was IP-Dip.

Measurement	Detection	Z-Position [µm]	Average difference [µm]
IP-Dip Before Alignment	Manual	10146.156 ± 1.322	42.89 ± 1.53
IP-Dip Before Alignment	Automatic	10189.048 ± 0.615	
IP-Dip After Alignment	Manual	10234.741 ± 3.044	39.65 ± 2.92
IP-Dip After Alignment	Automatic	10274.391 ± 0.283	
IP-Q After Alignment	Manual	10201.994 ± 3.531	2.99 ± 3.45
IP-Q After Alignment	Automatic	10203.981 ± 0.987	
IP-Q After Alignment	Manual	10329.668 ± 3.967	8.78 ± 4.06
IP-Q After Alignment	Automatic	10338.447 ± 0.541	

As was expected, the automatic interface detection method is more consistent than the manual one. Another expectation are differences between the method's resulting average z-position. But unexpectedly, for IP-Dip they are far greater than for IP-Q. This might be due to the difference between the additives used (see section 2.3.5). The manual interface was always detected at a lower z-position. So, if the polymerization threshold is reached sooner, the difference between automatic and manual detection reduces.

The maximum (not average) difference of the aligned case for IP-Q and IP-Dip was calculated and implemented in scripts that require manual interface detection in case substrates are not viable for automatic detection.

Interface measurements were conducted using the automatic interface detection method to determine the standard deviation between individual measurements and to find the difference between the two objectives 63x and 10x, when detecting the same substrate interface. Both objectives were installed for the experiment, as well as a Si substrate that was cleaned using Acetone and IPA. The resist was applied to the substrate and after allowing ~30 minutes to reach temperature equilibrium, the 63x and 10x objectives were put to use in succession.

Twenty individual z-positions were recorded for each measurement named in Tab. 5.11. In between subsequent measurements, the substrate was moved back and forth 1 mm using piezo stage 1 at stage velocity 2 mm/s and the objective was retracted manually approximately 100 µm. The measurements were made after the optical path alignment mentioned earlier. As expected, the automatic interface detection using the higher resolution 63x objective results in z-positions with a reduced averaged deviation in IP-Q of ±0.082 µm compared to the ±0.641 µm of the 10x objective.

Tab. 5.11: Automatic interface detection comparison between objectives.

Objective	Resist	Date	Z-Position [µm]	Average difference [µm]
63x	IP-Q	25.02.21	10401.806 ± 0.034	174.49 ± 0.42
10x	IP-Q	25.02.21	10227.319 ± 0.662	
63x	IP-Q	03.06.21	10383.159 ± 0.045	172.05 ± 0.87
10x	IP-Q	03.06.21	10211.111 ± 0.407	
63x	IP-Q	08.06.21	10391.168 ± 0.167	180.39 ± 0.66
10x	IP-Q	08.06.21	10210.776 ± 0.854	
63x	IP-PDMS	28.10.21	10521.375 ± 0.029	57.39 ± 1.91
10x	IP-PDMS	28.10.21	10463.990 ± 1.897	
63x	IP-PDMS	04.11.21	10491.116 ± 0.193	195.58 ± 0.61
10x	IP-PDMS	04.11.21	10295.540 ± 0.524	
63x	IP-PDMS	07.05.22	10530.804 ± 0.126	102.05 ± 0.62
10x	IP-PDMS	07.05.22	10428.752 ± 0.637	

The average difference between the two objectives primarily comes from their size disparity, which comes to (175.6 ± 3.5) µm and (118.3 ± 57.6) µm when averaged, for IP-Q and IP-PDMS, respectively. The deviation between the measured sets can be explained by the installation method. The objectives have to be screwed into a revolver and could end up at a different z-position this way. Particles, residual resist, thread grease and other contaminants can also interfere with the objective installation. The strongly deviating measurements with IP-PDMS might have suffered from contamination or installation error. The size disparity measured in IP-Q in addition to its deviation totaling 179.1 µm was implemented in scripts that require automatic interface detection and subsequent fabrication using the 63x and 10x objectives in succession.

In case of the CMUT, the successive approach was applied to make use of the increased precision. Furthermore, the 63x compared to the 10x objective provides an approximate detection area of 0.006 rather than 0.15 mm², respectively. The particular type of CMUT used in this work has sufficient undisturbed areas for the former, but not for the latter, making the successive approach even more useful, even when considering the additional work involved to prepare, utilize and subsequently clean the second objective.

Interface measurements were conducted on assembled CMUT dies using the automatic and manual interface detection method with the 63x as well as the 10x objective to determine the differences. After allowing the resist IP-Q ~30 minutes to reach temperature equilibrium, the

63x and 10x objectives were put to use in succession. Fig. 5.23a shows measurements of an example chip as a bar chart to illustrate the height differences between employed objectives and detection method combinations. The legend contains standard deviation values of the 63x automatic detection that originated during the triple measurement on the example chip. The 10x auto. and 10x man. Standard deviation values represent the average of the values found in Tab. 5.10 and Tab. 5.11.

The z-position actually used for fabrication was calculated using the previously calculated average objective height difference subtracted from the z-position measured using the 63x objective and the automatic detection method. It falls between the two measurements taken with the 10x objective, which are engaged with further in the rest of Fig. 5.23a. Fig. 5.23b depicts the average height difference between variations of objectives and detection methods averaged over 40 measurements conducted on CMUT chips. The average difference between 10x auto. and 10x man. was noted earlier as 2.99 µm for a standard Si substrate and IP-Q resist. On a CMUT, the average was (102.1 ± 20.1) µm, probably because with the 10x objective, the FOV covers most of the chip surface, including structured areas and areas with materials of varying reflectivity, e.g., the aperture and connector pads of the device. The same effect is noticeable when comparing the difference between 63x and 10x with automatic detection noted earlier for a standard Si substrate, with the one noted here. The deviations are quite large compared to the ones shown earlier, probably due to inconsistencies with measurements on very reflective parts of the substrate and the mentioned z-position error during objective installation. The difference of the 63x auto. to the 10x manual detection may be found in future works.

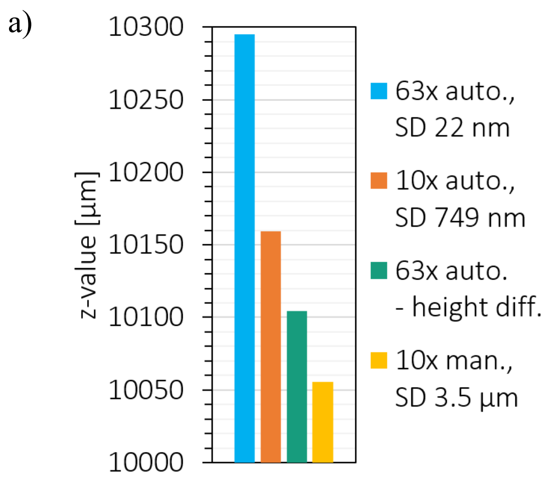

b)

Objective & det. method	Objective & det. method	Average height difference [µm]
63x auto.	10x auto.	140.7 ± 13.6
63x auto.	10x man.	242.8 ± 18.5
10x auto.	10x man.	102.1 ± 20.1

Fig. 5.23: a) Interface measurements of an example CMUT die using variations of objectives and detection methods, as well as a calculated value of the average objective height difference subtracted from the z-position measured using the 63x objective and the automatic detection method. b) Height differences of variations of objectives and detection methods averaged over 40 measurements on CMUT dies.

The interface measurements were conducted on tilt compensated chips, where residual tilt was reduced to less than 0.04° per axis. The following section will explain the origin, measurement and compensation of tilt on assembled CMUT dies.

5.6.4 Tilt Compensation Upgrade

As described in section 2.3.1, the TPP system used for this work originally comprises only components active on the x-, y-, and z-axis. This means, tilt angles cannot be compensated directly.

Internal to the operating software of the TPP system is a "tilt correction", that adapts the z-positions of individual x and y coordinates of a job file. This consequently leads to a deformation of the structure itself, as visualized in Fig. 5.24. At least, the disconnection and burial of structures can be prevented this way.

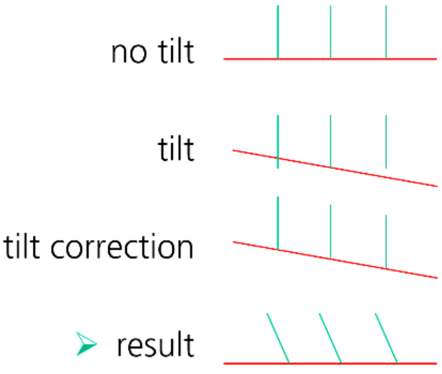

Fig. 5.24: Schematic of structures (green) on a substrate (red), with tilt and after using the software based "tilt correction" available to the TPP system used in this work.

For standard substrates, the "tilt correction" can be sufficient, but as stated in Tab. 5.8, the tilt angles on assembled CMUT chips are significantly larger. True tilt compensation became essential and various additional features were conceptually established before a solution approach was manifested. It must address the following requirements:

(A) $\alpha, \beta > 3.1°$

The tilt angles α and β (see Fig. 5.21a) addressable by the compensation system must be larger than the maximum tilt angle measured on assembled CMUT dies, see Tab. 5.8.

(B) $\Delta z < 700$ nm

The target residual height difference Δz due to tilt after compensation over the chip size must be less than the accepted voxel z-height of the highest resolution objective of 700 nm. Thus, in case of a CMUT die surface with 1 mm side length, the target residual tilt angle is ±0.04° per axis.

(C) $d_A = 65$ mm

The dimensions of the upgrade in x and y direction have to fit into the square aperture of piezo stage 2 with $d_A = 65$ mm, see Fig. 2.3d. Or they have to be an equivalent exchange for one of the system's original components. Height was limited to ~15 cm by the safety hatch of the TPP system.

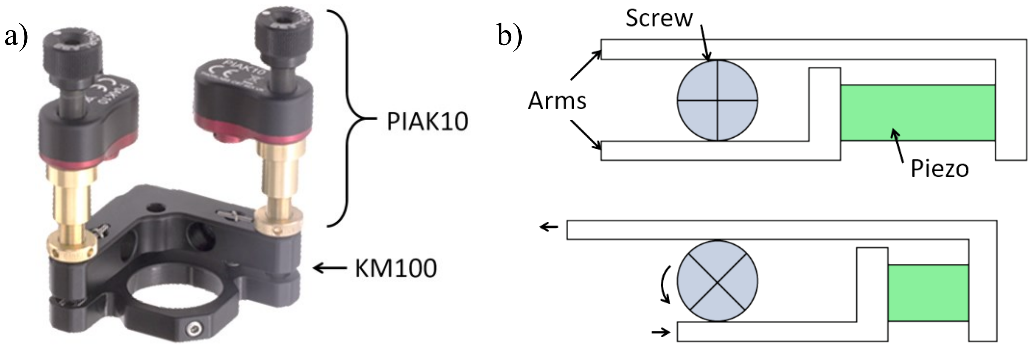

Fig. 5.25: a) Photograph of mount KM100 with two PIAK10 piezo drives inserted into the corners [212]. b) Schematic of the „slip-stick“ principle implemented in the PIAK10 [212].

For example, piezo stage 2 could have been exchanged for a version including additional degrees of freedom. Currently available systems did not achieve the required precision or total angle per axis, though.

The manifested solution approach followed in this work stems from an engineering area, where large angles have to be manipulated with high precision at a compact scale: photonics. Here, optical elements, e.g., lenses and mirrors, are commonly positioned by manual micrometer screws to direct light to the intended target.

The selected ±4° adjustable mirror mount KM100 (Thorlabs GmbH) was originally designed for 1” optics. The choice fell on it due to its compact size of approximately (50 x 50) mm² and the availability of driving the adjustments via piezo inertia actuators PIAK10 (Thorlabs GmbH), which are compact themselves. Both components assembled are depicted in Fig. 5.25a.

The KM100 is originally driven via thumbscrews and attains a resolution of 0.5° per revolution that way. The inertia actuators replace the thumbscrews in the two corners of KM100, where they sit in a socket and can push the active plane to adjust tilt. The third corner is free, the fourth has a ball joint. That means, adjustment of one of the angles will also affect the other, although at a reduced amount.

The parameters of a PIAK10 are compiled in Tab. 5.12. The actuators rotationally drive their screws via the “slip-stick” principle [212], see Fig. 5.25b: A rapidly extending piezo stack drives an arm over the side of the screw, overcoming its coefficient of friction and not turning the screw due to its inertia. Then, the stack slowly contracts, turning the screw via friction.

Tab. 5.12: Inertia actuator parameters [212].

Parameter	**Value**
Travel	10 mm
Typical Step Size	20 nm
Step size variation	<20 %
Maximum Step Frequency	2 kHz
Maximum Axial Load Capacity	2.5 kg
Speed (Continuous Stepping)	<210 mm/s
Sawtooth max. voltage	125 V

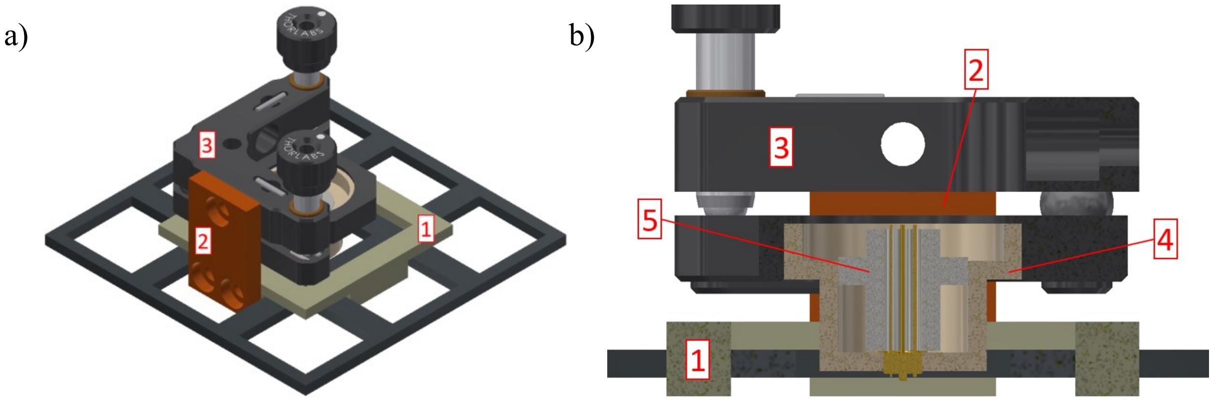

Fig. 5.26: a) Isometric view CAD model of the substrate holder with mounted manual version of the tilt compensation upgrade, including the base, connection plate and KM100 indicated by 1, 2 and 3, respectively. b) Side section view CAD model of the substrate holder with mounted manual version of the tilt compensation upgrade and a TO-18 component, including the base, connection plate, KM100 optical mount, KMTO adapter and stamp fixture, indicated by 1, 2, 3, 4 and 5, respectively.

This action is repeated by application of a saw tooth voltage. The order can be reversed, depending on the direction in which the screw needs to be turned.

The change of direction, component variance, piezo hysteresis and application conditions can lead to step size variations of up to 20 % [212].

The design of the tilt compensation upgrade developed for this work adapts the mirror mount and its drivers to the top of the 9-slot substrate holder, see Fig. 5.26. Furthermore, a CAD representation of the TO-18 chip mount was mounted to the setup via multiple adapter parts. The tilt compensation upgrade numbered in Fig. 5.26 comprises the following:

1. the **base** inserted into the 9-slot substrate holder (*black*),
2. the **connection plate**, which fastens the base to the KM100 via M10 screws,
3. the optical mount **KM100**, which enables the angular adjustment,
4. the **KMTO**, the adapter between the slot in the KM100 and the TO-18 (*gold*) and
5. inside the KMTO, the **stamp** sits on the rabbet of the TO-18 to secure it in place. The stamp is then fastened to the KMTO via duct tape to impede its movement.

The complete setup fits into the aperture of piezo stage 2 and allows the safety hatch to close, thereby requirement C was fulfilled, see Fig. 5.26 and Fig. 5.27b. It slots into the substrate holder and is securely linked to it during fabrication by the interlocking features of the base. Assuming no angular motion between the added structures and the constant step size of 20 nm listed in Tab. 5.12, the tilt compensation upgrade should achieve a resolution of 0.5 µrad or 30.6×10^{-6} deg per step.

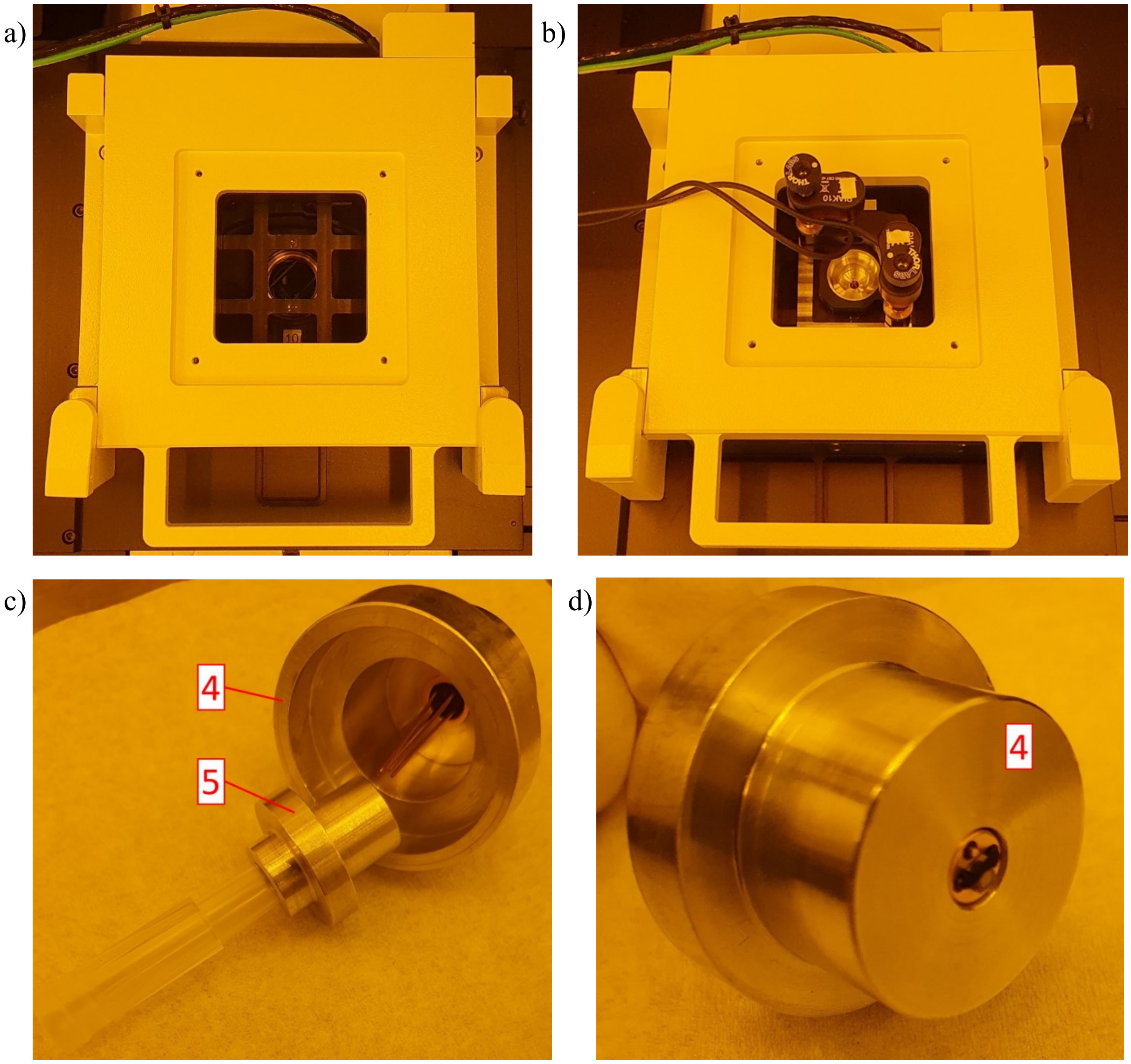

Fig. 5.27: a) Top view of the substrate holder inside its place in piezo stage 2, with the LED background lighting element removed and the objective revolver visible. b) The same with the automated tilt compensation upgrade inserted, including a CMUT assembled on a TO-18. c) TO-18 inserted into the KMTO (4) with the stamp (5) next to it including an additional polymer holder for improved handling. d) CMUT assembled on a TO-18 and inserted into the KMTO (4).

The parts 1, 2, 4 and 5 were milled from aluminum, assembled with the other parts and installed in the TPP system, see Fig. 5.27. Fig. 5.27a shows the inside of the TPP system from a top view.

The LED transmission illumination element, which is usually fixed above the aperture via four screws, is removed for this work. This way, the substrate holder and the objective revolver below it become visible, see Fig. 5.27a. On the substrate holder, the tilt compensation upgrade was placed, see Fig. 5.27b. The control unit, with which the PIAK10 actuators are driven, was placed outside of the fabrication chamber. The assembly of the KMTO is depicted in Fig. 5.27c and d, with the stamp and the TO-18 including a CMUT die.

Another feature added by this design is the manual z-axis rotation. By turning the clear thermoplastic stem inserted into the KMTO adapter depicted in Fig. 5.27c, angles to the z-axis can be adjusted without limit while monitoring the live view to check the current position. This way, chip placement errors that occur during assembly can be corrected. After tilt compensation and rotation correction, the remaining angle to the z-axis of CMUT dies was (0.079 ± 0.057)°, which was measured using the crosshairs of live view and calculated from the x and y positions of piezo stage 2 along one of the 1 mm side lengths of the die surface.

The tilt compensation upgrade was successfully implemented to compensate the tilt of CMUT chips assembled on TO-18 mounts. The chips were set up with the 10x objective and IP-Q, while interface detection was carried out using the 63x objective. Both were inserted into the system and supplied with resist. After ~30 minutes to achieve temperature equilibrium in all parts and setting the driven axes to their origin position, the following process was executed:

1. Find the interface using the 63x objective, record the z-position.
2. Move in x direction (500 to 900 µm, further is better), repeat step 1.
3. Move in y direction (500 to 900 µm, further is better), repeat step 1.
4. Repeat at least once from step 1 to determine deviation of the three interface z-positions. After the first run through, this repetition can be ignored.
5. Calculate current x and y tilt angles from average z-positions
6. Calculate the number of steps to take in x and y to compensate tilt angles.
7. Drive the axis that exhibits the largest angle the proposed number of steps.
8. Repeat from step 1 as long as any tilt angle is larger than the required ±0.04°.

Usually, after less than five repetitions, the required ±0.04° residual tilt angle was achieved. This approach compensates the unintended step size variation and the unintended effect one driven axis has on the other, because both problems reduce with the number of steps driven. Also, the impact of the latter problem gets reduced by always addressing the axis with the highest tilt angle first.

The maximum angle of ±4° proposed by the KM100 manufacturer was found accessible, thereby requirement A was fulfilled.

The example noted in Tab. 5.13 reveals how the process was implemented in Microsoft Excel (Microsoft Corporation). On the left, the three z-position values of the interface measurements were entered. The average was used to calculate the tilt angles, which were in turn used to calculate Δz and then propose a number of steps (highlighted in purple) based on the increment (Inc.) per axis.

Tab. 5.13: Example tilt compensation process for a CMUT assembled on a TO-18 mount, including the PIAK10 position (Pos.) and the increment (Inc.) in nm/step.

#	z [µm]	1	2	Average [µm]	Standard deviation [µm]	Tilt x [°]	Tilt y [°]	Δz x [µm]	Δz y [µm]	Pos. x [step]	Pos. y [step]
1	left	10127.975	10128.254	10128.11	0.14	0.36	-0.13	6.21	-2.35	15616	0
	right	10123.702	10123.833	10123.77	0.07					Inc. x	66
	top	10129.847	10129.674	10129.76	0.09					Inc. y	66
2	left	9927.152	9927.083	9927.12	0.03	-0.32	-0.07	-5.50	-1.25	1780	0
	right	9930.920	9931.018	9930.97	0.05					Inc. x	66
	top	9927.969	9928.020	9927.99	0.03					Inc. y	66
3	left	10023.412		10023.41	0.00	**0.02**	-0.06	0.33	-1.09	1780	-2741
	right	10023.181		10023.18	0.00					Inc. x	50
	top	10024.175		10024.18	0.00					Inc. y	50
4	left	10039.886		10039.89	0.00	**0.01**	**-0.03**	0.25	-0.58	1780	-2741
	right	10039.714		10039.71	0.00					Inc. x	50
	top	10040.295		10040.30	0.00					Inc. y	50

The increment was initially based on the 20 nm step size listed in Tab. 5.12, which was found to be too small for the completed setup. Increments of 66 nm/step for the initial movement were found to reduce the risk of overshooting. Overshooting would subsequently require reversal of the drive direction, increasing the step size variation.

The increment was reduced to 50 nm/step after a few movements, as was found to work well due to the amount of unintended slippage reducing with the reduced number of steps taken. The deviation of the increment of 66 nm/step compared to the 20 nm step size proposed by the manufacturer is most likely due to the increased force required to move the screw against the KM100 mount including the added parts to enact an angular movement.

As illustrated by Tab. 5.13, the repetition of the interface detection becomes superfluous after the first few repetitions, because the deviation reduces drastically. The whole tilt compensation process takes approximately 20 minutes. It could be further automated by implementing it within a python script, but there are advantages to the manual approach. The main one is that the location of the FOV of the objective has to be free of structures of the chip and free of particles and other contaminants, to result in viable measurements. This location can change over the compensation process with the change in tilt angles, which is hard to automate. Furthermore, the human supervision reduces the likelihood of crashing.

After tilt compensation using the upgrade developed during this work, the remaining tilt angle averaged over both axes of 53 CMUT chips was (0.035 ± 0.018)°, a second set of 52 CMUT chips resulted in (0.025 ± 0.019)°. Requirement B was thereby fulfilled.

Fabrication was not restricted by the upgrade, all features of the TPP system were able to be used as before, except for the background illumination. The tilt compensation was applied to opaque chips in this work, so this feature was superfluous. It can be adapted to include this feature, perspectively. The tilt compensation upgrade can fit other substrates, it was also used for the tilt compensation of the NED-µPS chip described in section 3.2. Other chips and substrates might require alterations to the KMTO. Another use case for the upgrade is the fabrication of structures on angled surfaces of the substrate.

6 Investigation of Two-Photon Polymerization Lithography on Capacitive Micromachined Ultrasonic Transducers

With the compensation efforts established in previous chapters, the requirements for fabrication on a CMUT chip are fulfilled. The chip can be placed in the fabrication system, tilt and reflection issues can be addressed, and additional knowledge about parameters and particularities of TPP that affect the exposure dose have been established. The fundamentals of the CMUT were presented in section 0.

In this chapter, the application examples of AM using TPP on assembled CMUT devices proposed in section 1.2.1 are investigated. The fabrication of structures on the chip is presented, thereby providing a proof of concept for AMOC. Furthermore, the reliability of AM on CMUTs was studied via individual experiments for the various process steps of TPP.

6.1 On-Plate Fabrication

In order to facilitate the direct fabrication of structures on the active element of CMUT devices via TPP, or on-plate fabrication, compensation methods may be necessary, depending on the composition and construction of the CMUT, see chapter 5. For this work, an experimental test structure was designed to find a viable parameter space. The design depicted in Fig. 6.1a to c also served as an inspiration for the exposure dose and compensation experiment, where some key ideas were reused, see section 5.4.1. For example the missing corner depicted in Fig. 6.1a and the arrangement in a 4 x 4 field of 16 iterations per plate, see Fig. 6.1d. The voxel line simulation of the 10 x 4.5 x 4.5 µm³ test structure indicates – via color – two sections – top and base – of different laser power, see Fig. 6.1a. The fabrication per plate starts in the bottom left, completes the row and then continues row per row to the top right, see Fig. 6.1d. The individual structure was designed with consistent settings for the top found in preceding parameter sweeps.

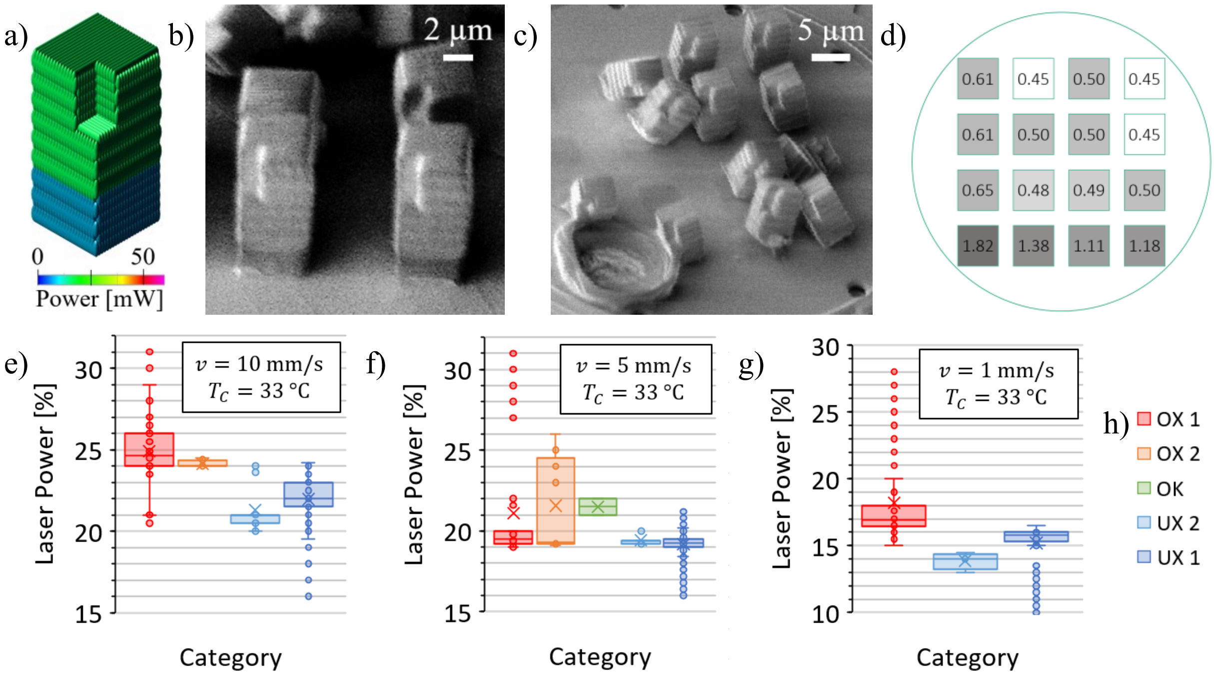

Fig. 6.1: a) Voxel line simulation of the on-plate experiment test structure including two step laser power adjustment. b) Tilted view SEM micrograph of correctly fabricated on-plate structures. c) The same of OX and UX structures. d) Schematic of the arrangement of the 16 on-plate test structures including category deviation per fabrication location with higher numbers indicating stronger average deviation. e) Viability depending on laser power of structures fabricated at 10 mm/s scan speed. f) The same at 5 mm/s. g) The same at 1 mm/s. h) Legend for diagrams e to g.

The settings for the base were adjusted strategically in parameter sweeps towards improving viability. The effects of the top on the base are not negligible.

As expected, some base settings lead to OK structures, some to OX and UX, compare Fig. 6.1b and c. Further categorization was implemented, see Fig. 6.1h, including the following notations:

OX 1	–	Destroyed structure, usually bubbles larger than 1 µm.
OX 2	–	Intact structure, usually bubbles smaller than 1 µm.
OK	–	Intact structure, attached to the plate, correct size, see Fig. 6.1b.
UX 2	–	Intact structure attached to the plate but reduced base volume.
UX 1	–	Detached structure.

The structures were fabricated using the 63x objective and IP-Dip resist, after tilt compensation and allowing ~30 minutes to reach temperature equilibrium. The 544 specimens studied in this evaluation exhibit – at any of the selected scan speeds – overlapping categories, see Fig. 6.1e to g. Especially instances of OX 1 and UX 1 overlapping indicate that the parameter space is very small. Only very few OK structures were produced, even during previous trial and error testing of the study described here.

Furthermore, depending on the fabrication location on the plate, the categories deviate. To evaluate this claim, a 304-specimen subset of 4 x 4 fields where exclusively 16 identical structures were fabricated, was selected. Each position was correlated with the categories found for the structures fabricated there. An average category score was established from 1 to 5, indicating OX 1 to UX 1, respectively. Then, the deviation from that average was calculated per location. Averaging over all deviations results in the score found in Fig. 6.1d. It indicates that the high scoring structures are more likely to deviate, or, if they do, more strongly deviate from the average result of the individual set. Bottom left structures were found more often with OX. A possible explanation, residual tilt, was ruled out after the investigated chips were compensated to less than 0.04°. By fabricating each piece of the 4 x 4 field in the center of the FOV, misalignment was ruled out as a contribution, see section 2.3.1. To find a practical correlation of settings to the OK category, or conclusive explanations of the category deviation effect, further investigations have to be performed in subsequent works. As the area for on-plate fabrication is extremely limited, the effort for such investigations is large and they would benefit strongly from automatic marker alignment and whole-wafer processing.

6.2 Packaging via Coating

As discussed in [2] and chapter 5, the fabrication of structures on CMUT chips using TPP requires additional attention, e.g. due to substrate reflectivity, diffracting elements and poor heat dissipation, as well as substrate tilt. Even with compensation efforts, these obstacles still complicate direct fabrication on CMUT devices.

Original advances made in [213], present a deconstruction of the superstructure devised in that work to establish viable settings per component. The superstructure designed for acoustic experiments was separated into the contour, base and a center structure containing multiple microchannels, see Fig. 6.2a. These components were each studied concerning their design, dimensions, fabrication parameters and hatch strategies in [213] and section 4.4.

6.2.1 Contour Structure on Substitute Substrate

Here, the contour and its interior can work as a coating of the fragile plates within the aperture, which is indicated in red in Fig. 6.2b. Furthermore, a contour structure fabricated on a CMUT device could function as a protective element itself, e.g., for particles larger than the aperture.

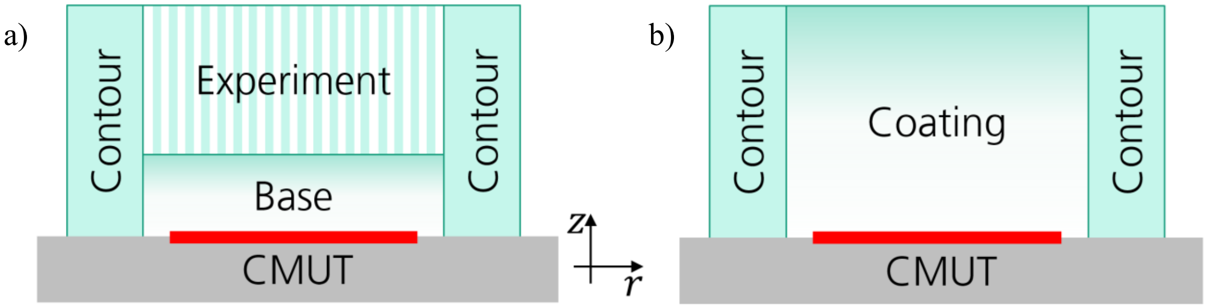

Fig. 6.2: a) Schematic of a section view of the superstructure for acoustic experiments on a CMUT die including its aperture indicated in red [213]. b) Similar schematic for a CMUT coating approach.

The contour component is a toroid with a rectangular cross section. It was designed to surround the aperture of the CMUT chip, fabricated on the Si area of the chip, see Fig. 3.1b. That area is relatively vacant, except the TiAl contact pads that connect the bond pads with the plates. Both bottom and top contact pads have to be surmounted by the contour, because of the maximum FOV addressable by the 10x objective. Any structuring outside of the recommended 1 mm diameter can become affected by optical aberrations [132]. With a fresh alignment of the optical path by a Nanoscribe engineer, the boundary was pushed to 1.2 mm, with some effects still appearing at reduced scale. With the current structure being combined by multiple voxel lines and slices, the issue was overcome.

Another way to overcome the restrictions of the FOV would be to stitch multiple blocks together, which would require moving the objective, in-between fabrication of blocks. This was found to be counterproductive. The interior of the contour has to be fabricated at a reduced dose to compensate substrate effects, which can lead to weakly polymerized structures. These can then get detached by moving the objective to stitch blocks. Furthermore, the stitching itself would most likely have to be compensated within the script to prevent OX from multiple exposure.

The parameter sweeps of the contour structure performed in [213] are discussed here in order to increase comprehension, especially concerning the intended use in the coating approach.

The inner contour radius was set up depending on the aperture of the CMUT device, here 570 µm, which would encircle the largest aperture found on the chips used in this work of 1 mm. The contour thickness and height were both set to 50 µm, which gives a result that can be visually evaluated quickly due to its square shape.

The employed hatch strategy was the concentric circle strategy shown in the example in section 4.4.1, with concentric rings approximated by chord lines at an angle of $2\pi/720$ and a hatch distance of 100 nm.

The sweep parameters are the laser power and a rounds value. The latter indicates how often the same slice was exposed before moving to the next. This allows to increase the dose without decreasing the scan speed, as the latter can lead to OX or thermal issues as discussed in section 5.2. This way, the time before the same hatch line was hit with another dose was increased, which provided a longer cool down period.

To imitate the two materials present on the CMUT surface, the parameter sweeps were fabricated on substitute substrates: a 725 µm Si wafer and a 725 µm Si wafer coated with 520 nm of TiAl. Both wafers were diced into 25.4 mm by 25.4 mm pieces to fit into the standard substrate holder. The fraction of the total parameter sweep depicted in Fig. 6.3a covers part of the underexposed domain found for the Si wafer, indicated in blue.

Next to it is a domain which suffers from UX, but still some segments of the contour were fabricated, indicated in yellow. Then there is the rest, fabricated with OK dose and displaying the respective contour thickness measured using the RLM. The thicknesses are colored blue for under- and red for overachieving the set thickness of 50 µm. The correlation between thickness and the dose is not very drastic in this example, but still recognizable, as the higher the round count and laser power, generally the thicker the contour becomes. The characterization error of the RLM and the fabrication error for TPP structures of similar design were established to be ±0.13 µm and ±0.32 µm, respectively, see section 4.4.3.

The previously discussed sweep is also represented in Fig. 6.3b, along with other sweeps on Si wafers indicated by circles and Si wafers coated with TiAl indicated by asterisks.

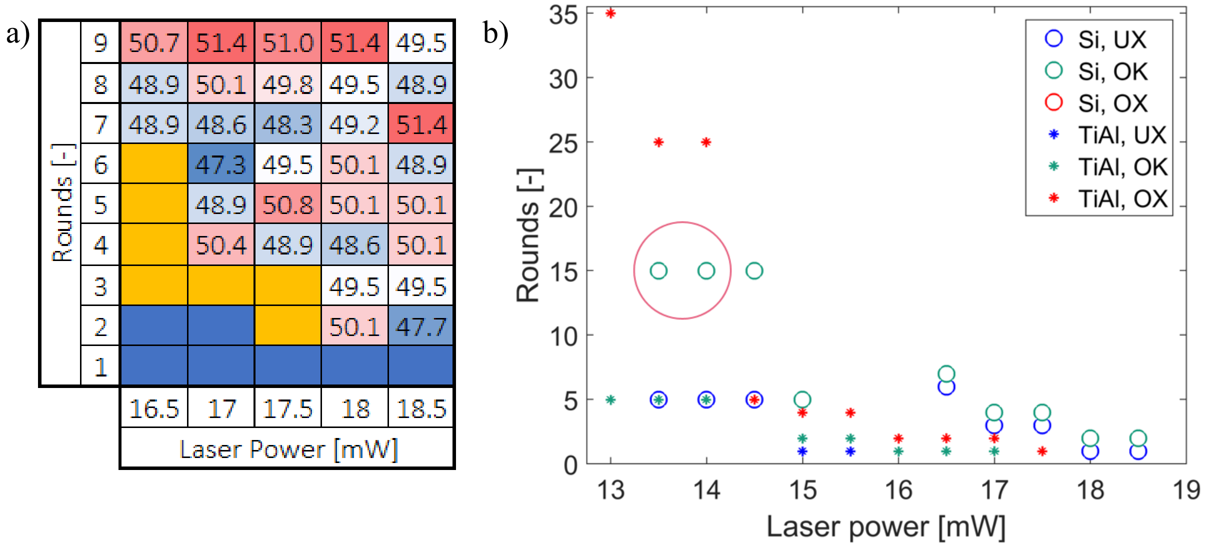

a)

Rounds [-]	16.5	17	17.5	18	18.5
9	50.7	51.4	51.0	51.4	49.5
8	48.9	50.1	49.8	49.5	48.9
7	48.9	48.6	48.3	49.2	51.4
6	🟨	47.3	49.5	50.1	48.9
5	🟨	48.9	50.8	50.1	50.1
4	🟨	50.4	48.9	48.6	50.1
3	🟨	🟨	🟨	49.5	49.5
2	🟦	🟦	🟨	50.1	47.7
1	🟦	🟦	🟦	🟦	🟦

Laser Power [mW]

b)

Fig. 6.3: a) Fraction of the laser power and rounds parameter sweep of the contour structure on a standard Si wafer including contour thickness values measured via RLM, including blue and yellow domains representing UX and partial UX. b) Comparison of contour parameter sweeps (laser power, rounds) on a standard Si wafer (○) and a Si wafer coated with 520 nm TiAl (*).

The laser power was stepped through in 0.5 mW steps. The number of rounds was stepped through in one round (1 to 10) and 10 round (5 to 35) steps, respectively. Here, the maximum dose where UX occurs is indicated blue. The minimum dose where OX and OK occurs are indicated red and green, respectively.

Fabricating a contour structure with laser power 15 mW on TiAl with just one round per slice results in UX, while two to three result in OK and 4 or more rounds result in OX. Above 15 mW laser power, the OX on TiAl occurs at a lower count of rounds than the OK or even UX on the Si substrate, indicating the difference in reflectivity of the substrate.

The pink circle refers to a region in which both substrates overlap with OK dosage, which required repetitions exceeding 10 rounds. That setting would increase fabrication time drastically, especially if contours with higher total height are required.

6.2.2 Contour Structure on Chip

The contour design shown in Fig. 6.4 was split in two parts that were fabricated using different settings, in order to reduce fabrication time. By selecting two angles in the script, the section covering the contact pads can be arranged. More precisely, each 360° hatch circle was split in two parts, so that no change came to the previously determined hatch strategy. A hatch distance of 100 nm and a slice distance of 1 μm were employed. The section covering the contact pads was fabricated with a decreased laser power and an increased number of rounds, while the Si section was fabricated with one round per slice. This approach reduced fabrication time of the described test structure by 67 %.

The micrographs in Fig. 6.4 depict an example contour with 382 μm inner radius, 157 μm height and 40 μm thickness, which was fabricated using IP-Q on a CMUT chip with a ~700 μm aperture. The chip was tilt compensated in x and y from (0.39 and -0.34)° to (0.02 and -0.04)° using the tilt compensation upgrade.

The contour section covering the contact pads makes up approximately half of the total structure, which is visualized in Fig. 6.4b, where the tilted view allows a look at both pads. The micrograph also exhibits a slightly darker area in the center of the aperture, which is an artifact of the SEM focusing process. One drawback of the time saving fragmentation of the contour is the added stop and start of the hatch line where the section changes, which results in an increased dose and a subsequent volume increase and/or OX. The transition between sections can be distinguished in Fig. 6.4c, where the volume increase produces a bump.

The bottom part of the transition is visualized in Fig. 6.4d, where the tapered volume towards the surface illustrates the reduced dose.

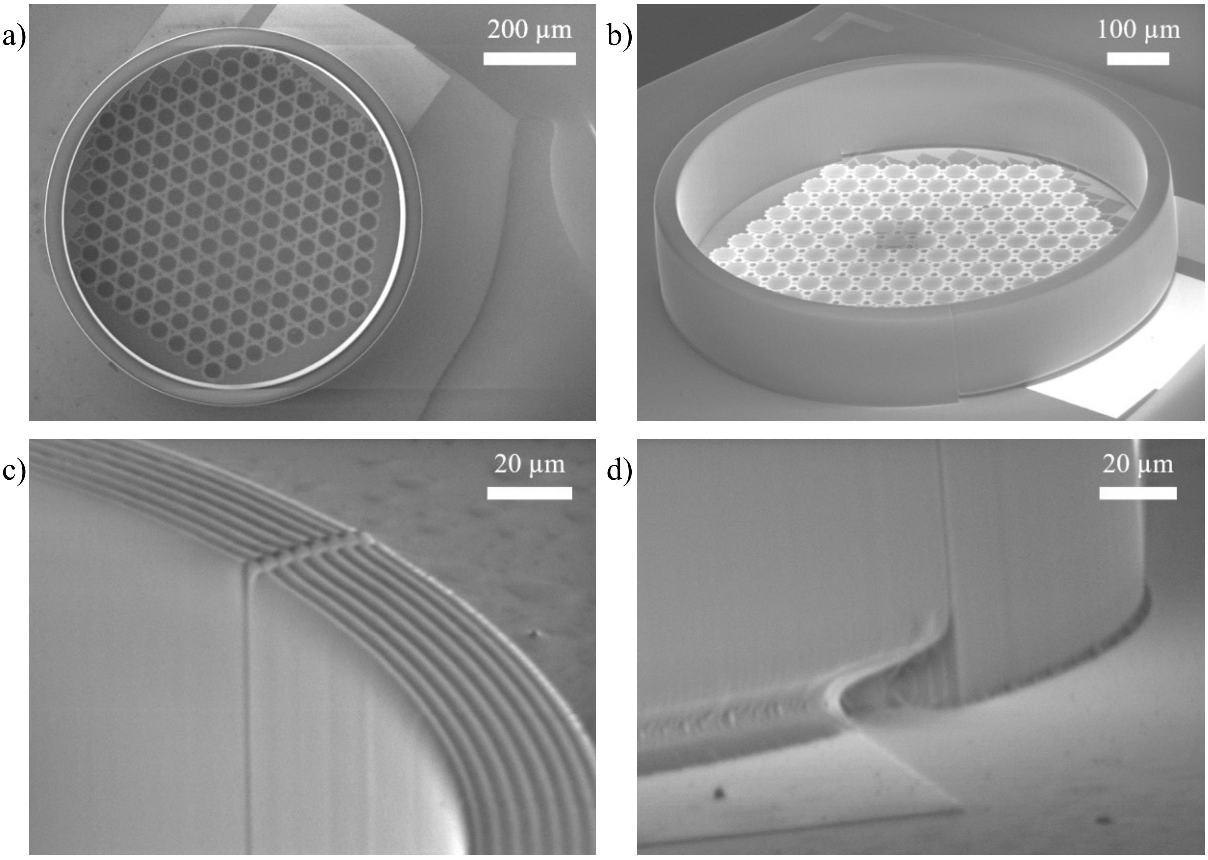

Fig. 6.4: a) Top view SEM micrograph of an example contour structure fabricated using IP-Q on a 700 µm aperture CMUT. b) Tilted view SEM micrograph of the same. c) Tilted view SEM micrograph of a close up of the top of the contour at the intersection of the different sections including voxel line structures. d) Tilted view SEM micrograph of the same intersection at the chip surface, showing volume reduction due to dose decrease and part of the contact pad.

In this early specimen, the substrate effect compensation was preceded by a static reduced laser power of 12 mW, compared to 40 mW in the off-pad section. A linear reduction of the rounds variable from 15 to 1 rounds per slice was arranged over the first 30 µm of height, after which the laser power was switched to 40 mW. These settings were found in this work via a parameter sweep. An even more acute volume reduction appears before the surface transition between pad and Si, see Fig. 6.4d. There, the section angle was set, so that the section starts 3° before the substrate transition, to make sure no OX occurs. The CMUT chip has topological differences not only within the area of the aperture, but also at the contact pads. The pads are raised approximately 520 nm from the Si surface, see Fig. 6.4d. The edges of these areas can diffract the incident beam, which can lead to an increased absorption and subsequent OX at a lower dose.

The contact pads were examined all around, no visible through-holes were found, see Fig. 6.4d and Fig. 6.5a. However, the structural impairment due to low polymerization and missing volume can be prevented using the dose compensation developed in chapter 5.

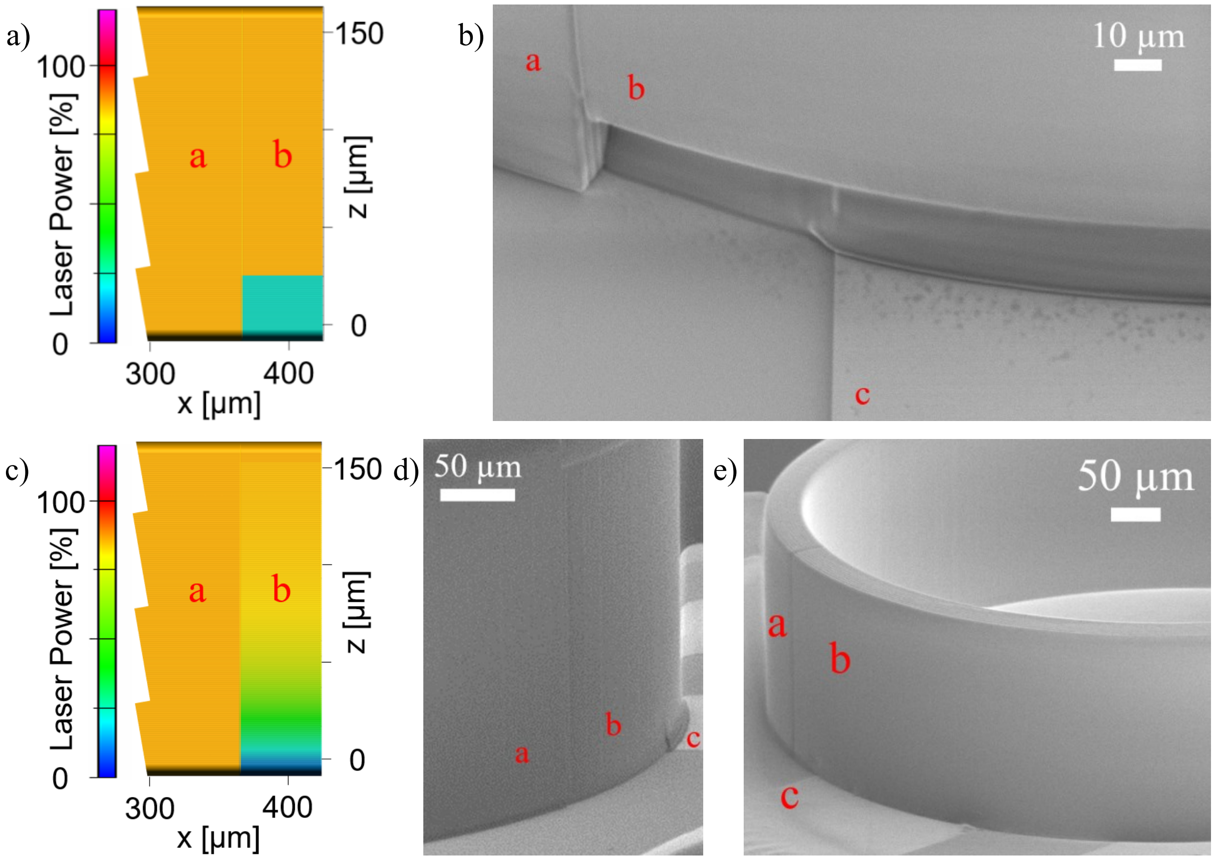

Fig. 6.5: a) Partial side view voxel line simulation of the contour structure comprising two sections indicated by “a” and “b” with the latter having a reduced laser power feature, including a scale indicating laser power by color. b) Tilted view SEM micrograph of a contour fabricated on a CMUT. Close-up of the intersection between the contour sections “a” and “b” at the chip surface including a part of the contact pad indicated by “c”, showing volume reduction due to the dose decrease. c) Partial side view voxel line simulation of the contour structure comprising two sections indicated by “a” and “b” with the latter having a compensated laser power feature, including a scale indicating laser power by color. d) Tilted view SEM micrograph of a contour fabricated on a CMUT, where the dose of the contact pad section b was compensated, exhibiting no volume reduction on or off of the pad “c”. e) Another example of the same, including a bond wire in the foreground.

For comparison, contour structures with and without compensation were fabricated on CMUT chips with 400 µm aperture, see Fig. 6.5. The settings were 382 µm inner radius, 157 µm height, 40 µm contour thickness, 100 mm/s scan speed, 1 µm slice distance and 100 nm hatch distance. The contact pad sections of Fig. 6.4d and Fig. 6.5b were fabricated using a constant laser power of 12 mW and four additional exposures, see Fig. 6.5a.

The examples shown in Fig. 6.5d and e were fabricated with a per-layer-compensation of the laser power 40 mW determined by the factors k_r and k_m set to 2.68 and 4.00, respectively, see Fig. 6.5c. These factors were found via incremental increases of step size 0.2 from their respective starting points, which were established in the compensation experiments for the 10x objective and IP-Q in section 5.4.4.

The modeled Rayleigh length $z_{r,G}$ and gradient m_{FEM} of 5.79 µm and 25.1 K/mW were compensated by these factors to z_r = 15.5 µm and m = 101 K/mW, respectively.

The structure similar to the one depicted in Fig. 6.5d and e was fabricated successfully and reliably on 35 CMUT specimens of various apertures. Size variations in thickness and height were viable, depending on the available space and the subsequent intentions.

6.2.3 Contour & Coating Structure

The interior of the contour structure can be filled to form a protective coating. There are multiple approaches, to achieve this:

a) Directly fabricate the coating concurrent with the contour structure using TPP.
b) Fabricate a cap on top of the contour structure using TPP and subsequently cure the interior using the UV flood polymerization setup.
c) Dispense resist into the interior of a previously fabricated contour structure and cure it.

Approach a) was followed in [213], where the challenges of fabrication directly on CMUT plates were investigated based on the know-how presented in [2]. These results and the established substrate effect compensation methods of chapter 5 were restructured to evaluate the viability of fabricating a coating concurrent with the contour structure, see Fig. 6.2b.

The Rayleigh factor k_r and the gradient factor k_m for the internal coating were determined via parameter sweeps on Si wafers coated with 520 nm TiAl, serving as substitute substrates. The coating structure design for the sweeps was a 50 µm height cylinder of radius 250 µm, which is reduced when compared to the target application on chip, in order to decrease fabrication time.

The 162 specimens were fabricated using a dedicated hatch strategy, with only parallel lines at a hatch distance of 100 nm and a slice distance of 1 µm. All hatch lines were illuminated starting from the same side, not in a meander, to increase the time between exposures of neighboring lines as much as possible. This strategy was also devised, so that start and end points exclusively appear outside of the center, where the aperture would present increased reflection on a CMUT. The 10x objective and the IP-Q resist were employed after ~30 minutes to reach temperature equilibrium. The step sizes for k_r and k_m were 0.5 and 5, respectively. An additional sweep was carried out with decreased step sizes of 1 and 10, respectively, to increase the investigated parameter space to the presented 4 to 12 and 10 to 60, respectively. The spaces indicated red in Fig. 6.6b represent OX, which can be seen on the left hand side in Fig. 6.6a. Less problematic OX was indicated in yellow, where bubbles are reduced in size (<10 µm) and number (<10).

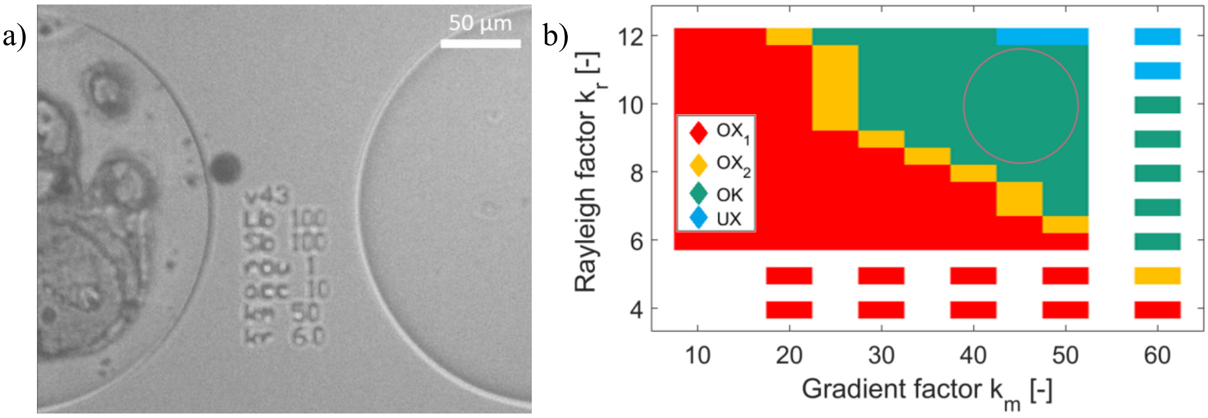

Fig. 6.6: a) Image of the live view during fabrication of the IP-Q coating structure parameter sweep including an OX (left) and an OK (right) sample, as well as structured text in-between, on a Si wafer coated with 520 nm TiAl. b) Evaluation of the Rayleigh and gradient factor results of the sweep.

The blue spaces indicate UX, where the structure detaches partly or completely, or polymerization thresholds are not achieved, see Fig. 6.6b. In comparison to the substitute substrate employed for these parameter sweeps, thermal problems due to the thin plates present on a CMUT are increased, see section 6.1. Anticipating this effect, a wide viable parameter space was selected for further fabrication attempts on chip. It is indicated by the pink circle in Fig. 2.1b. The result presented here was based on the model published in [2], which was adjusted, see section 5.4.4. The revised approach was not reproduced for the present application, as the principle was demonstrated thoroughly.

The contour and coating following approach b) with the contour, cap and subsequent flood polymerization was fabricated on a CMUT device with 400 µm aperture, see Fig. 6.7. The radius and height were set to 570 and 280 µm. The contour width, slice distance and hatch distance were set to 40, 1 and 0.1 µm. The 10x objective and the IP-Q resist were employed after ~30 minutes to reach temperature equilibrium.

As depicted in Fig. 6.7a and b, the coating covers the aperture of the CMUT die. Although a shrinkage of 2 % in height and 6 % in radius occurred, the structure does not exhibit a deformed flank comparable to Fig. 4.7d. It did not seem detached but may contain internal stress.

Fig. 6.7c shows a 90° tilted view micrograph; however, the top plane of the die was not orthogonal to the primary plane of the manual tilt stage of the SEM, which might have influence on the measurements made. Nonetheless, a 21 % height increase in the central part of the coating can be seen as evidence of the increased reflectivity of the plates. The contribution to the dose from the 400 µm aperture would have to be compensated via additional design rules. Multiple iterations of this coating were fabricated.

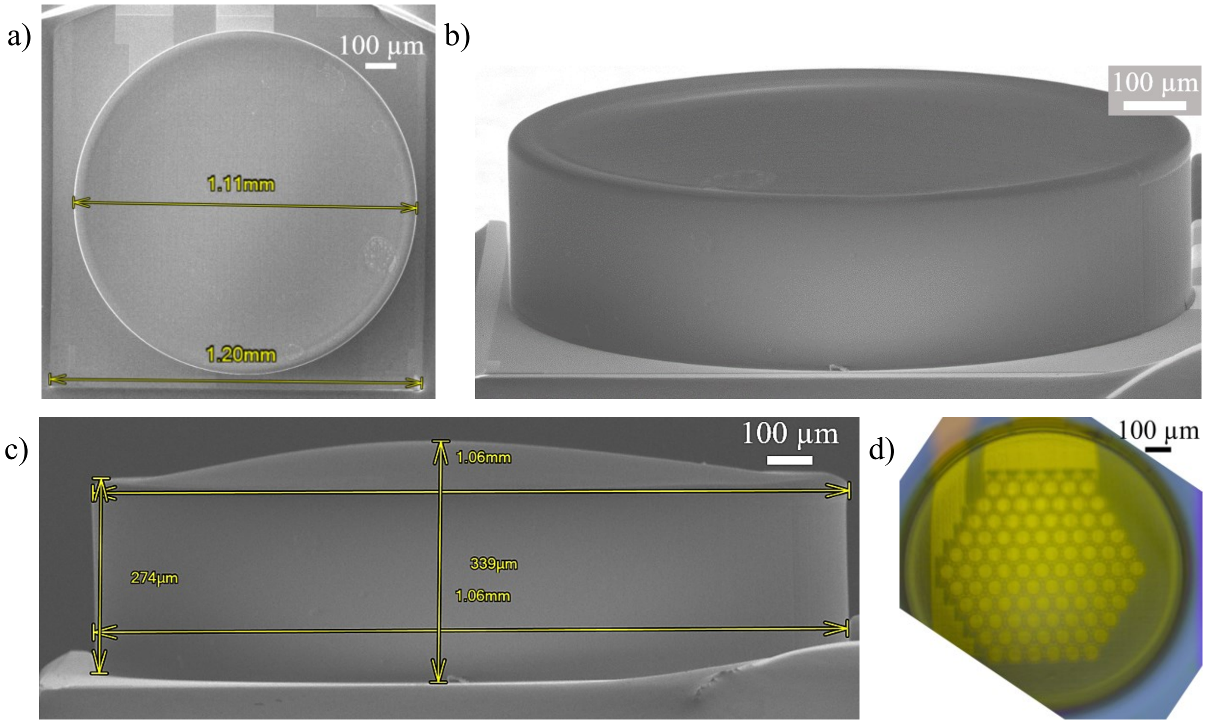

Fig. 6.7: a) Top view SEM micrograph of an example contour and coating structure fabricated using IP-Q on a 400 µm aperture CMUT, including measurements. b) 60° tilted view SEM micrograph of the same. c) 90° tilted view SEM micrograph the same including measurements. d) Top view RLM image of a CMUT with 700 µm aperture, including the same contour and coating structure fabricated on it (Image missing corners due to size and rotation corrections).

On 700 µm aperture CMUT dies, the height increase occurred stronger and even beyond the center, indicating the same correlation. An example fabricated on the 700 µm aperture is presented in the RLM image in Fig. 4.7d, where the structure appears transparent and allows the examination of the plates below. When comparing to images before TPP, the chip seems intact, see Fig. 3.1b. This issue has to be kept in mind when fabricating any structure directly in contact with or above reflective components.

The approach c) was investigated for contour structures fabricated from IP-Q, which were developed, dried and subsequently filled with IP-PDMS using syringe dispensers. Then, curing was performed using TPP with various settings on eleven specimens. However, no successful coating structure was fabricated, due to strong shrinkage effects, see annex K.

6.3 Packaging via Grating

The contour structure can also be used as a base element for further fabrication of structures. Gratings intended for packaging a chip would have to fulfill multiple requirements:

- The acoustic functionality of the chip has to be upheld, depending on the application,

- the grating has to protect the chip structurally or from contamination according to a predetermined rule, e.g. Ingress Protection Code [214].
- the grating structure itself must be structurally viable.

The latter requirement was preliminarily studied for this work by fabrication of a simple grating in a parameter sweep on surrogate substrate and subsequently on CMUT devices. The main issue with fabrication of a grating when it comes to structural viability is the requirement for overhanging structures, see section 2.3.3. When fabrication of a layer starts without supporting features like polymerized structures or the substrate, the layer can float away before it is structurally stable enough to keep its position. Although the liquid resist has a larger viscosity than water, so structures fall slowly due to gravity. The resist also has internal movement induced by temperature disparities and the moving objective, which can transfer motion into weak or floating layers. The contour reduces resist movement on its inside during fabrication, which might enable increased overhangs.

For this study, gratings were fabricated after conclusion of the contour structure at a height h_G where it overlaps with the contour, see Fig. 6.8a. Resulting from a parameter sweep comprising 450 specimen, the grating laser power and scan speed were found to produce a minimally deviating bar width d_G of (46.5 ± 0.84) µm at 50 mW and 80 mm/s.

An example contour and grating structure was fabricated on a CMUT device with 400 µm aperture, see Fig. 6.8b and c. The contour radius and width, slice distance and hatch distance were set to 570, 40, 1 and 0.1 µm. For the grating, t_G, h_G and d_G were set to 25, 235 and 50, as illustrated in Fig. 6.8a. The 10x objective and the IP-Q resist were employed after ~30 min to reach temperature equilibrium. The individual beams of the grating were fabricated one after the other, to increase the speed with which a subsequent layer connects to the previous.

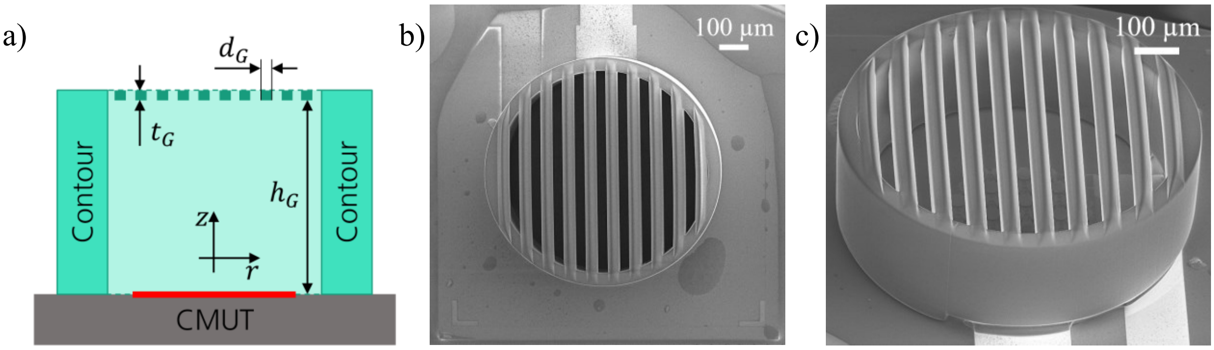

Fig. 6.8: a) Schematic of a section view of a contour and grating structure on a CMUT including aperture indicated in red, as well as the grating height h_G, thickness t_G and bar width d_G. b) Top view SEM micrograph of an example contour and grating structure fabricated on a CMUT. c) Tilted view SEM micrograph of the same, showing the plates below the grating.

Low laser power produced sagging bars in the sweep, any viable results were enlarged in t_G. This could be due to the increased power necessary to bridge the overhang. Low scan speed samples resulted in detached structures, most likely due to the inhomogeneous tension introduced by shrinkage, see section 4.4.3.

The contour and grating structure was successfully fabricated on six CMUT chips. Acoustic and protective gratings for CMUT chips are part of ongoing research which benefits from the advances presented in this section. Subsequent works need to investigate the acoustic viability of the gratings and their protective qualities.

6.4 Waveguides

Acoustic waveguides are commonly used to transmit sound. Various forms of waveguides can be distinguished [68, S. 230, 70] and could benefit the CMUT as discussed in section 1.2.1. Assuming non-curved wavefronts and infinitesimal amplitudes, the exponential waveguide can be calculated using Webster's horn equation [215]

$$\frac{\partial^2 p}{\partial z^2} + \frac{d \ln S}{dz}\frac{\partial p}{\partial z} - k^2 p = 0 \tag{6.1}$$

with pressure p, the direction of wave propagation z, wavenumber k and an exponential waveguide's cross section

$$S(z) = S_0 e^{uz} \quad \text{or} \quad r_H(z) = r_{H,0} e^{uz/2} \tag{6.2}$$

where the waveguide's radius is r_H and u modifies the exponential slope. A partial solution of equ. 6.2 results in [216]

$$p(x) = p_0 e^{-\frac{uz}{2}} e^{-izk\sqrt{1-\frac{u^2}{4k^2}}} \tag{6.3}$$

To solve for maximum pressure, the derivate of equ. 6.3 was set to 0 to find

$$\frac{dp(u)}{du} = \frac{uz}{4k\sqrt{1-\frac{u^2}{4k^2}}} e^{-\frac{uz}{2}} e^{-zk\sqrt{1-\frac{u^2}{4k^2}}} - \frac{z}{2} e^{-\frac{uz}{2}} e^{-zk\sqrt{1-\frac{u^2}{4k^2}}} = 0 \rightarrow u = k\sqrt{2} \tag{6.4}$$

Due to the high operating frequencies of CMUTs, higher order acoustic effects can have an impact on waveguide transmission, e.g., non-linearity of the medium, which is air in this case.

To maintain the scope of this study, these effects were neglected, as well as viscosity, friction, waveguide wall rigidity and roughness. Equ. 6.4 was implemented in equ. 6.2 and used to find the exponential waveguide trajectory $r_H(z)$ for CMUT devices, see Fig. 6.9a. The same schematic depicts the assembly of a contour structure to support waveguide. The former was created with adjusted parameters depending on the chip, the latter was designed in CAD and fabricated with FOV stitching, immediately following the former. The SEM micrographs of Fig. 6.9b, c and d show the contour and waveguide structure on a CMUT fabricated from IP-Q using the 10x objective, the fabrication steps can be found in annex L.
Webster’s equation is based on a waveguide of infinite height, which was reduced considering the fabrication methods [71]. The absolute height maximum was 8 mm, the range of motion of the z-axis of the TPP system. To reduce fabrication time and to prevent destruction due to the large structure being a target for destruction during handling, this height was limited to 2 mm.

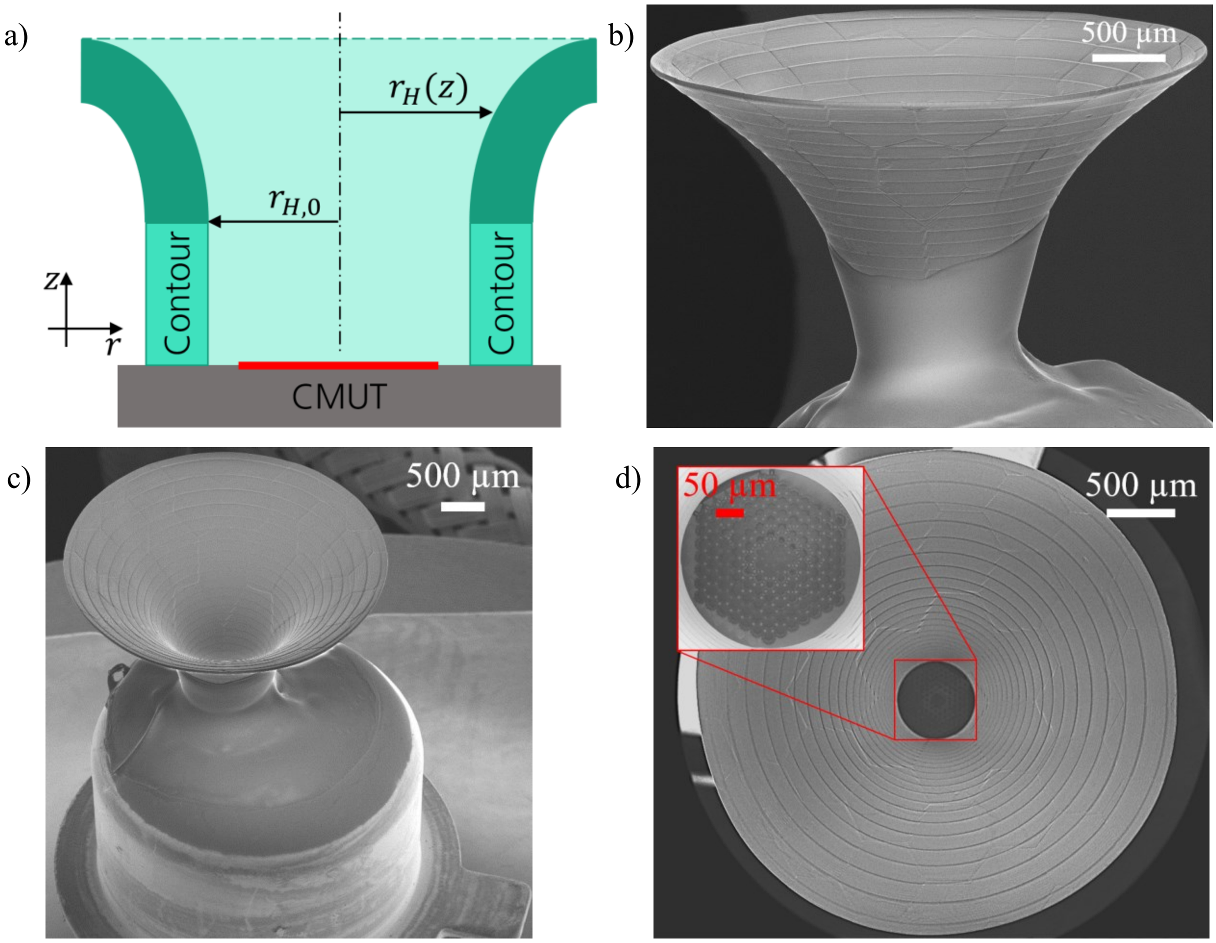

Fig. 6.9: a) Schematic of a section view of a contour and waveguide structure on a CMUT including the waveguides initial and exponential radii $r_{H,0}$ and r_H, as well as the aperture indicated in red. b) 70° tilted view SEM micrograph of a contour and waveguide structure fabricated from IP-Q on a CMUT with adhesive bonding between glob top and waveguide. c) 45° tilted view of the same with the TO-18 visible. d) Top view of the same including inset close-up of the 700 µm aperture.

This way, space was available below the waveguide`s mouth, to manually dispense the adhesive Fixogum (Marabu Beteiligungs-GmbH) for the improvement of stability during handling, see Fig. 6.9b and c. The same micrographs depict the stitching between blocks comprising the waveguide structure, see also Fig. 6.9d. The maximum of r_H was set to 2 mm in order to fit through the KMTO adapter after fabrication, which is part of the tilt compensation upgrade and shown in Fig. 5.27d. Based on these determinations, the section of the exponential curve was chosen so that a gradual transition between the straight contour to the exponentially receding waveguide was formed, which should reduce diffraction effects. The waveguide and contour thicknesses were set to 100 µm, which was found to have improved connection to the CMUT and a structurally more stable behavior during fabrication, development, drying and handling compared to a tested example with 50 µm.

The inset in Fig. 6.9d presents a close-up of the plates, which seem intact. The dark discoloration in this case is not an artifact of SEM focusing but seems to be residue from the resist or development agents.

6.5 Findings on the Reliability of Two-Photon Polymerization Lithography on the Capacitive Micromachined Ultrasonic Transducer

To initiate this section, the general circumstances and the approach followed in its subsequent parts are explained at an example. Furthermore, hypotheses are proposed and generalizations for the subsequent investigations are explained. Then, the impact of individual treatments applied during TPP processing is presented. After that, the on-plate fabrication and its effects on the CMUT are discussed, both subsections consider the electrical behavior of the chip. Then, the acoustic characteristics of CMUT devices with waveguides fabricated via AMOC are investigated. Lastly, the findings are compared to the hypotheses and viable implications as well as prospective works are proposed.

6.5.1 Reliability Investigation Approach & Hypotheses

During TPP processing – including additional pre- and postprocessing steps – on an assembled CMUT chip, the die, bond wires, glob top and TO-18 can come into contact with liquid resist materials and development agents. During these processes, contaminants from the bonding and packaging processes can get agitated by liquid substances. Chemical reactions like corrosion, as well as particles and residues spawned by wear, or by the employed processes and materials could impact the chip's functionality. After the development process, the drying of resist materials and development agents can leave residual contaminants on the substrate, which could affect it as well. The thermal load, especially of pre- and postprocessing treatments, could also interfere with the regular operation of the chip.

The microscopy images depicted in Fig. 6.10 were recorded before and after a CMUT received its treatment. In this example, the chip was handled, a drop of IP-Q was manually applied,

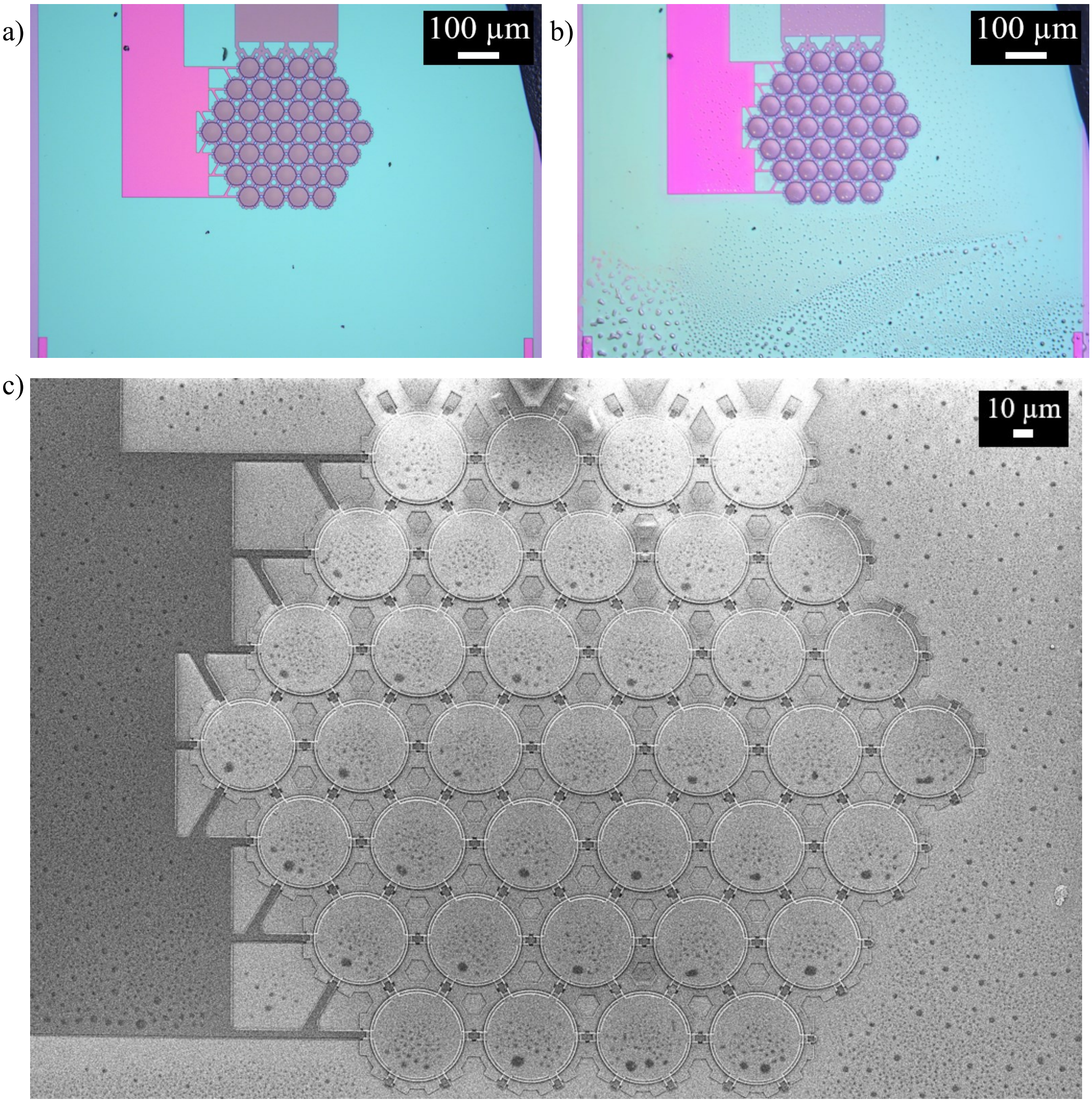

Fig. 6.10: a) Top view RLM image of an untreated CMUT with 400 µm aperture including unwanted particles. b) Top view RLM image of the same CMUT successively treated with resist IP-Q for 10 min, IPA for 20 min and NOVEC for 20 min including most of the same particles, as well as dried drops of residual materials. c) Top view SEM micrograph of the same chip showing various sizes of dried drops of residual materials on individual plates.

compare annex A. The resist was left on the chip for 10 min, and subsequently developed in a 20-minute bath of 60 ml of IPA and NOVEC each. Then the chip was dried as described in section 2.3.4. No other processes nor fabrication was performed on it. Handling entails the manual pick and place of the assembled chip using electrostatic-discharge-safe materials and tools. The particles on the untreated CMUT shown in Fig. 6.10a most likely originate from packaging materials for transport. The particles remain on the chip even after the treatment, see Fig. 6.10b. The image shows many drop-shaped entities of various size remaining after the drying process. Even after weeks of storage, these residual materials do not disappear.

The distribution seems to increase towards the bottom. The micrograph depicted in Fig. 6.10c shows a close-up of the treated CMUT surface and reveals the condition of the plates. Many entities exist per plate with varying size and shape. Similar to Fig. 6.10b, the distribution density seems to increase towards the bottom of the image, which is most likely due to the assembled chip being stored lying on its side during drying.

Using the methods described in section 3.1.3 and 3.1.4, a treated CMUT can be examined, and its characteristics can be compared regarding their status before and after a treatment. The resistance and capacity measurements of an example chip treated the same way as the one illustrated in Fig. 6.10 is depicted in Fig. 6.11. The influence of the successively applied liquids can be seen in Fig. 6.11a, where the resonance peak reduces in resistance by 50 % and slightly increases in FWHP by 3.5 % from before (Pre) to after (Post) the treatment. The standard deviation recorded for the measurement setup including the evaluation method revealed a prominence and FWHP error of 6.05 and 0.74 %, respectively, see section 3.1.3.

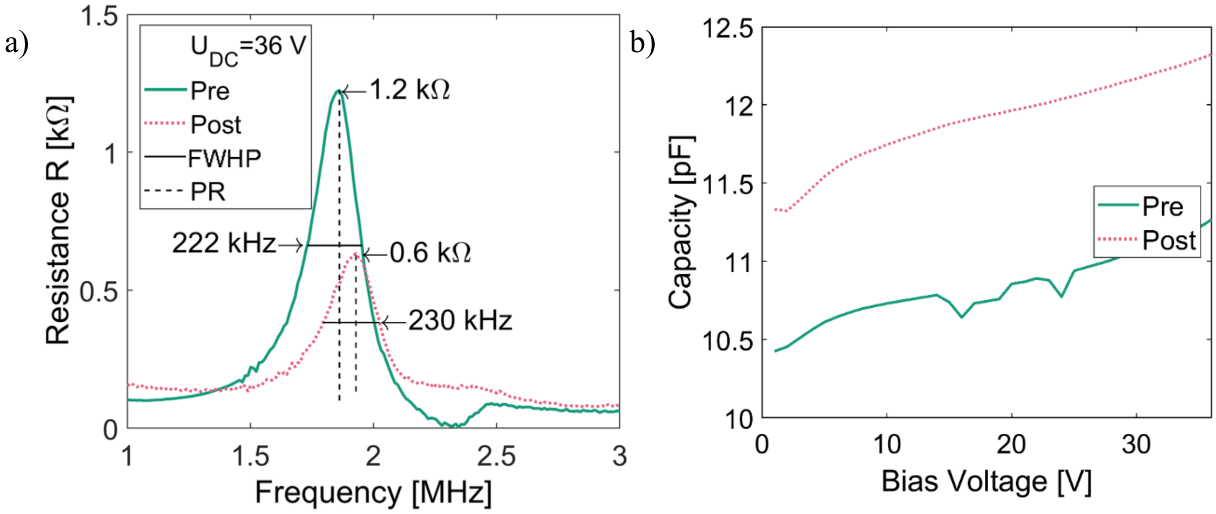

Fig. 6.11: a) Resistance vs. frequency plot of a CMUT before (Pre) and after (Post) a treatment with IP-Q for 10 min, IPA for 20 min and NOVEC for 20 min, including prominence (PR) and full width at half prominence (FWHP) indicators. b) Capacity vs. bias voltage plot of the same chip.

Both effects are larger than the measured deviation, meaning they could be results of the treatment.

The main hypothesis A proposes that the residual material left by the resist and development agent after drying causes these alterations. The additional mass of the residue could lead to a change in the effective mass of the plate and thus affect the dynamic behavior. The stochastic development and drying processes do not leave a uniform coating, but rather unequal droplets most likely with varying resist-to-development-agent-concentrations. Thus, the uniformity of the effective mass of the plates is altered, resulting in a less uniform, more distributed resonance frequency per plate. Due to the distribution, the combined resonance peak reduces in height and the FWHP widens.

The positive frequency shift of the resonance peak in Fig. 6.11a of 3.2 % was not expected. The frequency drift during long term storage of CMUT chips was determined in Fraunhofer IPMS internal studies for 46 CMUT chips to be (-1.49 ± 1.91) % after ~28 months [217]. A deviation calculated for the location of the frequency peak of 0.34 % was determined for the chips employed here, see section 3.1.3. Residual materials from resist or development agents contributing to the effective mass of the plate along hypothesis A would expectedly decrease the frequency, see equ. 3.3.

The effect might be explained by hypothesis B: the electrical measurements were not performed in a temperature-controlled environment. A decreased temperature during the second compared to the first measurement could lead to an increased Young's modulus of the plate [218], thereby increasing plate stiffness, resulting in the positive shift, see equ. 3.3.

Another explanation is proposed in hypothesis C: the resist within the residual contaminants polymerizes in environmental UV light received by the chip after leaving the wavelength controlled TPP laboratory, e.g., on the way to the microscope. By this effect, the effective plate stiffness could increase, leading to the positive frequency shift.

As the main goal of the electrical characterization was the comparison of chips before and after various treatments, the qualitative approach based on the Signal Processing Toolbox was suitable. However, any plate damping effects can affect this comparison, e.g. radiation into the surrounding medium, radiation into the substrate, the squeeze film damping of the air inside the cavities of unsealed devices, the heat loss by conduction and convection because of air compression as well as the heat loss by conduction through the plates caused by internal friction [154]. These effects would decrease the resistance peak with increasing frequency, compare term 3 of eq. 3.1. The contribution to the resistance from damping due to the frequency shift could be evaluated by modeling of the plate behavior including stiffness moderation to fit the behavior of effects, e.g., from residues or temperature. As measurement errors are similar in scale to the shifts found in this work, the contribution from damping effects was neglected. Furthermore, the frequency shifts measured here are similar in scale to the long-term measurements mentioned earlier and negligible when compared to the generally large resistance offsets including their strong deviations.

The capacity measurements depicted in Fig. 6.11b can be seen as qualitative, as the absolute capacity depended on partly flexible connection cables used in the experimental setup, which changed with each calibration. For twelve similar specimens, the capacity at maximum bias voltage changed (43.1 + 75.6) % from before (Pre) to after (Post) the treatment. The issue was eliminated by using fixed connections for all subsequent measurements, resulting in a standard deviation of the capacity of 0.52 %, see section 3.1.3. The capacity drift during long term storage of CMUT chips was determined in Fraunhofer IPMS internal studies for 42 CMUT chips to be (5.1 ± 7.6) % after ~22 months [217].

The upward gradient of the capacity, however, resembles the expected increase in capacity with increasing bias voltage and can indicate that the plates remain movable. The flexible plate deflects and gets closer to the static plate, which increases the capacity, see equ. 3.5. The quartic plate deflection w discussed in [155] produces a likewise nonlinear capacity response. As the total range of deflection was not accessed by a bias voltage U_{dc} of 0 to 36 V used in the capacity measurements, only a seemingly linear section of the response appears in Fig. 6.11b. The voltage was limited to prevent pull-in events, see section 3.1.1.

To complete the set, the last hypothesis regards chips that receive treatments that induce thermal changes larger than room temperature fluctuations, e.g., plasma activation and UV flood illumination. Hypothesis D proposes that such treatments might influence the plate behavior via thermal annealing. Stresses from wafer-level fabrication processes might be reduced, see equ. 3.3. This effect might also lead to resistance reductions, FWHP alterations and peak frequency shifts, as the stress individual plates receive during fabrication and subsequently loose with the thermal annealing might not be uniform. Furthermore, reduced stress would allow the electrodes to converge at a lower electrostatic force, resulting in an increase in capacity.

6.5.2 Treatments Applied During the Fabrication Process

To gauge the effects induced by the treatments necessary for fabrication using TPP, further experiments were conducted on CMUT chips. The following treatments were commonly performed for TPP and were tested individually for this study:

- Base treatments
    - Handling, as if fabrication via TPP were conducted, including manual transport and contact with clamping systems as well as the tilt compensation upgrade. All while in electrostatic discharge safe environment and without contact to liquids.
    - O_2 plasma treatment, 3 min, see section 2.3.2.
    - 20 min IPA bath
    - 20 min PGMEA bath
    - 20 min NOVEC bath
    - IP-Q, 20 min IPA bath
    - IP-PDMS, 20 min PGMEA bath
    - IP-Q, IPA 20 min, NOVEC 20 min
- Fabrication in the vicinity of plates
    - IP-Q, fabrication of a contour & grating structure, 20 min IPA bath, see section 6.3.
    - IP-Q, fabrication of a contour & waveguide structure, 20 min IPA bath, see section 6.4.
    - IP-Q, fabrication of a contour & waveguide structure, 20 min NOVEC bath, see section 6.4.

The application of two drops of resist was performed manually, see section 2.3.2 and annex A. The resist was left for 10 min, then the chips were carefully placed in development baths, which were refreshed for each treatment and contained 60 ml of the respective substance.

Each chip was characterized before and after their respective treatment. The comparison between these measurements is illustrated in Fig. 6.12 and based on the resonance peak attributes described in section 3.1.3. The characteristic changes illustrated in the figure are listed in the following.

- The resistance offset – the total peak height difference between pre and post treatment.
- The resonance shift – the difference in peak location on the spectrum.
- The prominence alteration – the change in intrinsic peak height relative to the surrounding resistance level.
- The FWHP alteration – the change in peak width at half prominence.

Each treatment was carried out on multiple chips, indicated by the numbers before the respective legend entries in Fig. 6.12c and f. The standard deviation between measurements is indicated via error bars. The comparison was made using percentages, with the basic value at zero, indicated by a red cross.

The effects of the base treatments, e.g. handling, development and resist application, are shown in Fig. 6.12a and b, with their legend in Fig. 6.12c.

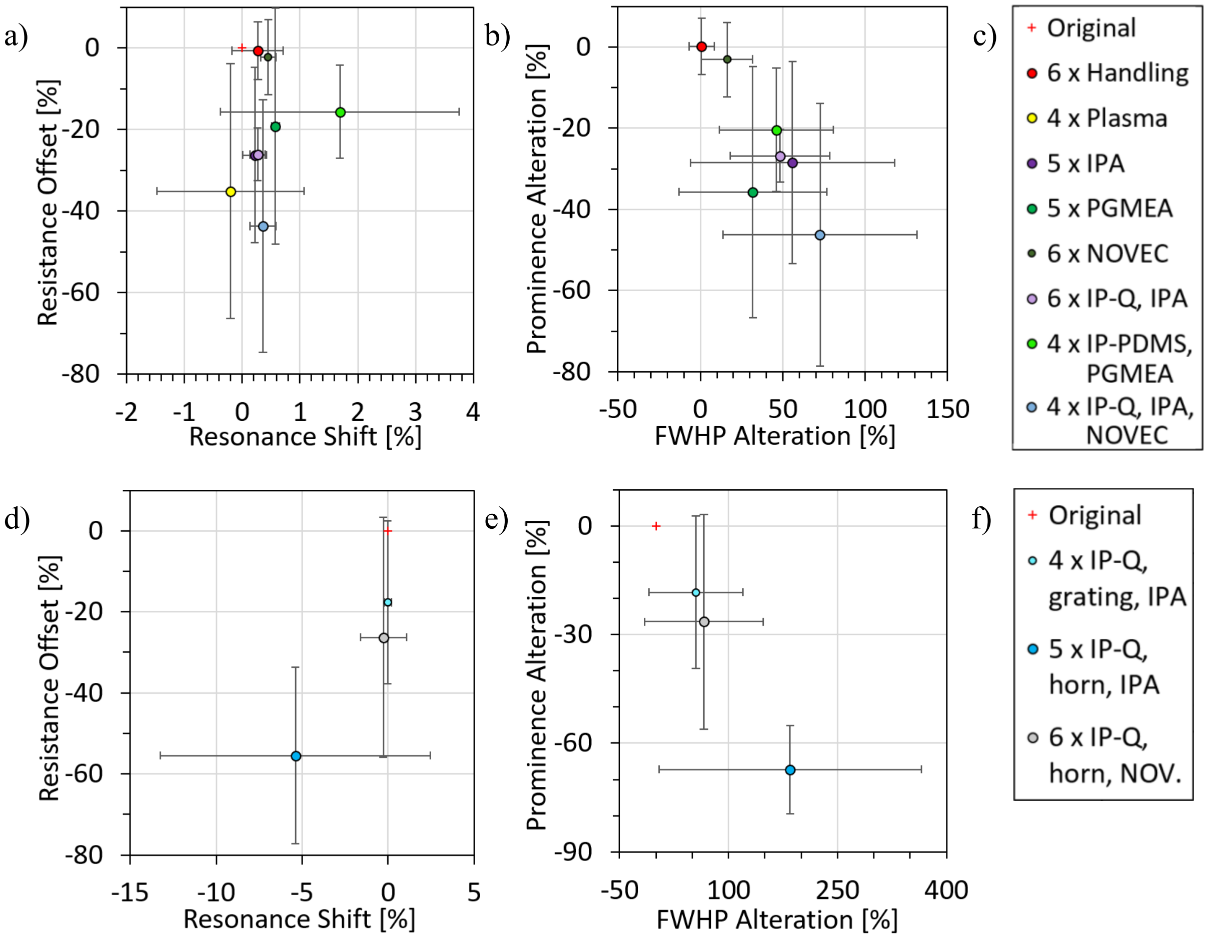

Fig. 6.12: a) Resistance offset vs. resonance shift of CMUT chips that underwent various treatments. b) Prominence alteration vs. FWHP alteration of CMUT chips that underwent the same. c) Legend to a and b, including respective number of chips. d) Resistance offset vs. resonance shift of CMUT chips that had structures fabricated on them. e) Prominence alteration vs. FWHP alteration of the same. f) Legend to d and e, including respective number of chips.

For the handling chips, an average resonance frequency shift of (0.27 ± 0.44) % was recorded for 6 chips, which is lower than the established 0.34 % peak frequency measurement and evaluation error. The FWHP and resistance of the handling chips were slightly altered by (0.75 ± 7.71) % and (0.14 ± 7.01) %, respectively. The hypotheses for a positive shift and the other alterations as well as standard deviations were discussed in section 6.5.1.

The chips that received the plasma activation treatment exhibit the - of the group of base treatments – strongest negative shift in resonance with strong deviation. Their FWHP alteration of (210 ± 301) % was too large to fit the plot in Fig. 6.12b. See hypothesis D in section 6.5.1.

The use of developing agents IPA, PGMEA and NOVEC led to dissimilar outcomes. IPA and PGMEA exhibit similar effects on CMUT resistance, the former more than the latter with an average offset of (-26.25 ± 21.53) % and (-19.2 ± 28.9) %, respectively. The NOVEC treatment did not have drastic effects on the resistance with (-2.26 ± 9.23) %, it also seems to be the most effective in leaving the chip without residual material, as found in SEM investigations, compare

Fig. 6.10. Similarly, the effects of the developing agents on FWHP are stronger for IPA and PGMEA, than NOVEC, indicating (55.8 ± 61.8) %, (31.9 ± 44.9) % and (16.2 ± 15.6) %, respectively.

The development of CMUT chips that had resist applied to them results in similar changes to the attributes. The prominence and FWHP alterations of IP-Q developed using IPA and IP-PDMS developed by PGMEA lie within the ranges found for chips exclusively treated with IPA and PGMEA.

Developing IP-Q using IPA and subsequently NOVEC shows an unexpected result. The performance of NOVEC by itself was only found to cause a resonance shift. In combination with IP-Q and IPA, all other attributes were found to have worsened, especially the FWHP and prominence alterations were the strongest found for the base treatments. The treatment even surpasses development of IP-Q using IPA, which was not expected.

The frequency shift found for IP-PDMS developed by PGMEA was the strongest in positive direction found for the whole study with (1.69 ± 2.07) %. The difference to PGMEA by itself and IP-Q developed by IPA (and NOVEC) could be due to the different resist formulation, see section 2.3.5 and annex B.

The effects of fabrication in the vicinity of the plates led to results comparable to the base treatments, see Fig. 6.12d and e as well as the legend in Fig. 6.12f. As the structures obstruct the developing agents during mixing and evaporation, more residual material and thus larger changes were expected.

For fabrication of contour and waveguide structures with IP-Q and development using IPA, a prominence loss of (-67.2 ± 12.2) % was recorded, compared to the (-28.5 ± 24.9) % when exclusively treating a chip with IPA. The former also shows a negative resonance shift of (-5.39 ± 7.84) % compared to positive (0.21 ± 0.21) % of the latter. The difference of prominence loss between waveguides developed using IPA and NOVEC with (-26.5 ± 29.7) % might be due to the superior developing qualities of the latter, e.g. lower viscosity, see Fig. 6.12e.

When comparing the NOVEC treatments with and without waveguide depicted in Fig. 6.12b and e, the actual effect of the waveguide might be perceived. However, the FWHP alterations of the grating and waveguide structure are very similar, which leads to believe the waveguide's effect cannot be extracted here. Furthermore, comparing the waveguide with the grating, both developed by identical agents, one could conclude that the effect of the structure hindering the evaporation is more significant than the acoustic effects themselves.

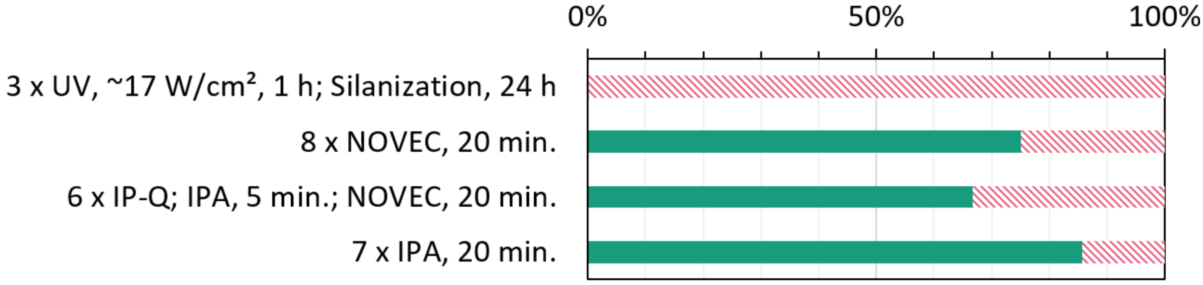

Fig. 6.13: Functional (green) to non-functional (red, hatched) proportion of chips that received respective treatments, including count.

The quasi-static capacity at maximum bias voltage of 33 chips that received a base treatment was increased by (3.3 ± 2.9) %, excluding shorted specimens. For the 14 chips with structures fabricated on them, it was (4.2 ± 4.2) %. Capacity measurements and evaluation were subject to a standard deviation of 0.49 %, see 3.1.3. Both values are within expectations set by the long-term storage discussed in section 6.5.1.

The change of the gradient of capacity over bias voltage from before to after the treatments does not have a significant correlation with any group of chip treatments, except plasma activation. A change of the capacity gradient from before to after the respective treatment of (-11.6 ± 18.0) % was evaluated for 43 chips, the four treated with plasma resulted in (23.8 ± 5.28) %. The strong difference could be explained by hypothesis D, see section 6.5.1.

A proportion of the chips treated in the experiments of this section were found non-functional during characterization, see Fig. 6.13.

The chips treated with UV activation and silanization were found non-functional in the electrical characterization. The UV treatment might have destroyed the chip via thermal strain. The other three treatments resulted in lower proportions of non-functional chips in the electrical characterization. The prevalent hypothesis for their destruction is user handling error during transport or treatment, resulting in electrical shorting.

6.5.3 Fabrication of Structures with Direct Contact to the Active Element

The electrical characterization of a CMUT at a bias voltage U_{dc} of 36 V depicted in Fig. 6.14 was measured before and after it received its treatment of handling and fabrication of a contour and coating structure. The latter entails a drop of IP-Q was manually applied, a structure similar to the one depicted in Fig. 6.7 was fabricated and then developed in a bath of IPA for 20 minutes. The resistance plot in Fig. 6.14a presents a resonance at 1.85 MHz before the treatment (Pre), but no peak afterwards (Post), even when examining the total recorded spectrum of 50 kHz to 20 MHz. The resistance is increased, more so at lower frequencies.

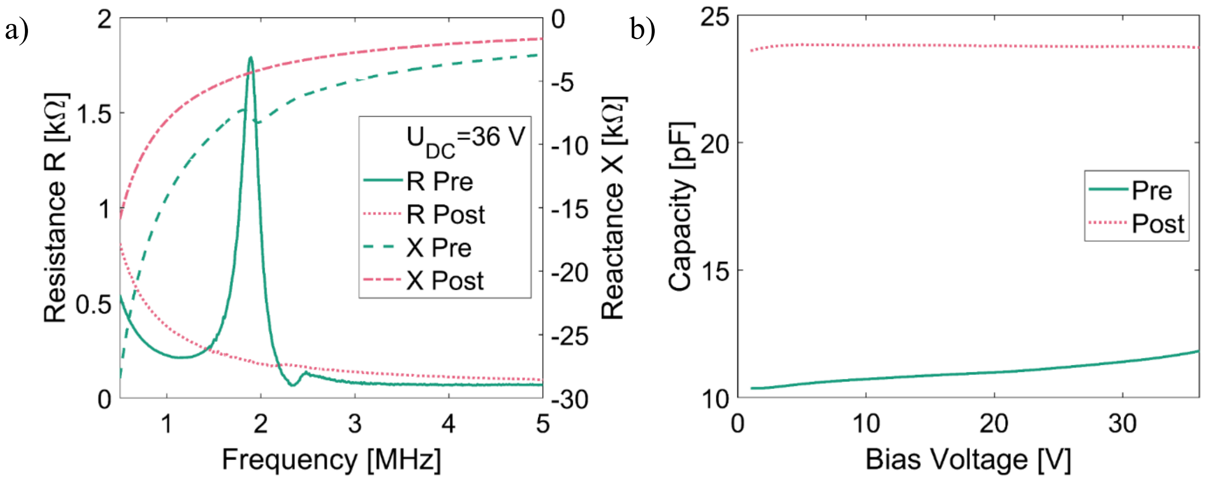

Fig. 6.14: a) Resistance and reactance vs. frequency plot of a CMUT pre and post fabrication of a contour and coating structure with direct contact to the plates. b) Capacity vs. bias voltage plot of the same chip.

The reactance depicted in the same plot is also increased and exhibits no downward slope where the resonance would be expected. The capacity is strongly increased by an average 44.8 %, see Fig. 6.14b. The expected rising slope is nonexistent. The constant capacity indicates, that even by increasing the bias voltage, no quasi-static movement of the flexible plate closer to the electrode can be observed at reasonable voltages.

These results indicate that the plates of the chip do not move after the treatment. This might be due to the effects of the coating structure on the plates of the CMUT. Assuming the plate's effective flexural stiffness and its effective mass change, so would its resonance, see equ. 3.3. As there is no resonance, the changes could have moved it out of bounds of the measurable, or the plate could have become overdamped.

Twelve specimens with various coating structure settings were examined as illustrated by the example in Fig. 6.14, with direct contact between their plates and coating of IP-Dip or IP-Q fabricated via TPP or UV flood polymerization. Their resulting characteristics were almost identical, with no resonance peak and constant capacity, indicating no plate movement.

Further testing of direct contact fabrication was conducted on CMUTs by drop application of IP-PDMS and subsequent UV flood polymerization, see annex M. In total, 22 chips received the resist via manual drop application. Various preprocessing treatments were applied beforehand, see section 2.3.2. The settings are listed in Tab. 6.1, where the functionality after the polymerization is noted as well. The UV treatment was performed with the exit of the light guide at a distance of 8 cm from the specimen. The noted intensity represents the value of the exit of the source given by the manual. The plasma treatment was carried out at maximum power, see section 2.3.2.

Tab. 6.1: Manual drop application of IP-PDMS on CMUT chips and UV flood polymerization.

Amount	Preprocessing	Resist [mg]	UV [min]	UV [W/cm²]	Resonance peak
9	None	2 x (6.28 ± 0.7)	3	~17	No
4	Plasma treatment, 3 min; Silanization, 1 h	2 x (6.28 ± 0.7)	3	~17	No
3	None; Heat treatment after resist application, 100 °C, 5 min	2 x (6.28 ± 0.7)	3	~8.5	No
1	Plasma treatment, 3 min; Silanization, 1 h	2 x (6.28 ± 0.7)	3	~8.5	No
2	Plasma treatment, 3 min; Silanization, 1 h	1 x (6.28 ± 0.7)	3	~8.5	Yes
3	Silanization, 1 h	1 x (6.28 ± 0.7)	3	~8.5	Yes

The chip functionality was determined using the electrical characterization setup. All of the 22 specimens exhibited increasing capacity with bias, suggesting quasi-static plate movement. The five specimen that received a reduced volume of resist demonstrated a resonance peak. They were coated with a lower amount of IP-PDMS and showed a capacitance change of (0.05 + 0.14) %, a resonance shift of (0.48 ± 0.21) %, a resistance offset of (-0.59 ± 3.17) % and a FWHP alteration of (3.42 ± 3.22) %. The other 17 chips exhibited a capacity at maximum bias voltage pre- to post-treatment change of (3.05 ± 1.09) %.

The dominant hypothesis to explain the non-functionality of the chips that received the thicker layer is, that the additional volume results in higher tension due to resist shrinkage, which could prevent the dynamic plate movement.

A combination of an IP-Q contour structure and a subsequent coating fabricated from IP-PDMS using TPP was tested in 39 variations, see annex K. However, the material was not suitable, due to strong shrinkage effects. These might be reduced by increasing the exposure dose, but at the scale of the 10x objective, the viable maximum was reached. A different resist formulation including higher concentrations of photoinitiator and monomer might be suitable for this setup.

6.5.4 Acoustic Characterization of Chips with Waveguides

A total of 27 CMUT chips were prepared for waveguide fabrication. As with all other chips of this work, they received an initial electrical characterization. An initial acoustic characterization was performed on 16 of them. Six were destroyed due to user handling error and design faults of the acoustic characterization setup. Two were destroyed during fabrication via TPP due to programming errors. A total of 19 CMUT chips were successfully equipped with contour and waveguide structures following the directions provided in section 6.4.

Subsequent acoustic characterization revealed 13 as non-functional, due to user handling error and design faults of the acoustic characterization setup leading to electrical shorting.

Of the remaining six functional chips, only one received the initial acoustic characterization. The other five received an additional acoustic characterization after the waveguide structure was removed from the chip, while remaining placed within the mount of the measurement setup, see Fig. 3.3a. This additional characterization was successfully performed on all five.

The distance and radial scan results depicted in Fig. 6.15a, b and c originate from the measurements performed on five of the six remaining chips, all with an aperture of 700 µm. The results of the other 400 µm aperture chip of the is shown in Fig. 6.15d. For comparison, four more initial acoustic characterizations of 700 µm aperture CMUTs were performed and can be found in Fig. 6.15a, b and c, indicated by “Pre”.

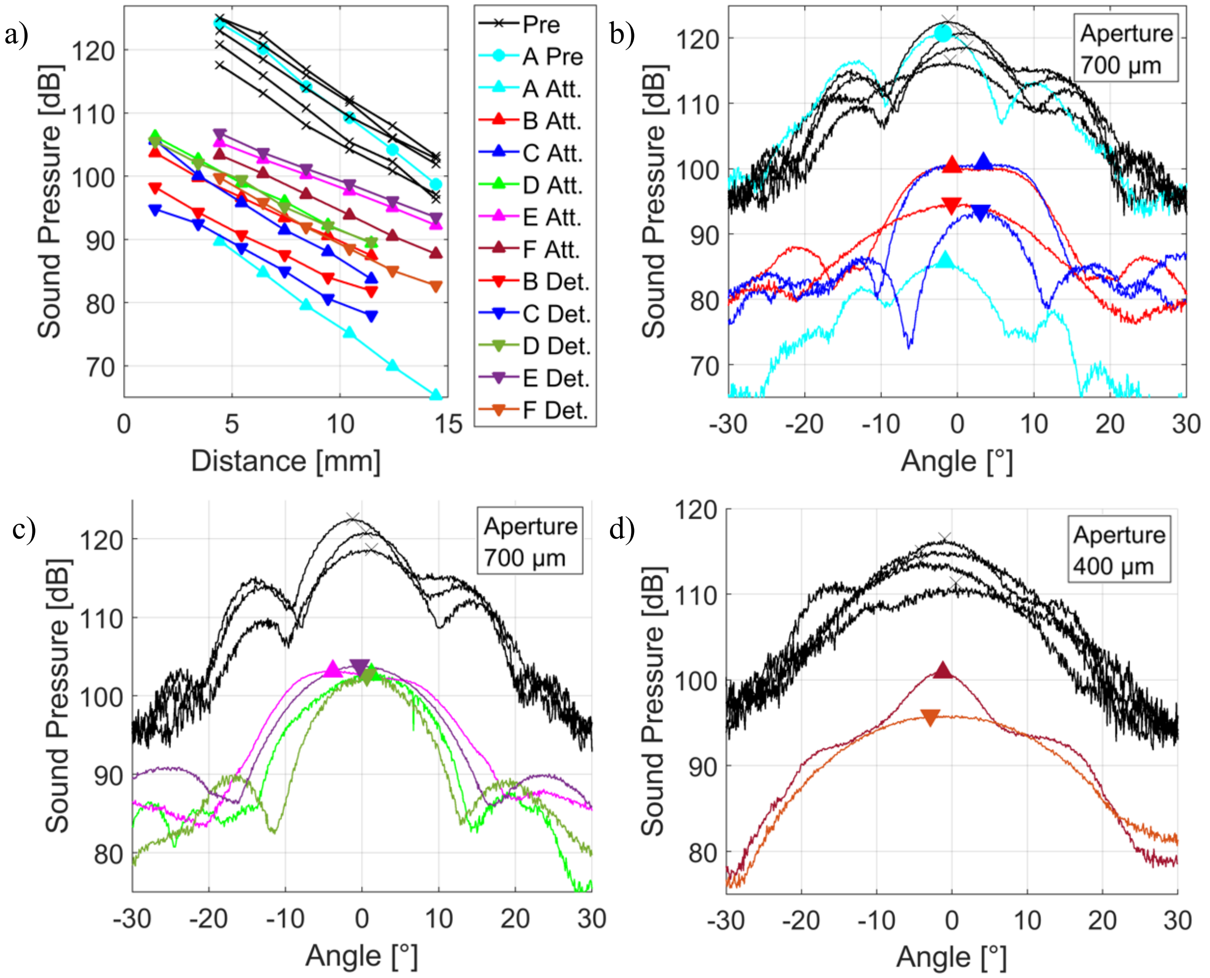

Fig. 6.15: a) Distance scan of the 0° angle of CMUTs with 700 and 400 µm aperture before fabrication of a waveguide (Pre) and versions indicated by A to F with waveguide attached (Att.) and detached (Det.). b) Radial scan of the sound pressure of the 700 µm chips A, B and C, as well as four unprocessed 700 µm chips for comparison, for legend, see ‘a’. c) Radial scan of the sound pressure of the 700 µm chips D and E, as well as four unprocessed 700 µm chips for comparison, for legend, see ‘a’. d) Radial scan of the sound pressure of the 400 µm chip F, as well as four unprocessed 400 µm chips for comparison, for legend, see ‘a’.

Similarly, four comparison characterizations of 400 µm aperture CMUTs were performed and are depicted in Fig. 6.15d.

The only chip characterized pre- and post-fabrication, denoted “A”, illustrates the overall result of this study. In the distance scan in Fig. 6.15a, the pre-TPP sound pressure is comparable to the comparison chips. After fabrication of the waveguide, the chip suffered strong losses in sound pressure. The radial scans in Fig. 6.15b show a similar result, the overall pressure was drastically reduced after fabrication, and no significant effect on the width of the main lobe can be asserted.

The chips indicated “B” and “C” present results after fabrication of the waveguide for the attached and detached state of the waveguide, indicated “Att.” and “Det.”, respectively, see Fig. 6.15a and b. The overall sound pressure of both conditions is lower compared to the pre-TPP examples. However, the comparison between the conditions illustrates, that the attached waveguide seems to improve the sound pressure of the main lobe. The samples with detached waveguides show strong deviation in the width of the main lobe, however, it is not consistent.

The similarly treated chips, indicated “D” and “E”, however, do not show the same result, see Fig. 6.15a and c. Their distance scans overlap almost completely and exhibit no difference between attached and detached waveguide, see Fig. 6.15c. The only 400 µm aperture chip, indicated “F”, shows similar results to “B” and “C”, see Fig. 6.15a and d. Although the overall sound pressure was strongly decreased compared to before fabrication, the main lobe produces a higher pressure with the attached waveguide, compared to when it was detached.

The CMUTs that received waveguides fabricated using TPP loose performance, which could be explained by hypothesis A, see section 6.5.1. The difference between chips with their waveguides attached and detached could also originate from damage to the chip suffered during the detachment process, which could explain the width deviation of the main lobe for samples “B” and “C”. Another hypothesis is, that the waveguide equations discussed in section 6.4 do not incorporate high frequency acoustical effects, leading to reduced waveguide efficiency. The deviations found for the measured sound pressure and distance between chip and detector d_{CD} including remounting of the chip were ±0.44 dB and ±0.63 mm, respectively, see section 3.1.4. The established hypotheses of this section do not alter when including these error margins.

To find conclusive proof of these hypotheses, the number of studied specimens must be increased, the effects of TPP processing in the vicinity of plates must be reduced and the handling and acoustic characterization issues must be sorted out in an upcoming study. Prospective works should consider the implementation of topology optimization for the design of the waveguides, as was presented for gratings in [15].

6.5.5 Reliability Discussion

The fabrication of structures via TPP with direct contact to the active element of the CMUT was found to disable the chips investigated in this work. A recommendation for further studies includes the use of resist materials with reduced stiffness and shrinkage.

For the chips without direct structural contact to the plate investigated in this reliability study, the frequency shift of the resonance from before to after a treatment was found insignificant for almost all treatments. Exceptions were posed by the treatments with IP-PDMS and plasma, as well as chips with waveguides, where shift margins exceed 1 %. As proposed by hypothesis D, the performance alterations of the thermally significant plasma treatments were most likely due to non-uniform stress relief within the plates. The shifts induced by treatments with IP-PDMS and waveguide fabrication could be explained by hypothesis A, see section 6.5.1.

The predominantly positive shift found for the other treatments was small compared to measurement deviations. However, its reversed sign compared to long term measurements indicates an effect, which could be explained by hypotheses B and C, see section 6.5.1.

Strong resistance offsets and prominence alterations >15 % were found for all treatments excluding the development agent NOVEC. The prevalent hypothesis A proposes residual resist and/or solvent material remaining on the plates, leading to a change in their effective mass and thus affecting their dynamic behavior. The processes proposed by hypotheses B and C could contribute to the effect. The effects were found stronger for specimen that underwent fabrication of structures via TPP in the vicinity of the aperture, most likely due to reduced effectivity of the development process, leading to increased amounts of residue on the plates.

Strong FWHP alterations were found for all treatments – excluding handling – at >15 %, indicating a stochasticity in the processes proposed by the hypotheses. Especially the drying step and the thermal annealing seem to non-uniformly affect individual plates, resulting in the wide distribution of resulting individual plate resonances.

The capacity of the treated chips was altered with no clear correlations, leading to inconclusive results. The only exclusion is the annealing via plasma treatment, which resulted in an increased gradient of capacity over bias voltage that could be explained by the effects proposed in hypothesis D.

A contribution from fringe or parasitic capacity of residues is most likely not a factor, as both PGMEA and IPA have very low conductivity compared to TiAl and NOVEC is nonconductive, see section 2.3.4. However, to evaluate the contribution, simulations of the electrical fields should be compared to a larger set of specimens with increased control over residue amounts. The same seems valid for corrosion, as all solvents are noted as non- or low-corrosive versus the wafer-level employed materials, see section 2.3.5. Optical investigations corroborate this assessment, no structural damage was found for the treated chips, see Fig. 6.10. However, damage below the residual materials or uniform damage across the chip could evade optical investigations. Focused ion beam milling could be employed to find such effects, as well as help estimate the residue contents and volume.

The most promising development agent seems to be NOVEC. However, it is not conclusive due to the findings for the agent in combination with resist materials. Notably, a comparably large contingent of chips treated with this agent were destroyed during characterization.

In general, the stochasticity of the resist application, development and drying processes resulted in strong deviations for almost all findings. To reach conclusive results, parameters that influence these processes, like development time, agent concentration and drying temperature should be studied individually, requiring much larger sample sizes. The scalability of the experiments presented in this section suffers due to the usage of assembled chips. By employing wafer-level tests or even diced sections with large quantities of individual chips, these problems could be overcome. For this work, the access was limited to the presented specimens.

Prospective works should replace the development and drying process employed in this work – see section 2.3.4 – by the use of the supercritical drying method, which was presented for CMUTs in [219, 220]. At the cost of increased complexity, the amount of residual material left on the specimen and the stochastic effects of the method employed here could be reduced.

7 Investigation & Reliability of Two-Photon Polymerization Lithography on Nanoscopic Electrostatic Drive Based Systems

In the following chapter, AMOC is presented for the NED-µPS based on the advances made in previous chapters to prepare the TPP system used in this work. Of the application examples of AM using TPP for NED based systems proposed in section 1.2.2, the fabrication of structures on chip is presented for end effectors. Furthermore, the requirements and reliability of the fabrication and the subsequent effects of the process on the chip are evaluated for the presented examples.

Section two comprises the investigation of microchannels for the implementation in microfluidic applications based on NED actuators. The fabrication of such channels is shown for the recently added IP-PDMS including the presentation of the smallest channels fabricated so far. Furthermore, the critical development of microchannels was investigated. For this purpose, a new method for the examination of the penetration depth for microchannels fabricated via TPP was devised and presented.

7.1 End Effector Structures

7.1.1 Gear Drive

End effector structures as described in section 1.2.2 can be directly fabricated via TPP on the NED-µPS, see Fig. 7.1.

An end effector for the NED-µPS was designed by Prashanth Akkal Devi and Shashank for demonstration purposes. It consists of a 3 mm tall pin with an approximately 500 µm diameter and a 1 mm diameter ball on top including gearing tracks. The latter were added to increase traction on a gear, which this end effector was designed to rotate.

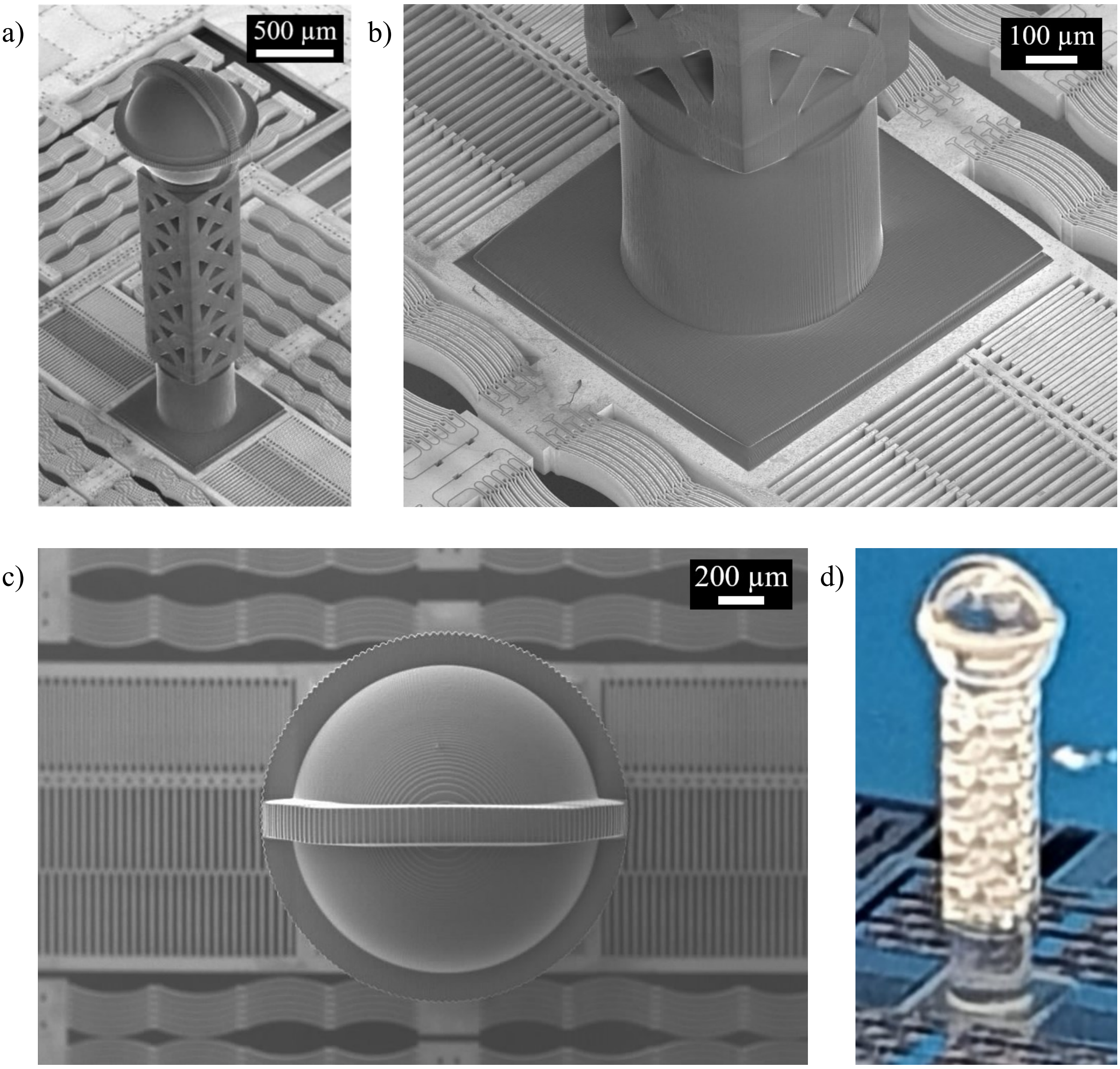

Fig. 7.1: a) Tilted and rotated SEM micrograph of a NED-µPS with an end effector fabricated from IP-Q on its load area using TPP. b) Close-up of the same. c) Top view of the same. d) Photo of the same, including reflective artifact from the substrate to the left of the structure.

The design was prepared for fabrication based on the AMOC know-how described in the previous chapters, including a 900 x 900 x 50 μm^3 base. The structure was fabricated from IP-Q using the 10x objective on a NED-µPS chip directly, see Fig. 7.1. The base feature depicted in Fig. 7.1b shows deformation due to shrinkage, which entails inherent stress within the structure. The top view shown in Fig. 7.1c depicts the gearing required for the subsequent demonstration application. The photo of the structure illustrates the appearance of the structure see Fig. 7.1d.

7.1.2 Additional Preprocessing

The flexible NED cells and thus the load area were able to move during fabrication via TPP. Their movement was induced by the relative movement between stage and objective carried through the viscous liquid resist. This resulted in offsets between layers, hatch lines and influenced block stitching on the first TPP trial on a NED-µPS, see annex N.

The movement could be inhibited by electrically locking the chip, which would require it being assembled or at least contacted during the fabrication, increasing complexity. For the fabrication of the end effector shown in the previous section, the velocity of piezo stage 2 was reduced to reduce the viscosity-transferred movement. Furthermore, the NED-µPS was fixed to a Si substrate of similar size via sticky tape, which inhibited movement away from the objective used for fabrication. By implementing these methods, the stitching errors were reduced.

The tilt of the NED-µPS chips intended for direct fabrication was compensated via the tilt compensation upgrade. For this purpose, the chip, fixed to the Si substrate, was then fixed to the KMTO adapter via adhesive. The latter is depicted in Fig. 5.27d. The tilt of the two chips of -0.74° and 0.62° in x direction and -0.39° and 0.93° in y direction over the 900 µm by 900 µm load area was compensated to <0.04° by implementing the method described in section 5.6.4.

The base discussed in the previous section was implemented to increase adhesion by expanding the contact area between structure and chip. Furthermore, it provided a simple structure for the programming of layer-wise laser power compensation, which was not required in this case.

Additional preprocessing for adhesion improvement could be necessary depending on the application, the best results would probably come from interlocking features within the load area itself, see section 3.2.

7.1.3 Effects of Two-Photon Polymerization Lithography

Due to the novelty of the NED-µPS, access to samples was restricted. Two chips with structures fabricated via TPP on them were successfully actuated and showed free motion of the NED elements. The leakage currents and displacement of the NED elements reached acceptable levels similar to untreated chips after few actuation cycles, suggesting no significant performance change due to any capillary effect based stiction or prominent residual materials [221]. Leakage currents can have multiple origins, e.g. field emission, quantum mechanical tunneling and currents along the surface of the insulating spacers [222].

However, some residues left over from the TPP process were found, see Fig. 7.2. The fabrication was performed using IP-Q and the development was carried out in a bath of IPA for 40 minutes.

The NED elements depicted in Fig. 7.2a belong to the NED-µPS chip depicted in Fig. 7.1, on which an end effector was fabricated directly using TPP. The elements shown in Fig. 7.2a seem to have residual resist material on and between them.

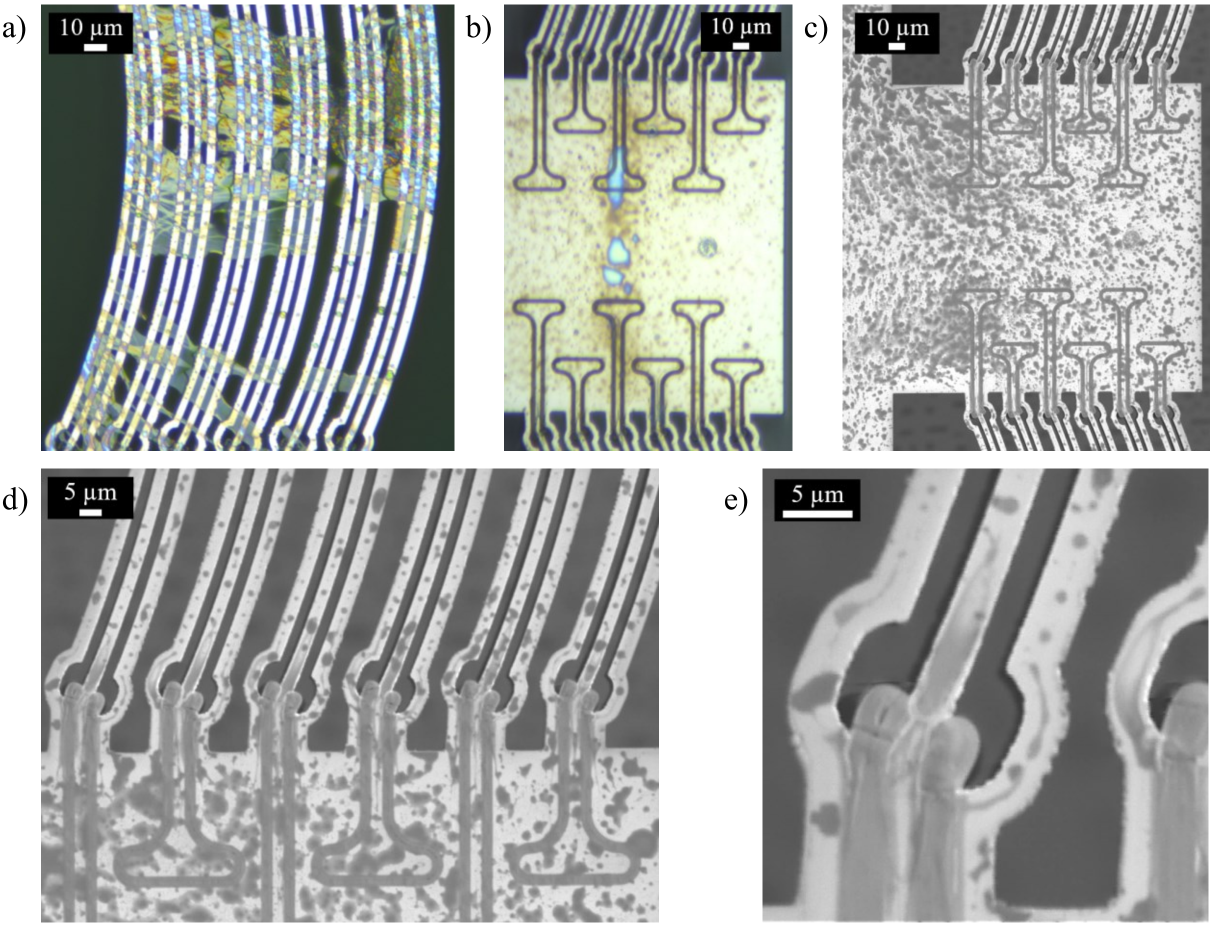

Fig. 7.2: a) Top view RLM image of the NED elements of a NED-µPS that had an end effector fabricated on it from IP-Q using TPP. b) RLM image of the contact pad of the NED elements of the same NED-µPS. c) Top view SEM micrograph of the same. d) Close-up of the same. e) Close-up of the same.

The material is most likely polymerized, because it was transported to the microscope under non-filtered light sources and received incidence from the RLM containing UV wavelengths.

Fig. 7.2b and c depict one of the contact pads displaying surface contamination, most likely residues from resist or development agents.

No negative effects on the performance of the two tested NED-µPS from the residual materials seen in Fig. 7.2 were found, the expected stiction due to contamination of the NED elements or other delicate features of the chip did not occur [221]. Previous research concludes strong effects on NED-based systems from liquid treatments even after drying [80, 223], indicating an exception in this case. This may be due to stronger restoring spring forces and other improvements originating from NED design changes [82, 221].

7.1.4 Probe Tip

Another viable end effector are probe tips, which could be fabricated on NED-µPS to precisely contact samples.

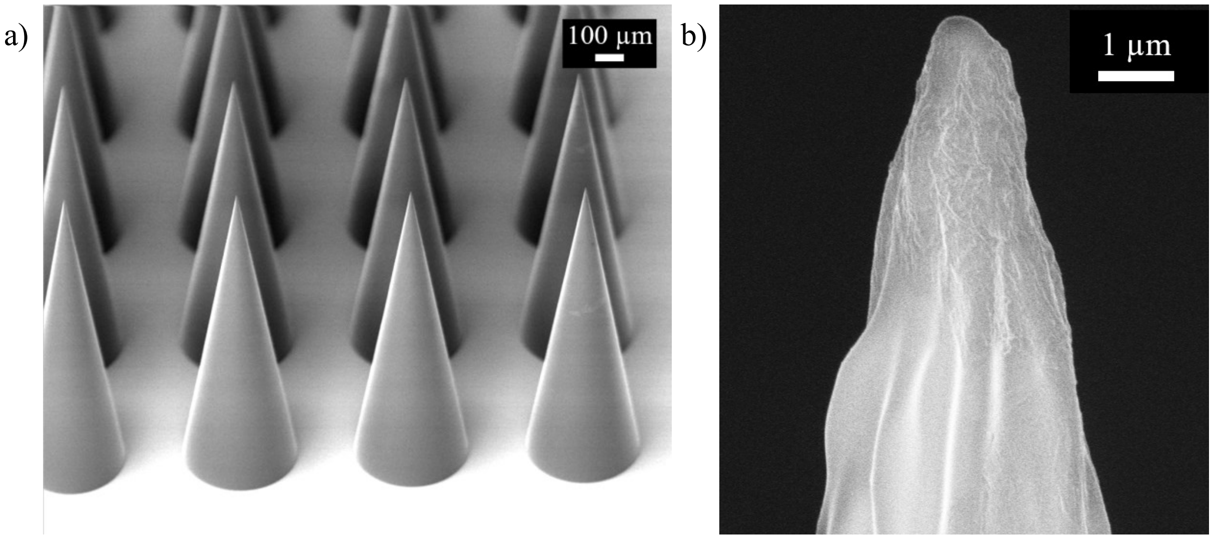

Fig. 7.3: a) Tilted view SEM micrograph of cone structures fabricated from IP-S using the 25x objective. b) Close-up of the same.

Originally devised as nano-imprint lithography (NIL) masters for a bioinstrumentation and microfluidics manufacturer [224], cone structures were fabricated from IP-S using the 25× 0.3 objective (Nanoscribe GmbH & Co. KG), hereinafter referred to as the 25x objective. The scan speed, laser power, hatch distance and layer height settings were 150 mm/s, 40 mW, 0.5 µm and 1 µm.

The 16 structures depicted in Fig. 7.3a have a set height and base diameter of 1.2 mm and 400 µm, respectively. Their tips achieve a size of ~1 µm, see Fig. 7.3b. The probe tips fabricated for this work present a starting point for the systematic refinement dependent on their applications. The tip size could be reduced by using a higher magnification objective or via parameter sweeps iterating through relevant factors, e.g., laser power, scan speed, slice distance. Further add-ons could be fabricated, e.g. microfluidic channels within the structure [85].

7.2 Microfluidics

As indicated by the previous section of this chapter, TPP on NED-based systems could be a reasonable undertaking. Microfluidic applications like the ones proposed for such systems in section 1.2.2 are commonly based on microchannels. The fabrication of such channels usually requires the ability to create cavities at a high aspect ratio between width and depth.

The first challenge is the fabrication of small-scale channels using TPP. The second challenge originates from the process itself, which leaves the channel filled with liquid resist after the structure is fabricated. Thus, the development process provides a bottleneck to the aspect ratio, as it must liberate the channel from residual materials. The following sections investigate these challenges.

7.2.1 Microchannel Fabrication

A previous study conducted by the author required the fabrication of microchannels made from IP-Q using the 10x objective [213]. As discussed in section 1.3, medical applications could benefit from microchannels fabricated from IP-PDMS.

Vertical microchannels of 50 µm depth were fabricated from IP-PDMS in parameter sweeps comprising scan speed, channel width d_C and wall thickness d_W, see Fig. 7.4. Multiple channels were grouped in a cylinder of 250 µm radius and were fabricated on standard Si substrates, see Fig. 7.4a.

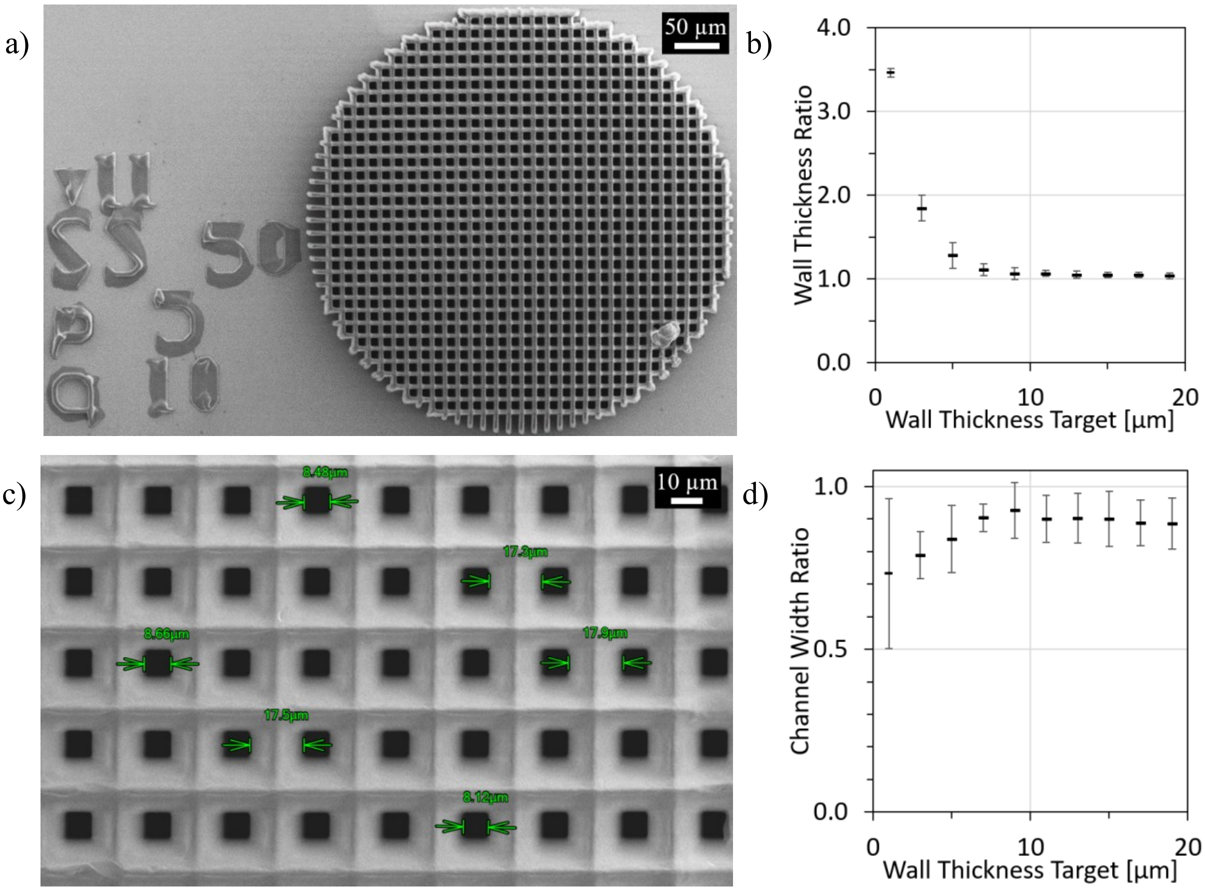

Fig. 7.4: a) Top view SEM micrograph of a microchannel cylinder fabricated from IP-PDMS on a standard Si substrate, including sweep parameters as structured text in the vicinity. b) Wall thickness ratio vs. target wall thickness, including error bars according to standard deviation. c) Top view SEM micrograph of a microchannel cylinder fabricated from IP-PDMS including measurements. d) Channel width ratio vs. target wall thickness, including error bars according to standard deviation.

The laser power was constant at 50 mW, the scan speed was stepped through from 50 to 75 to 100 mm/s, d_C was stepped through from 5 to 25 µm in steps of 5 µm and d_W was stepped through from 1 to 19 µm in steps of 2 µm.

The wall thickness ratio describes the measured thickness divided by the target thickness. Its dependency on the target wall size is depicted in Fig. 7.4b. Starting with a target of 9 µm, the ratio evens out to ~1. The structure shown in Fig. 7.4a displays a d_W of (6.80 ± 0.53) µm and a d_C of (7.80 ± 0.05) µm. The channel width ratio shown in Fig. 7.4d evens out to ~0.9 with target wall sizes above 7 µm. The structure depicted in Fig. 7.4c presents a d_W of (19.27 ± 0.17) µm and a d_C of (8.40 ± 0.10) µm.

The scan speed setting and the channel width target did not exhibit a significant effect on the ratios detailed in Fig. 7.4b and d. The average deviation measured over the entire sweep was 0.22 µm. The minimum d_C of (3.06 ± 0.23) µm and the minimum d_W of (2.23 ± 0.30) µm were found for targets of 5 and 1 µm, respectively, at a scan speed of 100 mm/s.

The characterized properties of the IP-PDMS microchannels presented here manifest as the current state of the art of the material. Minimum channel width is not the only significant metric for microchannels. However, the performance presented here can easily compete with regular PDMS fabrication, see Tab. 7.1.

Tab. 7.1: Comparison of crucial microchannel sizes reported in literature.

Reference	Material	Crucial size [µm]
Min et. al 2021 [225]	PDMS	115-120
Wei et. al. 2021 [102]	Silicone	75
Männel, et al. 2019 [226]	PDMS	75
Mandal et. al 2020 [227]	PDMS	22
Zhuang et. al 2018 [228]	PDMS	20
Abdelgawad et. al 2011 [229]	PDMS	5
This work	IP-PDMS	3.06 ± 0.23

Combined with NED-based micropumps, the channels shown here could be implemented as filters for the separation of particles from liquids. For NED-based acoustic systems, the microchannels could be implemented as absorbers.

7.2.2 Channel Penetration

To operate in most of the presented applications, the channel must be liberated from residual liquid precursors. When the aspect ratio of internal cavities becomes large due to a decreased channel width, the development and subsequent drying processes can be affected by the capillary effect. During development, the remaining liquid resist dissolves in the developing agent, which necessitates the agent to enter and subsequently evaporate from the channel. The development behavior of small square channels fabricated via TPP was investigated via X-ray micro-computed tomography (μCT), SEM and RLM, see Fig. 7.5.

A cylinder structure of 580 μm radius and 268 μm height containing vertical microchannels with d_C and d_W set points of 12 and 19 μm, including a contour, was fabricated from IP-Q on a (2 x 2 x 0.725) mm³ Si substrate to fit the sample size requirements of μCT, see Fig. 7.5a and b. The μCT process allows 3D depiction of the internal channels. However, the size restrictions for the specimen and the resolution restriction of ~1 μm of the Versa 620 (Carl Zeiss IQS Deutschland GmbH) as well as the long measurement time were impediments to finding

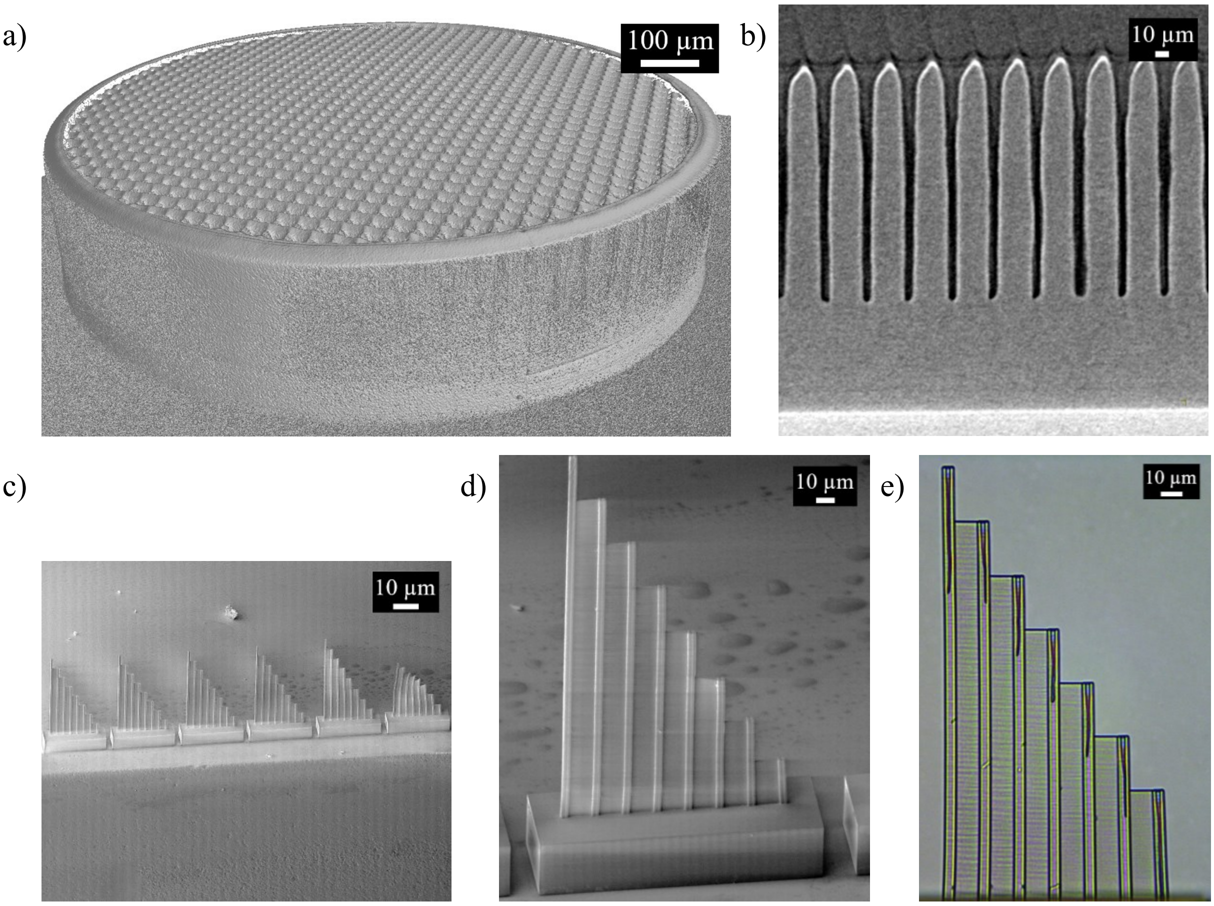

Fig. 7.5: a) Tilted view μCT micrograph of a microchannel structure fabricated from IP-Q on a (2 x 2 x 0.725) mm³ Si substrate including contour structure for increased repeatability. b) Close-up internal view of the same, showing open channels. c) Tilted view SEM micrograph of an example channel penetration parameter sweep fabricated from IP-Dip on the edge of a standard fused silica substrate. d) Close-up of the same, showing the 25 mW specimen. e) Side view RLM image of a penetration structure of channel width 2.5 μm and laser power 26.5 mW after a development in PGMEA for 10 minutes.

significant development correlations for the number of variable parameters in a reasonable timeframe. To overcome these issues, a channel penetration structure was designed, see Fig. 7.5c, d and e. It comprises square channels, a connecting wall in-between and a base of (50 x 50 x 140) µm³ to improve substrate adhesion and to reduce shrinkage effects. The size of the channel walls, their width, as well as height and the development time were studied, after a promising set of fabrication parameters had been established.

Each fabrication was carried out using (55.9 ± 2.9) mm³ IP-Dip drop cast via dispenser. Each group was developed using (60 ± 0.12) ml of PGMEA for a development time t_{dev}. Afterwards, the structures were cleaned using (60 ± 0.12) ml of IPA for one minute.

The main advantage of the design was the ability to check the inside of the channel via RLM, for which the structure was fabricated right at the edge of the substrate, see Fig. 7.5c and e.

The groups of structures depicted in Fig. 7.5c constitute a laser power parameter sweep, although channel height was a given parameter sweep within each individual structure. An individual of that sweep exhibits a channel width of 1 µm, see Fig. 7.5d. Channel height varies from 25 µm to a maximum of 175 µm. Fig. 7.5e depicts the ultimate design with height varying from 50 to 200 µm. The side view image of the structure was accomplished by rotating the substrate and clamping it in place. As the structure was fabricated on the edge, it was in the focal range of the RLM objective.

The solidified resist was found transparent at a wall thickness of 1 µm, making the channel content visible. This way, the penetration length L_P was measured and subsequently compared to calculations made using the Lucas-Washburn equation,

$$L_P(t_{dev}) = b\left(\frac{\gamma r_{cap} t_{dev} cos\theta_{cap}}{2\mu_d}\right)^c \tag{7.1}$$

where γ, r_{cap}, t_{dev}, θ_{cap} and μ_d are the surface tension, the average radius of the capillary, the development time, the contact angle between the liquid and the solid wall and the dynamic viscosity, respectively. To fit the equation, the parameters b and c were used. For PGMEA on IP-Dip a γ of 2.26 mN/m and a µ of 1.1 mNs/m² were assumed [230].

Using the contact angle measurement system OCA 20 (DataPhysics Instruments GmbH), a θ of 13.3° was found for IPA on a solid flat surface fabricated from IP-Dip by T. Grau at Fraunhofer IPMS. Evaporation and gravitational forces were not taken into account. Furthermore, the cavities were square instead of cylindrical and laminar flow was assumed.

Fig. 7.6a depicts a comparison of the measured penetration length versus the development time.

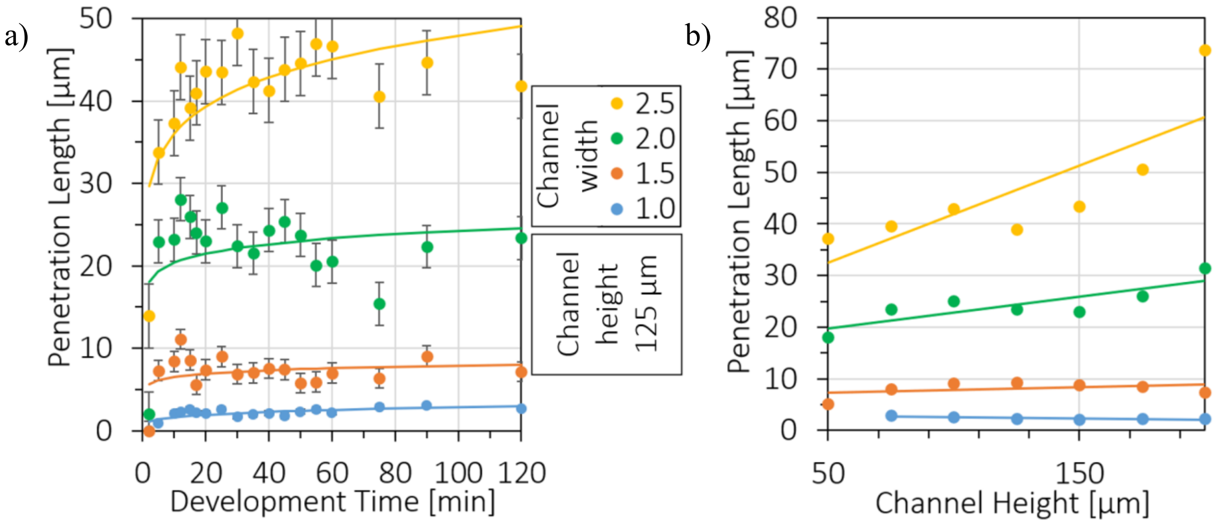

Fig. 7.6: a) Penetration length of microchannels with development agent versus development time t_{dev} measured for various channel widths and a channel height of 125 µm, including fitted Lucas-Washburn curves. b) Penetration length versus channel height for various channel widths of samples developed for 20 min, including a linear fit. Channel width legend in 'a'.

Each measurement was averaged over three copies of structures that received the same treatment. Channel widths of 1.0 to 2.5 µm were studied for the channel height 125 µm. Equ. 7.1 was fitted to the results while implementing the values of Tab. 7.2 and replacing r with half of d_C. The results listed in Tab. 7.2 and especially the error for parameter b show that there are effects not taken into account by the standard Lucas-Washburn equation.

The main dissenting assumption was, that the channels are circular and empty, which is not the case here. Nonetheless, the behavior expected from channels filling with a liquid hold true. The penetration approaches an asymptote, where further penetration seems impossible. The limit strongly depends on the channel width. In the standard Lucas-Washburn equation, fit parameter c is set to 0.5. Here, especially for low development times, not enough measurement points were supplied, which leads to extinction of the factor, see Tab. 7.2.

Another recorded effect was liquid rising in the corners of the rectangular channels, see Fig. 7.5e, which illustrates the dependence of penetration length on the channel height. Here, the structures were developed with PGMEA for 20 min and display a linear behavior, which changes in slope increasing with the channel width.

Tab. 7.2: Lucas-Washburn equation parameters.

Channel width [µm]	Fit parameter *b* [µm]	Error [µm]	Fit parameter *c*	Error
2.5	1.02	1.39	0.15	0.05
2.0	3.29	5.43	0.08	0.07
1.5	1.37	2.98	0.07	0.09
1.0	0.004	0.006	0.27	0.06

For low channel width the channel height has little effect, the slope starts taking effect with 2 and 2.5 µm, which means larger channels get developed even easier if they have higher aspect ratio. The critical development step of microchannels was investigated by devising a new method for the examination of the penetration depth for microchannels fabricated via TPP. By combination with the Lucas-Washburn equation, predictions about the maximum viable channel aspect ratio can be made, depending on the resist material, development agent and time. The presented method was studied for IP-Dip, as it is the manufacturer recommended material for small sized structures, other materials must be investigated in prospective works.

8 Conclusion & Outlook

The driving motivation of this work was the investigation of AMOC at the example of the CMUT and the NED-µPS. A suitable process was found in TPP. It was successfully applied on both chips by overcoming obstacles in the state-of-the-art of AMOC. Two research questions surmise the scope of this work, the first relates the identified obstacles into a task:

"Which additional process steps are necessary to realize fabrication via TPP on an assembled CMUT chip?"

This study provided an answer in the determination of four additional process steps. Firstly, an optical and thermodynamic model was established for the TPP process. On its basis, a compensation method for the excess energy within the voxel due to reflective substrates, as well as for the excess heat within the substrate due to transmission was established. The method was verified by parametric studies on substitute substrates and CMUT chips in this work.

The second additional process step identified in this work was the chip alignment. An upgrade to the fabrication system used in this work was devised, manufactured, implemented and successfully validated.

The third addition concerned the chip assembly, which was adjusted to enable TPP on CMUT chips. For this work, the bond wire and packaging concept was customized.

The fourth additional process was identified in the structure adhesion, resulting in an application dependent recommendation. For the AMOC applications presented in this work, the unaltered adhesion between structure and chip was found sufficient.

With the first research question answered, a TPP-based procedure for AMOC was presented for the first time on CMUT and NED-µPS chips. The procedure presented in this work was suitable for the latter after minor adjustments. Multiple expedient applications were demonstrated, including the implementation of acoustic waveguides on CMUT devices as well as end effector structures fabricated on the NED-µPS. Furthermore, the first ever fabrication of microchannels from IP-PDMS was demonstrated and compared to the state of the art. Additionally, a novel method for the characterization of the development agent penetration length within microchannels fabricated via TPP was devised and presented. The applications presented in this work revealed, that AMOC via TPP was feasible by implementation of the established procedure.

“In what way do the fabrication materials and processes of TPP affect the behavior of an assembled CMUT chip?”

This second research question was systematically investigated by decomposition into three parts. The impact of the fundamental process steps of TPP, the fabrication in the vicinity, as well as with direct contact to the active chip element were studied by comparison of the electrical and acoustic characterization of CMUT chips before and after the respective treatment. Although TPP was successfully employed for AMOC, the electromechanical and acoustic behavior of CMUT chips investigated in this work was changed in a way that makes the applied approach unfeasible for this chip type. The main hypothesis determined for the origin of the exhibited performance issues was the residue contamination of the active elements. Subsequent studies, however, have a high chance of overcoming the limiting factors found in this work by implementing advanced development approaches, e.g., super critical drying. For the NED-based chips the contamination was not found to alter the behavior, although a larger scale investigation must be performed to affirm this hypothesis.

As described in section 1.1, other chip types and classes can benefit from the advances made in this work, however, the feasibility of AMOC must be explored individually. AMOC substrates that comprise fragile dynamic, highly reflective and/or thermally problematic structures require additional attention as demonstrated in this work. The adaptability of the compensation methods and systems enable the exploration of further substrates. Especially the application of AMOC by TPP on optical systems is promising, as the resists generally offer beneficial optical characteristics [145].

Resist materials other than the acrylates used here can benefit from the transferable advances realized in this work and are commercially available or are getting researched, e.g. oligomers, hydrogels, epoxies and mixtures with dopants like nanoparticles, biomolecules, dyes or quantum dots [231].

At the moment, AMOC is not easily scalable to a level that compares with SF processing. However, substrate size and fabrication speed restrictions are engaged with in current system development, e.g. gray-scale TPP [24], multi-beam TPP [119], two-step lithography [232]. For the rapid prototyping approach in the development stage of the product life cycle, these restrictions do not reduce the relevance of AMOC, as was shown for the examples in this work.

Furthermore, AMOC could be used to introduce AM advantages, while subsequently transferring the fabrication to a scalable process, e.g., NIL or micro injection molding [104, S. 176–181, 233].

Scale was an issue for this work as well. The parameter sweep approach for statistical experimentation was successfully used on substitute substrates. By this method, complex simulations were supplied with suitable factorization. However, AMOC using wafer-scale substrates could result in faster model verification for the designated substrate.

The parameter sweep approach still requires enormous effort. An even better approach would be in-line monitoring of the TPP process. The optical behavior of the substrate could be determined by photodetectors. For thermodynamics, the dependency on substrate composition even below the surface is important, making non-destructive in-line testing difficult [193]. Raman characterization enables the detection of the degree of conversion of resists, e.g. IP-Dip [14], IP-Q [127]. The polymerization characteristics can be monitored this way as presented in [234], which could reduce experimental efforts and enable improved AMOC.

One step further, machine learning could be implemented to control the polymerization process [235]. By identification of the characteristics of the substrate, the voxel and of the fabricated structure using monitoring equipment, predictions for the adaptation of the fabrication parameters could be made by machine learning tools and synchronously implemented.

With the emergence of AM processes that enable fabrication of micro- and nanoscale structures, AMOC becomes an addition to the toolbox but not a surrogate for classic SF processes. As with all new fabrication technologies, old hindrances might be overcome, but new ones emerge.

The verified optical and thermal compensation model and substrate alignment upgrade for the AM process used in this work was found useful, as its advantages were demonstrated to transfer to the fabrication on chip, e.g., its convenience for rapid prototyping and the accessible range to fabricate millimeter as well as sub-micron structures.

References

[1] Kupfer, M. E., et al.: "In Situ Expansion, Differentiation, and Electromechanical Coupling of Human Cardiac Muscle in a 3D Bioprinted, Chambered Organoid," Circulation research, Vol. 127, No. 2, pp. 207–224, 2020.

[2] Schweiger, S.; Koch, S. G.; Schenk, H.: "Two-Photon-Lithography Substrate Reflection and Absorption Compensation for Additive Manufacturing of Metamaterials on MEMS," 2021 44th International Spring Seminar on Electronics Technology (ISSE), IEEE, 552021, pp. 1–7, 10.1109/ISSE51996.2021.9467575.

[3] Roman, M. C., et al.: "From 3D-Printing Lunar and Mars Habitats to Affordable Sustainable Housing on Earth," 50th International Conference on Environmental Systems, 2020.

[4] Islam, M. K., et al.: "Biomimetic armour design strategies for additive manufacturing: A review," Materials & Design, 2021.

[5] Meza, L. R., et al.: "Resilient 3D hierarchical architected metamaterials," Proceedings of the National Academy of Sciences of the United States of America, Vol. 112, No. 37, pp. 11502–11507, 2015.

[6] Zhu, X., et al.: "Implementation of dispersion-free slow acoustic wave propagation and phase engineering with helical-structured metamaterials," Nature communications, Vol. 7, p. 11731, 2016.

[7] Elmadih, W.; Chronopoulos, D.; Zhu, J.: "Metamaterials for simultaneous acoustic and elastic bandgaps," Scientific reports, Vol. 11, No. 1, p. 14635, 2021.

[8] Filho, A.: "3D printing techniques in the manufacture of microfluidic devices for generation of microbubbles," SCIOL Biomed, Vol. 3, p. 143, 2019.

[9] Beckwith, A. L.; Borenstein, J. T.; Velasquez-Garcia, L. F.: "Monolithic, 3D-Printed Microfluidic Platform for Recapitulation of Dynamic Tumor Microenvironments," J. Microelectromech. Syst., Vol. 27, No. 6, pp. 1009–1022, 2018.

[10] Haraldsson, K. T., et al.: "3D polymeric microfluidic device fabrication via contact liquid photolithographic polymerization (CLiPP)," Sensors and Actuators B: Chemical, Vol. 113, No. 1, pp. 454–460, 2006.

[11] Li, J., et al.: "3D-Printed Micro Lens-in-Lens for In Vivo Multimodal Microendoscopy," Small, Vol. 18, No. 17, 2022.

[12] Demirörs, A. F., et al.: "Three-dimensional printing of photonic colloidal glasses into objects with isotropic structural color," Nature communications, Vol. 13, No. 1, p. 4397, 2022.

[13] Lemma, E. D., et al.: "Mechanical properties tunability of three-dimensional polymeric structures in two-photon lithography," IEEE Trans. Nanotechnology, 2016.

[14] Bauer, J., et al.: "Programmable Mechanical Properties of Two-Photon Polymerized Materials: From Nanowires to Bulk," Adv. Mater. Technol., Vol. 4, No. 9, p. 1900146, 2019.

[15] Melnikov, A., et al.: "Microacoustic Metagratings at Ultra-High Frequencies Fabricated by Two-Photon Lithography," Advanced Science, p. 2200990, 2022.

[16] Wohlers Associates, Inc.: "Wohlers Report 2021," https://wohlersassociates.com/press-releases/new-wohlers-report-2021-finds-7-5-growth-in-additive/, Accessed: 17.11.22.

[17] Wohlers Associates, Inc.: "Wohlers Report 2022," https://wohlersassociates.com/press-releases/wohlers-report-2022-finds-strong-industry-wide-growth/, Accessed: 17.11.22.

[18] Muldoon, K., et al.: "High Precision 3D Printing for Micro to Nano Scale Biomedical and Electronic Devices," Micromachines, Vol. 13, No. 4, p. 642, 2022.

[19] Hassanin, H., et al.: "Microadditive Manufacturing Technologies of 3D Microelectromechanical Systems," Adv Eng Mater, Vol. 23, No. 12, p. 2100422, 2021.

[20] Lifton, V. A.; Lifton, G.; Simon, S.: "Options for additive rapid prototyping methods (3D printing) in MEMS technology," Rapid Prototyping Journal, Vol. 20, No. 5, pp. 403–412, 2014.

[21] Koll, M.: "fablab Cottbus," https://fablab-cottbus.de/blog/lausitzer-tueftelseminare, Accessed: 23.11.22.

[22] All3DP: "The Best 3D Printing Services Online in 2022," https://all3dp.com/de/1/online-3d-druck-service-dienstleister-3d-drucken-lassen/, Accessed: 23.11.2022.

[23] Sertoglu, K.: "Nanoscribe Launches Its Quantum X Align 3d Printer – Technical Specifications And Pricing," https://3dprintingindustry.com/news/nanoscribe-launches-its-quantum-x-align-3d-printer-technical-specifications-and-pricing-203016/, Accessed: 22.11.22.

[24] Grushina, A.: "Direct-write grayscale lithography," Advanced Optical Technologies, Vol. 8, No. 3, pp. 163–169, 2019.

[25] Demirak, O.; Tutsak, E.; Demirci, H.: "Additive Manufacturing of Custom-made Cranial PEEK Implant and Postoperative Evaluation," 2022.

[26] Lindenmann, N., et al.: "Photonic wire bonding: a novel concept for chip-scale interconnects," Optics express, Vol. 20, No. 16, pp. 17667–17677, 2012.

[27] Beutel, F., et al.: "Detector-integrated on-chip QKD receiver for GHz clock rates," npj Quantum Inf, Vol. 7, No. 1, 2021.

[28] Yu, S.; Gaylord, T. K.; Bakir, M. S.: "Fiber-Array-to-Chip Interconnections With Sub-Micron Placement Accuracy via Self-Aligning Chiplets," IEEE Photon. Technol. Lett., Vol. 34, No. 19, pp. 1023–1025, 2022.

[29] Parsi Sreenivas, V. V., et al.: "Three dimensional fabrication of optical waveguiding elements for on-chip integration," Micro-Optics 2014, SPIE, 2014, 10.1117/12.2052452.

[30] Tim Schulze: "MEMS-basierte Komponenten zur Modulation von Terahertzstrahlung in Hohlleitern," [unpublished doctoral dissertation], Fraunhofer IPMS, Brandenburgische Technische Universität Cottbus-Senftenberg, 2022.

[31] Williams, J. C., et al.: "Multiphoton Nanosculpting of Optical Resonant and Nonresonant Microsensors on Fiber Tips," ACS Applied Materials & Interfaces, Vol. 14, No. 17, pp. 19988–19999, 2022.

[32] Hsu, L.-Y., et al.: "A Facile Approach for 4D Microprinting of Multi-Photoresponsive Actuators," Adv. Mater. Technol., p. 2200801, 2022.

[33] Yu, S., et al.: "On-chip optical tweezers based on freeform optics," Optica, Vol. 8, No. 3, p. 409, 2021.

[34] Thiele, S., et al.: "Ultra-compact on-chip LED collimation optics by 3D femtosecond direct laser writing," Optics letters, Vol. 41, No. 13, pp. 3029–3032, 2016.

[35] Perez, E., et al.: "Automated on-axis direct laser writing of coupling elements for photonic chips," Optics express, Vol. 28, No. 26, pp. 39340–39353, 2020.

[36] Wessling, N. K., et al.: "Fabrication and transfer printing based integration of free-standing GaN membrane micro-lenses onto semiconductor chips," Opt. Mater. Express, Vol. 12, No. 12, p. 4606, 2022.

[37] Goi, E., et al.: "Nanoprinted high-neuron-density optical linear perceptrons performing near-infrared inference on a CMOS chip," Light, science & applications, Vol. 10, No. 1, p. 40, 2021.

[38] Kim, J., et al.: "On-chip fluorescence detection using photonic bandgap guiding optofluidic hollow-core light cage," APL Photonics, Vol. 7, No. 10, p. 106103, 2022.

[39] Pudis, D., et al.: "3D Photonic Technologies for Applications on a Chip and Optical Fiber," 2018 12th International Conference on Advanced Semiconductor Devices and Microsystems (ASDAM), IEEE, 2018, pp. 1–8, 10.1109/ASDAM.2018.8544529.

[40] Bürger, J., et al.: "3D-Nanoprinted Antiresonant Hollow-Core Microgap Waveguide: An on-Chip Platform for Integrated Photonic Devices and Sensors," ACS photonics, Vol. 9, No. 9, pp. 3012–3024, 2022.

[41] Loo, J. F. C., et al.: "Integrated Printed Microfluidic Biosensors," Trends in Biotechnology, Vol. 37, No. 10, pp. 1104–1120, 2019.

[42] Didier, C.; Kundu, A.; Rajaraman, S.: "Capabilities and limitations of 3D printed microserpentines and integrated 3D electrodes for stretchable and conformable biosensor applications," Microsystems & nanoengineering, Vol. 6, p. 15, 2020.

[43] Kaiser, B.: "Nanoscopic Electrostatic Drive – electrostatic MEMS bending transducer," https://www.ipms.fraunhofer.de/en/Components-and-Systems/Components-and-Systems-Actuators/Mechanical-Actuators/Nanoscopic-Electrostatic-Drives.html, Accessed: 05.01.2023.

[44] Betz, B.: "Capacitive Micromachined Ultrasonic Transducer (CMUT)," https://www.ipms.fraunhofer.de/en/Components-and-Systems/Components-and-Systems-Sensors/Ultrasonic-Sensors/Capacitive-micromachined-ultrasonic-transducer-CMUT.html, Accessed: 05.01.2023.

[45] Kaiser, B.: "Lateral Capacitive Micromechanical Ultrasonic Transducer (L-CMUT)," https://www.ipms.fraunhofer.de/en/Components-and-Systems/Components-and-Systems-Sensors/Ultrasonic-Sensors/Lateral-Capacitive-Micromechanical-Ultrasonic-Transducer.html, Accessed: 05.01.2023.

[46] Weinreich, W.: "Piezoelectric Micromachined Ultrasonic Transducers (PMUT)," https://www.ipms.fraunhofer.de/en/Components-and-Systems/Components-and-Systems-Sensors/Ultrasonic-Sensors/Piezoelectric-Micromachined-Ultrasonic-Transducers-PMUT.html, Accessed: 05.01.2023.

[47] Balvin, F.: "Fraunhofer institutes help small and medium-sized businesses develop innovative ultrasonic sensors," https://www.ipms.fraunhofer.de/de/press-media/press/2021/MUT-platform.html, Accessed: 27.11.2022.

[48] Haller, M. I.; Khuri-Yakub, B. T.: "A surface micromachined electrostatic ultrasonic air transducer," Ultrasonics: International symposium : Papers and programme, IEEE, 1994, pp. 1241-1244, 10.1109/ULTSYM.1994.401810.

[49] Koch, S. G., et al.: "Empowering Robots for Multimodal Tactile Gripping using Capacitive Micromachined Ultrasonic Transducers," 2021 Smart Systems Integration (SSI), IEEE, 4272021, pp. 1–5, 10.1109/SSI52265.2021.9467023.

[50] Moehring, M. A., et al.: "Apparatus and method for characterization of acute otitis media," US20200187899A1.

[51] Ohn-Bar, E.; Trivedi, M. M.: "Hand Gesture Recognition in Real Time for Automotive Interfaces," IEEE Trans. Intell. Transport. Syst., Vol. 15, No. 6, pp. 2368–2377, 2014.

[52] Matilainen, M.; Hannuksela, J.; Fan, L.: "Finger Tracking for Gestural Interaction in Mobile Devices," Image analysis Bd. 7944, Kämäräinen, J.-K., et al. (Eds.), Heidelberg, Springer, 2013, pp. 329–338, 10.1007/978-3-642-38886-6_32.

[53] Ochiai, Y., et al.: "Cross-Field Aerial Haptics," Ultrasound Sensing Technologies for Medical, Industrial, and Consumer Applications, 2018, pp. 3238–3247, 10.1145/2858036.2858489.

[54] Mills, D. M.; Smith, L. S.: "Real-time in-vivo imaging with capacitive micromachined ultrasound transducer (cMUT) linear arrays," 2003 IEEE Symposium on Ultrasonics

[55] Fortin, J. B.; Lu, T.-M.: "Ultraviolet radiation induced degradation of poly-para-xylylene (parylene) thin films," Thin Solid Films, Vol. 397, 1-2, pp. 223–228, 2001.

[56] D.W. Greve, J. J. Neumann, I. J. Oppenheim, S. P. Pessiki, and D. Ozevin: "Robust capacitive MEMS ultrasonics transducers for liquid immersion," 2003 IEEE Symposium on Ultrasonics, pp. 581-584.

[57] Jeanne, E., et al.: "Protection Layer Influence on Capacitive Micromachined Ultrasonic Transducers Performance," MRS Online Proceedings Library, No. 1052, 2008.

[58] X. Zhuang, A. Nikoozadeh, M. A. Beasley, G. G. Yaralioglu: "Biocompatible coatings for CMUTs in a harsh, aqueous environment," Journal of Micromechanics and microengineering, No. 17, 2007.

[59] Lin, D.-S., et al.: "Encapsulation of Capacitive Micromachined Ultrasonic Transducers Using Viscoelastic Polymer," Journal of MEMS systems, Vol. 19, No. 6, pp. 1341–1351, 2010.

[60] Xuefeng Zhuang, et al.: "Fabrication of Flexible Transducer Arrays With Through-Wafer Electrical Interconnects Based on Trench Refilling With PDMS," Journal of Microelectromechanical Systems, No. 17, pp. 446–452, 2008.

[61] Bayram, B., et al.: "Finite element modeling and experimental characterization of crosstalk in 1-D CMUT arrays," IEEE Trans. Ultrason., Ferroelect., Freq. Contr., No. 54, pp. 418–430, 2007.

[62] Campbell, E., et al.: "Cross-Coupling in Sealed cMUT Arrays for Immersion Applications," IEEE Ultrasonics Symposium Proceedings, 2007.

[63] Köble, S., et al.: "Capacitive Micromachined Ultrasonic Transducers (CMUT) Utilized as Tactile Sensors," 2021 44th International Spring Seminar on Electronics Technology (ISSE), IEEE, 552021, pp. 1–6, 10.1109/ISSE51996.2021.9467603.

[64] Köble, S.; Schweiger, S.; Koch, S. G.: "Influencing the Sound Field by Housing Capacitive Micro-mechanical Ultrasonic Transducers (CMUTs)," MikroSystemTechnik Kongress 2021, Lang, K.-D. (Ed.), Berlin, Offenbach, VDE Verlag GmbH, 2021, pp. 411–414.

[65] Krenkel, M., et al.: "CMUT with mechanically coupled plate actuators for low frequencies," J. Micromech. Microeng., Vol. 29, No. 4, p. 44001, 2019.

[66] Unger, A., et al.: "Finite element analysis of mechanically amplified CMUTs," 2013 IEEE International Ultrasonics Symposium (IUS), IEEE, 2013, pp. 287–290, 10.1109/ULTSYM.2013.0074.

[67] Rutsch, M., et al.: "Waveguide for air-coupled ultrasonic phased-arrays with propagation time compensation and plug-in assembly," The Journal of the Acoustical Society of America, Vol. 150, No. 5, p. 3228, 2021.

[68] Fahy, F.: "Foundations of engineering acoustics," Cambridge, Massachusetts, Academic Press, 2001.

[69] Kinsler, L. E.: "Fundamentals of acoustics," 4th ed., New York, Chichester, Wiley, 2000.

[70] Kolbrek, B.: "Horn Theory: An Introduction," Part 1, https://audioxpress.com/page/audioXpress-Supplementary-Material, Accessed: 06.09.2022.

[71] Meisel, T.: "Optimierung der Richtcharakteristik von MEMS-Ultraschallwandlern durch passive Strukturen," Bachelor's Thesis, Fraunhofer IPMS, Brandenburgische Technische Universität Cottbus-Senftenberg, 2022.

[72] Conrad, H., et al.: "A small-gap electrostatic micro-actuator for large deflections," Nature communications, Vol. 6, p. 10078, 2015.

[73] Kaiser, B.: "Simulation und Charakterisierung eines neuartigen mikromechanischen elektrostatischen Aktors," Dissertation, Fraunhofer IPMS, Brandenburgische Technische Universität Cottbus-Senftenberg, 2016.

[74] Kaiser, B., et al.: "Concept and proof for an all-silicon MEMS micro speaker utilizing air chambers," Microsystems & nanoengineering, Vol. 5, p. 43, 2019.

[75] Kaiser, B., et al.: "The push-pull principle: an electrostatic actuator concept for low distortion acoustic transducers," Microsystems & nanoengineering, Vol. 8, No. 1, 2022.

[76] Melnikov, A., et al.: "Coulomb-actuated microbeams revisited: experimental and numerical modal decomposition of the saddle-node bifurcation," Microsystems & nanoengineering, Vol. 7, p. 41, 2021.

[77] Monsalve, J. M., et al.: "Proof of concept of an air-coupled electrostatic ultrasonic transducer based on lateral motion," Sensors and Actuators A: Physical, Vol. 345, p. 113813, 2022.

[78] Guaracao, J. M. M., et al.: "First Time of nanoscopic electrostatic drives pushing for ultrasonic transmission for gesture recognition," Yuhas, Schneider (Ed.), pp. 1–4, 10.1109/IUS46767.2020.9251316.

[79] Keyvan Narimani, et al.: "Highly Modular Microsystem Inchworm Motor Based on a Nanoscopic Electrostatic Drive," MikroSystemTechnik Congress. https://ieeexplore.ieee.org/document/9698378, 2021.

[80] Uhlig, S., et al.: "Electrostatically Driven In-Plane Silicon Micropump for Modular Configuration," Micromachines, Vol. 9, No. 4, 2018.

[81] Uhlig, S.: "Silizium-basierte Mikropumpen mit dem lateralen nanoskopischen elektrostatischen Antrieb," Brandenburgische Technische Universität Cottbus-Senftenberg, 2022.

[82] Shashank: "Novel Electrostatic Bending Actuators Based Microsystems for In-plane Micro-positioning Applications," [unpublished doctoral dissertation], Fraunhofer Institute for Photonic Microsystems, Brandenburg University of Technology Cottbus–Senftenberg, 2023.

[83] Park, F. C.: "Modern robotics - mechanics, planning, and control," Cambridge University Press, 2017.

[84] Faraji Rad, Z., et al.: "High-fidelity replication of thermoplastic microneedles with open microfluidic channels," Microsystems & nanoengineering, Vol. 3, p. 17034, 2017.

[85] Faraji Rad, Z.; Prewett, P. D.; Davies, G. J.: "High-resolution two-photon polymerization: the most versatile technique for the fabrication of microneedle arrays," Microsystems & nanoengineering, Vol. 7, p. 71, 2021.

[86] Ma, Z.-C., et al.: "Femtosecond laser programmed artificial musculoskeletal systems," Nature communications, Vol. 11, No. 1, p. 4536, 2020.

[87] Jing, X., et al.: "Two-photon polymerization for 3D biomedical scaffolds: Overview and updates," Frontiers in bioengineering and biotechnology, Vol. 10, p. 994355, 2022.

[88] Sun, H.-B.; Matsuo, S.; Misawa, H.: "Three-dimensional photonic crystal structures achieved with two-photon-absorption photopolymerization of resin," Applied Physics Letters, Vol. 74, No. 6, pp. 786–788, 1999.

[89] Misawa, H., et al.: "Formation of photonic crystals by femtosecond laser microfabrication," First International Symposium on Laser Precision Microfabrication, SPIE, 2000, pp. 29–32, 10.1117/12.405730.

[90] Zohar, M., et al.: "Solar cell efficiency improvement using dip-pen nanolithography," J. Photon. Energy, Vol. 8, No. 02, p. 1, 2018.

[91] Fathy, A., et al.: "On-chip parallel Fourier transform spectrometer for broadband selective infrared spectral sensing," Microsystems & nanoengineering, Vol. 6, p. 10, 2020.

[92] Rothermel, F., et al.: "Towards magnetically actuated 3D-printed micro-optical elements," Doyle, Ellis et al. (Hg.) 08.2021 – Optomechanics and Optical Alignment, p. 21, 10.1117/12.2594213.

[93] Hong, Z.; Liang, R.: "IR-laser assisted additive freeform optics manufacturing," Scientific reports, Vol. 7, No. 1, p. 7145, 2017.

[94] Maruo, S.; Ikuta, K.: "Fabrication of freely movable microstructures by using two-photon three-dimensional microfabrication," Micro- and Nano-photonic Materials and Devices, SPIE, 2000, pp. 106–112, 10.1117/12.382800.

[95] Zhang, S., et al.: "Reconfigurable multi-component micromachines driven by optoelectronic tweezers," Nature communications, Vol. 12, No. 1, p. 5349, 2021.

[96] Duffy, D. C., et al.: "Rapid Prototyping of Microfluidic Systems in Poly(dimethylsiloxane)," Analytical Chemistry, Vol. 70, No. 23, pp. 4974–4984, 1998.

[97] Kumi, G., et al.: "High-speed multiphoton absorption polymerization: fabrication of microfluidic channels with arbitrary cross-sections and high aspect ratios," Lab on a Chip, Vol. 10, No. 8, pp. 1057–1060, 2010.

[98] Han, D., et al.: "A bio-inspired 3D-printed hybrid finger with integrated ECF (electro-conjugate fluid) micropumps," Sensors and Actuators A: Physical, Vol. 257, pp. 47–57, 2017.

[99] Mohd Fuad, N., et al.: "Characterization of 3D-Printed Moulds for Soft Lithography of Millifluidic Devices," Micromachines, Vol. 9, No. 3, p. 116, 2018.

[100] Duarte, L. C., et al.: "3D printing of microfluidic devices with embedded sensing electrodes for generating and measuring the size of microdroplets based on contactless conductivity detection," Sensors and Actuators B: Chemical, Vol. 251, pp. 427–432, 2017.

[101] Walczak, R.; Kawa, B.; Adamski, K.: "Inkjet 3D printed microfluidic device for growing seed root and stalk mechanical characterization," Sensors and Actuators A: Physical, Vol. 297, p. 111557, 2019.

[102] Wei, T., et al.: "Design and Fabrication of Multi-Layer Silicone Microchannel Cooler for High-Power Chip Array," 2021 22nd International Conference on Electronic Packaging Technology (ICEPT), IEEE, 2021, pp. 1–5, 10.1109/ICEPT52650.2021.9568232.

[103] Olanrewaju, A., et al.: "Capillary microfluidics in microchannels: from microfluidic networks to capillaric circuits," Lab on a Chip, Vol. 18, No. 16, pp. 2323–2347, 2018.

[104] Emely Harnisch: "Two-Photon Polymerization on Metal Surfaces for Structuring Moulding Tools," Ergebnisse aus der Produktionstechnik, No. 27, 2019.

[105] Gartner, L.: "UpNano introduces Tilt Frame to maximize precision in 2PP 3D-Printing," https://www.3printr.com/upnano-introduces-tilt-frame-to-maximize-precision-in-2pp-3d-printing-5658020/, Accessed: 24.12.2022.

[106] Engineer Nanoscribe GmbH & Co. KG: "IP-PDMS Characteristics," Oral, 06.2022.

[107] Raj M, K.; Chakraborty, S.: "PDMS microfluidics: A mini review," J Appl Polym Sci, Vol. 137, No. 27, p. 48958, 2020.

[108] Shimizu, A., et al.: "ECM-based microchannel for culturing in vitro vascular tissues with simultaneous perfusion and stretch," Lab on a Chip, Vol. 20, No. 11, pp. 1917–1927, 2020.

[109] Tao, Y., et al.: "A review on voids of 3D printed parts by fused filament fabrication," Journal of Materials Research and Technology, Vol. 15, pp. 4860–4879, 2021.

[110] THRE3D: "THRE3D Additive Manufacturing Process Schematics," https://thre3d.com/, Accessed: 23.05.2015.

[111] Regehly, M., et al.: "Xolography for linear volumetric 3D printing," Nature, Vol. 588, No. 7839, pp. 620–624, 2020.

[112] Nagarajan, B., et al.: "Development of Micro Selective Laser Melting: The State of the Art and Future Perspectives," Engineering, Vol. 5, No. 4, pp. 702–720, 2019.

[113] BMF: "Product Data Sheet," https://bmf3d.com/de/2%CE%BCm-series-3d-printers/, Accessed: 07.09.2022.

[114] Baldacchini, T. (Ed.): "Three-dimensional microfabrication using two-photon polymerization," Norwich, William Andrew, an imprint of Elsevier, 2020.

[115] Ramanathan, A. K., et al.: "Metal structures embedded with piezoelectric PVDF sensors using ultrasonic additive manufacturing," Manufacturing Letters, Vol. 31, pp. 96–100, 2022.

[116] Behera, D.; Cullinan, M.: "Current challenges and potential directions towards precision microscale additive manufacturing – Part I: Direct ink writing/jetting processes," Precision Engineering, Vol. 68, pp. 326–337, 2021.

[117] Lowe, P. S., et al.: "Scaling-up ultrasonic vibration assisted additive manufacturing to build 316 L 3 m3 waste container flange," Journal of Manufacturing Processes, Vol. 83, pp. 97–104, 2022.

[118] König, K., et al.: "Optically Induced Nanostructures: Biomedical and Technical Applications: Nanoprocessing using near-infrared sub-15 femtosecond laser microscopes," Berlin, 2015.

[119] Maibohm, C., et al.: "Multi-beam two-photon polymerization for fast large area 3D periodic structure fabrication for bioapplications," Scientific reports, Vol. 10, No. 1, p. 8740, 2020.

[120] Fischer, J.; Wegener, M.: "Three-dimensional direct laser writing inspired by stimulated-emission-depletion microscopy [Invited]," Opt. Mater. Express, Vol. 1, No. 4, p. 614, 2011.

[121] Blachowicz, T.; Ehrmann, A.: "3D Printed MEMS Technology-Recent Developments and Applications," Micromachines, Vol. 11, No. 4, 2020.

[122] Maruo, S.; Nakamura, O.; Kawata, S.: "Three-dimensional microfabrication with two-photon-absorbed photopolymerization," Opt. Lett., Vol. 22, No. 2, p. 132, 1997.

[123] Göppert-Mayer, M.: "Über Elementarakte mit zwei Quantensprüngen," Ann. Phys., Vol. 401, No. 3, pp. 273–294, 1931.

[124] Kaiser, W.; Garrett, C. G. B.: "Two-Photon Excitation in Ca F2 : Eu2+," Phys. Rev. Lett., Vol. 7, No. 6, pp. 229–231, 1961.

[125] Malinauskas, M., et al.: "Ultrafast laser nanostructuring of photopolymers: A decade of advances," Physics Reports, Vol. 533, No. 1, pp. 1–31, 2013.

[126] Jiang, L. J., et al.: "Two-photon polymerization: investigation of chemical and mechanical properties of resins using Raman microspectroscopy," Optics letters, Vol. 39, No. 10, pp. 3034–3037, 2014.

[127] Schweiger, S., et al.: "Characterization of two-photon-polymerization lithography structures via Raman spectroscopy and nanoindentation," J. Optical Microsystems, Vol. 2, No. 03, 2022.

[128] Spangenberg, A., et al.: "Recent Advances in Two-Photon Stereolithography," Updates in advanced lithography, Hosaka, S. (Ed.), Rejeka, Croatia, In Tech, 2014, 10.5772/56165.

[129] TOPTICA Photonics AG: "Femto-Fiber Brochure," https://www.toptica.com/fileadmin/Editors_English/11_brochures_datasheets/01_brochures/0623_Femto-Fiber.pdf, Accessed: 25.11.2022.

[130] Engineer Nanoscribe GmbH & Co. KG: "O-ring for resist reservoir," Oral, 10.2019.

[131] Engineer Nanoscribe GmbH & Co. KG: "Training and general introduction after installation," Oral, 05.2019.

[132] Engineer Nanoscribe GmbH & Co. KG: "Imperfect dose stability over FOV due to aberrations, exacerbated when fabricating with low doses.," E-Mail, 04.2021.

[133] Carl Zeiss AG: "Definite Focus Manual," https://www.zeiss.de/mikroskopie/produkte/light-microscopes/axio-observer-for-biology/definite-focus.html, Accessed: 26.11.2022.

[134] Technischen Regeln für Betriebssicherheit: "TRBS 2153 Vermeidung von Zündgefahren infolge elektrostatischer Aufladungen, 4th ed., Heidelberg, Jedermann-Verl., 2009.

[135] Shell plc: "1-methoxy-2-propyl acetate datasheet," 03.2016. https://www.shell.com/business-customers/chemicals/our-products/solvents-chemical/glycol-ethers/_jcr_content/par/tabbedcontent/tab/textimage.stream/1459930728277/599ee118ce19f1f136c427f9cd09c3d73bb3e47e/mpa-u5126.pdf, Accessed: 12.09.2022.

[136] 3M: "Novec 7100 High-Tech Flüssigkeit," https://www.3mdeutschland.de/3M/de_DE/p/d/b40044867/, Accessed: 12.09.2022.

[137] Oakdale, J. S., et al.: "Post-print UV curing method for improving the mechanical properties of prototypes derived from two-photon lithography," Optics express, Vol. 24, No. 24, pp. 27077–27086, 2016.

[138] Yu, T., et al.: "Chemically Amplified Positive Resists for Two-Photon Three-Dimensional Microfabrication," Advanced Materials, Vol. 15, No. 6, pp. 517–521, 2003.

[139] MicroChemicals GmbH: "Entwickeln von Fotolack," http://www.fotolack.eu/, Accessed: 08.05.2020.

[140] Engineer Nanoscribe GmbH & Co. KG: "Characteristics, shrinkage and composition of IP-Q," Oral, 04.2021.

[141] Liu, Y., et al.: "Deformation Behavior of Foam Laser Targets Fabricated by Two-Photon Polymerization," Nanomaterials (Basel, Switzerland), Vol. 8, No. 7, 2018.

[142] Schmitten, M.: "MSDS IP-Dip - Version EN 01/2017,"

[143] Maggi, A.: "Three-Dimensional Nano-Architected Materials as Platforms for Designing Effective Bone Implants," Dissertation, California Institute of Technology, 2018.

[144] Stein, O., et al.: "Fabrication of Low-Density Shock-Propagation Targets Using Two-Photon Polymerization," Fusion Science and Technology, Vol. 73, No. 2, pp. 153–165, 2018.

[145] Li, Y., et al.: "UV to NIR optical properties of IP-Dip, IP-L, and IP-S after two-photon polymerization determined by spectroscopic ellipsometry," Opt. Mater. Express, Vol. 9, No. 11, p. 4318, 2019.

[146] Massachusetts Institute of Technology: "Material Property Database: PMMA," http://www.mit.edu/~6.777/matprops/pmma.htm, Accessed: 05.01.2023.

[147] Dou, N. G., et al.: "Ultralow Thermal Conductivity and Mechanical Resilience of Architected Nanolattices," Nano letters, Vol. 18, No. 8, pp. 4755–4761, 2018.

[148] Nanoscribe GmbH & Co. KG: "MSDS IP-Dip Photoresist," 06.2021.

[149] Saha, S. K., et al.: "Effect of Proximity of Features on the Damage Threshold During Submicron Additive Manufacturing Via Two-Photon Polymerization," Journal of Micro and Nano-Manufacturing, Vol. 5, No. 3, 2017.

[150] Bauer, J., et al.: "Thermal post-curing as an efficient strategy to eliminate process parameter sensitivity in the mechanical properties of two-photon polymerized materials," Optics express, Vol. 28, No. 14, pp. 20362–20371, 2020.

[151] Mark, J.E. (Ed.): "Polymer data handbook," 2nd ed., New York u. a., Oxford Univ. Press, 2009.

[152] Mason, W. P.: "Electromechanical transducers and wave filters.," New York, D. Van Nostrand Co., 1948.

[153] Schmidt, J.-U.; Friedrichs, M.; Gehner, A.: "Amorphous TiAl films for micromirror arrays with stable analog deflection integrated on complementary metal oxide semiconductors," J. Micro/Nanolith. MEMS MOEMS, 7(2), 2008.

[154] Caronti, A., et al.: "An accurate model for capacitive micromachined ultrasonic transducers," IEEE Trans. Ultrason., Ferroelect., Freq. Contr., Vol. 49, No. 2, pp. 159–168, 2002.

[155] Wygant, I. O.; Kupnik, M.; Khuri-Yakub, B. T.: "An Analytical Model for Capacitive Pressure Transducers With Circular Geometry," J. Microelectromech. Syst., Vol. 27, No. 3, pp. 448–456, 2018.

[156] Haller, M. I.; Khuri-Yakub, B. T.: "A surface micromachined electrostatic ultrasonic air transducer," IEEE Trans. Ultrason., Ferroelect., Freq. Contr., Vol. 43, No. 1, pp. 1–6, 1996.

[157] Ventsel, E.: "Thin plates and shells: Theory, analysis, and applications," New York, Marcel Dekker, 2001.

[158] Tovstik, P.; Tovstik, T. M.: "Bending Stiffness of a Multilayered Plate," Papadrakakis (Ed.), 6.2016 – Proceedings of the VII European, pp. 3423–3435, 10.7712/100016.2045.10142.

[159] Pursula, P., et al.: "Analytical electromechanical model for CMUTs with multi-layered, non-uniform diaphragm," 23rd Micromechanics and Microsystems Europe Workshop, MME 2012 - Ilmenau, Germany

[160] Leissa, A. W.: "Vibration of Plates," Scientific and Technical Information Division, National Aeronautics and Space Administration, 1969.

[161] Keithley: "Impedance Measurement Handbook," USA, 11.2016.

[162] Brenner, K., et al.: "Advances in Capacitive Micromachined Ultrasonic Transducers," Micromachines, Vol. 10, No. 2, 2019.

[163] MathWorks: "Findpeaks: Returns a vector with the local maxima (peaks) of the input signal vector, data.," https://de.mathworks.com/help/signal/ref/findpeaks.html,

[164] Keithley: "Model 2450 Interactive SourceMeter® Instrument Specifications," Keithley Instruments, Inc. Cleveland, Ohio, 2017. https://download.tek.com/manual/SPEC-2450B_November_2017.pdf, Accessed: 20.01.2023.

[165] Keysight Inc.: "E4990A Impedance Analyzer Help," 2015.

[166] Keysight Inc.: "E4990A Impedance Analyzer Brochure," 06.2015.

[167] Fischer, B.: "Optical microphone hears ultrasound," Nature Photonics, Vol. 10, No. 6, pp. 356–358, 2016.

[168] XARION Laser Acoustics: "Eta450-ultra," https://xarion.com/de/produkte/eta450-ultra, Accessed: 31.08.22.

[169] Rus, J.; Grosse, C. U.: "Thickness measurement via local ultrasonic resonance spectroscopy," Ultrasonics, Vol. 109, p. 106261, 2021.

[170] Köble, S.: "Walther, Sonja; Kling, Christoph (2021): Charakterisierung von optischen Mikrofonen. Tagungsband der DAGA 2021. Deutsche Gesellschaft für Akustik. Berlin: Deutsche Gesellschaft für Akustik e.V. (DEGA)," Schriftlich, 08.2022.

[171] Köble, S., et al.: "Infrastructure for manufacturing and testing of megahertz ultrasound metamaterials," 47. Jahrestagung für Akustik - DAGA 2021

[172] Dongzhe He: "Lifetime Measurement for NED-Micropositioning Systems," Master's Thesis, Fraunhofer Institute for Photonic Microsystdems, Institute of Microtechnology, Faculty of Engineering, Technische Universität Braunschweig, 2022.

[173] Saleh, B. E. A.; Teich, M. C.: "Fundamentals of Photonics," United States of America, John Wiley & Sons, Inc., 1991.

[174] Correa, D. S., et al.: "Two-Photon Polymerization Fabrication of Doped Microstructures," Polymerization, Souza Gomes, A. (Ed.), InTech, 2012, 10.5772/36061.

[175] Feng, S.; Winful, H. G.: "Physical origin of the Gouy phase shift," Opt. Lett., Vol. 26, No. 8, p. 485, 2001.

[176] Hecht, E.: "Optics," 4th ed., Reading Mass., Addison-Wesley, 2002.

[177] Gaudet, M.; Arscott, S.: "A user-friendly guide to the optimum ultraviolet photolithographic exposure and greyscale dose of SU-8 photoresist on common MEMS, microsystems, and microelectronics coatings and materials," Anal. Methods, Vol. 9, No. 17, pp. 2495–2504, 2017.

[178] Emami, N.; Söderholm, K.-J. M.; Berglund, L. A.: "Effect of light power density variations on bulk curing properties of dental composites," Journal of Dentistry, Vol. 31, No. 3, pp. 189–196, 2003.

[179] Sharipova, M. I., et al.: "Effect of pyrolysis on microstructures made of various photoresists by two-photon polymerization: comparative study," Opt. Mater. Express, Vol. 11, No. 2, p. 371, 2021.

[180] Waller, E. H.; Freymann, G. von: "Spatio-Temporal Proximity Characteristics in 3D μ-Printing via Multi-Photon Absorption," Polymers, Vol. 8, No. 8, 2016.

[181] Schenk, H., et al.: "Single crystal silicon micro mirrors," phys. stat. sol. (c), Vol. 6, No. 3, pp. 728–735, 2009.

[182] Meisel, D. C., et al.: "Shrinkage Precompensation of Holographic Three-Dimensional Photonic-Crystal Templates," Advanced Materials, Vol. 18, No. 22, pp. 2964–2968, 2006.

[183] Bauhofer, A. A., et al.: "Harnessing Photochemical Shrinkage in Direct Laser Writing for Shape Morphing of Polymer Sheets," Advanced materials (Deerfield Beach, Fla.), Vol. 29, No. 42, 2017.

[184] Schmid, M.; Ludescher, D.; Giessen, H.: "Optical properties of photoresists for femtosecond 3D printing: refractive index, extinction, luminescence-dose dependence, aging, heat treatment and comparison between 1-photon and 2-photon exposure," Opt. Mater. Express, Vol. 9, No. 12, p. 4564, 2019.

[185] Palik, E. D.: "Handbook of optical constants of solids," Orlando, Academic Press, 1985.

[186] Muller, R. S.; Kamins, T. I.; Chan, M.: "Device electronics for integrated circuits," 3rd ed., New York, Chichester, Wiley, 2003.

[187] Lehmuskero, A.; Kuittinen, M.; Vahimaa, P.: "Refractive index and extinction coefficient dependence of thin Al and Ir films on deposition technique and thickness," Optics express, Vol. 15, No. 17, pp. 10744–10752, 2007.

[188] Rodríguez-de Marcos, L. V., et al.: "Self-consistent optical constants of SiO_2 and Ta_2O_5 films," Opt. Mater. Express, Vol. 6, No. 11, p. 3622, 2016.

[189] Petrişor, T., et al.: "Itinerant antiferromagnetism of TiAl alloys," Journal of Magnetism and Magnetic Materials, Vol. 59, 3-4, pp. 309–315, 1986.

[190] Wapler, M. C., et al.: "Magnetic properties of materials for MR engineering, micro-MR and beyond," Journal of magnetic resonance (San Diego, Calif. : 1997), Vol. 242, pp. 233–242, 2014.

[191] Aspnes, D. E.; Studna, A. A.: "Dielectric functions and optical parameters of Si, Ge, GaP, GaAs, GaSb, InP, InAs, and InSb from 1.5 to 6.0 eV,"

[192] Gao, L.; Lemarchand, F.; Lequime, M.: "Refractive index determination of SiO_2 layer in the UV/Vis/NIR range: spectrophotometric reverse engineering on single and bi-layer designs," JEOS:RP, Vol. 8, 2013.

[193] Mueller, J. B., et al.: "In-situ local temperature measurement during three-dimensional direct laser writing," Appl. Phys. Lett., Vol. 103, No. 12, p. 123107, 2013.

[194] Bird, R. B.; Stewart, W. E.; Lighfoot, E. N.: "Transport phenomena," New York, John Wiley, 1960.

[195] Yamamoto, O.; Kambe, H.: "Thermal Conductivity of Cross-linked Polymers. A Comparison between Measured and Calculated Thermal Conductivities," Polym J, Vol. 2, No. 5, pp. 623–628, 1971.

[196] Schmidt, J.-U.: "Material data," Fraunhofer IPMS, 09.2009.

[197] Büttgenbach, S.: "Mikromechanik," Stuttgart, B.G. Teubner, 1991.

[198] Ericsson, P.: "Thermal conductivity of amorphous TiAl thin films," Acreo Report, 2009.

[199] David R. (Ed.): "CRC Handbook of Chemistry and Physics: A Ready-Reference of Chemical and Physical Data," 85th ed., Boca Raton, CRC Press LLC, 2005.

[200] Piątkowski, J.; Przeliorz, R.; Jabłońska, M.: "The Specific Heat Capacity and Oxidation Kinetics of NiAl, FeAl and TiAl Alloys," SSP, 203-204, pp. 431–434, 2013.

[201] Koller, R.: "Konstruktionslehre für den Maschinenbau: Grundlagen zur Neu- und Weiterentwicklung technischer Produkte mit Beispielen," 3rd ed., Berlin, Heidelberg, Springer, 1994.

[202] Bělehrádek, J.: "Temperature Coefficients in Biology," Biological Reviews, Vol. 5, No. 1, pp. 30–58, 1930.

[203] Skliutas, E., et al.: "X-photon laser direct write 3D nanolithography," 2022.

[204] Borók, A.; Laboda, K.; Bonyár, A.: "PDMS Bonding Technologies for Microfluidic Applications: A Review," Biosensors, Vol. 11, No. 8, 2021.

[205] Ye, X., et al.: "Research on the selective adhesion characteristics of polydimethylsiloxane layer," AIP Advances, Vol. 8, No. 9, p. 95004, 2018.

[206] Holl, S. L., et al.: "UV Activation Treatment for Hydrophobic Wafer Bonding," J. Electrochem. Soc., Vol. 153, No. 7, G613, 2006.

[207] Martinson, E. and Lusk, J.: "Mechanical Design for 3D Printing," http://eikimartinson.com/engineering/3dparts/#dovetail, Accessed: 11.2012.

[208] Wang, Y., et al.: "Strong Wet and Dry Adhesion by Cupped Microstructures," ACS Applied Materials & Interfaces, Vol. 11, No. 29, pp. 26483–26490, 2019.

[209] Geometrische Produktspezifikation Oberflächenbeschaffenheit: Flächenhaft Teil 1: Angabe von Oberflächenbeschaffenheit, DIN EN ISO 25178-1:2016-12.

[210] Airaksinen, V.-M.: "Handbook of silicon based mems materials and technologies," William Andrew Publishing, 2015.

[211] Lange, N.: "Wafer bow," E-Mail, 05.2022.

[212] Thorlabs GmbH: "Slip-Stick Motor," https://www.thorlabs.com/newgrouppage9.cfm?objectgroup_ID=9776&pn=PIAK10, Accessed: 20.04.2022.

[213] Schweiger, S., et al.: "Two-Photon Lithography Parameter Study for Manufacturing of Acoustic Metamaterials on MEMS: MikroSystemTechnik Kongress 2021 Mikroelektronik/ Mikrosystemtechnik und ihre Anwendungen Innovative Produkte für zukunftsfähige Märkte 08. - 10. November 2021, Stuttgart-Ludwigsburg," 1st ed., Berlin, VDE Verlag GmbH, 2021.

[214] DIN EN 60529 Schutzarten durch Gehäuse, IEC 60529:1989.

[215] Webster, A. G.: "Acoustical Impedance and the Theory of Horns and of the Phonograph," Proceedings of the National Academy of Sciences of the United States of America, Vol. 5, No. 7, pp. 275–282, 1919.

[216] Lerch, R.; Sessler, G. M.; Wolf, D.: "Technische Akustik: Grundlagen und Anwendungen," Berlin, Springer, 2009.

[217] Köble, S.: "Long term frequency and capacity drift characterization report," 02.2021.

[218] Brotzu, A., et al.: "Mechanical properties of a TiAl-based alloy at room and high temperatures," Materials Science and Technology, Vol. 34, No. 15, pp. 1847–1853, 2018.

[219] Pirouz, A.; Degertekin, F. L.: "Low Temperature CMUT Fabrication Process with Dielectric Lift-off Membrane Support for Improved Reliability," J. Micromech. Microeng., Vol. 28, No. 8, 2018.

[220] Wang, M., et al.: "Fabrication and characterization of surface micromachined CMUT with a bossed membrane," 2008 IEEE Ultrasonics Symposium, IEEE, 2008, pp. 394–397, 10.1109/ULTSYM.2008.0097.

[221] Shashank: "Actuation of NED-µPS after AMOC.," Oral, 06.2022.

[222] Schenk, H., et al.: "A contribution to the expansion of the applicability of electrostatic forces in micro transducers," MOEMS and Miniaturized Systems XVI, SPIE, 2017, p. 1011603, 10.1117/12.2249575.

[223] Gaudet, M., et al.: "Electrostatic bending actuators with a liquid filled nanometer scale gap," 2017 IEEE 30th International Conference on Micro Electro Mechanical Systems (MEMS), IEEE, 2017, pp. 175–178, 10.1109/MEMSYS.2017.7863369.

[224] GeSiM – Gesellschaft für Silizium-Mikrosysteme mbH: "Micro-contact-printer," https://gesim-bioinstruments-microfluidics.com/micro-contact-printer/, Accessed: 08.11.2022.

[225] Min, K., et al.: "Fabrication of Perforated PDMS Microchannel by Successive Laser Pyrolysis," Materials (Basel, Switzerland), Vol. 14, No. 23, 2021.

[226] Männel, M. J., et al.: "Optimizing Process Parameters in Commercial Micro-Stereolithography for Forming Emulsions and Polymer Microparticles in Nonplanar Microfluidic Devices," Adv. Mater. Technol., Vol. 4, No. 1, p. 1800408, 2019.

[227] Mandal, S., et al.: "Gold-nanoparticle-embedded microchannel array for enhanced power generation," Lab on a Chip, Vol. 20, No. 15, pp. 2717–2723, 2020.

[228] Zhou, L.; Zhuang, G.; Li, G.: "A facile method for the fabrication of glass-PDMS-glass sandwich microfluidic devices by sacrificial molding," Sensors and Actuators B: Chemical, Vol. 261, pp. 364–371, 2018.

[229] Abdelgawad, M., et al.: "A fast and simple method to fabricate circular microchannels in polydimethylsiloxane (PDMS)," Lab on a Chip, Vol. 11, No. 3, pp. 545–551, 2011.

[230] The Dow Chemical Company: "PGMEA Technical Data Sheet, 2012.

[231] Jaiswal, A., et al.: "Two decades of two-photon lithography: Materials science perspective for additive manufacturing of 2D/3D nano-microstructures," iScience, Vol. 26, No. 4, p. 106374, 2023.

[232] Hahn, V., et al.: "Light-sheet 3D microprinting via two-colour two-step absorption," Nature Photonics, Vol. 16, No. 11, pp. 784–791, 2022.

[233] Peixoto, C., et al.: "Injection molding of high-precision optical lenses: A review," Precision Engineering, Vol. 76, pp. 29–51, 2022.

[234] Baldacchini, T.; Zadoyan, R.: "In situ and real time monitoring of two-photon polymerization using broadband coherent anti-Stokes Raman scattering microscopy," Optics express, Vol. 18, No. 18, pp. 19219–19231, 2010.

[235] DebRoy, T., et al.: "Metallurgy, mechanistic models and machine learning in metal printing," Nat Rev Mater, Vol. 6, No. 1, pp. 48–68, 2021.

[236] Nanoscribe GmbH & Co. KG: "MSDS IP-Q," 05.2021.

[237] Nanoscribe GmbH & Co. KG: "MSDS IP-PDMS," 05.2021.

Publications

Parts of the present thesis have already been published. The following is a list of the publications, the author contributed to during the creation of the present thesis.

Patents

Schweiger, S.; Koch, S. G.; Grafe, M.; Lange, N.; Amelung, J.:
"An impedance matching device, a converter device, and a method of manufacturing an impedance matching device," DE102018206937A1.

Peer-Reviewed Contributions

Schweiger, S.; Schulze, T.; Schlipf, S.; Reinig, P.; Schenk, H.:
"Characterization of two-photon-polymerization lithography structures via Raman spectroscopy and nanoindentation," J. Optical Microsystems, Vol. 2, No. 03, 2022.

Melnikov, A.; Köble, S.; **Schweiger, S.**; Chiang, Y.; Marburg, S.; Powell, D.:
"Microacoustic Metagratings at Ultra-High Frequencies Fabricated by Two-Photon Lithography," Advanced Science, p. 2200990, 2022.

Conference Contributions

Schweiger, S.; Koch, S. G.:
"A Review of Acoustic Impedance Matching Methods to Validate Additive Manufactured Metamaterial for Capacitive Micromachined Ultrasonic Transducers," 41st International Spring Seminar 2018, 10.1109/ISSE.2018.8443702.

Schweiger, S.; Koch, S. G.; Schenk, H.:
"Two-Photon-Lithography Substrate Reflection and Absorption Compensation for Additive Manufacturing of Metamaterials on MEMS," 2021 44th International Spring Seminar on Electronics Technology (ISSE), IEEE, 552021, pp. 1–7, 10.1109/ISSE51996.2021.9467575.

Köble, S.; **Schweiger, S.**; Melnikov, A.; Ziebarth, J.; Koch, S. G.:
“Infrastructure for manufacturing and testing of megahertz ultrasound metamaterials”, 47. Jahrestagung für Akustik – DAGA, 2021, https://www.dega-akustik.de/fileadmin/dega-akustik.de/publikationen/DAGA/DAGA_21_Inhalt.pdf

Köble, S.; **Schweiger, S.**; Koch, S. G.:
"Beeinflussung des Schallfeldes durch Housing von Kapazitiven Mikromechanischen Ultraschallwandlern (CMUTs)," MikroSystemTechnik Congress. https://www.vde-verlag.de/proceedings-de/455656104.html, 2021.

Schweiger, S.; Melnikov, A.; Koch, S. G.; Schenk, H.:
"Two-Photon Lithography Parameter Study for Manufacturing of Acoustic Metamaterials on MEMS: MikroSystemTechnik Kongress 2021 Mikroelektronik/ Mikrosystemtechnik und ihre Anwendungen Innovative Produkte für zukunftsfähige Märkte 08. - 10. November 2021, Stuttgart-Ludwigsburg," 1st ed., Berlin, VDE Verlag GmbH, 2021.

Original Contributions

I, Severin Schweiger, as author of this dissertation, hereby declare which share I contributed to the creation of the present thesis.

Selection, setup and preparation of process equipment and materials, was largely based on my research and comparison of possible options before the acquisition of the TPP system employed in this work, in consultation with the strategic leaders of the Fraunhofer IPMS, see chapter 2. The selection of chip substrates was informed by strategic considerations by the department heads and performed by me, in consultation with the respective technologists of the Ultrasonic Components and Monolithically Integrated Actuator groups of Fraunhofer IPMS.

The requirements to the CMUT die assembly were established by my experiments and the design changes were results of the cooperation with the assembly companies mentioned in section 3.1.2. The electrical and acoustic measurement setups were established and operated by the Ultrasonic Components group of Fraunhofer IPMS, see section 3.1.3 and 3.1.4.

The simulations and experiments presented in sections 4.2, 4.3, and 4.4 were conceived, designed, performed, characterized and evaluated by me.

The simulations and calculations presented in section 5.1, 5.2 and 5.3 were conceived, designed, performed and evaluated by me. The test structure designs presented in section 5.4 were created by me. The experiments presented in the same section were conceived, designed, performed, characterized and evaluated by me, excluding the characterization of the experiments presented in section 5.4.3, which were performed by a student colleague of the Sensory Micro Module group of Fraunhofer IPMS. The experiment presented in section 5.5 was conceived, designed, performed, characterized and evaluated by me. The calculations and experiments presented in section 5.6 were conceived, designed, performed, characterized and evaluated by me. The compensation upgrade concept, design, fabrication and characterization was performed by me, excluding the Al part fabrication, which was performed by the workshop staff of Fraunhofer IPMS, see section 5.6.4.

The experiments presented in sections 6.1, 6.2, 6.3 and 6.4 were conceived, designed, performed, characterized and evaluated by me. The experiments presented in sections 6.5.3, 6.5.2, 6.5.3 were conceived, designed, performed and evaluated by me. Their characterization was performed by the Ultrasonic Components group of Fraunhofer IPMS.

The experiment presented in sections 7.1.1, 7.1.2 and 7.1.3 was conceived, designed and evaluated in cooperation with two colleagues of the Monolithically Integrated Actuator and Sensor Systems business unit. The experiment was performed and characterized optically by me and characterized electrically by the same colleagues. The experiment presented in section 7.1.4 was conceived, designed, performed, characterized and evaluated by me. The experiment presented in section 7.2.1 was conceived, designed, performed and evaluated by me, characterization was performed by a student colleague of the Sensory Micro Module group of Fraunhofer IPMS. The experiment presented in section 7.2.2 was conceived and designed and partly evaluated by me. It was performed, characterized and partly evaluated by a student colleague of the Sensory Micro Module group of Fraunhofer IPMS. The contact angle measurements were performed by colleagues of the Engineering, Manufacturing & Test business unit of Fraunhofer IPMS.

Annex

A. Drop Casting Methods – Section 2.3.2

Fig. A 1 shows a comparison of the drop casting methods used in this work at the example of IP-Dip. The manual method uses a spatula, the automatic one uses the dispense mechanism of the FINEPLACER system with two different nozzle tip sizes.

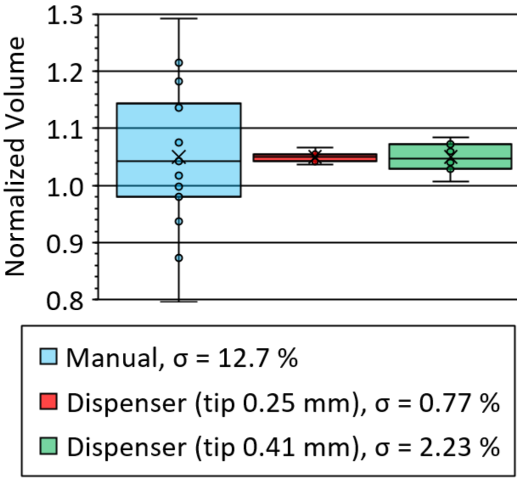

Fig. A 1: Comparison of the deviation of drop casting methods.

The measurements were performed on the scale PX225D (OHAUS Corporation), which showed a standard deviation of 14.46 µg. The single drop weight of IP-Dip was measured for 15 specimen and resulted in (87.1 ± 1.1) mg. For IP-PDMS, (6.28 ± 0.70) mg was determined for ten specimen by using the syringe the material comes in. The lower deviation and drop size most likely is due to the lower viscosity.

B. Photoresist contents – Section 2.3.5

IP-Q contains >95 % 7,7,9/7,9,9-trimethyl-4,13-dioxo-3,14-dioxa-5,12-diazahexadecane-1,16-diyl bismethacrylate, <2 % Bis(2-methacryloxyethyl)-N,N'-1,9-nonylene biscarbamate, and <1 % 2,6-Di-tert-4-butylhydroxytoluol [236].

IP-Dip contains 60-80 % aliphatic alcohol containing acrylates, <24 % hydrocarbon acrylate, <24 % acrylate- and polyether containing alicyclic hydrocarbon and <10 % other components [148].

IP-PDMS contains >90 % (acryloxypropyl)methylsiloxane dimethylsiloxane copolymer, >5 % N,N-dioctyl-1-octanamin and <5 % 3-acryloxy-2-hydroxypropoxypropyl terminated by poly(dimethylsiloxane) [237]. IP-PDMS is an elastomer, a polymer with viscoelasticity. IP-Dip and -Q however are thermoset polymers, all three cannot be reshaped via melting.

C. Bias-Tee – Section 3.1.3

The bias-tee shown in Fig. A 2 as described as the external DC voltage bias protection circuit in the impedance analyzer manual [161]. The shielded high current H_c, low current L_c, high potential H_p and low potential L_p connections lead to the impedance analyzer.

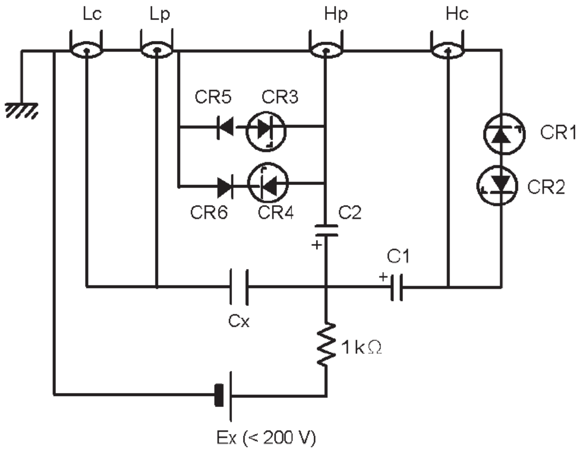

where Cx: Sample capacitor

Ex: External DC bias voltage source

C1: Blocking capacitor

Capacitance value $\geq \dfrac{1}{10\pi f}$

(f: measurement frequency (Hz))

DC withstand voltage: > Ex

C2: Blocking capacitor

Capacitance value: 1 μF

DC withstand voltage: Ex

CR1, CR2: Diode-zener, 47 V, 5% 1 W

CR3, CR4: Diode-zener, 3.3 V, 5% 1 W

CR5, CR6 : Diode-power, 200 V, 1 A

Fig. A 2: Bias-Tee including external voltage source [161].

D. Sound Power Level – Section 3.1.4

Recalculation of the sound pressure p measured using the Eta450 Ultra into sound pressure level L_p relative to the reference sound pressure p_0 of 20 µPa using the following equation.

$$L_p = 20\log_{10}\left(\frac{p}{p_0}\right)$$

The standard deviation of the sound pressure σ_p was also recalculated to indicate the sound pressure level deviation σ_L using following equation.

$$\sigma_L = 20\log_{10}\left(\frac{p+\sigma_p}{p_0}\right) - L_p$$

E. Reflectance Derivation and Optical Fundamentals – Section 5.1

The Maxwell equations for monochromatic light in a linear, homogeneous, isotropic, nondispersive and source-free medium are [173, S. 168]

$$\vec{\nabla} \times \vec{\mathrm{H}} = j\omega\varepsilon\vec{\mathrm{E}}$$
$$\vec{\nabla} \times \vec{\mathrm{E}} = -j\omega\mu\vec{\mathrm{H}}$$
$$\vec{\nabla} \cdot \vec{\mathrm{H}} = 0$$
$$\vec{\nabla} \cdot \vec{\mathrm{E}} = 0$$

with the curl operator $\vec{\nabla}\times$, the magnetic field $\vec{\mathrm{H}}$, the angular frequency ω, the permittivity ε, the electrical field $\vec{\mathrm{E}}$, the magnetic permeability μ and the divergence operator $\vec{\nabla}\cdot$. Considering a uniform plane sinusoidal electromagnetic wave [173, S. 170]

$$\vec{\mathrm{E}}(\vec{z}) = E_0 e^{-j\vec{k}\cdot\vec{z}}$$
$$\vec{\mathrm{H}}(\vec{z}) = H_0 e^{-j\vec{k}\cdot\vec{z}}$$

with the respective magnitudes E_0 and H_0, the wave vector $\vec{k}$ with its magnitude $k = \omega\sqrt{\varepsilon\mu}$. Substitution of the previous equations into the Maxwell equations [173, S. 170] provides

$$\vec{k} \times \vec{\mathrm{H}}_0 = -\omega\varepsilon\vec{\mathrm{E}}_0$$
$$\vec{k} \times \vec{\mathrm{E}}_0 = \omega\mu\vec{\mathrm{H}}_0$$

Thus, the magnitudes can be written as [173, S. 170][173, S. 170]

$$H_0 = \sqrt{\frac{\varepsilon}{\mu}}E_0$$

where, due to the conservation law and assuming continuous fields, the incident (i), reflected (r) and transmitted (t) fields at the interface can be written as [173, S. 205]

$$E_i + E_r = E_t$$
$$H_i cos\theta_i + H_r cos\theta_i = H_t cos\theta_t$$

with the angle of the beams to the orthogonal θ. Combining the previous equations and assuming normal incidence

$$1 + r = t$$
$$\sqrt{\frac{\varepsilon_i}{\mu_i}} + \sqrt{\frac{\varepsilon_i}{\mu_i}}r = \sqrt{\frac{\varepsilon_t}{\mu_t}}t$$

where the subscripts i and t refer to the materials through which the incident and transmitted beam travels, respectively. The reflectance coefficient can then be calculated as [173, S. 209]

$$R = |r|^2 = \left|\frac{\sqrt{\frac{\varepsilon_1}{\mu_1}} - \sqrt{\frac{\varepsilon_2}{\mu_2}}}{\sqrt{\frac{\varepsilon_1}{\mu_1}} + \sqrt{\frac{\varepsilon_2}{\mu_2}}}\right|^2$$

By using $\mu = \mu_0\mu_r$, $\varepsilon = \varepsilon_0\varepsilon_r$ and [173, S. 163]

$$n = \sqrt{\varepsilon_r\mu_r}$$

with the magnetic and electric constants μ_0 and ε_0 and the relative magnetic permeability μ_r and relative permittivity ε_r, the reflectance coefficient becomes

$$R = \left|\frac{\hat{n}_i\mu_t - \hat{n}_t\mu_i}{\hat{n}_i\mu_t + \hat{n}_t\mu_i}\right|^2 = rr^*$$

The relative permeability depends on volume magnetic susceptibility χ, as $\mu_r = \chi + 1$. The extinction coefficient of photoresists employed in the present work was calculated from the measurements in [184] by

$$\kappa = \frac{\ln{(T_m)}\lambda}{4\pi}$$

where T_m is the measured transmission and λ is the wavelength, here 780 nm. The complex reflectance r can be written with its conjugate r^* as

$$r = Re(r) + iIm(r) = \frac{r + r^*}{2} + i\frac{r - r^*}{2i}$$

The real part of reflectance can then be written as

$$Re(r) = \frac{1}{2}\left(\frac{(n_i + i\kappa_i)\mu_t - (n_t + i\kappa_t)\mu_i}{(n_i + i\kappa_i)\mu_t + (n_t + i\kappa_t)\mu_i} + \frac{(n_i - i\kappa_i)\mu_t - (n_t - i\kappa_t)\mu_i}{(n_i - i\kappa_i)\mu_t + (n_t - i\kappa_t)\mu_i}\right)$$

Substituting with

$$a = (n_i + i\kappa_i)\mu_t$$
$$b = (n_t + i\kappa_t)\mu_i$$
$$c = (n_i - i\kappa_i)\mu_t$$
$$d = (n_t - i\kappa_t)\mu_i$$

yields

$$Re(r) = \frac{1}{2}\left(\frac{a-b}{a+b} + \frac{c-d}{c+d}\right)$$
$$Re(r) = \frac{ac - bd}{ac + ad + bc + bd}$$

with

$$ac = (n_i^2 + \kappa_i^2)\mu_t^2$$
$$bc = \mu_i\mu_t(n_i n_t - i n_t\kappa_i + i n_i\kappa_t + \kappa_i\kappa_t)$$
$$bd = (n_t^2 + \kappa_t^2)\mu_i^2$$
$$ad = \mu_i\mu_t(n_i n_t + i n_t\kappa_i - i n_i\kappa_t + \kappa_i\kappa_t)$$

Back substitution leads to

$$Re(r) = \frac{(n_i^2 + \kappa_i^2)\mu_t^2 - (n_t^2 + \kappa_t^2)\mu_i^2}{(n_i^2 + \kappa_i^2)\mu_t^2 - (n_t^2 + \kappa_t^2)\mu_i^2 + 2\mu_i\mu_t(n_i n_t + \kappa_i\kappa_t)}$$
$$Re(r) = \frac{(n_i^2 + \kappa_i^2)\mu_t^2 - (n_t^2 + \kappa_t^2)\mu_i^2}{(n_i\mu_i + n_t\mu_i)^2 + (\kappa_i\mu_i + \kappa_t\mu_i)^2}$$

The imaginary part of reflectance can similarly be written as

$$Im(r) = \frac{1}{2i}\left(\frac{(n_i + i\kappa_i)\mu_t - (n_t + i\kappa_t)\mu_i}{(n_i + i\kappa_i)\mu_t + (n_t + i\kappa_t)\mu_i} - \frac{(n_i - i\kappa_i)\mu_t - (n_t - i\kappa_t)\mu_i}{(n_i - i\kappa_i)\mu_t + (n_t - i\kappa_t)\mu_i}\right)$$

Substituting with

$$a = (n_i + i\kappa_i)\mu_t$$

$$b = (n_t + i\kappa_t)\mu_i$$
$$c = (n_i - i\kappa_i)\mu_t$$
$$d = (n_t - i\kappa_t)\mu_i$$

yields

$$Im(r) = \frac{1}{2i}\left(\frac{a-b}{a+b} - \frac{c-d}{c+d}\right)$$
$$Im(r) = \frac{1}{i}\frac{ad-bc}{ac+ad+bc+bd}$$

with

$$ac = (n_i^2 + \kappa_i^2)\mu_t^2$$
$$bc = \mu_i\mu_t(n_i n_t - i n_t\kappa_i + i n_i\kappa_t + \kappa_i\kappa_t)$$
$$bd = (n_t^2 + \kappa_t^2)\mu_i^2$$
$$ad = \mu_i\mu_t(n_i n_t + i n_t\kappa_i - i n_i\kappa_t + \kappa_i\kappa_t)$$

Back substitution leads to

$$Im(r) = \frac{2\mu_i\mu_t(n_t\kappa_i - n_i\kappa_t)}{(n_i\mu_i + n_t\mu_i)^2 + (\kappa_i\mu_i + \kappa_t\mu_i)^2}$$

F. Substrate backside Reflection – Section 5.1

The contributions from substrate backside reflection are illustrated in Fig. A 3.

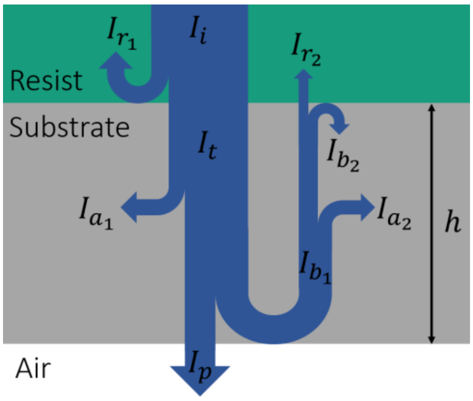

Fig. A 3: Flowchart of the reflection and absorption processes of the fabrication laser beam interacting with a plate of thickness h = 520 nm above air and coated with resist. Not to scale, including the intensities: reflected I_{r_1}, transmitted I_t, absorbed I_{a_1}, passing I_p, backside reflected I_{b_1}, absorbed I_{a_2}, frontside reflected I_{b_2} and the effective backside reflected I_{r_2}.

Material dependent contribution from substrate backside reflections to the dose at the voxel calculated for a plate of thickness h = 520 nm and the 63x and 10x objectives with IP-Dip and IP-Q, respectively.

The reflection and absorption processes of the fabrication laser beam interacting with a plate are illustrated in Fig. A 3 and the calculation input and output values are listed in Tab. 2.2, Tab. 2.3 and Tab. 5.3., as well as Tab. A 1. The latter contains the material dependent values for TiAl, Si, SiO_2 and Al, as well as the resulting percentage of the incident dose represented by the effective backside reflection for the 63x and 10x objectives.

Tab. A 1: Input and output values of the reflection and absorption process calculation for various plate materials.

Material	TiAl	Si	SiO_2	Al
I_{r_1}/I_i Reflected fraction (IP-Dip) [%]	59.6	35.7	4.81	88.5
I_t/I_i Transmitted fraction (IP-Dip) [%]	40.4	64.3	95.2	11.5
I_{a_1}/I_i Absorbed fraction (IP-Dip) [%]	40.4	3.53	1.02	11.5
I_p/I_i Passing fraction (IP-Dip) [%]	0.00	40.7	90.7	0.00
I_{b_1}/I_i Backside refl. fraction (IP-Dip) [%]	0.00	20.1	3.45	0.00
I_{a_2}/I_i Absorbed fraction (IP-Dip) [%]	0.00	1.10	0.04	0.00
I_{b_2}/I_i Frontside refl. fraction (IP-Dip) [%]	0.00	6.78	0.16	0.00
I_{r_2}/I_i Effective backside reflected fraction (IP-Dip) [%]	0.00	12.2	3.24	0.00
D_{r_2}/D_i Eff. Backside reflected fraction of the dose (IP-Dip) [%]	0.00	0.01	0.00	0.00
D_{r_2}/D_i Eff. Backside reflected fraction of the dose (IP-Q) [%]	0.00	0.02	0.00	0.00

G. Intensity Calculation – Section 5.1

Calculation of the incident intensity I_i in the focal point $(r = 0, z = 0)$, including OPA in the resist for the path of the working distance d_{WD}, see equ. 4.10:

$$I_i = e^{-\alpha d_{WD}}$$

Intensity I_r reflected by the substrate, back to the focal point, including the substrate reflectance R as well as the OPA for the path of the working distance d_{WD} and double the distance between focal point and substrate z_{fs}:

$$I_r = R \frac{1}{1 + \left(\frac{2z_{fs}}{z_r}\right)^2} e^{-\alpha(d_{WD}+2z_{fs})}$$

Intensity I_t transmitted into the substrate, including the transmittance of the substrate T as well as the OPA for the path of the working distance d_{WD} and the distance between focal point and substrate z_{fs}:

$$I_t = T \frac{1}{1 + \left(\frac{z_{fs}}{z_r}\right)^2} e^{-\alpha(d_{WD}+z_{fs})}$$

H. Heat Maps – Section 5.4.2

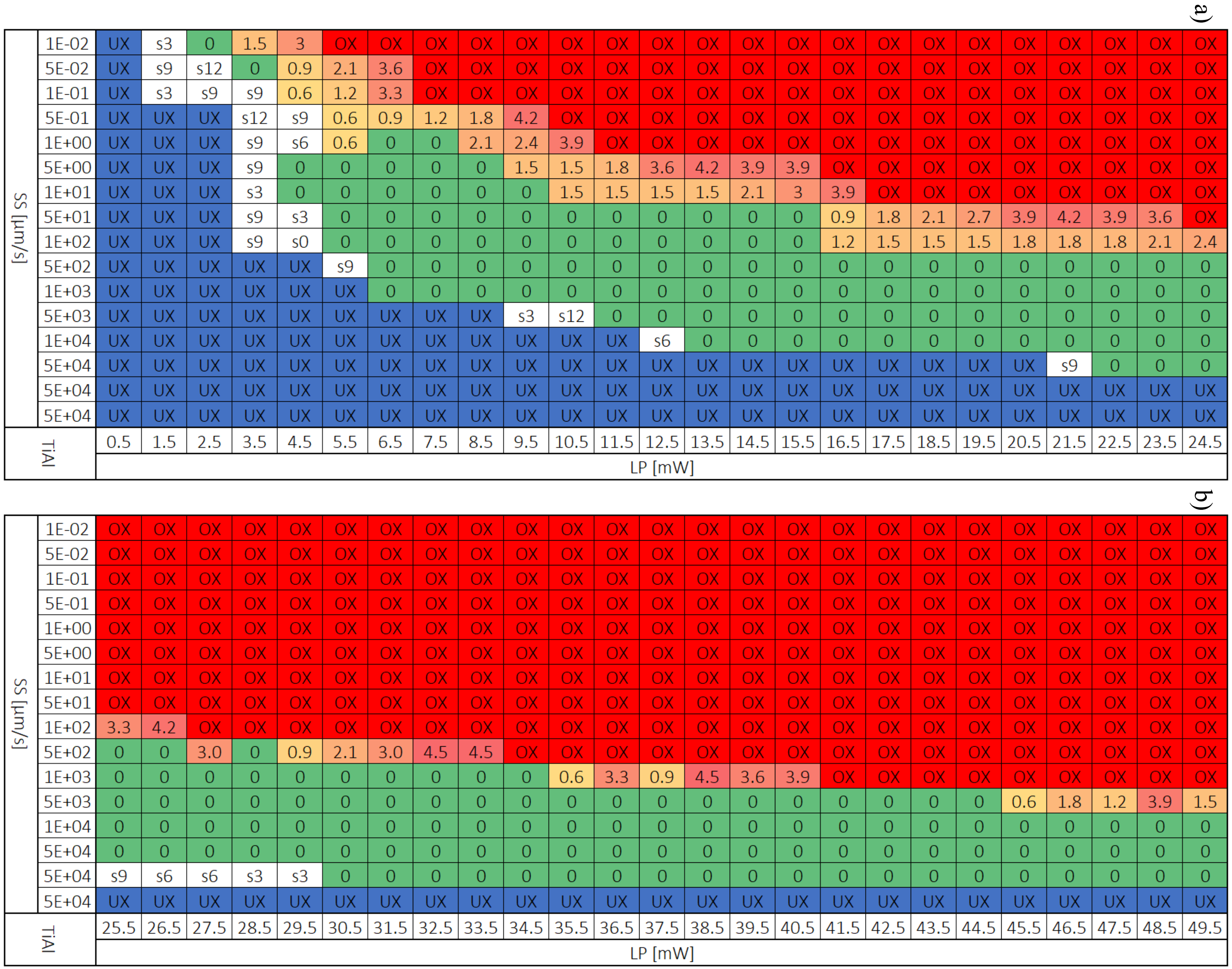

a)

SS [µm/s]	LP [mW]																								
TiAl	0.5	1.5	2.5	3.5	4.5	5.5	6.5	7.5	8.5	9.5	10.5	11.5	12.5	13.5	14.5	15.5	16.5	17.5	18.5	19.5	20.5	21.5	22.5	23.5	24.5
1E-02	UX	s3	0	1.5	3	OX	OX	OX	OX	OX	OX	OX	OX	OX	OX	OX	OX	OX	OX	OX	OX	OX	OX	OX	OX
5E-02	UX	s9	s12	0	0.9	2.1	3.6	OX	OX	OX	OX	OX	OX	OX	OX	OX	OX	OX	OX	OX	OX	OX	OX	OX	OX
1E-01	UX	s3	s9	s9	0.6	1.2	3.3	OX	OX	OX	OX	OX	OX	OX	OX	OX	OX	OX	OX	OX	OX	OX	OX	OX	OX
5E-01	UX	UX	UX	s12	s9	0.6	0.9	1.2	1.8	4.2	OX	OX	OX	OX	OX	OX	OX	OX	OX	OX	OX	OX	OX	OX	OX
1E+00	UX	UX	UX	s9	s6	0.6	0	0	2.1	2.4	3.9	OX	OX	OX	OX	OX	OX	OX	OX	OX	OX	OX	OX	OX	OX
5E+00	UX	UX	UX	s9	0	0	0	0	0	1.5	1.5	1.8	3.6	4.2	3.9	3.9	OX	OX	OX	OX	OX	OX	OX	OX	OX
1E+01	UX	UX	UX	s3	0	0	0	0	0	0	1.5	1.5	1.5	1.5	2.1	3	3.9	OX	OX	OX	OX	OX	OX	OX	OX
5E+01	UX	UX	UX	s9	s3	0	0	0	0	0	0	0	0	0	0	0	0.9	1.8	2.1	2.7	3.9	4.2	3.9	3.6	OX
1E+02	UX	UX	UX	s9	s0	0	0	0	0	0	0	0	0	0	0	0	1.2	1.5	1.5	1.5	1.8	1.8	1.8	2.1	2.4
5E+02	UX	UX	UX	UX	UX	s9	0	0	0	0	0	0	0	0	0	0	0	0	0	0	0	0	0	0	0
1E+03	UX	UX	UX	UX	UX	UX	0	0	0	0	0	0	0	0	0	0	0	0	0	0	0	0	0	0	0
5E+03	UX	UX	UX	UX	UX	UX	UX	UX	UX	s3	s12	0	0	0	0	0	0	0	0	0	0	0	0	0	0
1E+04	UX	UX	UX	UX	UX	UX	UX	UX	UX	UX	UX	UX	s6	0	0	0	0	0	0	0	0	0	0	0	0
5E+04	UX	UX	UX	UX	UX	UX	UX	UX	UX	UX	UX	UX	UX	UX	UX	UX	UX	UX	UX	UX	UX	s9	0	0	0
5E+04	UX	UX	UX	UX	UX	UX	UX	UX	UX	UX	UX	UX	UX	UX	UX	UX	UX	UX	UX	UX	UX	UX	UX	UX	UX
5E+04	UX	UX	UX	UX	UX	UX	UX	UX	UX	UX	UX	UX	UX	UX	UX	UX	UX	UX	UX	UX	UX	UX	UX	UX	UX

b)

SS [µm/s]	LP [mW]																								
TiAl	25.5	26.5	27.5	28.5	29.5	30.5	31.5	32.5	33.5	34.5	35.5	36.5	37.5	38.5	39.5	40.5	41.5	42.5	43.5	44.5	45.5	46.5	47.5	48.5	49.5
1E-02	OX	OX	OX	OX	OX	OX	OX	OX	OX	OX	OX	OX	OX	OX	OX	OX	OX	OX	OX	OX	OX	OX	OX	OX	OX
5E-02	OX	OX	OX	OX	OX	OX	OX	OX	OX	OX	OX	OX	OX	OX	OX	OX	OX	OX	OX	OX	OX	OX	OX	OX	OX
1E-01	OX	OX	OX	OX	OX	OX	OX	OX	OX	OX	OX	OX	OX	OX	OX	OX	OX	OX	OX	OX	OX	OX	OX	OX	OX
5E-01	OX	OX	OX	OX	OX	OX	OX	OX	OX	OX	OX	OX	OX	OX	OX	OX	OX	OX	OX	OX	OX	OX	OX	OX	OX
1E+00	OX	OX	OX	OX	OX	OX	OX	OX	OX	OX	OX	OX	OX	OX	OX	OX	OX	OX	OX	OX	OX	OX	OX	OX	OX
5E+00	OX	OX	OX	OX	OX	OX	OX	OX	OX	OX	OX	OX	OX	OX	OX	OX	OX	OX	OX	OX	OX	OX	OX	OX	OX
1E+01	OX	OX	OX	OX	OX	OX	OX	OX	OX	OX	OX	OX	OX	OX	OX	OX	OX	OX	OX	OX	OX	OX	OX	OX	OX
5E+01	OX	OX	OX	OX	OX	OX	OX	OX	OX	OX	OX	OX	OX	OX	OX	OX	OX	OX	OX	OX	OX	OX	OX	OX	OX
1E+02	3.3	4.2	OX	OX	OX	OX	OX	OX	OX	OX	OX	OX	OX	OX	OX	OX	OX	OX	OX	OX	OX	OX	OX	OX	OX
5E+02	0	0	3.0	0	0.9	2.1	3.0	4.5	4.5	OX	OX	OX	OX	OX	OX	OX	OX	OX	OX	OX	OX	OX	OX	OX	OX
1E+03	0	0	0	0	0	0	0	0	0	0	0.6	3.3	0.9	4.5	3.6	3.9	OX	OX	OX	OX	OX	OX	OX	OX	OX
5E+03	0	0	0	0	0	0	0	0	0	0	0	0	0	0	0	0	0	0	0	0	0.6	1.8	1.2	3.9	1.5
1E+04	0	0	0	0	0	0	0	0	0	0	0	0	0	0	0	0	0	0	0	0	0	0	0	0	0
5E+04	0	0	0	0	0	0	0	0	0	0	0	0	0	0	0	0	0	0	0	0	0	0	0	0	0
5E+04	s9	s6	s6	s3	s3	0	0	0	0	0	0	0	0	0	0	0	0	0	0	0	0	0	0	0	0
5E+04	UX	UX	UX	UX	UX	UX	UX	UX	UX	UX	UX	UX	UX	UX	UX	UX	UX	UX	UX	UX	UX	UX	UX	UX	UX

Fig. A 4: a) Heat map of the TiAl field positions showing the UX and OX as well as intermediate domains, where the number indicates the closest distance to the substrate in µm, where the bridge line was viable. Field positions marked by "s" indicate bridge lines disconnected from the mount and fallen to the substrate. b) Continuation.

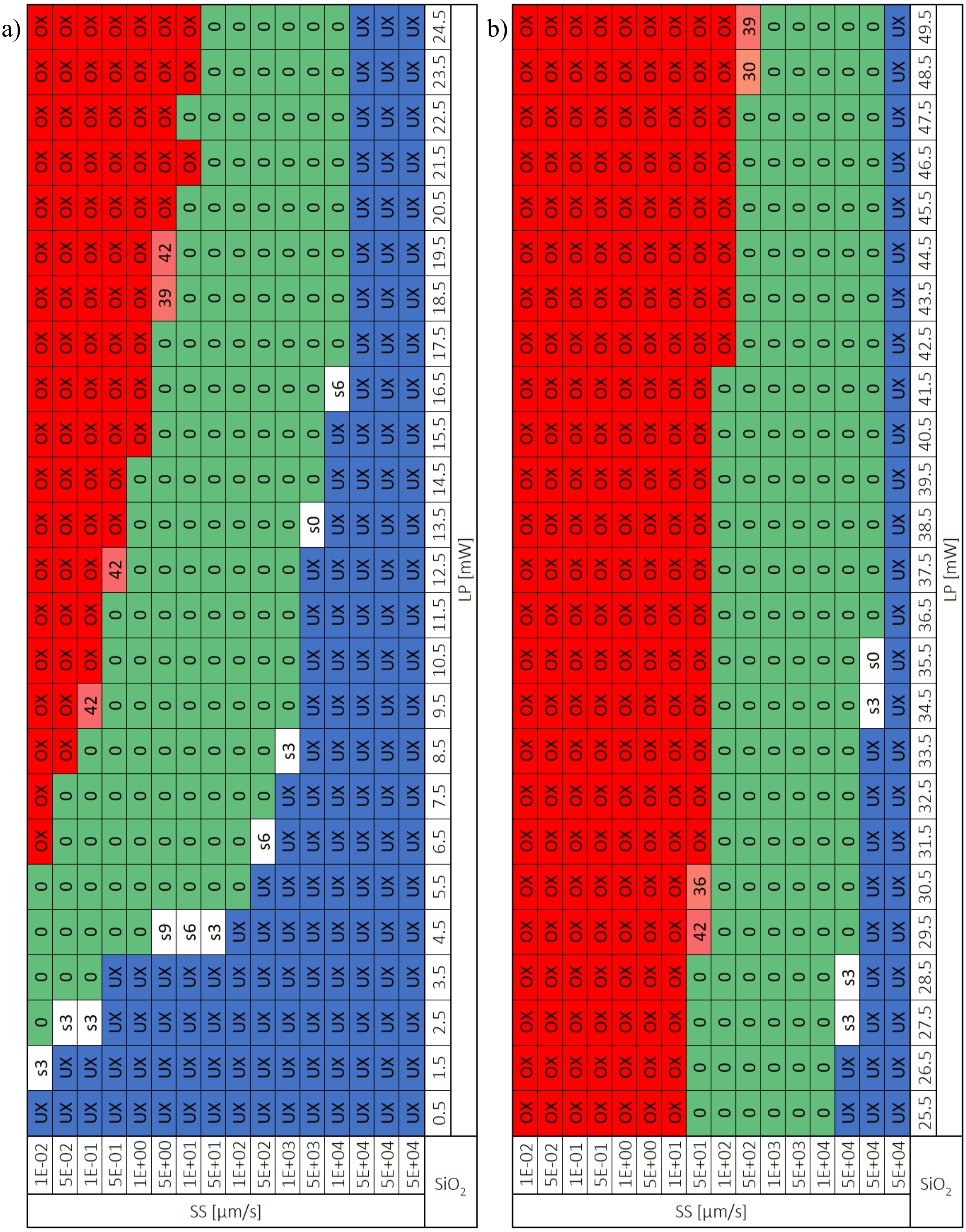

a)

SiO$_2$	SS [µm/s]															
LP [mW]	1E-02	5E-02	1E-01	5E-01	1E+00	5E+00	1E+01	5E+01	1E+02	5E+02	1E+03	5E+03	1E+04	5E+04	5E+04	5E+04
0.5	UX	UX	UX	UX	UX	UX	UX	UX	UX	UX	UX	UX	UX	UX	UX	UX
1.5	s3	UX	UX	UX	UX	UX	UX	UX	UX	UX	UX	UX	UX	UX	UX	UX
2.5	0	s3	s3	UX	UX	UX	UX	UX	UX	UX	UX	UX	UX	UX	UX	UX
3.5	0	0	0	UX	UX	UX	UX	UX	UX	UX	UX	UX	UX	UX	UX	UX
4.5	0	0	0	0	0	s9	s6	s3	UX	UX	UX	UX	UX	UX	UX	UX
5.5	0	0	0	0	0	0	0	0	0	UX	UX	UX	UX	UX	UX	UX
6.5	OX	0	0	0	0	0	0	0	0	s6	UX	UX	UX	UX	UX	UX
7.5	OX	0	0	0	0	0	0	0	0	0	UX	UX	UX	UX	UX	UX
8.5	OX	OX	0	0	0	0	0	0	0	0	s3	UX	UX	UX	UX	UX
9.5	OX	OX	42	0	0	0	0	0	0	0	0	UX	UX	UX	UX	UX
10.5	OX	OX	OX	0	0	0	0	0	0	0	0	UX	UX	UX	UX	UX
11.5	OX	OX	OX	0	0	0	0	0	0	0	0	UX	UX	UX	UX	UX
12.5	OX	OX	OX	42	0	0	0	0	0	0	0	UX	UX	UX	UX	UX
13.5	OX	OX	OX	OX	0	0	0	0	0	0	0	s0	UX	UX	UX	UX
14.5	OX	OX	OX	OX	0	0	0	0	0	0	0	0	UX	UX	UX	UX
15.5	OX	OX	OX	OX	OX	0	0	0	0	0	0	0	UX	UX	UX	UX
16.5	OX	OX	OX	OX	OX	0	0	0	0	0	0	0	s6	UX	UX	UX
17.5	OX	OX	OX	OX	OX	0	0	0	0	0	0	0	0	UX	UX	UX
18.5	OX	OX	OX	OX	OX	39	0	0	0	0	0	0	0	UX	UX	UX
19.5	OX	OX	OX	OX	OX	42	0	0	0	0	0	0	0	UX	UX	UX
20.5	OX	OX	OX	OX	OX	OX	0	0	0	0	0	0	0	UX	UX	UX
21.5	OX	OX	OX	OX	OX	OX	OX	0	0	0	0	0	0	UX	UX	UX
22.5	OX	OX	OX	OX	OX	OX	0	0	0	0	0	0	0	UX	UX	UX
23.5	OX	OX	OX	OX	OX	OX	OX	0	0	0	0	0	0	UX	UX	UX
24.5	OX	OX	OX	OX	OX	OX	OX	0	0	0	0	0	0	UX	UX	UX

b)

SiO$_2$	SS [µm/s]															
LP [mW]	1E-02	5E-02	1E-01	5E-01	1E+00	5E+00	1E+01	5E+01	1E+02	5E+02	1E+03	5E+03	1E+04	5E+04	5E+04	5E+04
25.5	OX	OX	OX	OX	OX	OX	OX	0	0	0	0	0	0	UX	UX	UX
26.5	OX	OX	OX	OX	OX	OX	OX	0	0	0	0	0	0	UX	UX	UX
27.5	OX	OX	OX	OX	OX	OX	OX	0	0	0	0	0	0	s3	UX	UX
28.5	OX	OX	OX	OX	OX	OX	OX	0	0	0	0	0	0	s3	UX	UX
29.5	OX	OX	OX	OX	OX	OX	OX	42	0	0	0	0	0	0	UX	UX
30.5	OX	OX	OX	OX	OX	OX	OX	36	0	0	0	0	0	0	UX	UX
31.5	OX	OX	OX	OX	OX	OX	OX	OX	0	0	0	0	0	0	UX	UX
32.5	OX	OX	OX	OX	OX	OX	OX	OX	0	0	0	0	0	0	UX	UX
33.5	OX	OX	OX	OX	OX	OX	OX	OX	0	0	0	0	0	0	UX	UX
34.5	OX	OX	OX	OX	OX	OX	OX	OX	0	0	0	0	0	0	s3	UX
35.5	OX	OX	OX	OX	OX	OX	OX	OX	0	0	0	0	0	0	s0	UX
36.5	OX	OX	OX	OX	OX	OX	OX	OX	0	0	0	0	0	0	0	UX
37.5	OX	OX	OX	OX	OX	OX	OX	OX	0	0	0	0	0	0	0	UX
38.5	OX	OX	OX	OX	OX	OX	OX	OX	0	0	0	0	0	0	0	UX
39.5	OX	OX	OX	OX	OX	OX	OX	OX	0	0	0	0	0	0	0	UX
40.5	OX	OX	OX	OX	OX	OX	OX	OX	0	0	0	0	0	0	0	UX
41.5	OX	OX	OX	OX	OX	OX	OX	OX	0	0	0	0	0	0	0	UX
42.5	OX	OX	OX	OX	OX	OX	OX	OX	OX	0	0	0	0	0	0	UX
43.5	OX	OX	OX	OX	OX	OX	OX	OX	OX	0	0	0	0	0	0	UX
44.5	OX	OX	OX	OX	OX	OX	OX	OX	OX	0	0	0	0	0	0	UX
45.5	OX	OX	OX	OX	OX	OX	OX	OX	OX	0	0	0	0	0	0	UX
46.5	OX	OX	OX	OX	OX	OX	OX	OX	OX	0	0	0	0	0	0	UX
47.5	OX	OX	OX	OX	OX	OX	OX	OX	OX	0	0	0	0	0	0	UX
48.5	OX	OX	OX	OX	OX	OX	OX	OX	OX	30	0	0	0	0	0	UX
49.5	OX	OX	OX	OX	OX	OX	OX	OX	OX	39	0	0	0	0	0	UX

Fig. A 5: a) Heat map of the SiO$_2$ field positions showing the UX and OX as well as intermediate domains, where the number indicates the closest distance to the substrate in µm, where the bridge line was viable. Field positions marked by “s” indicate bridge lines disconnected from the mount and fallen to the substrate. b) Continuation.

I. Objective and Resist Alternative – Section 5.4.3

Laser power vs. scan speed vs. line distance to substrate parameter sweep rows for three scan speeds 10, 50, 100 and 500 µm/s showing concave and convex deformations, indicated by “c” and “v”, respectively, see Fig. A 6. The row for 1000 µm/s only showed five deformations similar to 500 µm/s and thus was omitted. Parameter sweep fabricated from IP-Q utilizing the 10x objective.

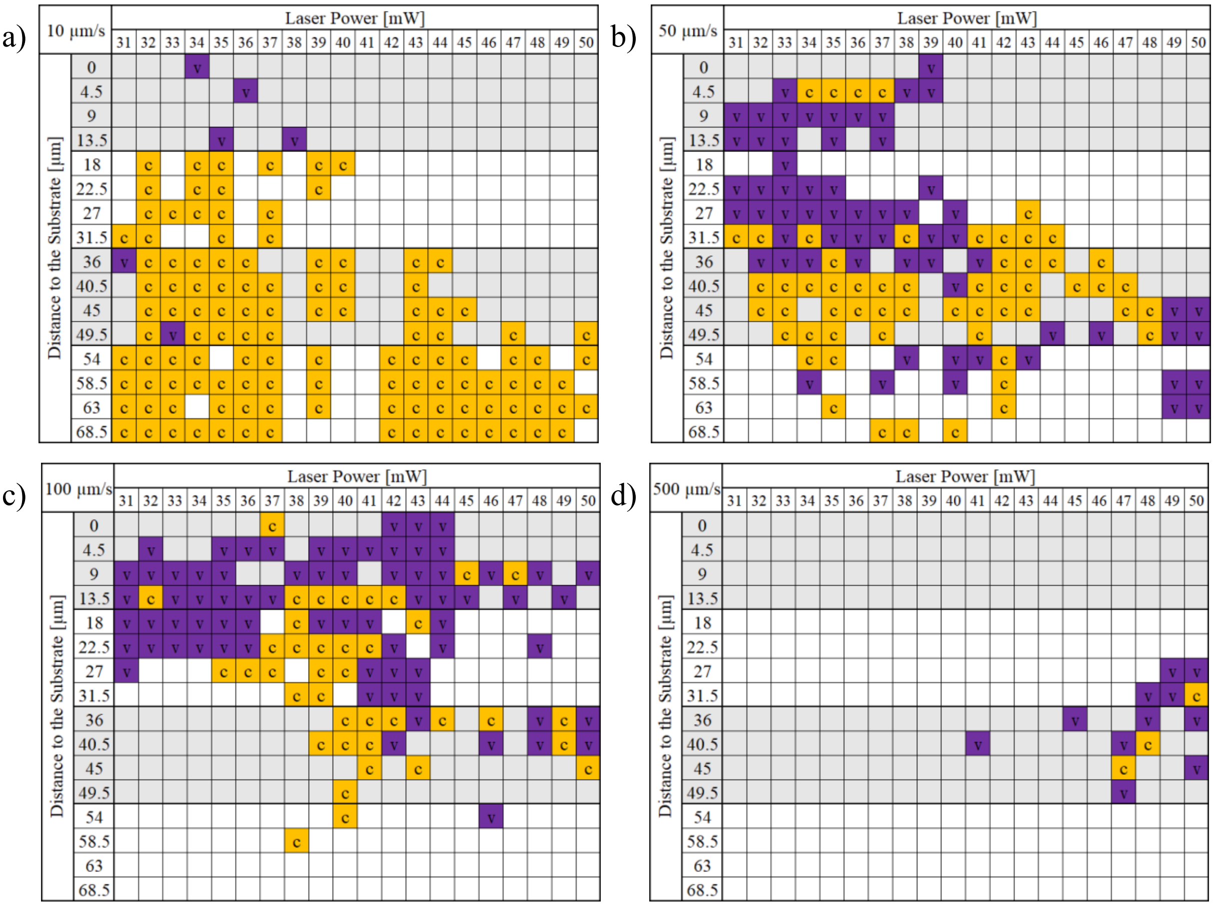

a)

10 µm/s		Laser Power [mW]																			
		31	32	33	34	35	36	37	38	39	40	41	42	43	44	45	46	47	48	49	50
Distance to the Substrate [µm]	0				v																
	4.5						v														
	9																				
	13.5					v			v												
	18		c		c	c		c		c	c										
	22.5		c		c	c				c											
	27		c	c	c	c		c													
	31.5	c	c			c		c													
	36	v	c	c	c	c	c			c	c			c	c						
	40.5		c	c	c	c	c	c		c	c			c							
	45		c	c	c	c	c	c		c	c			c	c	c					
	49.5		c	v	c	c	c	c						c	c			c			c
	54	c	c	c	c		c	c		c			c	c	c	c		c	c		c
	58.5	c	c	c	c	c	c	c		c			c	c	c	c	c	c	c	c	
	63	c	c	c		c	c	c		c			c	c	c	c	c	c	c	c	c
	68.5	c	c	c	c	c	c	c					c	c	c	c	c	c	c	c	

b)

50 µm/s		Laser Power [mW]																			
		31	32	33	34	35	36	37	38	39	40	41	42	43	44	45	46	47	48	49	50
Distance to the Substrate [µm]	0									v											
	4.5			v	c	c	c	c	v	v											
	9	v	v	v	v	v	v	v													
	13.5	v	v	v		v		v													
	18			v																	
	22.5	v	v	v	v	v				v											
	27	v	v	v	v	v	v	v	v		v			c							
	31.5	c	c	v	c	v	v	v	c	v	v	c	c	c	c						
	36		v	v	v	c	v		v	v		v	c	c	c		c				
	40.5		c	c	c	c	c	c	c		v	c	c	c		c	c	c			
	45		c	c		c	c	c	c		c	c	c	c				c	c	v	v
	49.5			c	c	c		c				c			v		v		c	v	v
	54				c	c			v		v	v	c	v							
	58.5				v			v			v		c							v	v
	63					c							c							v	v
	68.5							c	c		c										

c)

100 µm/s		Laser Power [mW]																			
		31	32	33	34	35	36	37	38	39	40	41	42	43	44	45	46	47	48	49	50
Distance to the Substrate [µm]	0							c					v	v	v						
	4.5		v			v	v	v		v	v	v	v	v	v						
	9	v	v	v	v	v			v	v	v		v	v	v	c	v	c	v		v
	13.5	v	c	v	v	v	v	v	c	c	c	c	c	v	v	v		v		v	
	18	v	v	v	v	v	v		c	v	v	v		c	v						
	22.5	v	v	v	v	v	v	c	c	c	c	c	v		v				v		
	27	v				c	c	c		c	c	v	v	v							
	31.5								c	c		v	v	v							
	36										c	c	c	v	c		c		v	c	v
	40.5									c	c	c	v				v		v	c	v
	45											c		c							c
	49.5										c										
	54										c						v				
	58.5								c												
	63																				
	68.5																				

d)

500 µm/s		Laser Power [mW]																			
		31	32	33	34	35	36	37	38	39	40	41	42	43	44	45	46	47	48	49	50
Distance to the Substrate [µm]	0																				
	4.5																				
	9																				
	13.5																				
	18																				
	22.5																				
	27																			v	v
	31.5																		v	v	c
	36															v			v		v
	40.5											v						v	c		
	45																	c			v
	49.5																	v			
	54																				
	58.5																				
	63																				
	68.5																				

Fig. A 6: a) IP-Q and 10x objective fabricated laser power vs. line distance to substrate parameter sweep row for the scan speed 10 µm/s showing concave and convex deformations, indicated by “c” and “v”, respectively. b) The same for 50 µm/s. c) The same for 100 µm/s. d) The same for 500 µm/s.

J. Transitional Domains – Section 5.4.5

The transitional domains of the other scan speeds of the exposure dose experiment are presented in Fig. A 7.

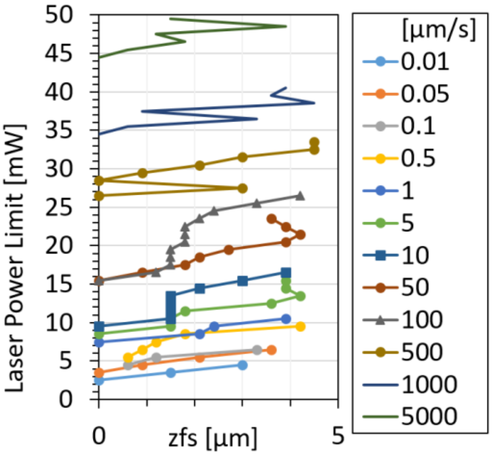

Fig. A 7: Laser power limits in the transitional areas of each scan speed row of the exposure dose experiment fabricated from IP-Dip on a Si wafer coated in 520 nm TiAl.

K. IP-PDMS Coating – Section 6.2.3

The following shows a combination of a contour structure fabricated from IP-Q, developed and subsequently filled with an IP-PDMS coating cured using TPP, see Fig. A 8. Shrinkage of IP-PDMS leads to structure deformation and subsequent destruction.

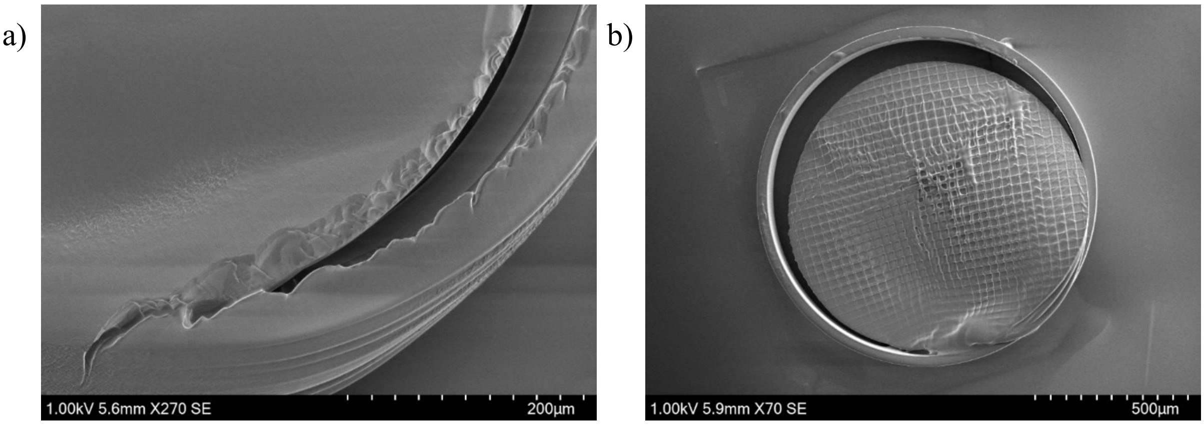

Fig. A 8: a) Contour structure fabricated from IP-Q on a CMUT, developed and subsequently filled with an IP-PDMS coating cured using TPP. b) The same with a different parameter set.

L. Waveguide Fabrication Steps – Section 6.4

The steps performed to fabricate a waveguide structure on a CMUT are:

1. Insertion of the CMUT into the KMTO and application of resist to it and the objectives.
2. Tilt compensation using the 63x objective.
3. Fabrication of the waveguide structure using the 10x objective.
4. Extraction of the CMUT including the waveguide from the TPP system.
5. Development of the CMUT exclusively below the mouth of the waveguide, followed by drying.
6. Application of adhesive, followed by drying.
7. Development of the complete waveguide in IPA/Novec, followed by drying.

M. Coated CMUT – Section 6.5.3

An assembled CMUT manually coated with two (6.28 ± 0.70) mg drops of IP-PDMS and solidified using UV flood polymerization, see Fig. A 9.

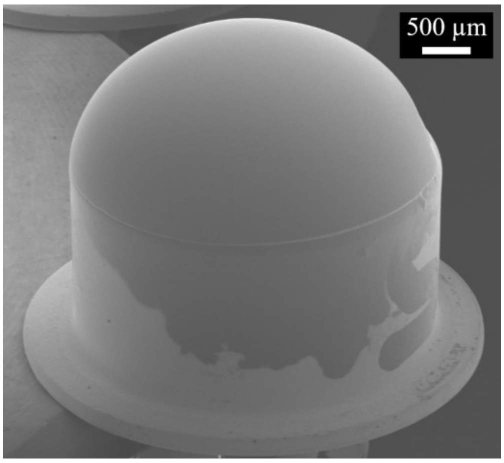

Fig. A 9: CMUT chip assembled on a TO-18 with 2x (6.28 ± 0.70) mg IP-PDMS manually applied and solidified using UV flood polymerization.

N. TPP on NED Trial – Section 7.1.2

The first TPP trial on a NED-µPS, showing offsets between layers, hatch lines and influenced block stitching, see Fig. A 10.

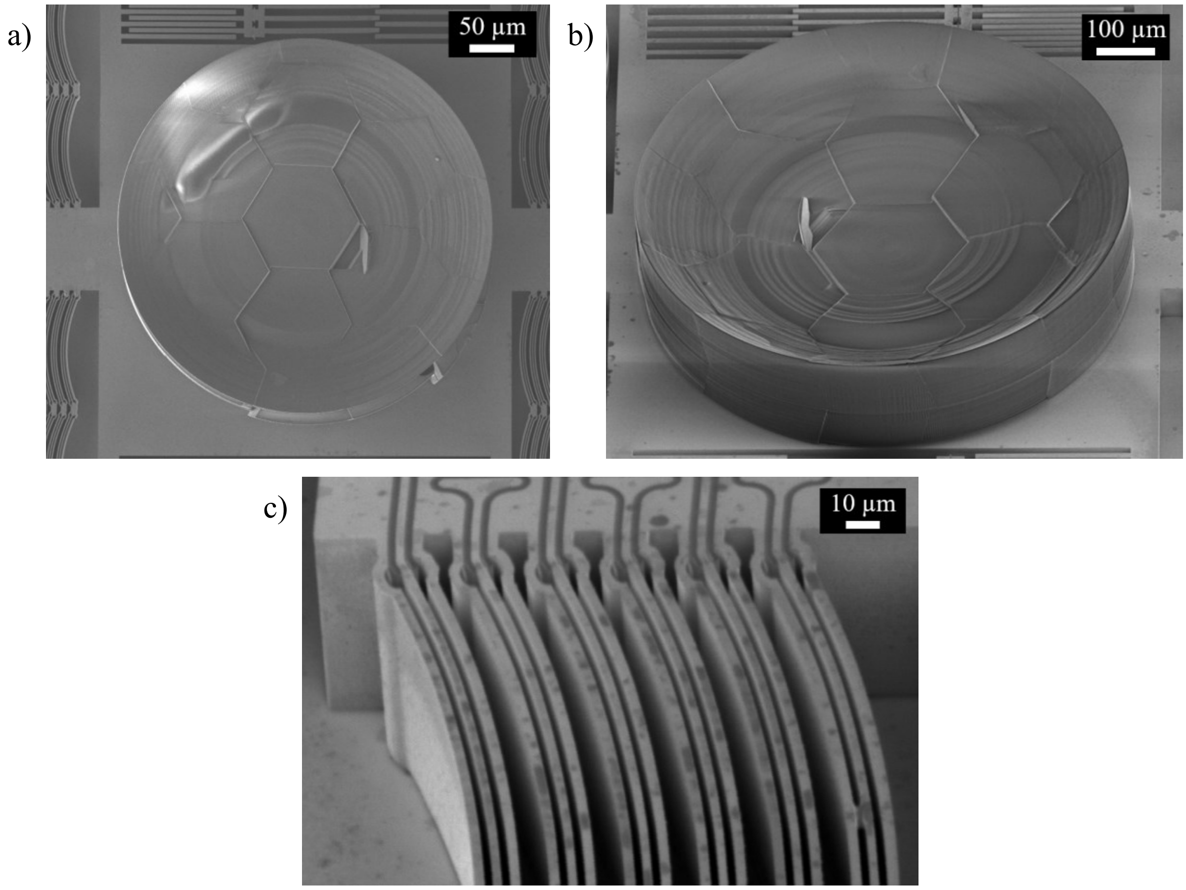

Fig. A 10: a) Top view SEM micrograph of a NED-µPS with a structure fabricated from IP-Q on its load area using TPP. b) Tilted view of the same. d) Tilted view micrograph of the same chip showing the NED elements.